Sensitivity Studies of CdZnTe Semiconductor Detectors for the COBRA Experiment

Dissertation
zur Erlangung des akademischen Grades
eines Doktors der Naturwissenschaften
der Fakultät Physik
an der Technischen Universität Dortmund

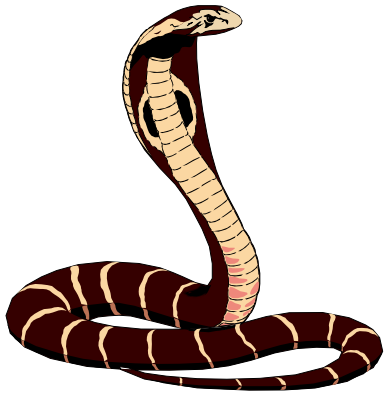

vorgelegt von

Dipl. Phys. Tobias Köttig
Lehrstuhl für Experimentelle Physik IV
Fakultät für Physik

technische universität
dortmund

Dortmund, September 2012

Sensitivity Studies of CdZnTe Semiconductor Detectors for the COBRA Experiment

Dissertation zur Erlangung des akademischen Grades eines Doktors der Naturwissenschaften der Fakultät Physik an der Technischen Universität Dortmund

vorgelegt von

Dipl. Phys. Tobias Köttig

Lehrstuhl für Experimentelle Physik IV

Fakultät für Physik

TU Dortmund

Dortmund, September 2012

Gutachter:	Prof. Dr. C. Gößling, TU Dortmund
Zweitgutachter:	Prof. Dr. K. Zuber, TU Dresden
Beisitzer:	Dr. B. Siegmann, TU Dortmund
Termin der mündlichen Prüfung:	25. Oktober 2012

Contents

1. Introduction

1.1. Neutrino Physics

Neutrinos play an important role in many fields of physics, for example particle- and astroparticle physics or cosmology. Detailed descriptions of the field can be found in many papers and textbooks, many aspects of neutrino physics are explained in detail e.g. in [Zub12]. Here only a brief overview of the most important properties regarding this work (and a few historical aspects) are given.

1.1.1. Neutrino Properties

The neutrino is one of the longest known elementary particles. It was initially introduced by Wolfgang Pauli in 1930 as "neutron" to solve an apparent failure of energy and angular momentum conservation in nuclear β-decay. The now established name neutrino (Italian diminutive for neutron, i.e. "neutrino" = "small neutron") was later formed by Enrico Fermi. The neutrino is the only elementary fermion in the Standard Model of Particle Physics (SM) that carries no charge. It interacts only via the weak force and can therefore pass through matter with nearly no interaction at all. This leads to a large experimental challenge for neutrino experiments. Therefore, it took more than 25 years until the existence of the neutrino could be verified experimentally [Rei56, Cow56b].

Although more than 50 years have passed since the discovery, several neutrino properties are still unknown. For example its nature as either Dirac or Majorana particle (see Subsection 1.1.2) and its absolute mass are still unknown. Initially the neutrino was introduced in the SM as massless particle. This assumption was disproved with the observation of neutrino oscillations, see below, but still only limits on the absolute value of its mass are known.

Neutrinos play an important role in most particle- and nuclear physics processes that influence our daily life. For example they are emitted from nuclear power plants and in β-decays of isotopes from the natural radioactive decay chains. A large flux of 6.5×10^{10} neutrinos per second per cm^2 [Bel04, Ber12] arrives on earth from the nuclear reactions that power the sun. The flux from primordial neutrinos from the big bang (relic neutrinos) is even higher. To verify solar models the flux of electron neutrinos from the sun was measured and compared to theoretical predictions. The flux determined in [Dav68] was significantly lower than expected. This result was confirmed later on by other experiments. At first, inaccuracies in the solar model were expected [Bah68],

but no other evidence for such flaws were found. In [Hir88] also a much smaller flux of cosmic ray induced atmospheric muon neutrinos compared to the predicted flux was measured with the Kamiokande experiment. Both inconsistencies could be resolved with the concept of massive neutrinos and neutrino mixing (also called neutrino oscillation).

Analogously to the well known Cabibbo–Kobayashi–Maskawa (CKM) mixing matrix [Cab63, Kob73, Hal84] of the quark sector, the Pontecorvo-Maki-Nakagava-Sakata (PMNS) matrix [Pon60, Mak62], can be defined for neutrino mixing. Initially it was defined for the two neutrino flavours ν_e and ν_μ that were known at that time, but it was extended to three flavours. The principle idea is that the eigenstates of the weak interaction, ν_e, ν_μ and ν_τ, are different from the mass eigenstates ν_1, ν_2 and ν_3. Neutrinos propagate through space and time with their mass eigenstates and interact via the electroweak force with their flavour eigenstates. Both eigenstates are connected by the unitary PMNS matrix

$$\begin{pmatrix}\nu_e\\ \nu_\mu\\ \nu_\tau\end{pmatrix} = \begin{pmatrix}U_{e1} & U_{e2} & U_{e3}\\ U_{\mu1} & U_{\mu2} & U_{\mu3}\\ U_{\tau1} & U_{\tau2} & U_{\tau3}\end{pmatrix} \begin{pmatrix}\nu_1\\ \nu_2\\ \nu_3\end{pmatrix}, \quad \nu_\alpha = \sum_{i=1}^{3} U_{\alpha i}\nu_i \quad \text{with } \alpha = e,\, \mu,\, \tau\,. \tag{1.1}$$

If the neutrino masses are not identical, the mass components propagate with different phase velocities. That means that during the propagation through space the "ratio" (amplitude) of ν_1, ν_2 and ν_3 can change over time. Consequently a neutrino that was produced in one flavour eigenstate can interact in a different flavour eigenstate after it propagated through space. Some electron neutrinos from the sun therefore are detected on earth as muon neutrinos.

The PMNS matrix can also be expressed as a product of three mixing matrices with three mixing angles (θ_{12} describing solar mixing of neutrinos from the sun, θ_{23} describing atmospheric neutrino mixing of neutrinos from interactions in earth's atmosphere and the smallest angle θ_{13}) and an additional CP-violating phase δ. If the neutrino is its own antiparticle, a so called Majorana particle, two additional Majorana phases α_1 and α_2 have to be added.

Neutrino oscillation was experimentally confirmed for atmospheric muon neutrinos ν_μ with the Super-Kamiokande detector [Fuk98] and afterwards by many other experiments, e.g. with a high statistical significance in [Ahm01, Ahn06]. Numbers for θ_{12} and θ_{23} are given in [Hos06], only recently it could be shown that $\theta_{13} > 0$ [Abe11, An12, Ahn12]. An up-to date compilation of the neutrino parameters are listed for example in the neutrino chapter of the latest PDG Review of Particle Physics [Ber12].

The oscillation probability amplitude is dependent on the mixing angles. The period of the oscillation is dependent on the energy E_ν of the neutrino, the travelled distance L and the mass squared difference $\Delta {m_{ik}}^2 = {m_i}^2 - {m_k}^2$ of the mass eigenstates. For example the survival probability for down-going atmospheric electron neutrinos is given by [Hos06]

$$P(\nu_e \to \nu_e) = 1 - \sin^2(2\theta_{13})\, \sin^2\left(\frac{1.267\, \Delta {m_{31}}^2[\mathrm{eV}^2]\, L[\mathrm{km}]}{E_\nu[\mathrm{GeV}]}\right). \tag{1.2}$$

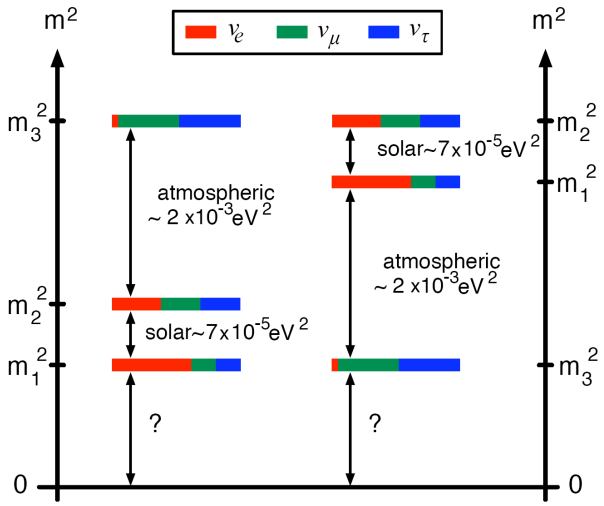

Figure 1.1: Neutrino mass differences in normal and inverted neutrino mass hierarchy, taken from [Mü07]. The left side shows the so called normal (${m_1}^2 < {m_2}^2 < {m_3}^2$) and the right side the inverted (${m_3}^2 < {m_1}^2 < {m_2}^2$) hierarchy. With neutrino oscillation experiments the mass differences $\Delta {m_{ik}}^2$ were determined ($\Delta {m_{21}}^2 \approx 7.6 \times 10^{-5}\,\mathrm{eV}^2$ and $|\Delta {m_{31}}^2| \approx 2.4 \times 10^{-3}\,\mathrm{eV}^2$ [Ber12]), and it is maybe possible to determine the mass hierarchy, but these experiments cannot give information on the absolute neutrino mass.

It can be seen that neutrino oscillation experiments are sensitive to the mass squared difference, but they cannot provide a value for the absolute neutrino mass.

The hierarchy (or ordering) of the mass eigenstates, see Figure 1.1, could also not be clarified yet. The recently determined comparatively large value of θ_{13} increases the chances that the mass hierarchy can be determined in long baseline neutrino oscillation experiments, such as NOνA [Dav11]. They can derive information on the hierarchy from differences of the oscillation probability of neutrinos and anti-neutrinos while propagating through solid matter [Hos06].

There are mainly three methods that are currently applied to probe for the absolute mass of the mass eigenstates. A good overview of neutrino masses in general can be found in [Ott08].

From relic neutrinos in cosmology a value for $\sum m_i$ can be deduced. An analysis of WMAP data resulted in a limit of $\sum m_i < 0.58\,\mathrm{eV}$ (95 % Confidence Level (CL)) [Kom11]. These values from cosmology are strongly model dependent.

From kinetic energy end-point measurements of β-decays another measure for the neutrino mass, to be more precise of the mass of the electron neutrino, can be deduced. As the energy that is equivalent to the mass of the outgoing neutrino cannot contribute to the kinetic energy of the electron (β-particle), a deviation of the end-point of the β-particle's kinetic energy spectrum compared to the case of a vanishing neutrino mass exists. The mass that can be measured with such experiments is connected to the mass eigenstates and the PMNS matrix elements as follows [Kra05]

$$m^2(\nu_e) = \sum_{i=1}^{3} |U_{ei}|^2 \, m_i^2 \tag{1.3}$$

The best limit $m(\nu_e) \leq 2.3\,\mathrm{eV}$ (95 % CL) for this neutrino mass was obtained by the Mainz experiment [Kra05]. The currently commissioned KATRIN experiment [Wol10]

will probe a region down to 0.2 eV. The planned MARE experiment [Nuc10] aims for a comparable sensitivity.

The third method for a mass measurement arises if the neutrino is its own antiparticle, a so called Majorana particle. Then a neutrinoless double beta decay is possible and, as will be explained in the next section, with a measurement of the half-life of this decay a measure for the neutrino mass can be obtained.

1.1.2. Neutrinoless Double Beta Decay

Neutrinoless double beta decay gained more and more attention over the last years. Consequently there are several publications describing the theory and the applied experimental approaches in detail, see the citations in the following section and especially [Rod12] for a detailed description of the field, also regarding influences of the PMNS mixing angles and the mass hierarchy.

Since the beginning of neutrino physics the possibility of the identity of the neutrino ν and its antiparticle, the anti neutrino $\bar{\nu}$, was discussed. Particle and antiparticle, for example the electron e^- and its antiparticle, the positron e^+, have conjugate charge. As neutrinos do not carry charge, applying charge conjugation does not affect them and it is theoretically possible that they are their own antiparticles. Majorana even refused the Dirac theory of particle and antiparticle (with the negative energy state that is connected to this theory) for neutral particles, but described them as two states of the same particle corresponding to its spin [Maj37, Fur39].

First experiments [Dav55, Cow56a] disfavoured this possibility as no hints to predicted processes in this so called Majorana case were observed. Nowadays it is assumed that the Majorana hypothesis is probable, but that the directly measurable effects are very small and need extensive experiments with a high sensitivity for their detection.

One reason for the willingness of the acceptance of the Majorana hypothesis is the possibility to introduce an additional mass term. In the SM the masses of the e, μ and τ fermions are generated by coupling of a left-handed weak isospin doublet and a right-handed isospin singlet to the Higgs doublet [Hal84]. The weak force couples only to left-handed particles (and right handed antiparticles). As neutrinos interact only by the weak force a right handed neutrino would not be able to interact at all. Therefore it is convenient that right handed neutrinos are not included in the SM and only right handed singlets for the upper members of the doublets (i.e. e_R, μ_R, τ_R) exist. This also means that the Higgs does not couple to neutrinos and they are massless in the SM. This was a reasonable prediction at the time of development of the SM because the neutrino masses are indeed very small.

Now that a non zero neutrino mass is established it seems straight forward to give a Dirac mass to the neutrino by simply adding a right handed neutrino singlet. From the point of view that the difference between the lepton Yukawa couplings, which are a measure for the particle mass, is about four orders of magnitude higher without a theoretical explanation, it is very unsatisfactory that the Yukawa couplings for neutrinos

should be even at least five orders smaller (compare the electron mass $m_e = 511\,\mathrm{keV}$ and the limit $m(\nu_e) < 2.3\,\mathrm{eV}$).

The assumption of the Majorana nature of the neutrino allows for an additional Majorana neutrino mass term in the Lagrangian. It leads to a light left handed neutrino ν_1 and a heavy right handed neutrino ν_2 with the masses [Ott08]

$$m_{\nu_1} \approx \frac{m_D^2}{m_{RR}}\,, \quad m_{\nu_2} \approx m_{RR}\,. \tag{1.4}$$

m_D is the Dirac mass of the neutrino (similar to the other fermion masses in the SM) and the mass m_{RR} derives from the Majorana assumption. The heavier m_{RR} (m_{ν_2}) is, the lighter m_{ν_1} becomes and m_D can be in the order of the other fermion masses. For this reason the approach is called (type I) seesaw mechanism. Also other approaches (seesaw II and III mechanism) exist.

If the neutrino is in fact its own antiparticle, the non SM process of neutrinoless double beta decay ($0\nu\beta\beta$-decay) is possible and it is directly connected to the neutrino mass. For isobaric nuclei with an even mass number A, the nuclear pairing energy leads to a splitting of the mass parabola, which describes the masses of nuclei according to the Bethe-Weizsäcker mass formula [Wei35, Bet36, Pov08], see Figure 1.2.

Due to the splitting it is possible that for a nucleus with nuclear charge Z an energetically lower state with $Z \pm 2$ exists, but the state with $Z \pm 1$ is energetically higher. The nucleus cannot decay to the energetically higher $Z \pm 1$ state, but M. Goeppert-Mayer calculated in [GM35] the possibility of two simultaneous β-decays, i.e. a double beta decay with emission of two electrons and two anti neutrinos (two-neutrino double beta decay ($2\nu\beta\beta$-decay))

$$(Z, A) \;\rightarrow\; (Z+2, A) + 2\,e^- + 2\,\bar{\nu}_e\,. \tag{1.5}$$

This formula is for the case of β^- decay, in principle the decay is also possible for β^+ and Electron Capture (EC) decays. The decay can be described as a second order SM process. It is strongly suppressed and has a very long half-life. The observation of $2\nu\beta\beta$-decay was first reported in [Ing50] for $^{130}\mathrm{Te} \rightarrow {}^{130}\mathrm{Xe}$ by an isotopic analysis of xenon traces contained in old tellurium ores. Due to the long half-life of the $2\nu\beta\beta$-decay it took more than 35 years until also a direct measurement of a $2\nu\beta\beta$-decay was successful, in this case for ^{82}Se [Ell87]. Since then $2\nu\beta\beta$-decay was observed for several isotopes with half-lives in the order of $10^{19} - 10^{21}$ years, see for example Table 1.1.

If the neutrino is a Majorana particle with non vanishing rest mass a second possibility arises. In this case our definition of "neutrino" and "anti neutrino" will refer to its state of left- or right handedness, i.e. to its helicity. For a massive particle the wave function of the outgoing "neutrino" is a superposition of a left handed and a small fraction of a right handed particle. Therefore it is possible that an outgoing right handed "anti neutrino" from a β^- decay is absorbed as a left handed "neutrino" in a following inverse β-decay.

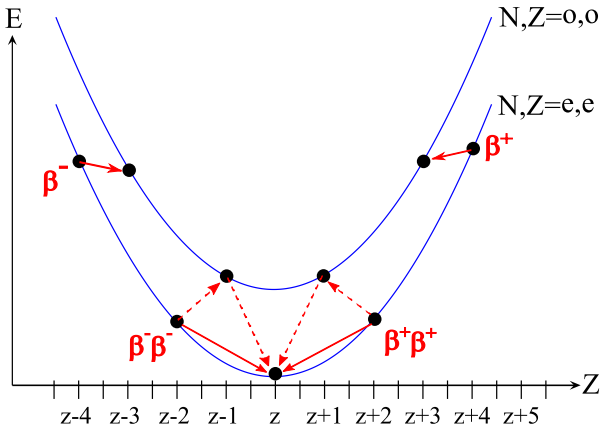

Figure 1.2: Mass parabola for isobaric nuclei with even atomic mass number $A = N + Z$ (i.e. (N, Z) = (odd, odd) or (N, Z) = (even, even)). The nuclear pair energy causes a splitting into two parabolas. Single β-decays change the nuclear charge Z by a value of ± 1. They can only occur if the energy of the daughter nucleus is smaller than the energy of the parent nucleus. If this condition is not fulfilled but the nucleus with $Z \pm 2$ has a lower energy level, a double beta decay via a virtual intermediate $Z \pm 1$ state is possible.

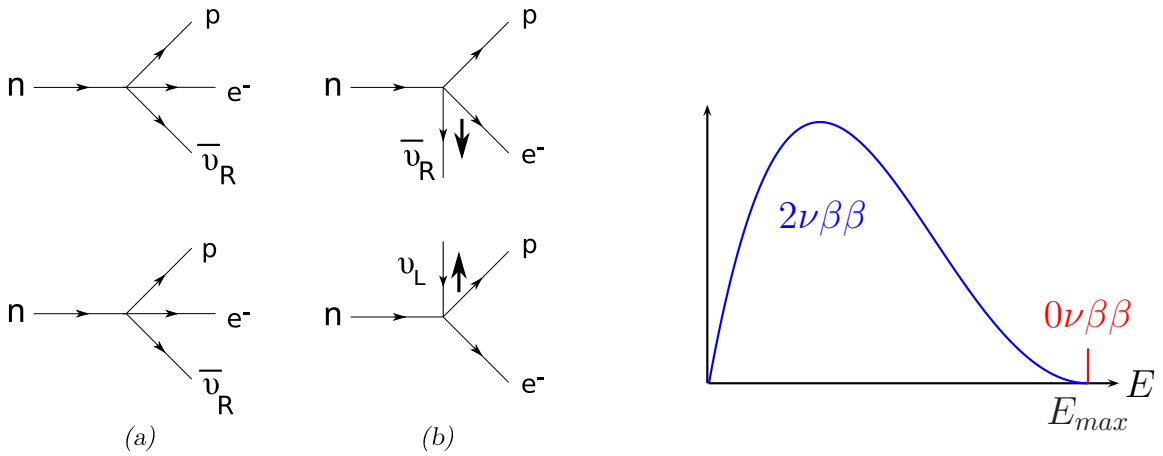

Figure 1.3.: Left: Diagrams of the two neutrino ($2\nu\beta\beta$, a) and the neutrinoless ($0\nu\beta\beta$, b) double beta decay. For the $0\nu\beta\beta$-decay the anti neutrino $\bar{\nu}_R$ emitted from one neutron has to be absorbed from the second neutron as neutrino ν_L. If the neutrino is a Majorana particle with non vanishing rest mass, this can be achieved by a helicity flip. Right: In $2\nu\beta\beta$-decay the neutrinos carry away some energy, which cannot be measured inside the detector. Therefore the measured energy spectrum of the $2\nu\beta\beta$-decay is continuous. This decay mode was already observed in several experiments, see Table 1.1. In the case of $0\nu\beta\beta$-decay the whole decay energy is measured in the detector if the electrons do not escape the detector. The observed energy will be a line at the decay energy of the isotope. This decay mode, if present at all, is strongly suppressed compared to $2\nu\beta\beta$-decay, therefore the $0\nu\beta\beta$-decay line is drawn smaller than the $0\nu\beta\beta$-decay spectrum, see also Figure 1.4.

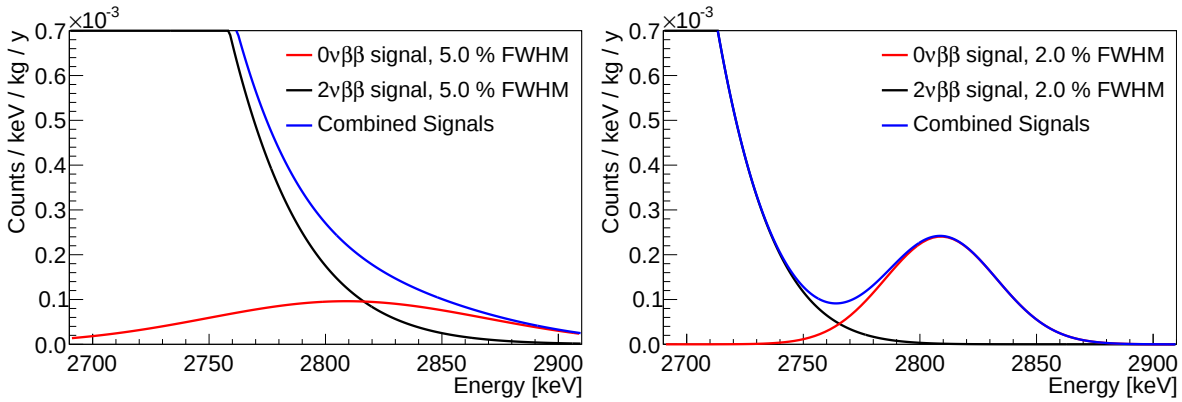

Figure 1.4.: Combined theoretical ^{116}Cd $2\nu\beta\beta$-decay ($T^{2\nu\beta\beta}_{1/2} = 2.88 \times 10^{19}$ y) and $0\nu\beta\beta$-decay spectrum for $T^{0\nu\beta\beta}_{1/2} = 1.0 \times 10^{26}$ y with different energy resolutions. For the plots the theoretical $2\nu\beta\beta$ spectrum was taken from [Tre95] and convoluted numerically with a Gaussian shaped energy resolution. Isotopic enrichment ot 90 % in ^{116}Cd is assumed. To disentangle both decay modes for a high $T^{0\nu\beta\beta}_{1/2}$, a good energy resolution is necessary. This holds especially if it is taken into account that the collected statistic will be limited to a few $0\nu\beta\beta$-decays, what leads to large statistical fluctuations. Therefore disentanglement on the basis of expected $2\nu\beta\beta$-decays in the $0\nu\beta\beta$-decay region will significantly reduce the sensitivity of the experiment.

This process was first mentioned in [Rac37] and therefore is often called Racah-sequence

$$\begin{aligned}(Z, A) &\rightarrow (Z+1, A) + e^- + \overset{(-)}{\nu}_{e,R}, \\ (Z+1, A) + \nu_{e,L} &\rightarrow (Z+2, A) + e^- .\end{aligned}$$

Two years later the Majorana formalism was actually applied to double beta decay in [Fur39]. Interestingly, a much lower half-life for $0\nu\beta\beta$-decay than for $2\nu\beta\beta$-decay was predicted, and rather the detection of $2\nu\beta\beta$-decay than the detection of $0\nu\beta\beta$-decay was assumed to be impossible.

At first glance this is a reasonable assumption also from the experimentalists point of view. For $2\nu\beta\beta$-decay the sum energy spectrum of the emitted electrons is distributed over a wide energy range, whereas a sharp line at the Q-value is expected for $0\nu\beta\beta$-decay, see Figure 1.3. The sharp $0\nu\beta\beta$-decay line should in principle be better detectable than the broad $2\nu\beta\beta$-decay spectrum, but in fact, due to the very long half-life of the $0\nu\beta\beta$-decay the $2\nu\beta\beta$-decay becomes even an irreducible background that can severely limit the sensitivity of double beta experiments with a low energy resolution and comparatively low $2\nu\beta\beta$-decay half-life, see Table 1.1 and Figure 1.4.

The half-life of the $0\nu\beta\beta$-decay

$$\left(T^{0\nu}_{1/2}\right)^{-1} = G^{0\nu}(Q, Z) \left|M^{0\nu}\right|^2 \left(\frac{\langle m_{\nu_e} \rangle}{m_e}\right)^2 \tag{1.6}$$

Isotope	Q-Value [keV]	Nat. Abund. [%] [Bö05]	$G^{0\nu}$ [$10^{-14}\,y^{-1}$] [Suh98]	$T^{2\nu\beta\beta}$ [10^{19} y]
^{48}Ca	4274 [Giu10]	0.19	6.43	4.4 [Bon11]
^{76}Ge	2039 [KK01b]	7.83	0.63	155 [KK01b]
^{82}Se	2995 [Giu10]	8.73	2.73	9.6 [Bon11]
^{96}Zr	3350 [Bon11]	2.80	5.70	2.35 [Bon11]
^{100}Mo	3034 [Giu10]	9.67	11.30	0.72 [Bon11]
^{116}Cd	2814 [Rah11]	7.49	4.68	2.88 [Bon11]
^{130}Te	2527 [Rah11]	33.80	4.14	70 [Arn11]
^{136}Xe	2459 [McC10]	8.86	4.37	238 [Gan12]
^{150}Nd	3371 [Kol10]	5.56	19.40	0.92 [Bon11]

Table 1.1.: Summary of the most promising $0\nu\beta^-\beta^-$ isotopes. An objective comparison of the prospects of the isotopes is difficult, see also text. To compare isotopes on the basis of Equation (1.6), besides the given phase space $G^{0\nu}$ also matrix elements are necessary. Calculated matrix elements for several isotopes are plotted in Figure 1.5. In general a low two neutrino half-life $T^{2\nu\beta\beta}$ requires a higher energy resolution to disentangle the $2\nu\beta\beta$ and the $0\nu\beta\beta$-decay, see Figure 1.4 for an example of ^{116}Cd. A compilation of various $2\nu\beta\beta$-decay measurements can also be found in [Bar10]. The natural abundance of most isotopes shows that isotopical enrichment is needed for a high sensitivity. Here also the number of source nuclei per kg (or volume) of the actual detector should be taken into account, which is dependent on the actual detector material composition (e.g. CaF_2, TeO_2, $CdWO_4$, CdZnTe etc.).

is connected to the so called effective Majorana neutrino mass

$$\langle m_{\nu_e} \rangle = \left| \sum_i U_{ei}^2 \, m_i \right| . \tag{1.7}$$

Note the difference to the mass definitions from cosmology and kinematic measurements (1.3). For the effective Majorana neutrino mass a negative interference between the m_i is possible, which can even lead to $\langle m_{\nu_e} \rangle = 0$ by complete cancellation.

The phase space integral $G^{0\nu}(Q, Z)$ can be calculated numerically. It is very energy and charge dependent. For small Q-values it scales with $G^{0\nu} \propto Q$, whereas for very high Q values $G^{0\nu} \propto Q^5$ can be approximated [Doi93]. But also the Z dependence is high, compare e.g. $G^{0\nu}$ of ^{48}Ca and ^{150}Nd listed in Table 1.2.

The calculation of the matrix element $M^{0\nu}$ is more difficult. Several theoretical approaches exist. Their results differ strongly, see Figure 1.5. For the comparison of double beta isotopes on the basis of Equation (1.6) the largest uncertainty therefore derives from $M^{0\nu}$.

The half-life of the $0\nu\beta\beta$-decay is assumed to be even several orders of magnitude higher than for $2\nu\beta\beta$-decay. A measurement of such a low decay rate, which is equivalent to only a few decays per year in several kilograms of source material, is an ambitious

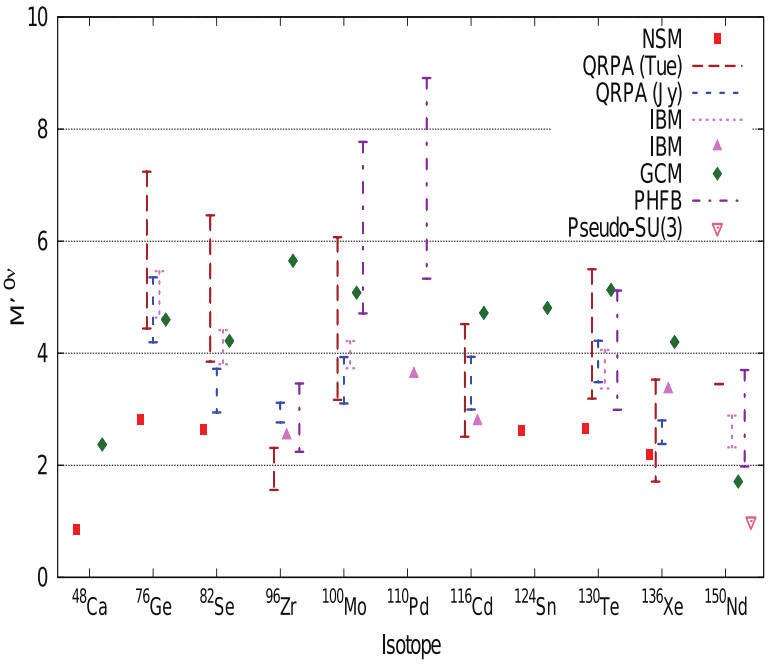

Figure 1.5: Matrix element calculations for several $0\nu\beta\beta$ isotopes with various approaches, taken from [Rod12]. The determined values for an isotope differ strongly and are momentarily the largest uncertainty for comparisons of the sensitivity prospects of double beta isotopes and obtained $0\nu\beta\beta$-decay limits, e.g. the discovery claim from [KK01a] for ^{76}Ge ($T_{1/2}^{0\nu\beta\beta} = 2.2 \times 10^{25}$ y) and the currently highest non-germanium limit ($T_{1/2}^{0\nu\beta\beta} > 1.6 \times 10^{25}$ y) for ^{136}Xe [Aug12].

challenge. Several $0\nu\beta\beta$-decay experiments are currently taking data, are commissioned at the moment or proposed for the future. An objective comparison of the expected sensitivities of these experiments is difficult because several uncertainties, e.g. of $M^{0\nu}$ on the theoretical side or the actually achievable resolution and background level on the experimental side, exits. In Subsection 3.3.3 a sensitivity approximation for the planned large scale COBRA experiment is given. Comparisons between several experiments can be found in [Giu10, GC11, Sch12b]. As expected, depending on the chosen basis the ranking of experiments concerning $0\nu\beta\beta$-decay sensitivity differs between these authors.

The currently highest limits on $0\nu\beta\beta$-decay were obtained for ^{76}Ge by the Heidelberg-Moscow experiment [KK01b]

$$T_{1/2}^{0\nu\beta\beta} > 1.9 \times 10^{25}\,\text{y at } 90\,\%\text{ CL}$$
$$\langle m_{\nu_e} \rangle < 0.35\,\text{eV}\,.$$

and for ^{136}Xe by the EXO-200 experiment [Aug12]

$$T_{1/2}^{0\nu\beta\beta} > 1.6 \times 10^{25}\,\text{y at } 90\,\%\text{ CL}$$
$$\langle m_{\nu_e} \rangle < (0.18 - 0.38)\,\text{eV}\,.$$

The corresponding limits on the neutrino masses depend on the applied nuclear matrix elements.

Based on the Heidelberg-Moscow data a part of the collaboration independently claimed evidence for the observation of $0\nu\beta\beta$-decay [KK01a]. In a later paper with different analysis methods the subgroup even claimed a statistical significance for the

Isotope	Decay mode	a[%]	N_0/1g $Cd_{0.9}Zn_{0.1}Te$	Q-value [keV]
^{106}Cd	$\beta^+\beta^+, \beta^+/EC, EC/EC$	1.25	2.889×10^{19}	2775.4 [Gon11]
^{108}Cd	EC/EC	0.89	2.057×10^{19}	272.0 [Smo12]
^{114}Cd	$\beta^-\beta^-$	28.73	6.640×10^{20}	534
^{116}Cd	$\beta^-\beta^-$	7.49	1.731×10^{20}	2813.5 [Rah11]
^{64}Zn	$\beta^+/EC, EC/EC$	48.2	1.248×10^{20}	1096
^{70}Zn	$\beta^-\beta^-$	0.6	1.541×10^{18}	1001
^{120}Te	$\beta^+/EC, EC/EC$	0.096	2.465×10^{18}	1714.8 [Sci09]
^{128}Te	$\beta^-\beta^-$	31.69	8.137×10^{20}	865.9 [Sci09]
^{130}Te	$\beta^-\beta^-$	33.80	8.680×10^{20}	2527.0 [Rah11]

Table 1.2.: Decay modes, Q-values, natural abundances a (taken from [Bö05]) and number of nuclei per gram CdZnTe of double beta isotopes contained in CdZnTe. Partly taken from [Kie05], Q-values updated as indicated by citations.

detection of more than 6σ and gave the following results [KK06]:

$$T_{1/2}^{0\nu\beta\beta} = \left(2.23^{+0.44}_{-0.31}\right) \times 10^{25}\,\mathrm{y}$$
$$\langle m_{\nu_e} \rangle = \left(0.32^{+0.03}_{-0.03}\right)\,\mathrm{eV}.$$

The GERDA [Mei11] and the Majorana [Sch12a] experiments will test the claim for ^{76}Ge. The claim is already incompatible with the EXO results for most nuclear matrix element calculations. However, this discrepancy clearly shows that $0\nu\beta\beta$-decay has to be observed with several isotopes to verify the results. Also from the point of view of the currently large uncertainty in the nuclear matrix element calculations the observation with several isotopes is desirable to check at least for consistency of the same calculation methods for different isotopes.

1.2. The COBRA Experiment

Current and past $0\nu\beta\beta$-decay experiments have a sensitivity of up to $\approx 10^{25}$ years. Judging from the results of EXO-200 it seems unlikely that Klapdor's claim will be confirmed. Even if it will be confirmed it will be necessary to reconfirm $0\nu\beta\beta$-decay with several isotopes and preferably different experimental approaches, see the reasons given in the previous section. Furthermore a precise measurement of the half-life and a high significance of a discovery are desirable. As will be shown in sensitivity studies in Subsection 3.3.3, the sensitivity, which is usually defined as the sensitivity for the exclusion of a half-life, is not equivalent to a discovery potential of an experiment. Therefore new experiments are necessary to either confirm the observation of $0\nu\beta\beta$-decay and measure the half-life precisely or to provide a sensitivity of more than 10^{25} years.

COBRA [Zub01] is a Research and Development (R&D) project to develop a concept for such an experiment with CdZnTe (or CdTe) semiconductor detectors. The general

idea is to build a three dimensional array of CdZnTe detectors to achieve a source mass of several hundred kg. CdZnTe contains nine double beta candidates, see Table 1.2. The most interesting ones are ^{130}Te, ^{116}Cd (compare also Table 1.1) and ^{106}Cd.

^{130}Te has a high Q-value. Even though it is not above the highest naturally occurring γ-line with significant intensity, the 2615 keV γ-particle from ^{208}Tl (see also Section 2.4), it is exactly between the full-energy peak and the Compton edge of this line. This is helpful to reduce the γ-background, which is very hard to shield. The certainly most important features of ^{130}Te are its high natural abundance and its high $2\nu\beta\beta$-decay half-life. Among the most promising double beta isotopes listed in Table 1.1, it is outstanding in both properties. Expensive isotope enrichment will be cheaper or can possibly be omitted at all (depending on the required sensitivity and the cost-benefit ratio compared to a larger detector). The high $2\nu\beta\beta$-decay half-life results (in principle) in less $2\nu\beta\beta$-decay background in the $0\nu\beta\beta$-decay signal region of ^{130}Te. For a short discussion of the currently world leading $0\nu\beta\beta$-decay half-life limits and current COBRA limits see Subsection 3.3.3.

^{106}Cd is one of the most promising candidates for $0\nu\beta^+\beta^+$-decay. Here three decay modes exist, namely $0\nu\beta^+\beta^+$, $0\nu\beta^+/EC$ and $0\nu EC/EC$. The emission of a positron leads to the reduction of the phase space by $2 \times m_e = 1022$ keV. Therefore longer half-lives than for the $0\nu\beta^-\beta^-$-decay are expected, especially for the $0\nu\beta^+\beta^+$ mode, and the current attention of most experiments is focused on $0\nu\beta^-\beta^-$-decay. On the other hand a confirmation for at least one of the β^+ modes would further strengthen a discovery of the $0\nu\beta^-\beta^-$-decay. The β^+/EC mode is especially sensitive to a possible contribution of a right handed current [Hir94]. This decay mechanism is the second most popular theory for $0\nu\beta\beta$-decay after the mass driven mechanism. World best limits for double beta decays of ^{106}Cd can be found in [Bel12a] and references therein.

The most important isotope for COBRA is certainly ^{116}Cd. With its Q-value of 2813.5 keV it is well above the energy of the ^{208}Tl γ-line. This is a large advantage concerning the achievable background level, see results of Section 2.4. In Subsection 2.4.2 the currently world leading limits for ^{116}Cd are briefly discussed and in Subsection 3.3.3 limits achieved with the current COBRA R&D set-up are calculated.

The drawback of ^{116}Cd is its comparatively low $2\nu\beta\beta$-decay half-life. A sufficient resolution to disentangle the $0\nu\beta\beta$-decay and the $2\nu\beta\beta$-decay even for half-lives $T_{1/2}^{0\nu\beta\beta} > 10^{26}$ years was already achieved (compare Figure 1.4 and the actually achieved average detector resolution of 1.5 % full width at half maximum (FWHM) at 2.8 MeV shown in Figure 3.18, Subsection 3.3.2), but the sensitivity for decays (to ground state) of the other double beta isotopes with lower Q-values, e.g. ^{130}Te, will be limited by the $2\nu\beta\beta$-decay of ^{116}Cd. On the other hand COBRA is planned as an array of several thousand CdZnTe detectors. This opens the possibility for a coincidence analysis. Such an analysis focuses on the detection of simultaneous detection of signals in more than one detector, see e.g. Subsection 2.4.3 for an example of a coincidence analysis for ^{116}Cd into the first excited state of ^{116}Sn. For β^+ emitters (^{120}Te and ^{64}Zn) or decays to excited states it

may be possible to achieve a high sensitivity by searching for the energy deposition of the electrons in one detector and for the emitted γ-particle in another. The sensitivity of this analysis method will not be affected by the low $2\nu\beta\beta$-decay half-life of ^{116}Cd, and besides ^{116}Cd also other double beta isotopes can be studied simultaneously in COBRA.

1.2.1. CdZnTe Semiconductor Detectors

An introduction to semiconductor detectors can be found in [Leo94, Gil08]. The principle is briefly explained in Figure 1.6. For a detailed description of the coplanar grid (CPG) and the pixel detector principle for CdZnTe and its theoretical basis see e.g. [He01].

Properties of several widely applied semiconductor detectors are listed in Table 1.3. From the table it can be seen that CdZnTe has much lower charge carrier mobilities and especially lifetimes than other semiconductor detector materials. Furthermore, the mobility and the lifetime of the holes are even smaller than for the electrons. Holes can only move a short distance (compared to a detector size of several millimetres) during the typical charge collection time of a preamplifier. Therefore, unlike for germanium detectors, the holes do not (or only little) contribute to the induced charge. For a simple planar electrode design, as is used e.g. for germanium detectors, this will result in an interaction-depth dependent signal because the induced charge is dependent on the drift length of the charge carriers through the detector. That is, an interaction close to the cathode will lead to a high signal as the electrons have a long drift path through the detector, whereas the induced charge for an interaction close to the anode will be much smaller. The dependence of the induced charge ΔQ_e on the anode from the interaction depth $0 < Z < 1$ (0 denotes the cathode, 1 the anode) can be calculated to be [He01]

$$\Delta Q_e \approx n e_0 (1 - Z) \tag{1.8}$$

where ne_0 is the charge from n electrons moving towards the anode. Consequently, a common planar electrode design with a simple measurement of the signal height cannot be applied to build a CdZnTe detector for γ-spectroscopy.

In [Luk94] an alternative anode design, the so-called CPG design, was introduced. The anode is divided in two comb-shaped parts, the collecting anode (CA) and the non-collecting anode (NCA), see Figure 1.7. The CA is set to ground potential, the NCA is set to a small negative potential with the so-called grid bias (GB) voltage that is applied between the two anodes. On the planar cathode side a negative high voltage (HV) is applied. The HV ($\sim 1\,\mathrm{kV}$) is much higher than the GB (about 40 V up to 120 V), but due to the small distance between the anode grids ($\sim 0.3\,\mathrm{mm}$) compared to the detector thickness ($\sim 1\,\mathrm{cm}$) the electric field between the anode grids is higher than between the anodes and the cathode. The potential for one CPG electrode is shown in Figure 1.8.

For most parts of the detector the linear potential from the HV is dominating. While the electron cloud travels through these parts of the detector, charge is equally induced on both CA and NCA. Very close to the anodes the electric field between CA and NCA

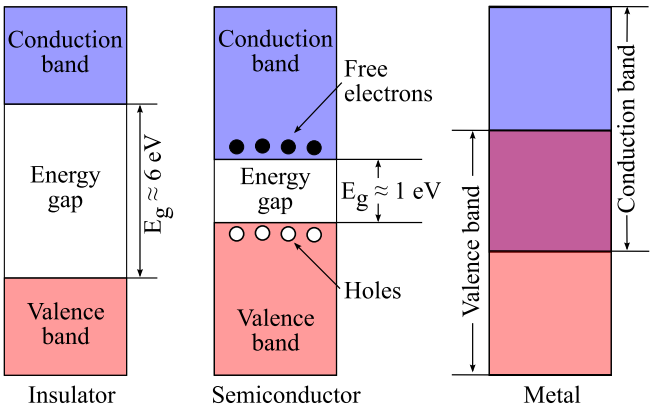

Figure 1.6: Energy band structure of insulators, semiconductors and metals (conductors), according to [Leo94]. For semiconductors the band gap between the valence- and the conduction band is small. The valence band contains nearly no electrons, but electrons from the valence band can be excited to the conductive band. They leave *holes* inside the valence band that behave similar to positive charge carriers. Electrons in the conduction- and holes in the valence band then contribute to the conductivity.

Property	$Cd_{0.9}Zn_{0.1}Te$	CdTe	Ge	Si
Atomic numbers	48,30,52	48,52	32	14
Density ρ [g/cm^3]	5.78	5.85	5.33	2.33
Band gap E_g [eV]	1.57	1.5	0.67	1.12
Pair creation Energy E_{pair} [eV]	4.64	4.43	2.95	3.63
Resistivity ρ [Ω cm]	3×10^{10}	10^9	50	$< 10^4$
Electron mobility μ_e [cm^2/Vs]	1000	1100	3900	1400
Electron lifetime τ_e [s]	3×10^{-6}	3×10^{-6}	$> 10^{-3}$	$> 10^{-3}$
Hole mobility μ_h [cm^2/Vs]	50 - 80	100	1900	480
Hole lifetime τ_h [s]	10^{-6}	2×10^{-6}	10^{-3}	2×10^{-3}
$(\mu \cdot \tau)_e$ [cm^2/V]	$(3 - 10) \times 10^{-3}$	3.3×10^{-3}	> 1	> 1
$(\mu \cdot \tau)_h$ [cm^2/V]	5×10^{-5}	2×10^{-4}	> 1	≈ 1

Table 1.3.: Properties of CdZnTe, CdTe, Ge and Si, taken from [End11].

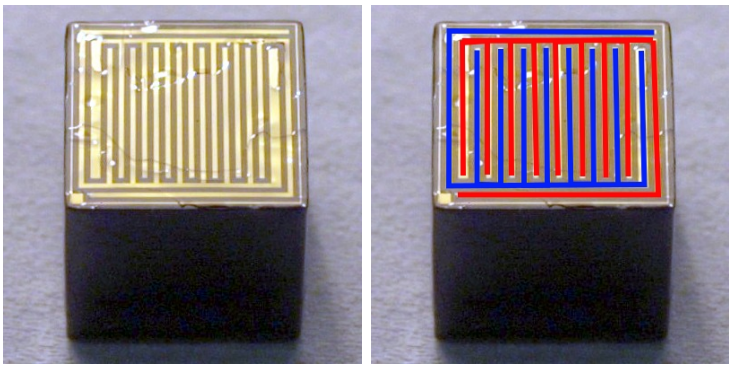

Figure 1.7: CdZnTe detector with CPG anodes. On the right picture the two grids are highlighted in red and blue. Which anode is the CA and which is the NCA is defined by the GB between the two anodes. The CA is the anode that is set to zero potential and the NCA is set to a small negative potential.

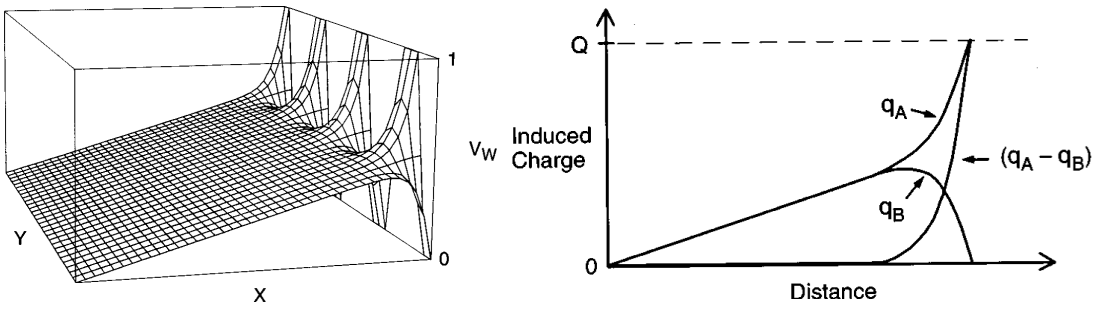

Figure 1.8.: Left: Weighting potential for one of the CPG electrodes. Right: Induced charge at the collecting anode (q_A) and the non collecting anode (q_b) together with the difference signal ($q_A - q_B$) as a function of the distance travelled by a charge Q. The small bias of the NCA influences a moving charge cloud at the end of its path close to the anodes. Even though the GB is smaller than the HV, the electric field is stronger at the anodes due to the small distance between the anods. This can be seen from the slow rise of the induced charge Q for smaller depth and a steep rise vicinity of the anodes. Both figures are taken from [Luk94].

is dominating. The electrons drift towards the CA, what is equivalent to a drift away from the NCA. While the electrons drift away from the NCA, the induced charge on the NCA is reduced, charge is transferred from the NCA to the CA. An example for an interaction close to the cathode is shown in Figure 1.8.

For events with full drift length through the zone of influence of the GB (i.e. in the vicinity of the anodes), the amount of transferred charge from the CA to the NCA during the drift through this area is always the same. For areas far away from the anodes the induced charge is equal on both anodes. By subtracting the NCA signal from the CA signal, the interaction depth dependent induced charge cancels out and only the depth independent part from the path directly beneath the anodes remains. It can be shown that the difference of the anode signals equals the number of electrons that finally arrive at the surface of the coplanar anodes, independent from the interaction depth of the initial energy deposition [He01].

The amount of electron-hole pairs (and thus the amount of e^- charge within the detector) that are created in an interaction is proportional to the deposited energy of the event. Therefore a measure for the deposited energy E can be obtained from

$$E \propto CA - w \cdot NCA\,. \tag{1.9}$$

$w < 1$ is a correction factor for electron trapping. From the numbers in Table 1.3 it can be seen that trapping in CdZnTe is not only a problem for holes, but also for electrons. The amount of trapped charge is dependent on the path length. The longer the path of the charge is, the more charge is trapped. In events close to the cathode the charge has to travel through the whole detector, whereas events close to the anodes only have to travel a small way. As shown in Figure 1.8, the induced charge on the NCA returns finally to zero for cathode events. For events closer to the anodes, the NCA signal becomes

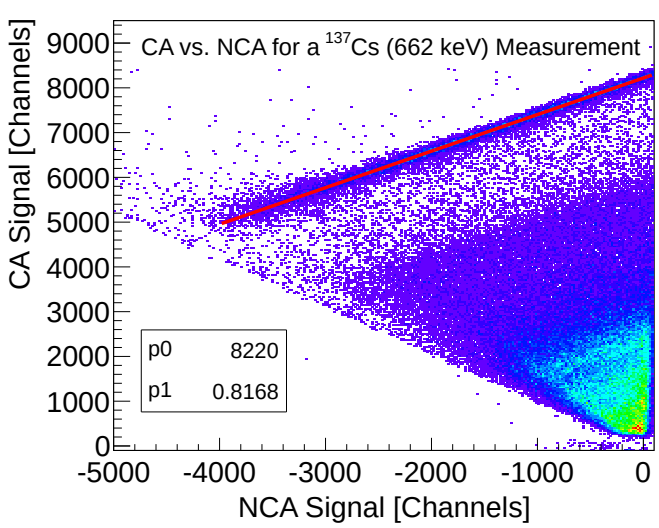

Figure 1.9: CA vs. NCA plot for a ^{137}Cs (662 keV) measurement. For events close to the cathode, the NCA signal is close to zero. It becomes negative for interactions that take place closer to the anodes. Events with the full energy deposition of 662 keV are according to Equation (1.9) visible as the straight line in the upper part of the plot. From the slope of a linear fit through this line (shown in red) $w = 0.82$ can be obtained. The triangular shaped structure on the lower right side derives from Compton scattering.

negative as the amount of charge that is transferred in the vicinity of the anodes is always the same, but the NCA does not collect as much charge from the path away from the anodes like for an event close to the cathode, see also Figure 1.9. Because the negative NCA signal is subtracted from the CA signal, effectively the difference signal is increased by the absolute value of the NCA. The contribution of the NCA is close to zero for events close to the cathode and large for events close to the anodes. By attenuating the NCA by w, a first order correction of the electron trapping is achieved by artificially reducing the signal for events close to the anodes, which have a short drift length, whereas the signal of events further away from the anodes, which have a longer drift length, is only marginally influenced by w. The weighting factor w depends on the quality of the detector material, the HV and the GB. Typical values vary between $0.6 < w < 0.9$. The optimal value of w for a detector can be obtained either by optimising the energy resolution of γ spectra that are calculated according to Equation (1.9) regarding w, or by fitting a linear function to the full energy line in a CA vs. NCA plot and taking w to be the slope, see Figure 1.9.

The energy reconstruction is not absolutely exact close to the cathode and close to the anodes. Directly at the cathode the holes can contribute to the signal. The energy calculated according to Equation (1.9) can differ from the actual energy deposition by about 1 % [Fri12]. Close to the anodes analogously holes can travel towards the NCA. In an area of about 5 % below the anodes the energy reconstruction is unreliable. In extreme cases, when the event takes place directly at the NCA, the hole signal can fully contribute and the energy deposition determined with (1.9) is twice as high as the true deposited energy. This effect was observed with COBRA CPG detectors in [Teb11].

An effect similar to the CPG principle can be achieved with pixelated CdZnTe detectors. Drifting electrons far away from the anode induce charge in many anode pixels due to charge sharing. Only in the vicinity of the anode pixels the induced charge increases rapidly in the pixel(s) directly above the charge clouds. The induced charge in one pixel

therefore is mainly dependent on the last part of the travelled path and is nearly interaction depth independent. For pixel detectors the effect is called small pixel effect because it works better for pixels that are small compared to the detector thickness [He01].

In [He96, He05] the reconstruction of the interaction depth Z from the cathode signal C and the energy deposition E determined from the anode signal

$$Z \propto C/E \tag{1.10}$$

was introduced. The readout of the cathode signal is not contained in the common COBRA readout electronics because it would require an additional readout channel. Instead, the approximation of the cathode signal as the sum of the CA and NCA signal was applied in [Sch11a].

In Equation (1.10) effects like hole and electron trapping are not taken into account. The method was modified to correct for electron trapping in [Fri12] to

$$Z = \lambda \cdot \ln\left(1 + \frac{1}{\lambda}\frac{\Delta q_{CA} + \Delta q_{NCA}}{\Delta q_{CA} - \Delta q_{NCA}}\right), \quad \lambda = \frac{1+w}{1-w}. \tag{1.11}$$

Here Δq_{CA} and Δq_{NCA} are the signal height of the CA and NCA and w is the weighting factor.

1.2.2. Experimental Set-Up at LNGS

COBRA is currently in the R&D phase to develop a concept for a large-scale experiment. The R&D set-up is located in the Italian Laboratori Nazionali del Gran Sasso (LNGS) underground laboratory close to Rome. The experimental set-up can house up to 64 CPG detectors and was temporarily extended for pixelated detectors [Sch11b].

The observation of decays with half-lives of more than 10^{25} years requires an extremely low background level. The main sources of background can be divided into background from decays of primordial nuclides like ^{40}K or ^{238}U and background from (secondary) cosmic rays. Further secondary background can arise from activation of materials from neutrons and cosmic rays.

Cosmic rays at the surface consist mainly of muons. The much smaller nucleonic component can be shielded with an overburden of a few meters of water equivalent (mwe). At sea level the muon flux is about $1\,\mathrm{cm^{-2}\,min^{-1}}$ [Ber12], what is equivalent to about 170 muons per $\mathrm{m^2}$ and second. The muons can produce background directly by interacting with detector material, or they can produce secondary background, e.g. by causing a delayed emission of neutrons in materials surrounding the detector. Due to their high penetration, a high overburden is necessary to effectively shield from muons. To achieve a very low background level a location with an overburden of several hundred mwe is necessary. Therefore ultra low background experiments are usually situated in underground laboratories.

The LNGS laboratory has an overburden of about 1400 meters of rock, what is equivalent to about 3800 mwe. The muon flux in the laboratory is $3.4 \times 10^{-4}\,\mathrm{m^{-2}\,s^{-1}}$ [Bel12b].

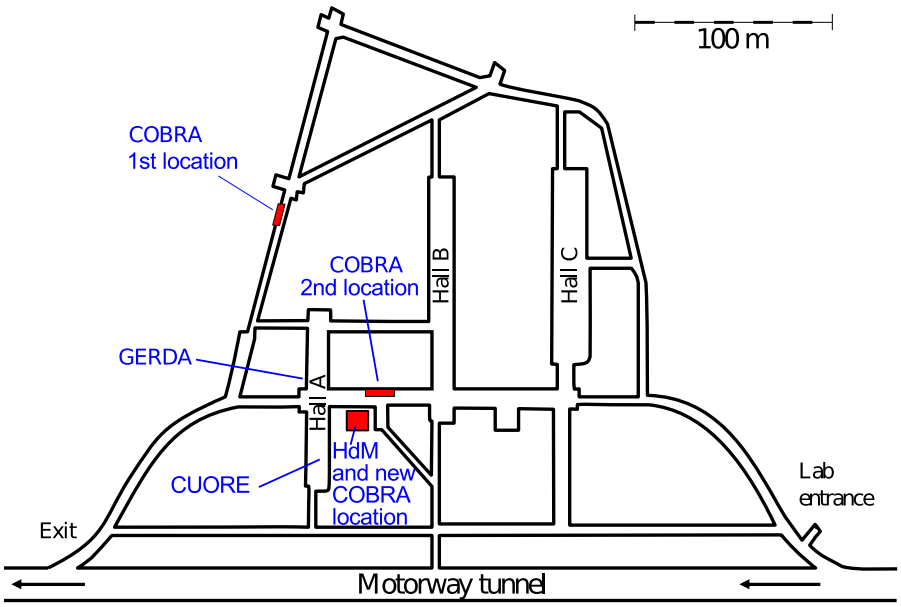

Figure 1.10: Former and current COBRA locations at LNGS (red), taken from [Ree09] and modified. Also shown are the locations of the other large $0\nu\beta\beta$-decay experiments at LNGS. The current COBRA location is in the hut of the former HdM $0\nu\beta\beta$-decay experiment.

Compared to the surface at sea level the muon flux is reduced by nearly six orders of magnitude. The rock of the Gran Sasso mountain contains comparatively little uranium and thorium contamination. This results in a neutron flux that is about three orders of magnitude lower than at sea level [Heu95]. Due to these benefits and a good infrastructure the LNGS laboratory hosted and hosts many well-known experiments. The current and former locations of the COBRA set-up in the underground laboratory are shown in Figure 1.10.

To protect the CdZnTe detectors from background, the set-up consists of several shielding layers. In 2011 the complete set-up was moved to a new location. In the scope of the move the set-up was upgraded and several shielding layers were modified. The current set-up is shown in Figure 1.11. In the following the shielding layers will be shortly discussed, beginning from the outermost parts. A good overview of of background sources in general and their suppression can be found in [Heu95]. An overview of the COBRA readout electronics is given in Subsection 1.2.3.

Neutron Shielding Natural Cadmium contains with 12 % abundance the isotope ^{113}Cd. This isotope has a very high cross section for thermal neutron capture. In a $^{113}\mathrm{Cd}(n,\gamma)^{114}\mathrm{Cd}$ reaction γ-particles with an energy of several MeV are released. These γ-particles can produce background in COBRA's Region Of Interest (ROI). Consequently, the detectors have to be shielded especially from thermal neutrons.

In [Oeh04] the first COBRA neutron shielding consisting of plates of borated Polyethylene (PE) and Parrafin wax bricks was constructed. The high amount of hydrogen in PE and Parrafin moderates neutrons to lower energies. ^{10}B in the borated PE plates has a very high cross section for $^{10}\mathrm{Be}(n,\alpha)^{7}\mathrm{Li}$ capture reactions. The α-decay can also go to the first excited state of ^{7}Li. Besides the α-particle then a γ-particle with 477.6 keV

is released. The α-particles are immediately stopped in the PE and the energy of the released γ-particle is far below COBRA's ROI.

The current outermost COBRA shielding layer consists of the 7 cm thick borated PE plates. It surrounds the passive lead- and copper shielding. The choice of the neutron shielding as outermost layer is suitable for experiments with a high overburden and thus low muon flux. For experiments with a smaller overburden, such as the Dortmund Low Background Facility (DLB) [Ned13], the neutron shielding has to be an inner layer of the shielding because muons can produce neutrons in the lead surrounding the detector [Heu95].

Shielding against Electromagnetic Interference Preamplifiers for semiconductor detectors have to be very sensitive. In an interaction with an energy deposition of a few MeV only a few hundred thousand electron-hole pairs are created within the detector. This small amount of charge has to be collected and amplified by the preamplifiers. Electromagnetic (EM) disturbances can fake a physics events, most likely in the cables from the detectors to the preamplifiers or in the preamplifiers themselves. A good shielding against electromagnetic interference (EMI) is therefore essential.

Former COBRA set-ups applied copper shieldings. Further inquiries showed that for the EM frequencies that can produce electronic disturbances for COBRA, shielding of the magnetic component is very important. The new EMI shielding was therefore build with steel plates [Ned13], which efficiently absorb the magnetic component.

For the signal cables from the preamplifiers, the power supply of the preamplifiers, the HV and GB many cables have to be fed into and out of the set-up. A cable feed through is often the weakest point of an EMI shielding. Therefore a copper chute was constructed for the COBRA EMI shielding, see Figure 1.11.

Nitrogen Flushing In the natural uranium and thorium decay chains, which are also contained in rock and concrete, radon isotopes are produced. Radon is a noble gas and can diffuse out of the rock and concrete and also through thin layers of light materials, such as plastic foils [Heu95]. The activity from airborne radon in buildings differs depending on the uranium and thorium content in the surrounding materials, but is usually in the order of several ten Bq/m^3.

The ^{232}Th decay chain contains ^{220}Rn, which has a short half-life of 55.6 s, and the ^{238}U decay contains ^{222}Rn with a half-life of 3.8 d. Due to its comparatively short half-life the influence of ^{220}Rn is small compared to ^{222}Rn. The half-life of ^{222}Rn is sufficient to diffuse out of rock and concrete and into the experimental set-up. The daughter isotopes of ^{222}Rn contain several α- and β-decays. One of them is the β-decay of ^{214}Bi with an energy of the β-particles of up to 3.3 MeV. β-decays are dangerous for COBRA because they have a much higher penetration depth than α-particles and they can even mimic the event topology of an $0\nu\beta\beta$-decay. Currently, α-decays are the main source of background in COBRA's ROI, see e.g. the discussions in Section 2.4 and Subsection 3.1.1. In [Mü07]

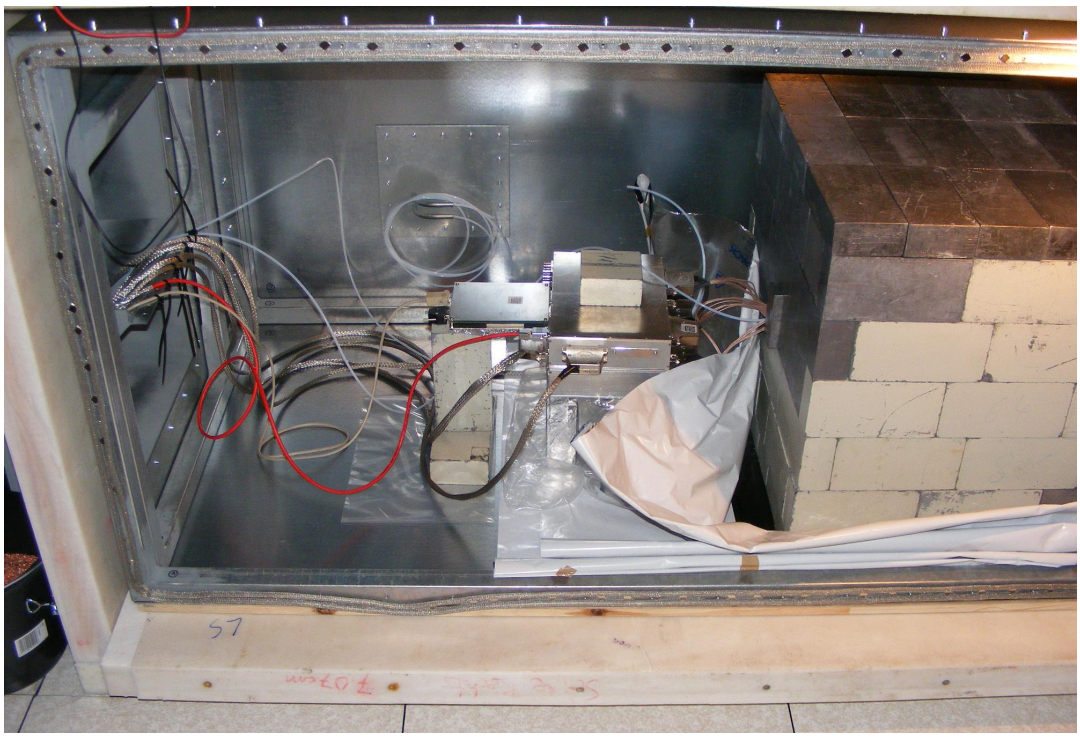

Figure 1.11.: COBRA prototype set-up at LNGS. Visible is the PE neutron shielding (white) and the EMI-shielding as outermost layers, a preamplifier box and the lead castle. The lead castle consists of several layers of lead surrounding a copper core (NEST) containing the detectors. Now the lead castle is surrounded by a radon-tight Tropac foil to ensure efficient flushing with evaporated nitrogen.

and [Koe08] it was shown that the main source of remaining background for the COBRA R&D set-up derived from radon diffusing into the inner parts of the set-up.

To reduce the background, a nitrogen flushing and monitoring system was developed [Mü07, Ale09, Sch11a]. The set-up is flushed with gaseous nitrogen that is evaporated from liquid nitrogen and filtered with a charcoal filter. Evaporation of liquid nitrogen instead of using bottled gaseous nitrogen is preferred because it is cheaper and also cleaner. Uranium and thorium impurities are also contained in steel. When nitrogen is stored in steel bottles, radon from the thorium and mainly the uranium daughters can slowly diffuse out of the steel of the bottles and concentrate in the nitrogen. The emission of radon from the walls of a nitrogen dewar is lower due to the low temperature of liquid nitrogen. The charcoal filter, which is covered by liquid nitrogen, has a much higher efficiency at liquid nitrogen temperature because the kinetic energy of the gas molecules is strongly decreased and thus they stick better to the large surface of the charcoal filter.

To increase the efficiency of the nitrogen flushing and to reduce the required consumption of nitrogen, a diffusion barrier for radon and an overpressure of nitrogen within the

set-up is desirable. Initially, the construction of a comparatively gas proof EMI shielding was tested. It turned out that this cannot be efficiently realised. Surrounding the set-up with a common plastic foil is also not sufficient because plastics are hardly a barrier for radon. Following the results of [Mam11], a radon tight enclosure of the whole lead-castle consisting of Tropac III foil and aluminium sheet angles was constructed in [Teb11].

Even though the immediate background from radon can be significantly reduced by permanent flushing of the set-up with clean nitrogen, it should be mentioned that the radon decay daughters stick to surfaces and can produce a long lived background. The ^{222}Rn sub-chain contains the long-lived isotope ^{210}Pb with a half-life of 22.3 years. The influence of this long-lived background on the current set-up is discussed in Subsection 3.1.1.

Lead Castle and Copper Nest α- and β-particles are absorbed within a thin layer of material. The attenuation coefficient for γ-particles on the other hand is comparatively small. Especially high energetic γ-radiation can deeply penetrate even heavy materials like lead. Even though COBRA's ROI is above the highest naturally occurring γ-line with significant intensity, the ^{208}Tl 2.6 MeV line, a good shielding against γ-radiation is necessary to have a high sensitivity to other interesting physics processes, such as the fourfold forbidden β-decay of ^{113}Cd [Daw09a] or $0\nu\beta\beta$-decays to excited states. As the results of Subsection 2.4.3 show, especially for the large scale set-up and a very low background level also higher energetic γ-lines with a low intensity can become a serious background source.

To shield the COBRA R&D set-up from external γ-radiation, the detectors are surrounded by a lead castle and an inner core of pure copper. Lead has the advantage of a high density and high nuclear charge and thus a high attenuation coefficient for γ-radiation. Furthermore, its cross section for neutron capture and interaction with cosmic rays is low. On the other hand it is problematic to produce intrinsically clean lead. The separation of the ^{210}Pb daughter ($T_{1/2} = 22.3$ years) of the ^{238}U decay chain from the lead ore is practically impossible. For intrinsically radiopure lead either ore from a mine with very low uranium contamination or ancient lead has to be used. The radiopurity of lead is usually given as the activity of ^{210}Pb per kg lead. Radiopure lead is expensive, therefore the lead castle is build with lead layers of different grades of radiopurity. In the scope of the recommissioning of the set-up after the move to the new location in the former HdM experiment, the innermost lead layer was replaced with 5 cm of ultra clean lead with a ^{210}Pb activity of less than 3 Bq/kg. In total the 60 cm × 60 cm × 60 cm lead castle provides a shielding of at least 20 cm of lead in every direction.

The detectors are shielded from remaining intrinsic decays from the outer lead layers with an innermost 5 cm layer of copper. Due to its high redox potential and its production process copper can be produced with a high purity [Heu95]. Furthermore the mechanical properties of copper make the machining much easier than for lead. The drawbacks of copper compared to lead are its lower attenuation coefficient, the higher

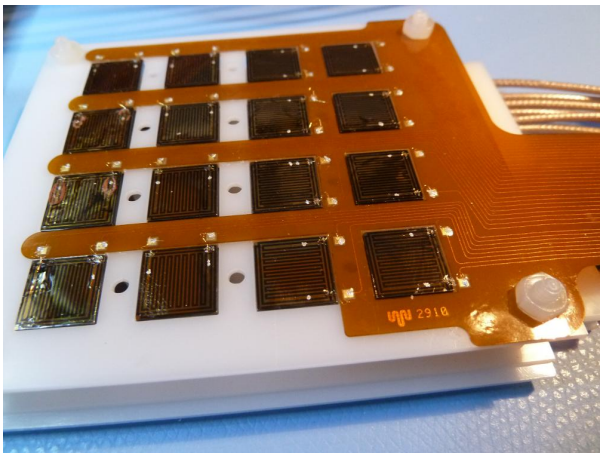

Figure 1.12: A 16 detector layer. The white detector holder structure is made from Delrin (POM). For the signal readout Kapton cables are applied to achieve a high density of signal traces. This high density is required to connect all 32 detector anodes within the little space that is available at the anode side of the layer. The HV is supplied with RG178 coaxial cables (visible at the upper right corner). The detector electrodes are connected to the solder pads of the Kapton and the RG178 cables with gold wire and LS200 conductive lacquer.

cross section for neutron caption and a higher production rate of radionuclides by activation from cosmic rays. The problem of activation is especially disturbing for sites with a low overburden and a high flux of cosmic rays. Experiments with a low overburden therefore usually apply only a thin inner layer of copper. For experiments like COBRA with a high overburden, the activation during the run-time of the experiment is negligible, but the production of long-lived cosmogenics during storage and machining at the surface has to be taken into account.

Detector Mounting and Contacting The inner copper part of the set-up can house up to 64 CPG detectors. They are arranged in four layers and each layer contains 16 detectors. A picture of such a detector layer is shown in Figure 1.12. The choice of the materials for the detector holders was done following the principles of using as little material as possible and as radiopure material as possible.

The holder structure for the detectors is made from the thermoplastic POM. Actually, POM produced by DuPont with trade name Delrin is applied. The readout of the anodes is done with Kapton cable [Raj]. The design of Kapton cables is necessary because a high density of signal traces is needed to read out all 32 detector anodes and still keep a decent accessibility to the detectors.

Initially, also for the HV Kapton cables were applied. It turned out that the Kapton is not suitable for HV and is prone to sparkovers. Therefore RG178 coaxial cables are applied in the current set-up for the supply of the HV.

The electrodes of the detectors are connected to the Kapton solder pads and the RG178 cables with gold wire and LS200 conductive lacquer [Koe08, Raj]. LS200 is a silver based conductive lacquer. ^{109}Ag can be activated by neutrons to the long-lived ^{110m}Ag ($T_{1/2}$ = 249.8 d). From the decay of ^{110m}Ag β-particles with an energy up to 2891 keV can be emitted and thus, in principle, produce background in COBRA's ROI. However, the emission probability of such a high energetic β-particle is very low and the amount of conductive lacquer is very small. The actual number of background events in COBRA's ROI therefore is expected to be negligible. Measurements of a LS200 sample

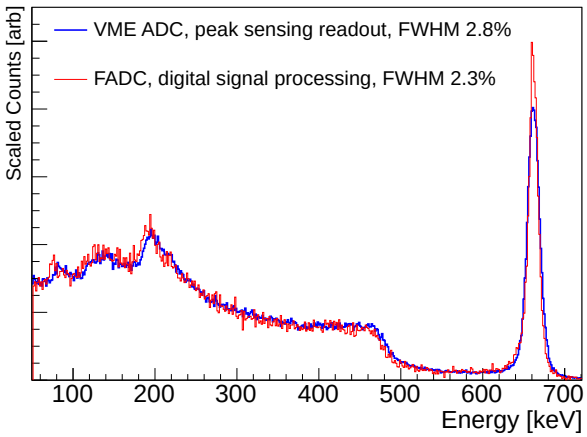

Figure 1.13: Comparison of spectra taken with the old peak sensing ADC and the new FADC (still with single-ended signalling). Both spectra were taken with the same detector and optimised settings. With the naked eye the better energy resolution is hardly visible from the smaller width of the red curve, but clearly visible from the increase in the height of the full-energy peak. With the new designed electronics with differential signalling the achieved resolution with this detector was further improved to 2 % FWHM at 662 keV, see Figure 1.17.

[Ned13] and recent simulations based on this measurement confirm this assumption.

1.2.3. Electronics

During the last few years major modifications were made in the COBRA data acquisition (DAQ). Until 2010 a preamplifier circuit with adjustable gain of the NCA signal and output of the CA-NCA difference signal was applied. The difference signal was shaped and amplified with a main amplifier (shaper) and the pulse height was recorded with a peak sensing analog to digital converter (ADC). The whole electronics, except the preamplifier modules, was designed and manufactured at TU Dortmund [Kie05, Mü07].

In 2009 several fast analog to digital converters (FADCs) (Struck SIS3300) were reassigned from the decommissioned AMANDA experiment to COBRA [Sch11a]. The application of FADCs instead of peak sensing ADCs allows for the recording of the whole signal shape instead of only the absolute signal amplitude. This additional information is very valuable to identify background events from the shape of the recorded pulses. This includes background from physics events as well as rejection of EM disturbances. Furthermore, also an improvement of the achievable energy resolution is possible as the whole signal processing can be done digitally and sophisticated filters and algorithms can be applied. A comparison of the achieved resolution with the old DAQ readout chain and an intermediate stage of the new DAQ readout chain is shown in Figure 1.13.

To profit from the benefits of the FADC data recording the whole DAQ readout chain had to be replaced. The design of the DAQ software was done in [Sch11a]. The design of the new electronics was done in close cooperation of Oliver Schulz [Sch11a], Jan Tebrügge [Teb11] and the author. Most of the electronics are already described in [Sch11a, Teb11], so here only the most important features are summarised and a few additional comments are given.

The cables between the detectors and the preamplifiers are kept as short as possible to reduce effects from cable capacities and EM disturbances that can affect the small detector signals before the amplification. The preamplifiers are contained within the EMI

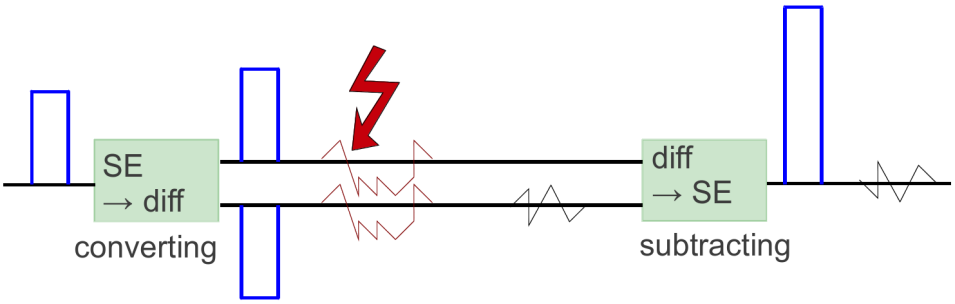

Figure 1.14.: Principle of differential signalling, taken from [Teb11]. To transmit a signal with differential signalling, at first the SE signal (indicated in blue) has to be duplicated in a differential transmitter. The duplicated signal is inverted to have two complementary signals. Both signals are transmitted from the transmitter to the differential receiver on wires that are close to each other, preferably in twisted pair cables. In the differential receiver the inverted signal is subtracted from the not inverted signal and thus converted to a SE signal. The resulting SE signal has an amplitude that is twice as high as the initial signal. EM disturbances that occur between the transmitter and receiver are likely to affect both wires similarly (indicated by the red flash). Therefore, they will cancel out during the subtraction process in the receiver. Even if a disturbance affects only one signal wire (indicated by the distorted signal on the lower wire), the signal to disturbance ratio is increased by a factor of two because the signal amplitude is increased by a factor of two.

shielding. The connecting cables between the preamplifiers and the linear amplifiers can be several meters long and are prone to EM disturbances as soon as they are lead out of the EMI shielding. To have a more stable signal transition it was decided to use differential signalling instead of single ended (SE) signal transition. The principle of differential signalling is explained in Figure 1.14.

The actual charge sensitive preamplifiers are commercially available preamplifier modules. Mainly Cremat[1] CR-110 preamplifier modules are applied in COBRA. Alternatively eV-5093 preamplifier modules from EI Detection & Imaging Systems (EIDIS) are used. They have a higher amplification and less noise, but are also more expensive, what has to be taken into account for the amount of readout channels that are necessary for COBRA.

To operate the preamplifier modules, preamplifier boxes were designed, see Figure 1.15 for a photograph of an eight channel preamplifier box. These preamplifier boxes contain the preamplifier modules, a circuitry for power buffering and filtering, SE input connectors for the input of the detector signals, a circuitry to convert the amplified SE detector signals to a differential signal and output connectors to transmit the differential signals to the linear amplifiers. In the following the term preamplifier will be used synonymously for the designed preamplifier box.

For the design of the preamplifier a four layer PCB board was chosen to ensure a

[1] `http://www.cremat.com/`

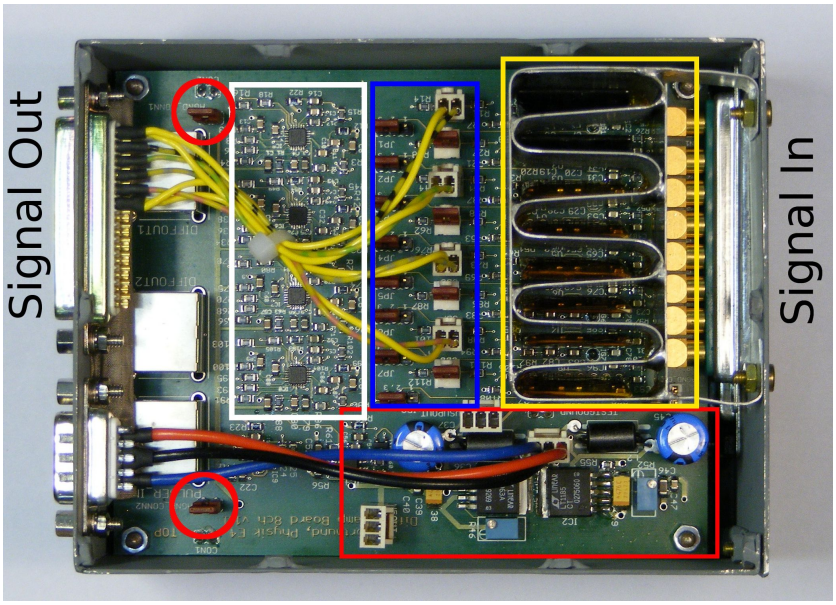

Figure 1.15.: Signal board of the eight channel (four detector) differential preamplifier box. The power supply circuitry for the preamplifier modules and the differential ICs is marked with a red rectangle. The preamplifier modules are surrounded by a sheet steel meander to shield them from crosstalk and EMI, marked in yellow. The SE to differential conversion of the preamplifier signals is done with the circuitry marked in white. The jumpers marked in blue are used to connect the preamplifier modules to an external pulser signal (left row) and to select CA and NCA channels by applying a negative bias voltage (white plugs) to one of the two readout channels for each detector (right row, the CA has to be connected to ground potential with the red jumpers). The jumpers marked with a red circle are used to connect or disconnect the shield of the RJ45 plugs (the upper two plugs are for the differential signal output, the lower plug for a differential input of an external pulser signal) to the ground of the board. A third similar jumper for the signal input plugs is hidden below the meander. The signal board is set on top of a HV filter board. The reference ground of each HV channel is connected to the ground of its corresponding signal channel to ensure a good signal return. The housing of the preamplifier is made from sheet steel to provide a good EMI shielding. The 32 channel (16 detector) preamplifier box is designed analogously.

solid ground- and voltage plane and enable a good routing of the signal traces. To have several grounding options, the ground plane of the board is divided into three ground planes, a major ground plane below the preamplifier modules and the other circuitry and two other ground planes beneath the input and output connectors. To be as flexible as possible the ground planes can be connected with jumpers. It turned out that the best signal quality is achieved when all ground planes are connected with each other and also with the housing of the preamplifier box.

The preamplifier modules have to be very sensitive to be able to process the small detector signals. This sensitivity makes them susceptible for EMI and crosstalk between the preamplifier channels. To reduce both disturbances, the preamplifier modules are surrounded by a meander made of steel.

GB and HV have to be supplied externally. Both voltages are buffered and filtered on the preamplifier board. To have a high flexibility, the GB is not fixed to certain preamplifier channels but can be applied on each channel as desired. This ensures a flexible choice of the detector anodes concerning operation as CA or NCA. For the HV a separate two layer board was designed. The signal board (i.e. the actual preamplifier board) is set on top of the HV board. The reference ground of the HV is directly connected to the ground of the preamplifier modules with plug contacts to ensure a short and well defined return path of the signal between the anode and cathode side of the detector. For the HV board it was taken care to apply only capacitors and resistors that are suited for HV operation. A first version of the HV board showed sparkovers due to too small distances between the applied standard solder pads. The solder pads were modified and the distance between them was extended as much as possible and the problem with sparkovers was eliminated. The sparkover between the solder pads is caused by impurities and leakage current on the PCB board surface. For older HV boards a gap was milled between the solder pads to take advantage of the high breakdown voltage of about 3 kV/mm of dry air (the dielectric breakdown of dry air occurs at an electric field strength of about 3×10^6 V/m [Tip87]).

At LNGS a detector layer consists of 16 detectors. In laboratory measurements sometimes smaller test layers with up to four detectors are operated, but mainly measurements are done with only one detector. For lab measurements a preamplifier box with eight readout channels for up to four detectors was designed, for the operation of many detectors at LNGS the board was extended to a 32 channel (16 detector) preamplifier box.

For test- and monitoring purposes the preamplifier boxes also contain a pulser input to connect an external pulser. Analogously to the differential preamplifier signal output the pulser input is also differential. To convert a SE pulser signal to a differential signal, hybrids of Nuclear Instrumentation Module (NIM) compatible differential amplifiers and SE to differential converters were build.

The output signal of the preamplifier modules is very small compared to the input range of the FADCs. To further amplify the signal and to convert it to a SE signal

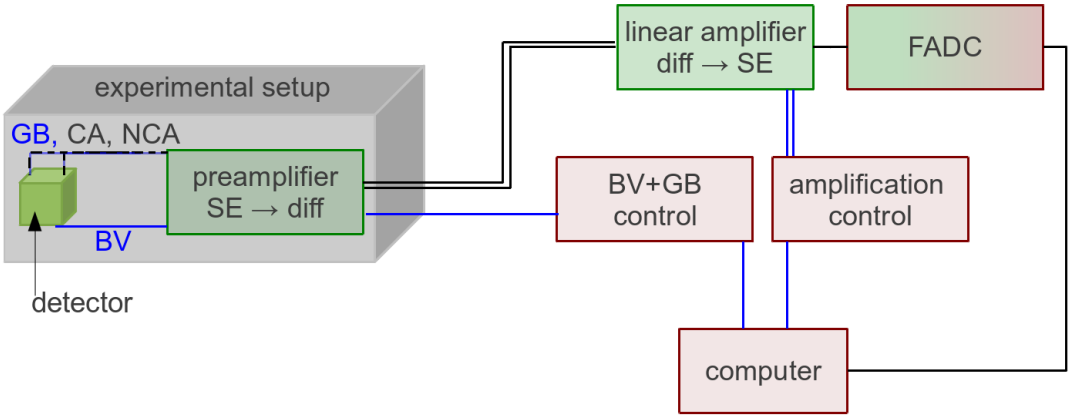

Figure 1.16.: Current DAQ chain, taken from [Teb11]. BV (Bias Voltage) is used synonymously for HV. The detectors and preamplifier boxes are kept within the EMI shielding (indicated in grey). The signals from the preamplifiers are transferred to the linear amplifiers with differential signalling. The linear amplifiers amplify the differential signal and afterwards convert it to a SE signal. They are connected to the VME FADCs with short coaxial cables. The FADCs are read out with a VME single board computer. The data is transferred to the actual DAQ computer with Ethernet cables and are stored to disk. The GB and HV are supplied by Wiener MPOD HV modules. Like the amplification of the linear amplifier they can be adjusted remotely. To control the linear amplifiers an Arduino micro controller and differential signalling between the controller and the linear amplifiers is used.

that can be processed by the FADCs, a differential linear amplifier was designed. The differential signal is amplified before the conversion to a SE signal. The amplification can be remotely adjusted in 16 steps of 3 dB, what is equivalent to a factor of $10^{3/20} \approx 1.41$ per step. With the lowest setting the signal input is attenuated by about a factor of 0.5, the highest amplification setting equals a factor of $0.5 \times 10^{15\times 3/20} \approx 89$. A schematic of the whole new readout chain is shown in Figure 1.16.

With the new readout electronics and the differential signalling the achieved energy resolution was further improved. Figure 1.17 shows a measurement with a ^{137}Cs source together with a reference pulser. The resolution that was achieved for the pulser signal is close to the value given by Cremat for the equivalent noise (resolution) of their preamplifier modules. This is a benchmark for the good quality of the designed electronics. The slightly worse resolution compared to the Cremat specification is certainly due to the imperfect pulser signal. A pulser amplitude of 8 mV is comparable to a detector response for a 662 keV energy deposition. To generate such a small pulser signal with an acceptable signal to noise ratio a good pulser (BNC PB-5 Pulse Generator) with internal attenuation and an additional external attenuator was applied, but the noise of the attenuated pulser signal can certainly not be neglected. However, the comparison of the resolution obtained with the pulser and with a good spectrometer grade CPG detector shows that the contribution of the electronics to the achievable resolution is

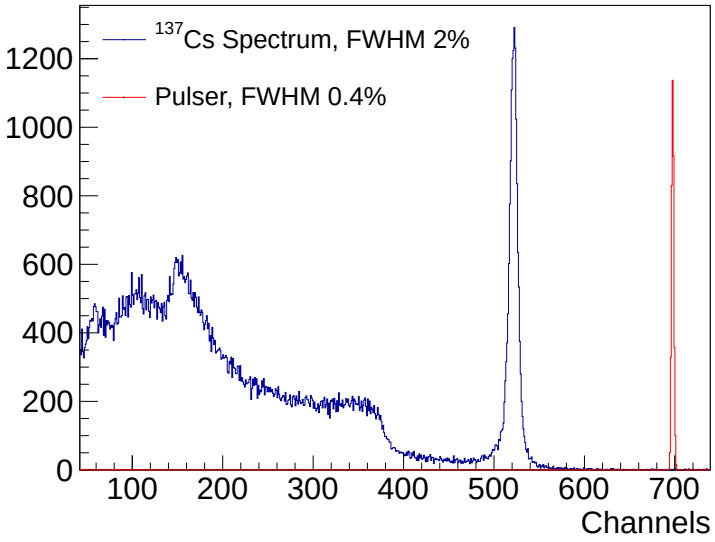

Figure 1.17: Comparison of a ^{137}Cs (662 keV) CPG detector spectrum and electronics resolution determined from a pulser. The detector spectrum and the pulser spectrum were taken simultaneously. For the measurement Cremat CR-110 preamplifier modules were applied. The electronics resolution of 0.4 % $\approx$ 2.6 keV is close to the value of 2.4 keV given by Cremat as resolution of their preamplifier modules.

not negligible, but the total resolution is still dominated by the intrinsic resolution of the detectors.

The complete preamplifier and linear amplifier electronics for the read out of the COBRA R&D 64 detector array and for laboratory measurements of the Dortmund COBRA group was build at the mechanical and electronics workshops of the TU Dortmund faculty of physics. The knowledge for the assembly of the electronics was also transferred to the DESY electronics workshop of the Uni Hamburg COBRA group. Additional five readout systems for the groups at Hamburg and Dresden were build there.

2. Simulation Studies

2.1. Geant4 and the VENOM Simulation Program

Important parameters of an experiment such as the detection efficiency or the expected background contribution can often not be measured directly. The analytical calculation of such parameters is usually also not possible due to the complexity of the underlying physical processes. Therefore experiments often rely on computer based simulations to obtain information on these parameters.

The simulation program developed for and applied by COBRA is called VENOM. It is based on the Geant4[1] [Ago03, All06] simulation framework for Monte Carlo (MC) simulations of the passage and transport of particles through matter. Therefore VENOM is, like Geant4, object orientated and written in C++.

Geant4 is applied by many high energy particle physics experiments such as ATLAS or ALICE, but is also used in space-based astroparticle physics, e.g. by several ESA projects, as well as in medical and biological applications, e.g. dosimetry and brachytherapy.

Models for various interactions of particles with matter are implemented in Geant4. This includes the interaction of hadrons such as protons and α-particles, as well as electromagnetic interactions of electrons, muons and γ-radiation. The cross sections of all these interactions are energy dependent. The various fields where Geant4 is applied require accurate simulations of particle interactions whose energies differ by several orders of magnitude. Especially EM processes, namely the interaction of charged particles such as electrons and ions, as well as γ-radiation, can be calculated analytically for high energetic particles. But for COBRA's main ROI of several keV up to few MeV, these analytical calculations become unreliable. Therefore Geant4 also provides low energy extensions for these cases [Cir10].

As Geant4 is a simulation toolkit it provides various methods of particle interactions, particle generations, geometry definitions and so on. To use these methods a program has to be designed that makes use of these methods and provides amongst others the choice of the appropriate interaction method, initialization of parameters, data output interfaces and geometry definitions. For COBRA this task is fulfilled by VENOM.

As the EM physics methods were revised with the Geant4 9.3 version and many processes were replaced or not supported any more, VENOM now applies the physics list of the Geant4 underground physics example. There the Livermore package for low

[1] See also http://geant4.web.cern.ch

energy EM processes is applied. It evaluates tabulated data of cross sections from several data bases to calculate particle interactions. Accurate calculation down to a particle energy of 250 meV is expected [Cir10].

2.1.1. Random Number Generator Initialisation

Geant4 offers several pseudo random number generators. The user can choose one of these random number generators and Geant4 methods relying on random numbers automatically receive the numbers from the chosen generator. VENOM applies the CLHEP RANECU random engine to create pseudorandom numbers. This algorithm first described by L'Ecuyer [L'E88] achieves a period of $\approx 10^{18}$ [Jam90] by applying two multiplicative linear congruential generators to produce random numbers. Therefore this generator has to be initialised with two seeds. For the initialisation in VENOM the timestamp (in seconds) of the start of the simulation program was used. To generate large data samples nowadays often many simulations are executed parallel on a cluster. Therefore it was possible, especially at the beginning of a simulation run and when the simulations are run on a cluster with computers with identical hardware, that several simulations had the same timestamps. Therefore, instead of generating many independent simulations, at some times a large number of exactly identical simulations were generated. Reviewing of the generated simulations revealed that up to 70% of the generated files for a simulation run had to be discarded as duplicate.

This issue was resolved by applying the ROOT [Bru97] TRandom3 random number generator [Mat98] to create unique seeds for RANECU and thus for the Geant4 methods applied in VENOM. CLHEP also contains a table with 215 seed pairs. These tables have maximum periods. When processing simulations in parallel the number of simulated events per simulation is in the order of $10^4 - 10^5$ and thus far below the period of the RANECU generator. But when processing just one simulation with many events it is desirable to avoid seeds with a low period and therefore the tabulated seeds with high periods should be taken. Therefore an interface was implemented that offers the possibility to use the Geant4 seed table.

Furthermore, logging of the initial seed that is generated from TRandom3 as well as for the initial RANECU seeds and for the final seeds at the end of the simulation run was implemented. The implementation of the possibility to set the initial seeds manually allows for the possibility to take the final seeds of a simulation with a long period as start values for the next simulation. The possibility to exactly reproduce simulations by applying the same seeds is even more important. This allows for a direct comparison after upgrades of Geant4 or changes in the VENOM program such as the physics lists. For this reason detailed logging of the applied Geant4 and VENOM version was implemented.

2.1.2. Position Generator

The generation of a primary vertex is divided into two parts. First, the primary particles with their energy and momentum are generated. Then positions within the set-up are generated and assigned to the particles to form the initial vertex. Usually it is desired to simulate decays inside a volume such as a detector or on the surface of a volume or within a thin coating on top of a volume, e.g. the passivation of a detector. These three possibilities were already implemented in VENOM. But confining decays to a volume was complicated. Besides the name of the confining volume also dimensions of an additional volume (the generating volume) had to be defined. Positions were generated randomly within this volume and were rejected if the coordinates were not within the confining volume.

This method had two major drawbacks. At first, the calculation of the generating volume was often difficult since the positions of the confining volumes had to be calculated partly from information that is only available in the geometry source code. When choosing a large generating volume with a large safety margin, the generation of positions could become inefficient as many positions had to be rejected. If this safety margin was omitted and the generating volume was not calculated properly, positions were only generated in parts of the confining volumes and there was no method to check for such failure. Each modification of the geometry, such as adding further detectors or changing their size, required a manual recalculation of the generating volume and the risk of the mentioned miscalculations arose again.

Secondly the method failed for complex geometries consisting of subvolumes, such as a pixelated detector consisting of volumetric pixels (voxels) or a complex source geometry. Often it is desired to generate decays in a volume, but not in subvolumes, e.g. ^{222}Rn decays inside gas surrounding the detectors, but not in the detectors themselves. As the detectors are subvolumes of the surrounding gas volume, in general decays in subvolumes were rejected from the algorithm. Therefore the generation within a complex volume was difficult and for some geometries even impossible.

For these reasons a new approach to position generation was taken. For this new method the user only has to define the confining volume by name. The algorithm searches for volumes with the given name in the simulation geometry. If there is more than one volume with the specified name, e.g. several detectors, the volume in which the event will be generated is chosen randomly for each event on the basis of the volumetric ratio of the confining volumes. Then the positions are generated within this volume in local coordinates and these coordinates are then transformed to global coordinates.

A base position generator class was written that contains this method for arbitrary volumes. Local positions are generated within the bounding box of the volume, which is obtained with Geant4 methods, and points that are not within the confining volume are rejected. Compared to the former VENOM method, the amount of rejected points is reduced significantly because the bounding box of a volume is the smallest rectangular volume that still contains all of the confining volume.

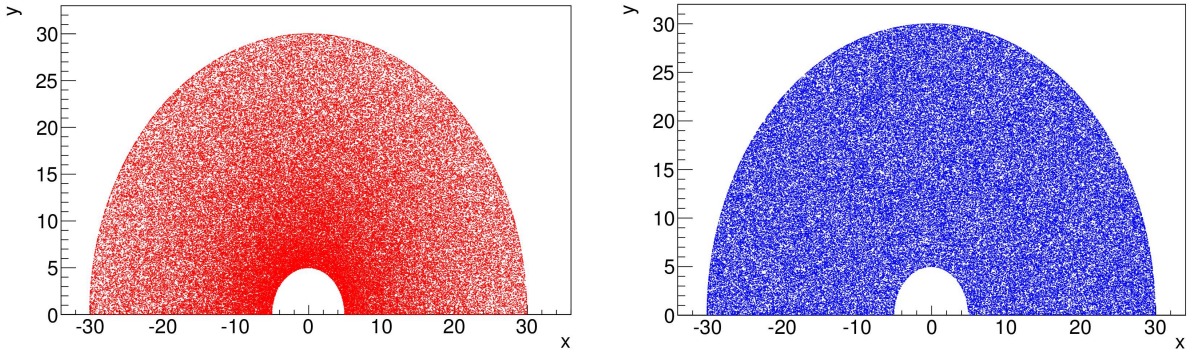

Figure 2.1.: Generated surface random points on the top side of a tube segment (G4Tubs). *Left:* Surface points returned by Geant4 methods. As the radius is generated as a uniformly distributed random variable the generated points cluster quadratically at a low radius. *Right:* Surface points generated with the new implemented VENOM surface generator. The points are uniformly distributed.

Generating uniformly distributed points on the surface of an arbitrary volume is more difficult. Geant4 offers methods to obtain points on the surface of any Geant4 volume, but examination of the source code revealed that these points usually are not uniformly distributed. In the examined methods, geometrical parameters, such as the radius and angles for the description of a sphere, are generated from uniformly distributed random variables and they are transformed by applying the common coordinate transformations, such as from Cartesian to spherical coordinates. But the transformation of the probability density functions (PDFs) that are required to obtain uniformly distributed surface points after the coordinate transformation is not taken into account (see for example Figure 2.1).

As there seems to be a need for uniformly distributed surface points from several users, currently there are are attempts to implement such general methods in Geant4[2]. Algorithms to make use of the Geant4 surface point generation methods have already been implemented in the new VENOM position generator base class and can be activated when these Geant4 methods are available.

Typical volumes defined in GDML (the format of the newly implemented VENOM geometry description method, see Subsection 2.1.3) such as cuboids, cylinders or spheres are imported to Geant4 as Constructed Solid Geometry (CSG) solids [Gea10]. These are simple solids that can be described by a small set of parameters such as width, height, radius and angles. To create surface points at least on simple geometrical volumes and to replace the volume point generation algorithm for general volumes with more efficient customised methods, it is possible to derive classes from the position generator base class. These classes overwrite the methods from the base class. For the most important CSG solids, i.e. rectangular volumes (G4Box), which are by far the most applied

[2]see discussion at `http://bugzilla-geant4.kek.jp/show_bug.cgi?id=1074`

solid type in COBRA, as well as tube segments (G4Tubs) and spherical shell segments (G4Sphere), such derived classes were implemented in VENOM. In these methods properly calculated random variable transformations (see Appendix A) are applied. A solid manager determines whether the confining volumes belong to the implemented types and chooses the appropriate generator and the general point generator otherwise.

The need for a method for the creation of uniformly distributed random surface points on arbitrary surfaces may arise before the problem is solved in Geant4, or possibly this problem will not be solved in Geant4 at all. In this case a universal but computational intensive approach, e.g as proposed in [Det08], can be implemented in VENOM.

2.1.3. GDML Geometry Implementation

The definition of the simulated set-up geometry is usually done by the user in the source code of his program. This includes the definition of the applied materials as well as the construction of the volumes composing the physical geometry. This approach is applied in VENOM. It has the advantage that, if such interfaces are implemented by the user, parameters such as the dimensions of a detector or a shielding layer can be changed at runtime. But there are also severe disadvantages.

To generate or modify a geometry a user has to possess a good knowledge of the C++ programming language, Geant4 methods and the user specific program, in this case VENOM. Especially generating a new geometry is complex, as a complete C++ class containing the geometry and often also a messenger class to change parameters at runtime have to be written. The geometry class then has to be registered to the user program and Geant4 administration classes. This makes it nearly impossible to design a new geometry quickly or even do simulations in the scope of a short based thesis such as a bachelor thesis.

The catenation of the actual simulation framework and the simulation geometry may also complicate the work with the same program in a larger collaboration. As in collaborations the programs are usually distributed to several people who download from a common version controlled source, customisation of a geometry by one person also affects the results of other users working with the same geometry. Furthermore hard coded geometries are not portable to other simulation packages as they strongly depend on the methods of a simulation package.

For these reasons, alternatives were discussed for the implementation of the complex DLB geometry for VENOM. It was decided to use GDML[3] [Chy06]. The main advantages of GDML are that it is developed at CERN and therefore is supported not only by Geant4 but also by ROOT. So GDML based geometries can be applied in both important software frameworks. Furthermore GDML is based on the XML document structure rules, it is both human-readable and editable with every editor program as well as machine-readable. The syntax of GDML can be learned fast, hence the effort to

[3]See also http://gdml.web.cern.ch/GDML/

set up a geometry and do a simulation is significantly reduced. Even the implementation of a complex set-up such as the DLB was possible as a part of a bachelor thesis [Sch10].

Geant4 provides methods to import GDML geometries. During the scope of this work these methods were applied to implement a GDML input and output interface in VENOM. The complete integration as exchangeable geometry module is not possible due to Geant4 issues, namely the incomplete recalculation of cross sections after the addition of materials.

At startup cross sections for several physical processes are calculated for the elements contained in the materials table. Usually materials applied in a GDML geometry are defined within the description file. When imported, these materials are added to the materials list, but for several physics processes the lists of cross sections are not properly updated. This holds especially for neutron capture cross sections from the HPNeutron-Data class[4]. Therefore, physics processes try to access data during the simulation that is not available, which leads to program termination.

To solve this problem two possibilities were found. First it is possible to apply only materials already predefined in the VENOM materials list and to omit the definition of materials in the GDML file completely. This method is contradictory to the main aims flexibility and independence of geometry and simulation framework. Therefore an option to initialise VENOM with a GDML geometry including material definitions instead of the standard geometry was added. The disadvantage of this method is that the standard materials and thus the hard coded geometries are not available during this simulation run. But as the change of geometry during one simulation run is very unlikely this is a minor issue.

As the data output format is left to the user by Geant4, the geometry importing methods do not provide a direct possibility to set a volume as sensitive volume to read out information on the deposited energy and to connect it with a data output format. VENOM contains three data output classes. The GermaniumSensitiveCrystalData class is for simple geometries and only contains information on the energy deposited in one volume. To handle more complex structures as a pixel detector and multi-detector set-ups the PixelDetectorData and Array64SensitiveCrystalData classes are implemented. Multi-detector set-ups or pixel detectors that consist of an array of pixels are realised by copying the same volume several times. Every copy is identifiable by its copy-level specific copy number. For example, a pixel is copied several times in a pixel detector. This pixel detector can than be copied again. The data output class then reads out the copy number of the pixel copy level and the detector copy level and assigns them to pixel- and detector identifiers (IDs).

To mark volumes as sensitive volumes, connect them to appropriate data classes and assign copy numbers for the volume identification in the output data, methods have been implemented to the VENOM GDML reader module. Here care was taken that this VENOM specific information can be implemented in a GDML file without extending or

[4]See e.g. Geant4.bug report #1156, `http://bugzilla-geant4.kek.jp/show_bug.cgi?id=1156`

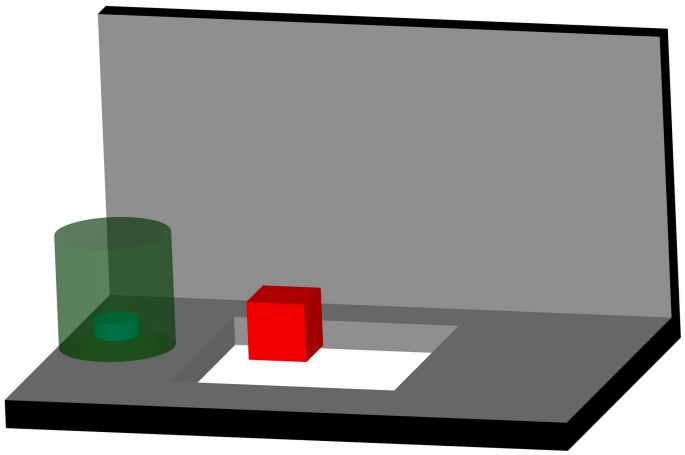

Figure 2.2: Simplified GDML model of a CPG (red) measurement set-up. To contact the cathode from below, a cut-out is below the detector. The Delrin structure that is holding the detector was omitted as it consists of a small amount of light material. The radioactive source is within an acrylic plastic container. The bottom and side plate of the set-up consist of Aluminium.

breaking the GDML scheme to keep the geometries readable also by other programs. Therefore the GDML possibility to attach auxiliary information to volumes was used.

As auxiliary GDML information is versatile, also the possibility to assign colours to volumes or materials for graphical output as auxiliary information was implemented. The applied parsing methods can easily be used to assign also other information to volumes if needed.

Several GDML examples have been added to VENOM in order to show the correct syntax usage and to provide a variety of geometries that can be customised and extended by the user.

2.1.4. Data Amount and User Cut Settings

In simulations with an external source that is some distance away from the sensitive volume, e.g. the measurements described in Section 2.2, only a small fraction of the generated events deposit energy in the sensitive volume. For example, in the ^{152}Eu simulation energy was deposited in the germanium crystal in only 3 % of the generated events. Nevertheless, for storing these events the same amount of memory as for events with energy deposition is needed. Keeping also events without energy deposition adds certain convenience during the data evaluation. But as especially for the simulation types described above the generation of many events is necessary, the size of the data output can be significantly reduced when information of the events without energy deposition is not stored. Therefore methods and a user interfaces were implemented to allow for discarding these events. Also the possibility to reduce the amount of information that is stored by the data classes mentioned in Subsection 2.1.3 (e.g. the ID and z-voxel information for a pixel detector when simulating only one two-dimensional detector) were added.

Furthermore often only γ-radiation from the source is able to reach the detector as electrons or α-particles from the primary decay cannot escape the source. Nevertheless,

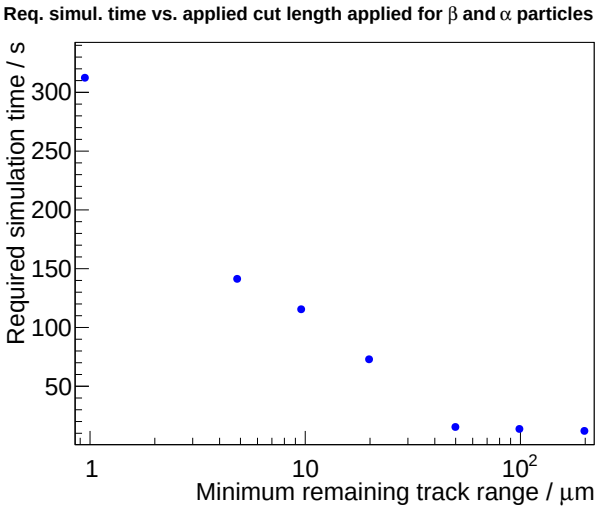

Figure 2.3: Saving of simulation time for user range cuts on minimum remaining track range in a ^{232}Th simulation. The geometry shown in Figure 2.2 was used and the cuts were set to the radioactive volume of the source. As the ^{232}Th chain contains many α- and β-decays and only 0.3 % of all generated events deposit energy in the sensitive CPG volume the CPU time for the simulation is decreased significantly with stronger cuts. Large cuts leading to very low simulation times may distort the simulation result in the low energy region as bremsstrahlung from electrons is also suppressed.

Geant4 tracks all particles in all volumes with the precision that is set in the physics list. Especially for set-ups with little mass such as the CPG test set-up (see Figure 2.2) it is very likely that γ-particles escape the geometry with no or only few interactions. Thus the tracking of γ-particles is often much less time consuming than the tracking and computation of the propagation of solid particles. Therefore often most of the computation time is used for particles that will not contribute to the result of the simulation.

For these cases, Geant4 offers the possibilities to connect volumes with so called user cuts. These cuts have to be specifically activated for particles. There are several user cuts such as the maximum allowed length of a step, the minimal remaining energy for a track or the minimum remaining range of a track. The user can set limits to these conditions. If one of these limits is exceeded, the particle is stopped and the tracking is aborted. As electrons and α-particles have a very short range in matter, the possibility to set the user cut of the minimal remaining range of a track for electrons, positrons, α-particles and also γ-particles was added to VENOM. The cuts can also be applied to several particle types simultaneously. The reduction of computation time for a ^{232}Th simulation with the CPG geometry from Figure 2.2 is shown in Figure 2.3. Here the range cuts were applied to the active source volume for α and β-particles. By applying such user cuts the required CPU computational time can be reduced in this case by more than an order of magnitude.

Some detector systems like the DLB have an energy threshold far above the Geant4 energy tracking limit of 250 eV, which is defined in the physics list. In the case of the DLB, the energy threshold is at about 40 keV due to the detector end-cap. To suppress tracking of particles below this threshold also the possibility to set a volume specific cut on the remaining kinetic energy of a track was implemented.

Year	Geant4 Version	Efficiency / %
2003	unknown, [Blo07]	66.5
2007	unknown, [Daw09b]	61.0
2010	9.2.p01	55.8
2012	9.4.p04	49.3

Table 2.1: Efficiencies for ^{116}Cd $0\nu\beta\beta$-decay full energy deposition determined with several Geant4 versions. As the logging of the Geant4 and VENOM version was only recently implemented the exact Geant4 version is not known for older simulations.

2.2. First Tests with DLB Geometry

Geant4 supports GDML from version 9.2. So VENOM was migrated together with T. Neddermann to the current Geant4 version, which was 9.3 at that time. As already mentioned in Section 2.1, several physics processes in the VENOM physics list were marked as deprecated and removed in Geant4 version 9.4. As Geant4 9.4 contained a better GDML support and to profit from the physics model improvements and keeping VENOM compatible with newer Geant4 versions, the VENOM physics list was replaced by the Geant4 underground physics example physics list.

Changes in the physics lists or Geant4 versions can lead to noticeable changes in the outcome of the simulation. As can be seen from Table 2.1, the efficiency of a full energy deposition in a $1.05 \times 1.05 \times 1.05\,\mathrm{cm}^3$ CdZnTe detector for a ^{116}Cd $0\nu\beta\beta$-decay event decreased steadily with improved Geant4 versions during the last years (because the logging of the software version for better reproducibility was introduced to VENOM just in the scope of this work, only for a few simulations the used Geant4 version is known). A verification of simulated data therefore is desirable.

There are efforts to validate the applied physics models and cross sections, see e.g. [Apo10, Cir10, Iva11]. They include cross checks with data bases such as NIST as well as experimental verifications, especially for higher energetic processes. There are also validation checks outside the Geant4 collaboration, e.g. [Bos11]. But as the simulated energies and material properties differ for each experiment, it was proposed to define VENOM standard simulations, if possible verify them experimentally and use them to validate VENOM with these simulations after major Geant4 upgrades or changes in the physics list. One good candidate will be explained in the following.

In 2008 the High Purity germanium detector facility DLB was set up at TU Dortmund [Ned13] to test the radiopurity of materials for COBRA. To calculate the activity of a material a detection efficiency has to be determined from MC simulations. Therefore the geometry of the whole set-up was implemented in GDML [Sch10]. As the germanium crystal itself is enclosed in a vacuum sealed housing, information from the manufacturer on the crystal dimensions and position were used. As there were several uncertainties regarding the specifications, an elaborate tuning of the detector geometry is crucial for an optimal agreement between simulation and measurement. This was done by T. Neddermann in [Ned13].

For a first test to validate VENOM's GDML extension and to verify the geometry

Energy [keV]	Meas. [1/s]	Sim., new PhyList [1/s]	Deviation [%]	Sim., old Phylist [1/s]	Deviation [%]
81.0	5.871 ± 0.005	5.87 ± 0.10	-0.1 ± 1.6	5.83 ± 0.10	0.7 ± 1.6
160.6	0.137 ± 0.002	0.14 ± 0.01	0.8 ± 10.2	0.19 ± 0.01	-38.4 ± 10.3
223.2	0.085 ± 0.001	0.07 ± 0.01	19.1 ± 13.7	0.08 ± 0.01	7.6 ± 13.9
276.4	1.180 ± 0.002	1.26 ± 0.03	-6.3 ± 2.2	1.23 ± 0.03	-4.0 ± 2.2
302.9	2.846 ± 0.003	3.06 ± 0.05	-7.4 ± 1.9	3.21 ± 0.06	-12.7 ± 1.9
356.0	8.608 ± 0.005	9.09 ± 0.14	-5.7 ± 1.7	9.04 ± 0.14	-5.0 ± 1.7
383.8	1.184 ± 0.002	1.35 ± 0.03	-13.8 ± 2.3	1.36 ± 0.03	-14.8 ± 2.3

Table 2.2.: Measured and simulated count rates of a ^{133}Ba source. Especially for higher energetic lines the simulated count rates in the full-energy peaks are higher than the measurement.

Energy [keV]	Meas. [1/s]	Sim., new PhyList [1/s]	Deviation [%]	Sim., old Phylist [1/s]	Deviation [%]
121.8	7.381 ± 0.005	7.74 ± 0.12	-4.9 ± 1.6	7.88 ± 0.12	-6.7 ± 1.7
244.7	1.520 ± 0.003	1.70 ± 0.03	-11.9 ± 1.9	1.70 ± 0.03	-11.7 ± 2.0
295.9	0.078 ± 0.001	0.08 ± 0.01	-1.8 ± 6.9	0.09 ± 0.01	-10.2 ± 9.8
344.3	4.320 ± 0.004	4.72 ± 0.07	-9.2 ± 1.7	4.67 ± 0.07	-8.0 ± 1.7
367.8	0.132 ± 0.001	0.14 ± 0.01	-4.5 ± 4.2	0.13 ± 0.01	-1.8 ± 5.7
444.0	0.416 ± 0.001	0.45 ± 0.01	-8.1 ± 2.3	0.44 ± 0.01	-5.4 ± 2.7
688.7	0.085 ± 0.001	0.090 ± 0.004	-6.0 ± 5.0	0.114 ± 0.006	-35.1 ± 7.4
778.9	1.177 ± 0.002	1.23 ± 0.02	-4.7 ± 1.8	1.28 ± 0.02	-8.8 ± 2.0
867.4	0.352 ± 0.001	0.38 ± 0.01	-7.1 ± 2.3	0.38 ± 0.01	-9.0 ± 2.9
964.1	1.149 ± 0.002	1.26 ± 0.02	-9.7 ± 1.8	1.24 ± 0.02	-7.6 ± 2.0
1112.1	0.963 ± 0.002	1.07 ± 0.02	-10.7 ± 1.9	1.08 ± 0.02	-11.7 ± 2.1
1213.0	0.096 ± 0.001	0.105 ± 0.003	-5.8 ± 3.6	0.105 ± 0.005	-9.4 ± 4.9
1299.1	0.103 ± 0.001	0.115 ± 0.003	-12.3 ± 3.3	0.113 ± 0.004	-9.9 ± 4.4
1408.0	1.258 ± 0.002	1.39 ± 0.02	-10.8 ± 1.8	1.44 ± 0.03	-14.8 ± 2.0

Table 2.3.: Measured and simulated count rates of a ^{152}Eu source. Especially for higher energetic lines the simulated count rates in the full-energy peaks are higher than the measurement.

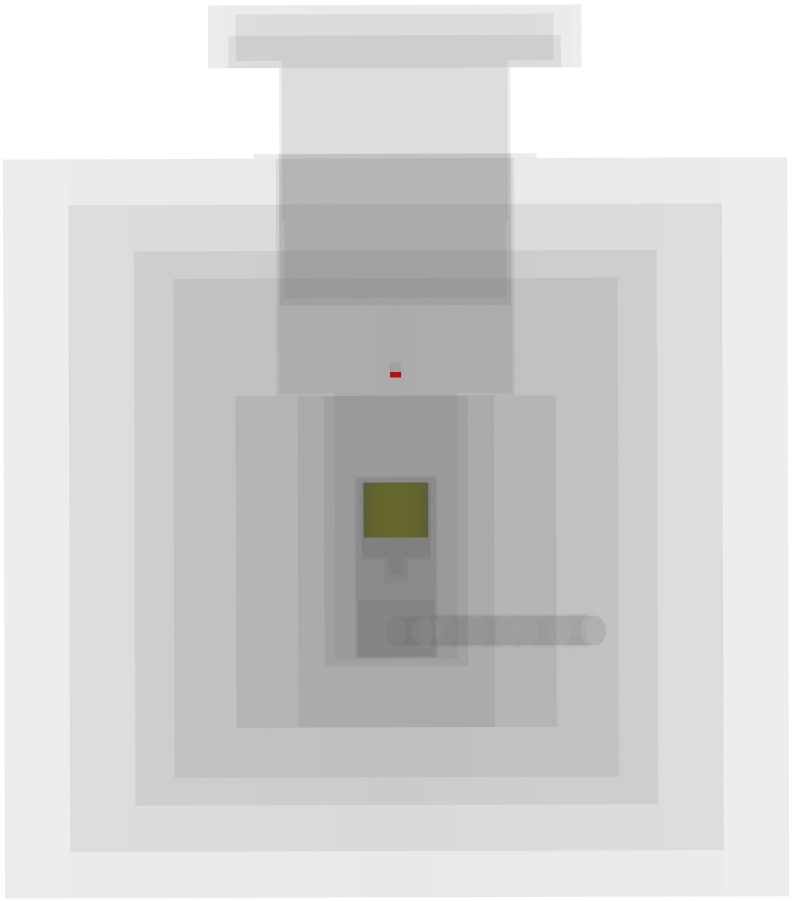

Figure 2.4: Geometry for DLB reference measurement. The reference source (the active area of the source is marked in red) is placed 21 cm above the germanium crystal (marked in yellow). The grey shades indicate the various layers of the shielding. The top cover of the set-up was raised to be able to put the source above the detector.

model and the simulation in general, simulations of two reference measurements provided by T. Neddermann were done and evaluated. As in the applied Geant4 version 9.3 the old and the new physics lists were still supported, the simulations were done with both of them to compare the results.

As reference sources ^{133}Ba and ^{152}Eu were taken because these sources were available with known activity and they provide γ-lines in a wide energy range between 81 keV and 1408 keV. The correct geometry (see Figure 2.4) of the reference source in the GDML set-up geometry was provided by T. Neddermann. The sources were placed 21 cm above the detector to avoid near detector effects, such as random or true coincidence summing of the emitted γ-particles. Additionally, small inaccuracies of the source position have a smaller influence for larger source-detector distances.

To compare the measurements and the simulations the activity of the sources was calculated from the manufacturer information of the activity and the reference date. The relative uncertainty of the activity was given with a 2σ confidence level to be 3 %, which equals $\sigma_{A,\mathrm{rel}} = 1.5\,\%$. The uncertainty of the activity was taken into account for the calculation of the time-equivalent of the simulation. This 1.5 % uncertainty is the largest contribution for the statistical uncertainty of the simulation (except for lines

with a very low intensity).

The simulation was convoluted with the resolution information obtained from the measurement. The peak content within $\pm 1.25\times$FWHM of the full energy peaks of γ-lines with a reasonable intensity was determined in the simulation and the measurement, and activities were calculated for these lines. The wide counting range of $\pm 1.25\times$FWHM (equivalent to $\pm 2.9\,\sigma$ or $> 0.997\,\%$ of a Gaussian distribution) ensures a minor influence of uncertainties in the exact width of the full energy peak. To obtain an approximation for the background within the counting area an area of $\pm 1.25\times$FWHM to the left and to the right of the signal region was used. Care was taken to choose only γ-lines that have no other lines in the signal or in the background region.

The results of the comparison are listed in Table 2.2 and Table 2.3 and for direct comparison the measured and simulated spectra together with the deviation

$$\mathrm{Dev} = \frac{N_{\mathrm{meas.}} - N_{\mathrm{sim.}}}{N_{\mathrm{meas.}}}$$

of the simulation from the measurement are shown in Figure 2.5 and Figure 2.6. As can be seen there the general shape and ratios of the intensities of the γ-lines fit well. The ratio of full energy peak to background is higher in the simulation than in the measurement. For low energies, readily visible in Figure 2.5 for the ^{133}Ba lines, the full energy peaks fit well and the simulated background is lower than the measured background. The simulated and measured background fit well at higher energies, but the full energy peaks are higher in the simulation than in the measurement. This can be seen from Figure 2.6 for the ^{152}Eu source. This results in an overestimation of the full energy peak detection efficiency. The effect is small for lower energies and increases to about 10 % for higher energies.

Similar effects, also in the same order of magnitude of several per cent, have also been observed in other Geant4 simulations of germanium detectors [Hau09, Hau10, Bos11]. In these publications, an inaccurate implementation of the geometry is often assumed to be one of the main reasons for the deviation. As already mentioned, the geometry applied for these first DLB simulations relied on the information of the manufacturer and this may not be absolutely precise. Another source of error for the comparison is the exact position of the reference source.

Other reasons can be inaccuracies in the applied physics processes. For the interaction of γ-particles with matter the cross sections for the underlying physics processes like photo- and Compton effect have to be implemented properly. As germanium is an often applied and well known material, this will certainly be the case. Furthermore also the propagation and energy deposition of the electrons after the interaction of the γ-particles have to be implemented properly. As can be seen from Table 2.1, this may be a major problem.

Finally, Geant4 only supplies the pure energy deposition in the sensitive volume. All detector effects, such as charge transport, charge trapping or imperfect field distributions, for example at the edges of the germanium crystal, are not taken into account and

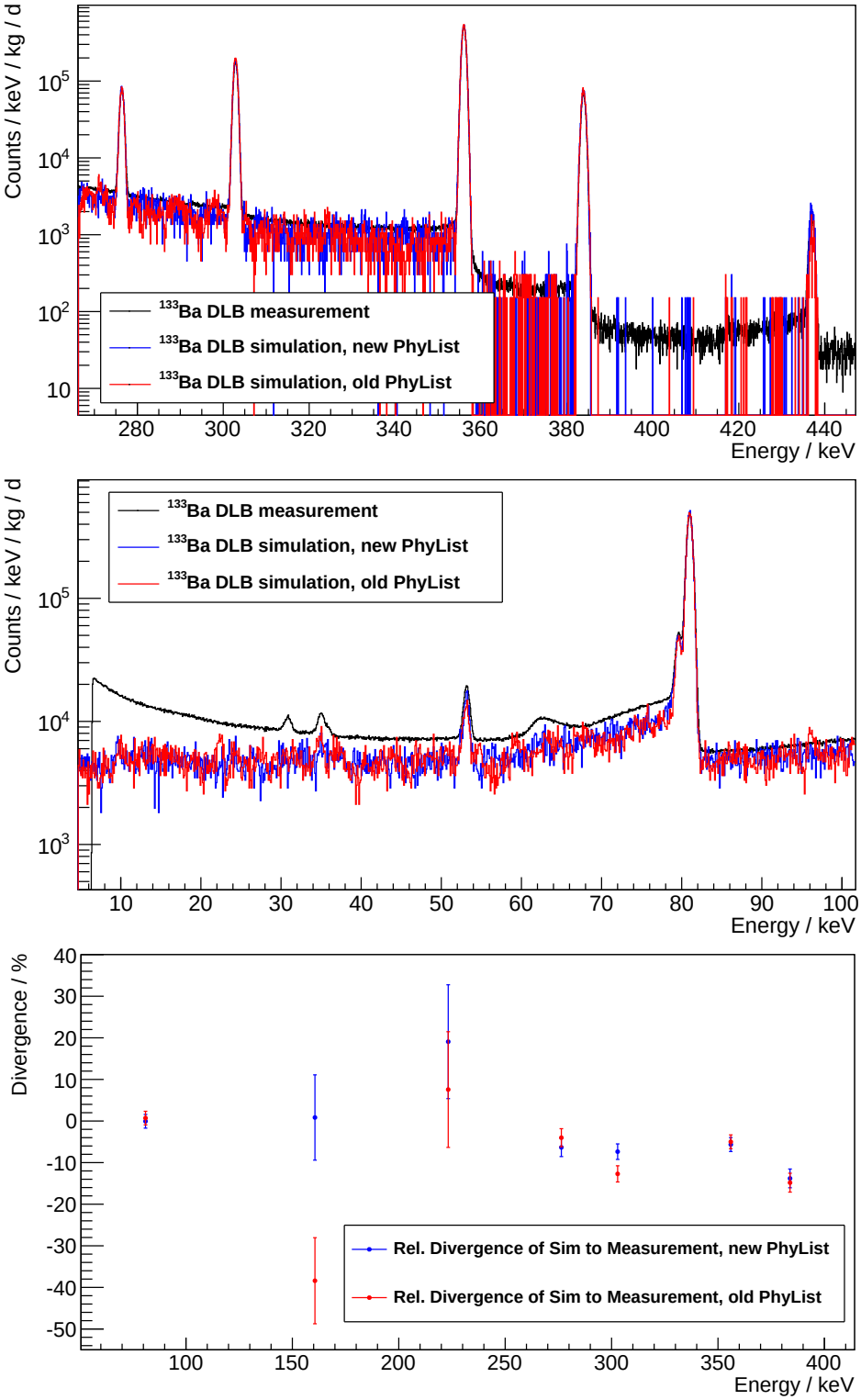

Figure 2.5.: ^{133}Ba DLB simulation and measurement. Even though the geometry model was not optimised, simulation and measurement agree well, especially at higher energies. The simulation shows a higher peak to background ratio than the measurement, especially for lower energies. The divergence of the full-energy peak contents of the simulation to the measurements is improved with the new physics list.

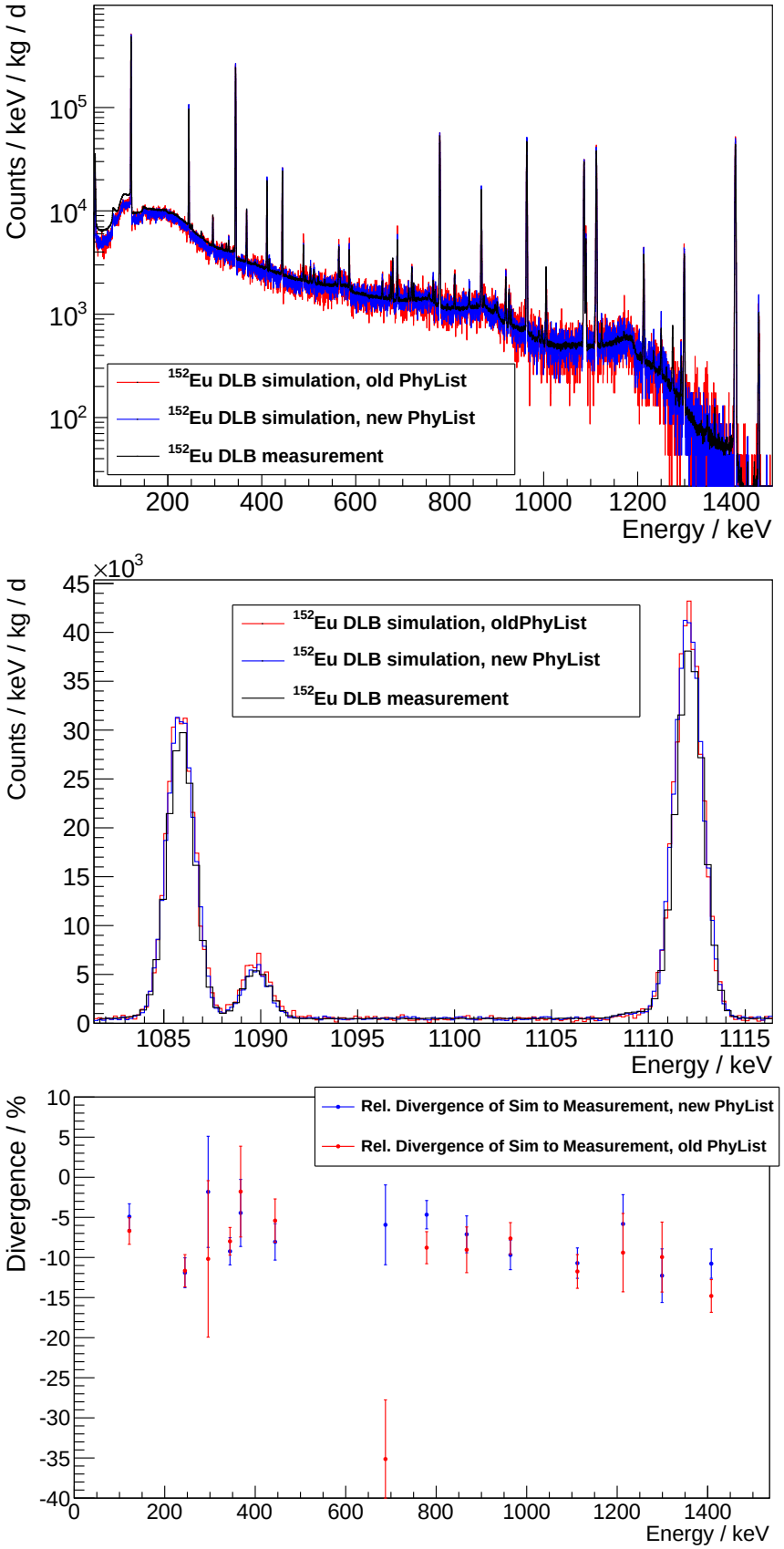

Figure 2.6.: ^{152}Eu DLB simulation and measurement. Simulation and measurement agree well. Like for the ^{133}Ba measurement, the peak to background ratio is noticeably too large for low energies and the full energy peak efficiency tends to be overestimated for higher energies. These discrepancies can be decreased by optimisation of the applied geometry [Ned13].

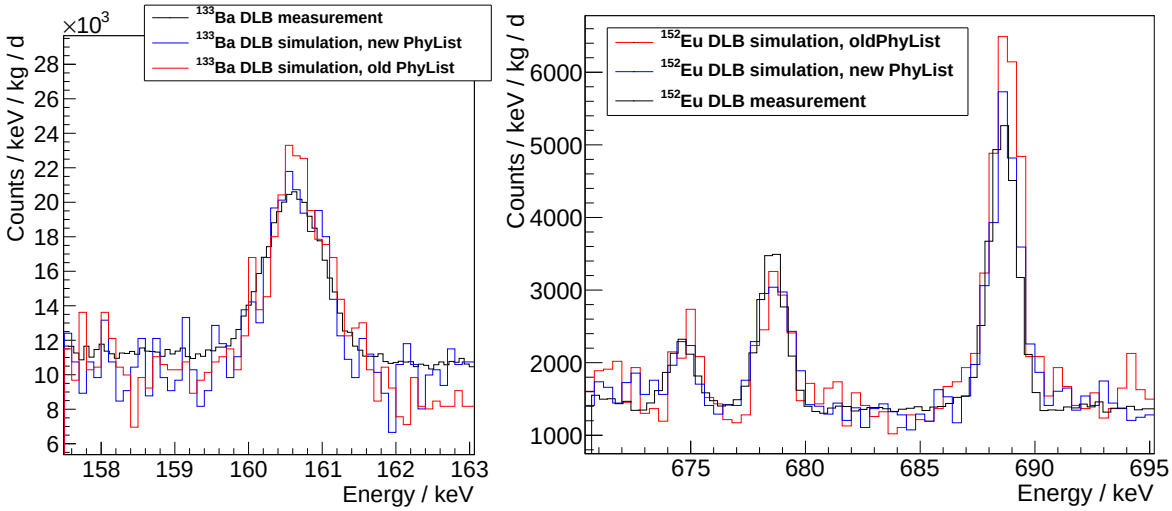

Figure 2.7.: *Left:* 161 keV ^{133}Ba line and *Right:* 689 keV ^{152}Eu lines with large divergences of measurement and simulation with the old physics list. It is not clear where these discrepancies derive from, especially as lines in the vicinity of the 689 keV line were reproduced correctly. However, the mismatch is corrected with the new physics list.

cannot be computed with Geant4. This is possibly the main reason of the deviations. An approach to this problem is a tuning of the geometry of the detector so that it may not reproduce the true detector geometry but agrees better with the measurements [Ned13].

Even though the observed discrepancies between the simulation and the measurement are in the order of a few per cent, the accuracy is quite good when taking into account the not optimised detector geometry and neglected detector effects. The large discrepancy in the simulation with the old physics list for the 689 keV ^{152}Eu and the 161 keV ^{133}Ba line (see Figure 2.7) were corrected with the new physics list.

2.3. Simulation and Measurement of a ^{232}Th Source for a CPG Detector

The main COBRA detector material is not germanium but CdZnTe. To test the validity of CdZnTe simulations therefore also a first test simulation with a γ-source was done. In the simulation the simplified GDML model of the measurement test set-up shown in Figure 2.2 was used. For a comparison between measurement and simulation the calibrated sources applied for the DLB simulations are not suitable because their activities are very low and the active mass of a CdZnTe detector is much smaller than for the germanium detector. Also the energy resolution is worse. Instead a ^{232}Th source was chosen to make a first comparison between measurement and simulation. The ^{232}Th chain contains many α-decays. Therefore the simulation of this decay chain requires a lot of computation time. On the other hand, only about 0.1 % of the simulated events

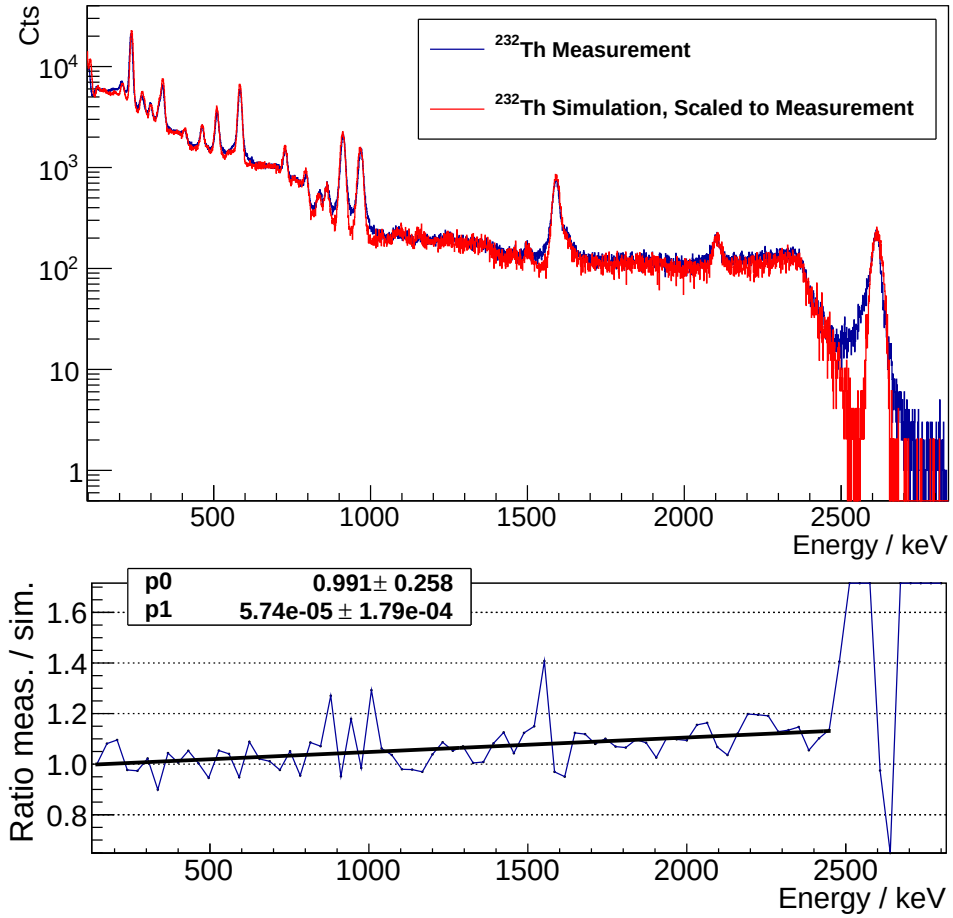

Figure 2.8.: ^{232}Th simulation and measurement for a CPG detector. For the simulation the geometry shown in Figure 2.2 and a 10 MeV cut to suppress extensive calculations of α-particles were used. The simulation was scaled by the ratio of events between 100 keV and 2650 keV in the measurement and the simulation (by a factor of 2.1). The 2.6 MeV line differs more certainly due to detector effects that cannot be reproduced with Geant4.

deposit energy in the active detector volume. To have a sufficient statistic, many events have to be simulated. In this case 2×10^9 events were processed. By applying an energy tracking cut for α-particles (see Subsection 2.1.4) of 10 MeV and only writing events with energy deposition, the computation time was reduced by more than a factor of 100 and the file size even by a factor of 1000. By not applying cuts to the range of the β-particles the risk of neglecting bremsstrahlung from the source was avoided.

To compare the measurement and the simulation, the simulated events were convoluted with a Gaussian whose parameters were determined from the resolution of the measured spectrum. The simulated spectrum was then scaled with the sum of events in the measurement between 100 keV and 2650 keV by a factor of 2.1. The measurement and the scaled simulation are shown in Figure 2.8 and an enlarged view in Figure 2.9.

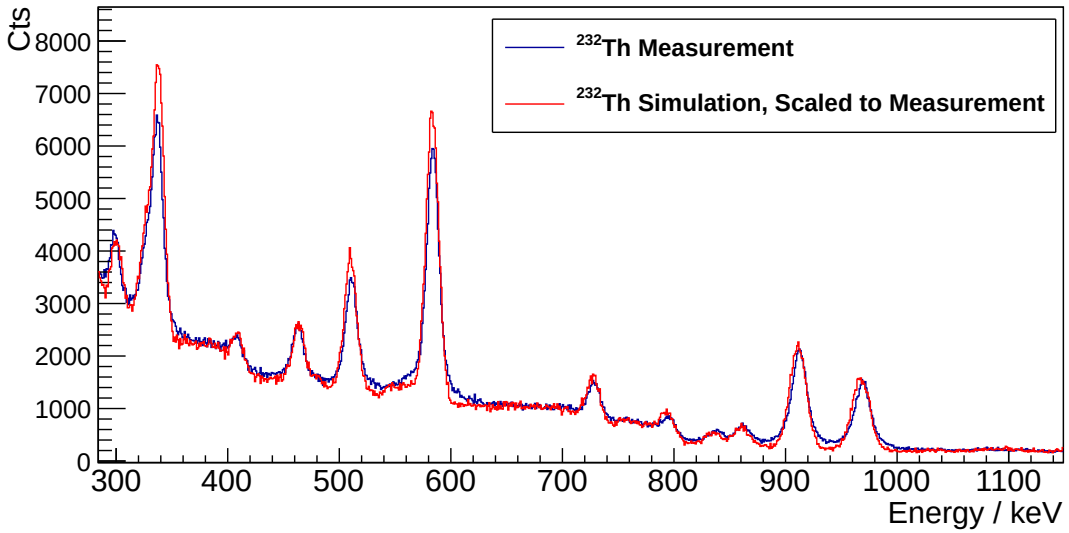

Figure 2.9.: Enlarged view of Figure 2.8. Similar to the DLB simulation the peak to background ratio is better in the simulation than in the measurement. For CdZnTe this is partly due to the more complex detector effects. This can be seen from the fact that a Gaussian energy resolution does not fit perfectly to the full energy peaks and consequently events with full energy deposition are partly in a low- and high-energy tail.

The general shape of the spectrum fits surprisingly well in the whole energy range, but it becomes obvious that detector effects play a larger role than for the simulation of germanium. The approximation of the energy resolution as a Gaussian function does not fit perfectly. For several peaks a low and high energy tail is visible. This effect is especially strong for the 2.6 MeV line. An explanation may be that for such a high energy the interaction process differs significantly from lower energies. The most dominating effect is Compton scattering followed by pair production (visible from the single escape peak at 2.10 MeV deriving from one 511 keV positron annihilation γ-particle escaping the detector and the double escape peak at 1.59 MeV deriving from both 511 keV positron annihilation γ-photons escaping the detector) . The probability for photoelectric absorption is up to two orders of magnitude lower than these processes. Therefore the full energy peak at 2.6 MeV derives mainly from γ-particles undergoing Compton scattering followed by photoelectric absorption of the scattered γ-particle, a so called multi site event. This may lead to a different charge transport or charge collection behaviour for the high energetic γ-particles.

As already observed for the germanium simulation the peak to background ratio seems to be higher in the simulation than in the measurement. In this case, the effect of the low and high energy tails described above is one of the main reasons for this mismatch as the height of the peaks in the measurement is reduced by the number of events in these tails. The mismatch of simulation and measurement differs also significantly for different γ-lines, as can be seen in Figure 2.9. This may also be a hint on not exactly implemented

intensities for the γ-lines in Geant4. For example the 911.2 keV and 969.0 keV from the ^{228}Ac fit well whereas the 338.3 keV line from the same decay is significantly too high.

In contrast to the DLB simulation, the ratio of measurement to simulation increases with higher energies from a value of 1 (due to the normalisation) at 100 keV to about a factor of 1.15 at 2500 keV. Even though an exact comparison of the simulation and the measurement is not possible due to the unknown activity of the applied source, one can conclude that the average deviation of the simulation from the measurement should be less than 10 %, which is an acceptable value. To confirm this assumption, reference measurements with a calibrated source and an exact implementation of the geometry should be made.

Another reassuring result of the comparison is the comparatively good agreement of the double escape peak with the rest of the spectrum. The double escape peak derives from pair creation of the 2.6 MeV γ-particle in the detector. As both 511 keV γ-particles escape the detector, the whole energy is deposited by the electron and the positron. This resembles a double beta decay. As the double escape peak is well reproduced also the simulations of the double beta events should be reliable.

2.4. Background Study for a Large Volume Pixel Detector

2.4.1. Description of the Large Volume Pixel Detector

Pixel detectors offer new possibilities for the reduction of background with their additional spatial information. For COBRA three types of pixelated detectors are under investigation [Sch11b]. Very promising results were achieved in [Sch11a] with a large pixel detector provided by the group of Z. He from the University of Michigan. All background events in a region of ± 1 FWHM around 2.8 MeV could be discarded by applying cuts on events in the outer volume and the number of hit pixels.

The applied γ-ray spectrometer detector system (Polaris System [Kay10, Zha07]) consists of up to 18 CdZnTe pixel detectors in a $(3 \times 3 \times 2)$ configuration. The system is read out with a 129 channel application-specific integrated circuit (ASIC). 11×11 anode pixels, the planar cathode and a grid structure, a so called steering grid (see Figure 2.11), can be read out. The steering grid is slightly negatively biased compared to the potential of the anodes. It focuses the drifting charge to the pixels in order to minimise the effect of charge sharing. By evaluating the cathode to anode ratio and/or information on the drift time of the charge, besides the 2D information from the hit pixel also depth information is available. So the full 3D position of an interaction can be obtained.

The prototype tested in [Sch11a] consisted of one $2 \times 2 \times 1.5\,\mathrm{cm}^3$ pixel detector mounted on a 3×3 detector board. It was housed on top of the COBRA CPG set-up at LNGS. The electronics and the detector were not low background optimised. Therefore a shielding of the system with 10 cm of lead was expected to be sufficient. As the heat producing

readout electronics are close to the detector, cooling inside the massive lead shielding is a problematic issue. It was solved by coupling the detector housing thermally to the lead. The temperature could be stabilised, but as the detector performance decreases with higher temperatures [Kay10] the heat production maybe negatively influenced the measurement (see Subsection 2.4.2).

The applied detector was a $2 \times 2 \times 1.5\,\mathrm{cm}^3$ detector crystal with 11×11 pixels, a pixel pitch of 1.8 mm and an anode steering grid. Recently the group of the University of Michigan achieved an energy resolution of up to 0.5 % FWHM at 662 keV, see [Zha12]. There it was stated that the achieved energy resolution strongly depends on the number of hit pixels because the electronic noise in each triggered pixel contributes and the signal crosstalk (charge sharing) between pixels also increases. The effect of charge sharing can be decreased by the already mentioned steering grid, see also [Kim11], but it is not compensated completely. In [Zha12] also Geant4 simulations of several sources, the highest energetic one being ^{60}Co, were compared with measurements. It turned out that while simulation and measurement agreed well in general for the lower energetic sources, the full energy peak efficiency for ^{60}Co in the inner 9×9 pixels also agreed well with the simulation, but the measured efficiency for the outer pixels was significantly smaller than predicted. It was assumed that this effect derives from incomplete charge collection below the steering grid at the edges of the detector. As can be seen from Figure 2.11, the outer part of the steering grid surrounds the pixels at the edge of the detector. So maybe the negative potential that focuses the charge inside the steering grid leads to a larger charge collection inefficiency at the edges.

To cross-check the obtained results and to explore the possibilities of pixel detectors with large pixel size, the influence and veto capabilities for several background sources as well as the $0\nu\beta\beta$-decay detection efficiency were simulated in the scope of this work. As detector effects cannot be taken into account and therefore exact comparability with measured data cannot be achieved, the used geometry was not a detailed model of the Polaris system but the general dimensions were included. The simulated set-up is shown in Figure 2.10. $2 \times 2 \times 1.5$ cm^3 CdZnTe pixel detectors with $11 \times 11 \times 11$ voxels with a 25 μm thick passivation on the sides of the detector (cathode and anode are not covered by the passivation) were put on a 1.5 mm thick FR4 PCB board. As with the Polaris system the detectors were arranged in two 3×3 detector layers and like for the test set-up at LNGS surrounded by 10 cm of lead. The distances between the detectors were approximated from information from [Zha07].

2.4.2. Results for $0\nu\beta\beta$-decay of ^{116}Cd

Detection Efficiency for $0\nu\beta\beta$-decay To obtain information on the distribution of ^{116}Cd $0\nu\beta\beta$-decay signal events and the influence to the detection efficiency, 5×10^6 $0\nu\beta\beta$-decay intrinsic events were simulated within the detector. The detection efficiency here is defined as the probability to observe an event with full energy deposition in the detector. Electrons from events close to the surface of the detector crystal can leave the

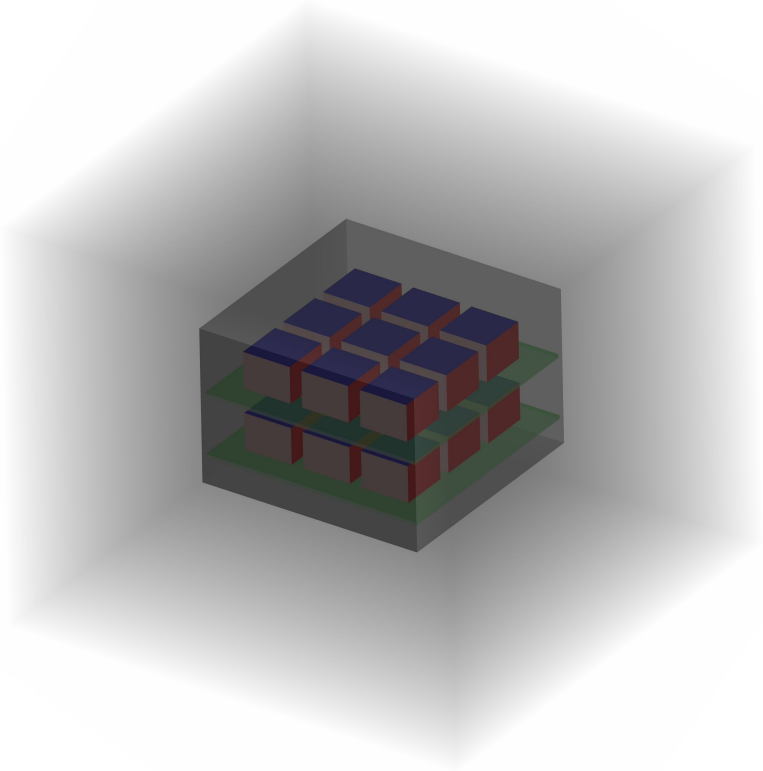

Figure 2.10: GDML implemented set-up for the large volume pixel simulations. Nine detectors (blue) with a volume of $2 \times 2 \times 1.5\,\mathrm{cm}^3$ and $11 \times 11 \times 11$ voxels are arranged in two 3×3 arrays on two PCB boards (green). The sides of the detectors are covered with a $25\,\mu\mathrm{m}$ thick passivation (red). The detectors are surrounded by a 10 cm thick layer of lead (grey). The horizontal distance between the detectors is 5 mm and the vertical distance 10 mm. The dimensions are roughly adapted from [Zha07]

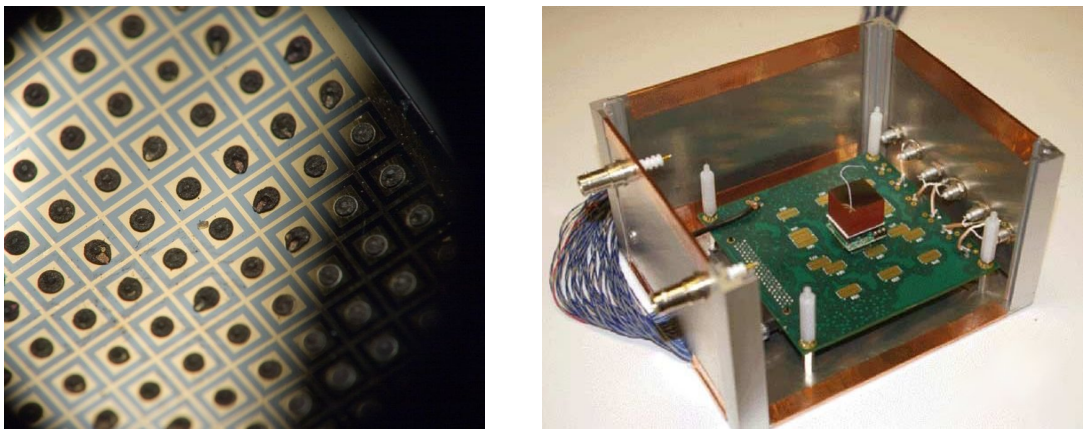

Figure 2.11.: *Left*: Steering grid of a Polaris detector, taken from [Sch11a]. *Right*: One assembled detector module mounted on a 3×3 detector motherboard, taken from [Zha12].

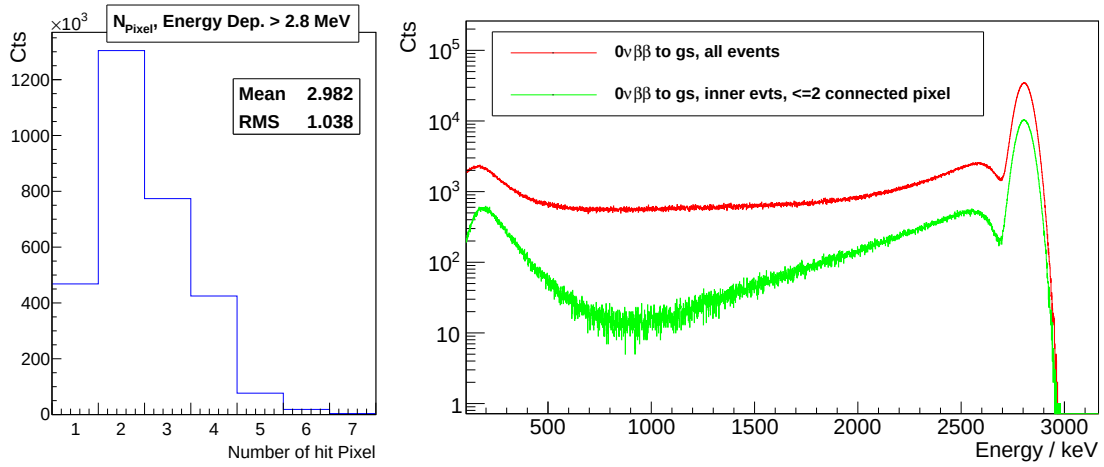

Figure 2.12.: Influence of applied large pixel cuts to $0\nu\beta\beta$-decay detection efficiency. *Left*: About 58% of all full energy events affect less than 3 pixels (here: ideal energy resolution, so all full energy events are above 2.8 MeV). *Right*: Spectra of energy deposition summed over all detector pixels. By applying the cut criteria of less than 3 connected pixels and only events from the inner $9 \times 9 \times 9$ voxels, the efficiency is reduced from 62% to 18%. The distortion of the cut histogram in the lower energy region compared to the uncut histogram derives from discarding most of the events with contribution of bremsstrahlung by applying the ≤ 2 connected pixel constraint.

crystal and thus do not deposit their full energy inside the detector.

Since CdZnTe is a high Z material, another significant process is the production of bremsstrahlung. As the range of γ-particles in material is longer than the range of electrons, the escape of the higher energetic bremsstrahlung is more likely than for electrons. It can also occur in events that are not close to the detector surface. γ-particles, unlike electrons, do usually not deposit energy on their path through matter. However, it is possible that also the bremsstrahlung is absorbed in the detector. But it is very likely that the energy deposition of the original electron and from the bremsstrahlung takes place in different, not connected parts of the detector. Such multi-site events are discarded as they often derive from background processes. This also reduces the signal detection efficiency. Spectra of the energy deposition for $0\nu\beta\beta$-decays together with the number of hit pixels for events with an energy $\geq 2.7\,\mathrm{MeV}$ is shown in Figure 2.12.

Without any cuts the full energy detection efficiency adds up to 62 %. By discarding all events with an energy deposition in the outer voxels, the efficiency is reduced by the loss of active volume, namely a factor of $\left(\frac{9}{11}\right)^3 = 0.55$ to 34 %. By additionally accepting only events with less than three connected pixels the efficiency is further reduced to 18 %.

Simulated Background Model and Background Reduction Possible background was assumed to derive from contaminations in the detector passivation paint, the PCB carrier board and the lead surrounding the set-up. For the paint the activity of the red

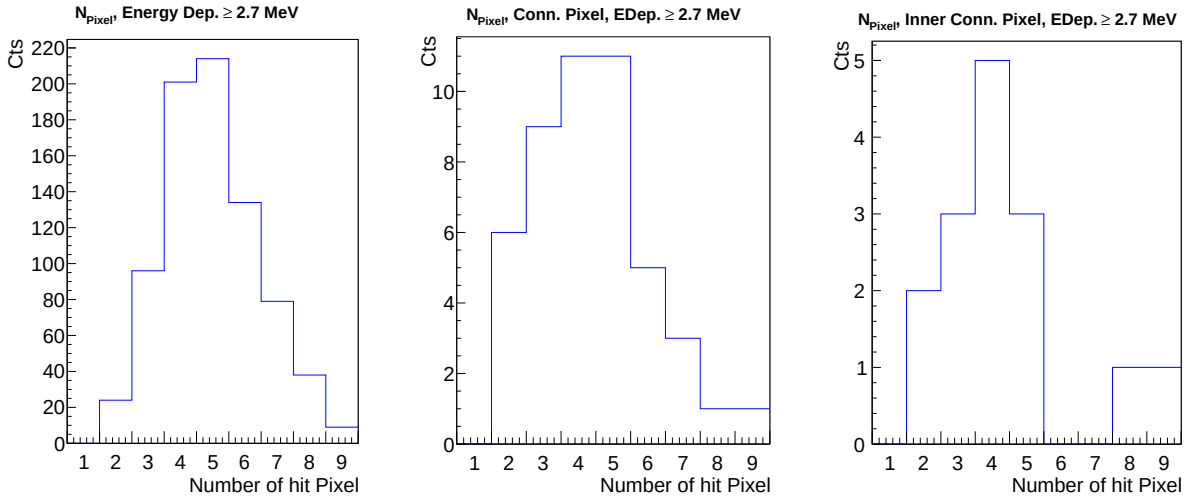

Figure 2.13.: Efficiency of large pixel cuts for γ-particles with energy deposition of more than 2.7 MeV from the simulation of ^{232}Th in lead. As all other particles are stopped in the lead layer, the energy deposition derives from ^{208}Tl γ-cascades (compare Table 2.6). Always at least two γ-particles are involved and Compton effect is dominating in this energy region. The requirement of connected pixels therefore reduces the background significantly. A comparison with the distribution of hit pixels for $0\nu\beta\beta$-decay of ^{116}Cd (see Figure 2.12) shows that a restriction to less than two pixels gives the optimal signal to background ratio.

Simul. BG Type	Sim. Events	Frac. of Fit Sim. to LNGS Data	BG Evts before Cuts	BG Events after Cut
Passivation	10×10^6	0.008	134411	0
^{232}Th in PCB Brd	30×10^6	0.1	6691	3
^{238}U in PCB Brd	30×10^6	0.1	4185	2
^{40}K in PCB Brd	10×10^6	0.01	0	0
^{222}Rn in Gas	10×10^6	0.05	29553	1
^{232}Th in Lead	5×10^9	0.01	790	2
^{238}U in Lead	1×10^9	0.02	43	2
^{40}K in Lead	10×10^6	0.01	0	0

Table 2.4.: Simulated background contributions for the Polaris System. As ROI events in the energy region 2700 keV-3300 keV were taken. Events with lower energies penetrating the ROI due to finite energy resolution are not included in this table. For the simulation of events in lead an energy cut < 10 MeV to α-particles was applied. The number of simulated events was chosen so that the simulation corresponds to at least 10 times the measured data.

passivation lacquer applied by EIDIS[5] (see Table 2.9, Section 2.5) was used.

Judging from the γ-lines in the measured spectrum and by taking into account the commonly known major background sources the main background derives from decays of the ^{232}Th chain, the ^{238}U chain, ^{40}K and airborne ^{222}Rn. For each of these background components separate simulations were produced assuming the decay chains to be in equilibrium.

Because the volume of the lead layer is large compared to the detector volume and the interaction probability of high energetic γ-particles from the lead is low, much more events had to be simulated for this background source. α-particles on the other hand are stopped immediately in the lead and therefore will not deposit energy in the detectors. Therefore a $< 10\,\mathrm{MeV}$ energy cut (see Subsection 2.1.4) on α-particles was used for the lead simulations to suppress the tracking of α-particles and reduce the computation time. For the other background sources no cuts were applied to ensure a correct reproduction of all possible contributions.

The energy (see e.g. Figure 2.14) and penetration depth of α, β- and γ-particles differ significantly. Therefore they have to be treated differently to achieve an optimal background suppression. The energy of α-particles is usually at least 1 MeV above COBRA's ROI. Their range in matter is very short, only several μm for most materials. So as their energy loss per travelling length is high, even in gaseous materials, α-decays in thick material layers such as the lead cannot deposit energy in the detectors. But decays on the surface of the detectors themselves or surrounding materials close to the detectors, in the thin passivation lacquer of the detectors or in the gas layer surrounding them are likely to lose a significant part of their energy and therefore the energy deposited in the detectors may be lowered to the ROI. In fact, $0\nu\beta\beta$-decay experiments with a high Q-value such as CUORE assume that their main background in their ROI derives from α-particles that have lost energy in surrounding materials [Pav08]. Also the evaluation of the simulations done in the scope of this work showed that e.g. most of the events in the ROI from the PCB boards derive from α-decays. The PCB board is comparatively thin, which favours decays close to the surface and PCB also consists mainly of light elements. Nevertheless these α-decays have to occur very close to or on top of the surface of the PCB board and directly beneath the detectors.

Even though the expected background from α-particles is very high it can be reduced effectively, because the range of the α-particles is very small and they do not produce bremsstrahlung. So they can be vetoed completely by discarding events in the outer voxels.

As can be seen from Figure 2.14, only the ^{238}U chain contains β-decays with energies up to 3.3 MeV (also ^{40}K emits β-particles with maximum 1.3 MeV). They derive from ^{214}Bi decays with a high probability of 20 % [Fir98]. For high energetic β-particles it has to be taken into account that their penetration depth even into high Z materials can be several mms (see Section 2.6) and significantly more in low Z materials like the PCB

[5] `http://www.evmicroelectronics.com/`

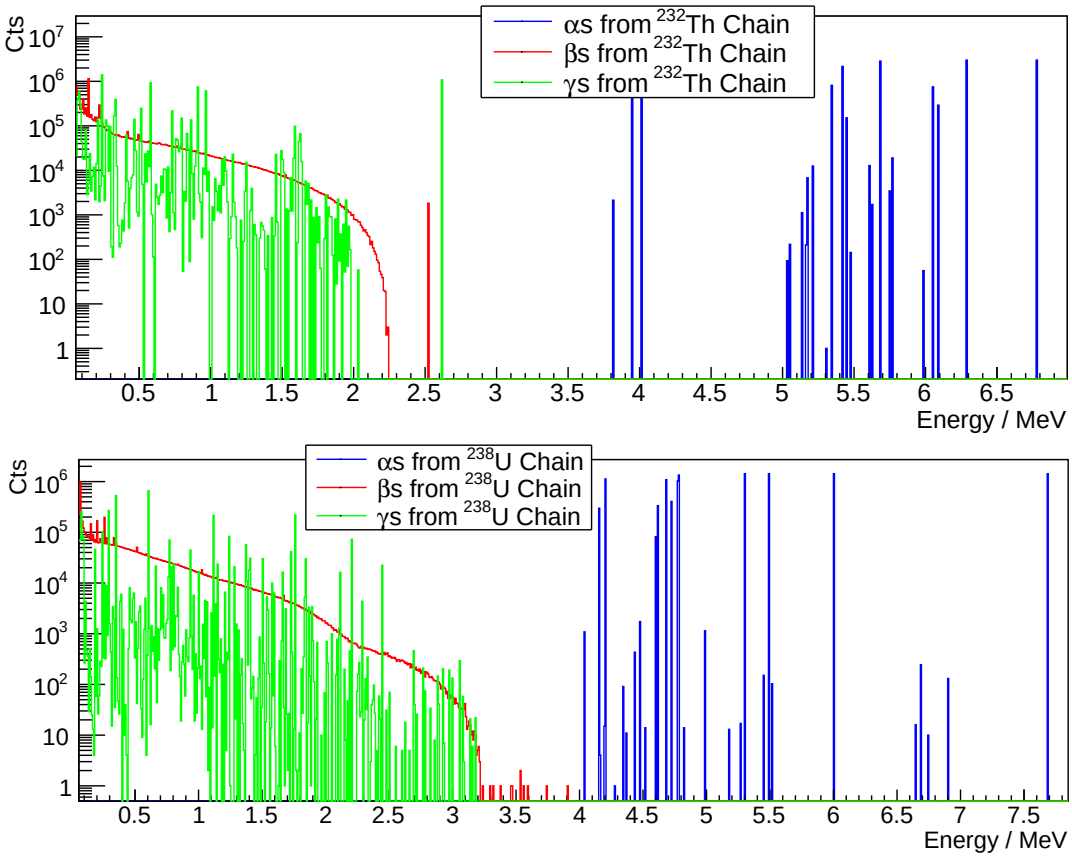

Figure 2.14.: Energy and particle dependent composition of decays from the ^{232}Th (top) and ^{238}U (bottom) chain. Plotted are primary particles from Geant4 simulations. The composition of the background in the main ROI for ^{116}Cd differs for both chains. While several γ- and β-particles from the ^{238}U chain have energies up to 3.2 MeV the background from these particles from the ^{232}Th chain stops at 2.6 MeV (not taking into account coincidences). The monoenergetic β-line in the ^{232}Th spectrum at 2.5 MeV derives from internal conversion of the 2.6 MeV excited state of ^{208}Pb (and therefore these electrons are technically not β-particles but electrons from the atom shell).

board. Energy loss in the passivation is negligible.

Like in the case of $0\nu\beta\beta$-decay the high energetic β-particles radiate bremsstrahlung on their way through matter. The bremsstrahlung can escape the detector completely or be deposited in another part of the same detector, also in the inner voxels. These events resemble Compton scattered γ-particles. On their path through dense matter, unlike γ-particles, the electrons constantly deposit energy in the material by ionising it. Most of the energy in events without emission of bremsstrahlung (see Section 2.6) is deposited at the end of their path. But still a significant fraction will be deposited along the path. Because the β-particles always have to pass through the outer voxel layers, whether they will produce bremsstrahlung or not, and the voxel size is large even compared to the average penetration depth of the highest energetic electrons, there is always a measurable energy deposition in the outer pixels. Thus interaction involving external high energetic β-radiation can also be vetoed by discarding events with energy deposition in the outer voxels.

Similar to the case of β-particles, the γ-background from the ^{238}U chain seems to be more dangerous than from the ^{232}Th chain. High energetic γ-particles usually derive from de-excitation of a nucleus after a β-decay. Even though also α-decays in principle are often accompanied by γ-radiation, the γ-energies and the intensities are usually much smaller than for β-decays. The only isotopes in the two decay chains with a higher Q-value than 2.3 MeV are the ^{214}Bi decay to ^{214}Po (3.3 MeV) from the ^{238}U chain and the ^{208}Tl decay to ^{208}Pb (5.0 MeV) from the ^{232}Th chain.

Both nuclei differ significantly regarding the emitted radiation. ^{214}Bi is a 1^- nucleus and its daughter ^{214}Po a 0^+ nucleus. Therefore the transition to the ground state is possible and results in 20% of the decays in the afore mentioned β-particle with up to 3.26 MeV. Also the decay to many excited states and the de-excitation via a γ-cascade is possible. The variety of emitted γ-particles is very high, with energies ranging from several hundred keV up to 3.2 MeV. As there are many decay channels, the intensity of most γ-lines are below 1 %. γ-particles from this decay with an energy > 2.7 MeV and intensities $> 0.1\%$ are listed in Table 2.6.

In this energy region Compton scattering is by far the dominating effect (see Figure 2.15). The maximum transferable energy via Compton effect for a 3 MeV γ-particle is about 2.8 MeV and thus in the ROI. For lower energetic γ-particles with the energy in the ROI, besides the rather unlikely full energy deposition via photoelectric effect also Compton scattering with subsequent Photoelectric effect of the scattered γ-particle is possible. As can be seen from Figure 2.15, this effect is especially likely for events with a high energy transfer to the electron and a low remaining energy of the scattered photon.

If an interaction with a high energy transfer to an electron takes place, this electron afterwards behaves like an intrinsic high energetic β-particle. The average range of a 2.8 MeV β-particle is higher than for (on the average) two 1.4 MeV electrons because $\frac{\mathrm{d}E}{\mathrm{d}x}$ usually is higher for lower energies. A simulation (see Figure 2.16) showed that on average nearly 0.5 more pixels are hit. By applying the same cuts like for $0\nu\beta\beta$-decay,

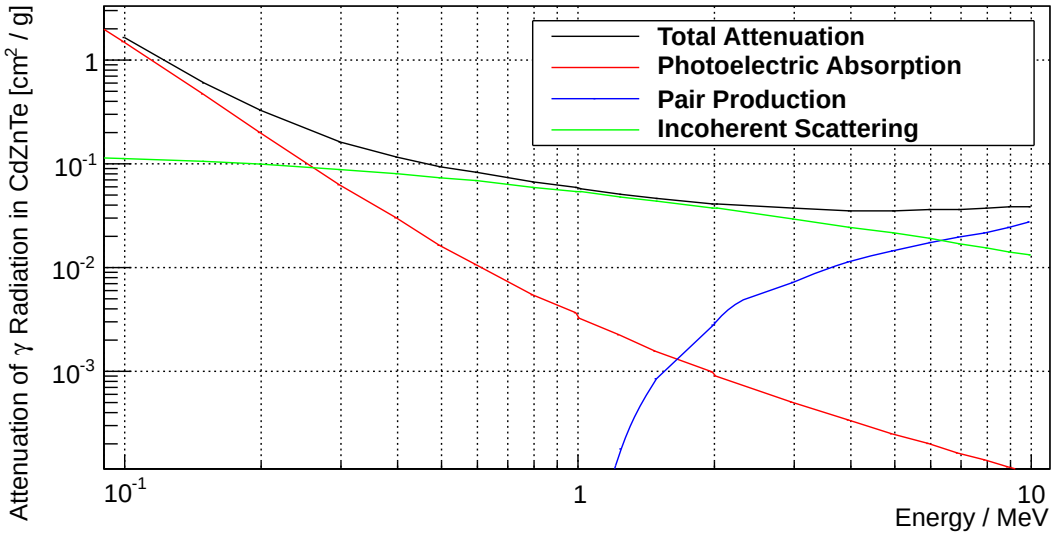

Figure 2.15.: Attenuation of γ-particles in CdZnTe. Data taken from NIST XCOM.

the full energy detection efficiency amounts to 10 %. Thus the signal to background ratio in this case is about 1.8.

^{208}Tl is a 5^+ and its daughter ^{208}Pb a 0^+ nucleus. Therefore the decay to the ground state is highly suppressed. The β-decay to the 3.2 MeV state of ^{208}Tl (49 %, 1.8 MeV) is the highest occurring decay. The de-excitation of the excited states nearly always ($I_\gamma = 99.2\,\%$) happens by emission of a 2614.5 keV γ. Thus in a ^{208}Th decay always at least two γ-particles, one being the 2.6 MeV γ, occurs. The most frequent coincident decays are also listed in Table 2.6.

Even though the interaction of one of these γ-particles will not result in an energy deposition within the ROI, the summing of energy depositions of two γ-particles can still produce background. The interaction of two γ-particles will often take place in separate regions of the detector. The background events can be reduced significantly by accepting only events with energy deposition in few connected pixels. This can be seen from the number of hit pixels from ^{232}Th chain events in the lead. α-particles and β-particles are stopped nearly immediately, therefore background with an energy deposition above 2.6 MeV can only derive from summing of the ^{208}Tl γ-particles. As shown in Figure 2.13, the number of events with energy deposition in more than two pixels is by far dominating. The number of events above 2.7 MeV is reduced by more than an order of magnitude by accepting only events with connected pixels and still by more than a factor of three for events with less than three hit pixels.

Coincident β-γ energy depositions, e.g. in the PCB close to the detectors, are vetoed again by discarding all events with energy deposition in the outer pixels.

Taking into account all background sources and the loss of $0\nu\beta\beta$-decay efficiency, the best signal to background ratio was found to be achieved by applying several cuts simultaneously. Events with energy deposition in the outer voxels have to be discarded

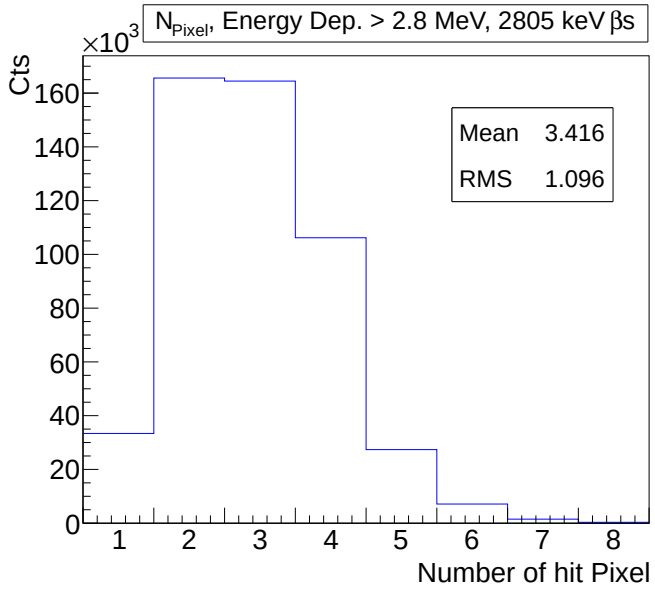

Figure 2.16: Number of hit pixels for full energy deposition of intrinsic 2805 keV electrons. Compared to a 2805 keV $0\nu\beta\beta$-decay event (see Figure 2.12, there $5 \cdot 10^6$ events and here $1 \cdot 10^6$ events were simulated in total) the average range is larger for a single electron with also 2805 keV. Applying the same cuts like for the $0\nu\beta\beta$-decay simulation the detection efficiency of a full energy event is 10 %, compared to 18 % for a $0\nu\beta\beta$-decay event.

Simul. BG Type	Energy Deposition in Detector [keV]	Decay	Energy of contributing γ-particles [keV]
^{232}Th in PCB Board	2891.9	^{208}Tl	2614.5 (PE) + 277.4 (PE)
^{232}Th in PCB Board	2796.7	^{208}Tl	2614.5 (CS) + 583.2 (PE)
^{232}Th in PCB Board	2787.0	^{208}Tl	2614.5 (CS+PE) + 583.2 or 510.7 (CS)
^{238}U in PCB Board	2752.2	^{214}Bi	3000.0 (CS)
^{238}U in PCB Board	2760.7	^{214}Bi	3053.9 (CS)
^{222}Rn in Gas	2769.9	^{214}Bi	2769.9 (PE)
^{232}Th in Lead	2802.2	^{208}Tl	2614.5 (CS) + 510.7 (PE)
^{232}Th in Lead	3204.0	^{208}Tl	2614.5 (CS) + 860.6 (CS)
^{238}U in Lead	2921.8	^{214}Bi	2922.1 (CS+PE)
^{238}U in Lead	2715.2	^{214}Bi	3053.9 (CS)

Table 2.5.: Remaining background for the large volume pixel detector after cuts. The remaining background derives from γ-particles, mainly from the ^{208}Tl γ-cascade. CS denotes an interaction of a γ-particle via Compton scattering and PE via Photo effect. If an interaction via Compton scattering is involved, the energy deposition within the detector does not have to be equal to the sum of energies of the contributing γ-particles. Note also the 0.3 keV difference between the 2921.8 keV line implemented in Geant4 and the energy of 2922.1 keV given by [Fir98].

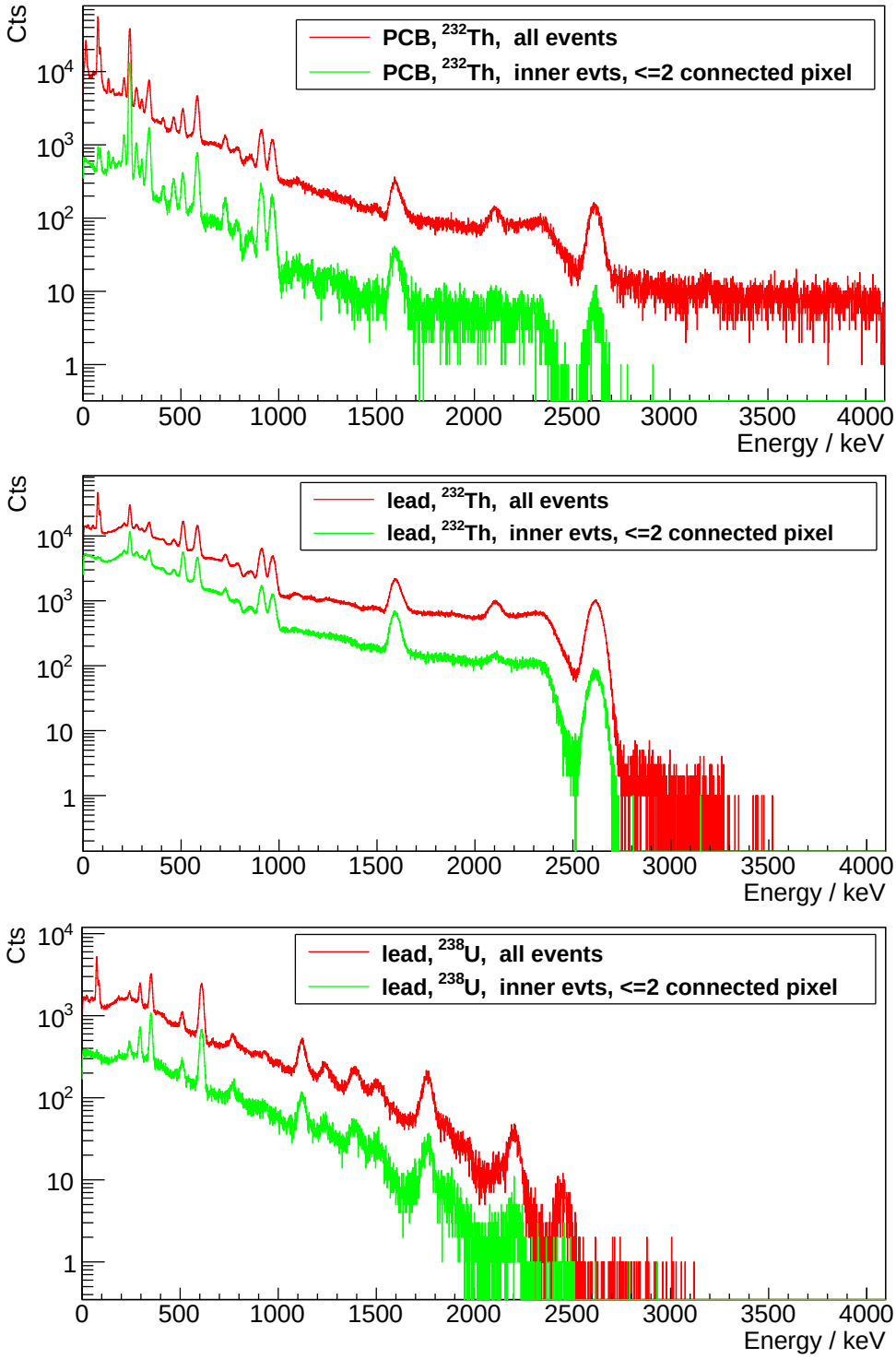

Figure 2.17.: Background reduction of cuts for a large volume pixel detector for several background types. By applying cuts on the inner volume of the pixel detector and the number of hit pixels the number of background events above 2.6 MeV can be reduced by several orders of magnitude, but not eliminated totally. The efficiency of the background reduction differs strongly for materials close to the detector (e.g. ^{232}Th in the PCB board) or further away in the lead of the shielding. See also Table 2.5.

to veto external α- and β-particles. Rejecting all multiple detector events reduces the background from decays with coincident γ-particles and γ-β-coincident decays. Accepting only events with connected pixels and energy deposition in less than three pixels reduces the remaining γ-background. These cuts are also favoured by the better energy resolution of events with few triggered pixels and the assumed charge collection inefficiency for edge pixels mentioned in Subsection 2.4.1. The background reduction and remaining background between 2.7 MeV and 3.2 MeV are listed in Table 2.4 and in detail in Table 2.5. Note that eight of the ten remaining background events are directly in COBRA's direct ROI between 2.7 MeV and 2.9 MeV. In Figure 2.17 the resulting spectra for ^{232}Th events in the PCB board and ^{232}Th and ^{238}U decays in the surrounding lead are shown.

From the tables and the figures it can be seen that the efficiency of the background reduction strongly depends on the particle type and the position of the surrounding material. Before applying cuts, the main entries in the ROI derive from α-decays in the surrounding gas, the PCB board and the passivation paint and only a small fraction from energy depositions of γ-particles. Because the reduction of background from α- and β-particles by discarding events with energy deposition in the outer voxels is very efficient, the background can be reduced by four to six orders of magnitude. The only remaining background that can not be discarded by applying the explained cuts derives from the comparatively small fraction of γ-particles.

Background from the surrounding lead cannot be reduced as effectively as background from other background sources due to the fact that it consists only of γ-radiation. For ^{232}Th decays the cut to two connected pixels still reduces the background by more than two orders of magnitude. This cut is efficient for this decay chain because the energy deposition in the ROI can only happen by the interaction of at least two γ-particles, and it is unlikely that they will interact in two neighbouring voxels.

In the case of γ-radiation from ^{238}U contaminations in the surrounding lead the background suppression has the lowest efficiency of all background types. The gain in signal to background ratio for the applied cuts is still a factor of six. But this ratio shows that γ-background from the ^{238}U chain certainly is the most dangerous background for pixel detectors with large pixel size, even though its fraction in the initially emitted particles is very small.

Comparison with LNGS Data To have an estimate on the main background sources, to cross-check the experimental results found in [Sch11a] and to obtain a prediction for the sensitivity of a full 9×9 polaris detector set-up the simulated background was fitted to the experimental data. For this purpose a histogram with identical binning to the measured spectrum was created for each background contribution. The spectra were convolved with the energy information obtained from the experimental data. A function

Isotope	E_γ [keV]	Intensity [%]	Isotope	E_γ [keV]	Intensity [%]
^{214}Bi	2770.0	0.024	^{208}Tl	2614.5 + 583.2	49
^{214}Bi	2880.4	0.010	^{208}Tl	2614.5 + 583.2+277.4	6
^{214}Bi	2922.1	0.017	^{208}Tl	2614.5 + 860.6	12
^{214}Bi	2978.8	0.015	^{208}Tl	2614.5 + 510.7 + 583.2	23
^{214}Bi	3000.0	0.010	^{208}Tl		
^{214}Bi	3053.9	0.020	^{208}Tl		

Table 2.6.: High energetic γ-particles and cascades from ^{214}Bi (^{238}U chain) and ^{208}Tl (^{232}Th chain) decays. Listed are the lines with the highest intensity for the ^{214}Bi decay and the most significant cascades for the ^{208}Tl line. Data taken from [Fir98].

with scaling factors a_i for each simulated background

$$f(E) = \sum_{i=1}^{N_{bg}} a_i \cdot \mathrm{BinContent}_{\mathrm{Hist}_i}(\mathrm{bin} \hat{=} E) \tag{2.1}$$

was fitted to the experimental data. The scaling factors a_i denote the ratio of measured to simulated time. Hence, together with the number of background events from this background source, they can also be understood as a measure for the order of importance of the background source. The determined scaling factors are listed in Table 2.4 and the resulting simulated spectrum is plotted in Figure 2.18 together with the measurement.

Data in the range from 350 keV up to 3.8 MeV was used for the fit. Below 320 keV the influence of the intrinsic ^{113}Cd decay influences the spectrum. The description of the shape of the ^{113}Cd spectrum is still debatable [Daw09a]. To avoid further uncertainties therefore only data above 350 keV was taken.

As can be seen from Figure 2.18, the fit of the simulated data and the measured data fit well below 1.4 MeV and above 2.7 MeV. Similar to the comparison of a measured and simulated ^{232}Th CPG detector spectrum in Section 2.3, the ratio of measurement and simulation increases with higher energies of the γ-particles. Also similar to Section 2.3, the divergence is worst for the tails of the 2.6 MeV line, again certainly because detector effects cannot be taken into account by Geant4 measurements. The slope in the ratio also suppresses the ^{40}K fraction in the fit. The ^{40}K γ-line at 1461 keV is nearly completely suppressed. ^{40}K only introduces background by a β-decay to ^{40}Ca with a branching ratio of 89 % and an energy up to 1312 keV and by the 1461 keV line deriving from electron capture to ^{40}Ar. Thus it cannot introduce background in COBRA's ROI but was originally introduced as background contribution for a better modelling of the overall spectrum. It is suppressed in the fit because a stronger contribution of its Compton continuum and β spectrum in the lower energetic region would result in a stronger deviation of the ratio of measurement to simulation in the region between 1.7 and 2.7 MeV. The average ratio of 1.4 in this energy region can be taken as a measure for a correction on the maximal upper uncertainty of the predicted background level

as the rest of the fitted spectrum fits well to the measured data (the average ratio in the whole fit are is 1.1), and except the ^{40}K line the lines of the ^{232}Th and ^{238}U decay chains were reproduced well. As the fit includes eight parameters and the influence of several uncertainties (see below) is not known, the resulting background composition can only be understood as a rough approximation of the true background. The fit depends strongly on the full energy peaks to obtain information on the single background component. The fit therefore also depends strongly on the applied energy limits, especially for the components with low contribution. For these reasons in Table 2.4 only the most significant digit without uncertainties is indicated.

There are certainly three main reasons for the stronger deviation in the middle energy range. First, as can be seen from the deviation of the tails of the 2.6 MeV line, detector effects like charge transport and collection, electron trapping, charge sharing or effects of the measurement electronics could not be taken into account. Usually these detector types are optimised for an optimal detector behaviour at standard energy lines used for comparison, such as the ^{137}Cs 661.7 keV line or the ^{60}Co 1173.2 keV and 1332.5 keV lines and therefore to energies below COBRA's ROI. Different detector parameters may improve the detector behaviour and diminish detector effects at higher energies.

Second, as the main focus lay on the general determination of main background sources for large volume pixel detectors and the exact dimensions of the Polaris system were not known, the simulated geometry was not a detailed model of the Polaris set-up. Small hard to measure inaccuracies like dead layers or the thickness of the passivation lacquer can change the simulation outcome especially in the energy region above 2.7 MeV as there the main background derives from α-decays. The detector behaviour and efficiency on the sides close to the steering grid is hard to predict and therefore was not taken into account. Thus, the deviation of at the most 40% between the γ and the α dominated part of the spectrum is a surprisingly good result. Also the simulation was done for a $3 \times 3 \times 2$ detector array whereas only one detector was operated at LNGS. Several of these discrepancies such as the differences in the distances to the lead will certainly be averaged out, but nevertheless will contribute to the deviation.

Finally, as no measurements of the radiopurity of the applied components existed, it was assumed that the decay chains are in equilibrium. Especially the ^{238}U chain has three very long lived members with half-lives $> 10^3$ years among the first five daughter nuclides. So if one of the chain daughters is partly removed, e.g. during the fabrication process of the PCB board, the chain is no longer in equilibrium. This will lead to a falsely simulated ratio of α and γ/β-decays in the chain.

A comparison of the measurement and the simulation after the cuts is shown in Figure 2.20. Here multiple detector events were not discarded because the Polaris operating system contained only one detector. Discarding multiple detector events changes the shape of the spectrum significantly, as can be seen in Figure 2.19 due to the large detector size and the small space between the detectors.

In the ratio of measurement to simulation again a slope is recognisable. In contrast

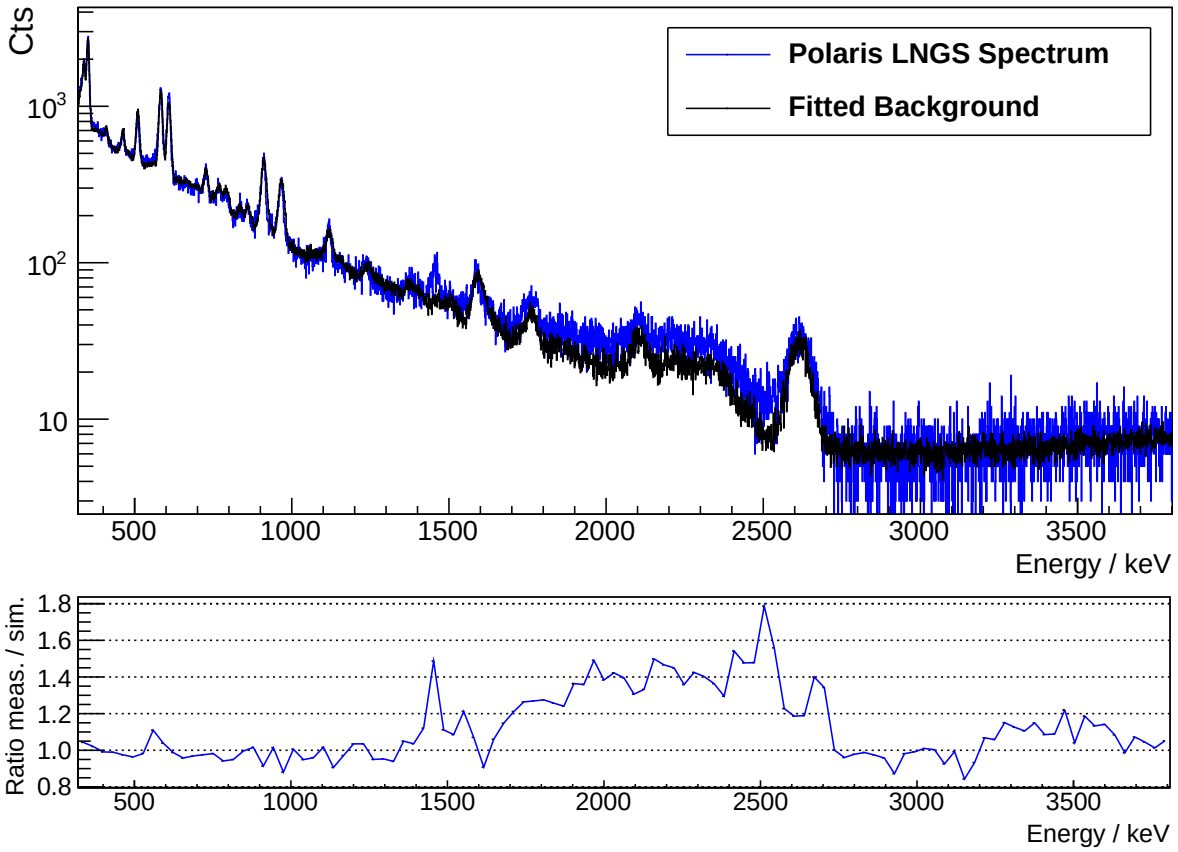

Figure 2.18.: Data taken with the Polaris detector system at LNGS [Sch11a] and the simulated background spectrum. The composition of the background was determined by a fit of the simulated expected background components to the experimental data in the range from 350 keV to 3800 keV (The region below 350 keV was not taken into account as intrinsic ^{113}Cd decays contribute significantly to this part of the spectrum). The calibration of the measured spectrum had to be corrected slightly. The simulation was convoluted with a Gaussian energy resolution determined from the measurement. Like for the simulation in Section 2.3 the ratio of measurement to simulation increases with higher energies. This effect is stronger here as the fit of several background components to the data adds a further uncertainty. Because systematic uncertainties are dominating, no error bars have been added to the ratio.

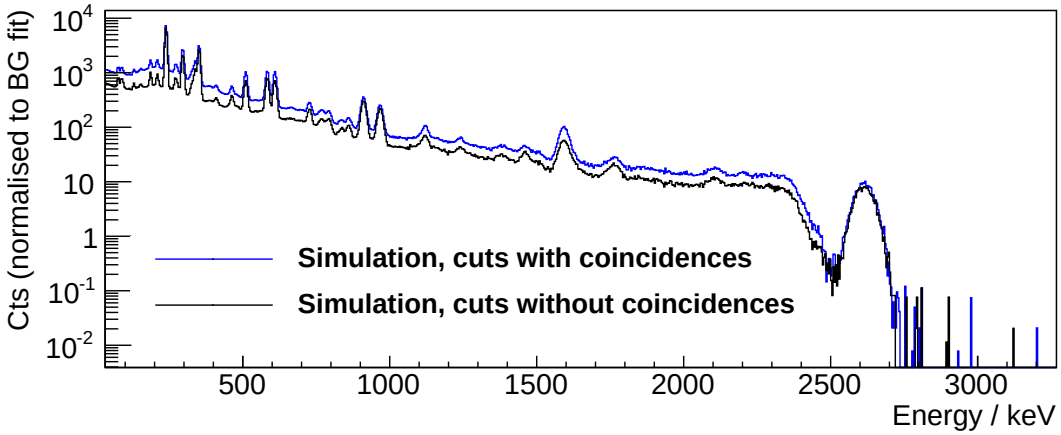

Figure 2.19.: Comparison between simulated spectrum with and without discarding multiple detector (coincident) events. Outer pixel and events with more than two hit pixels were discarded. The rejection of multiple detector events significantly reduces the Compton background.

to the fit to the full measured events in Figure 2.18, the ratio here is decreasing towards higher energies. For energies above 1.5 MeV the ratio is too small by about 30 %. Here the significance of the ratio, especially between the Compton edge and the full energy peak and at the high energy tail of the full energy peak, is low because only a little data remained in the measured spectrum after the cuts were applied. Like the deterioration of the energy resolution for high energies the smaller count rate in the simulation for the higher energetic region may be a hint to a stronger influence of charge sharing at higher energies. For further experiments this influence can certainly be reduced by optimising detector parameters like the steering grid voltage for higher energies. Below 800 keV the ratio is too high. This effect is especially strong at low energies. Between 700 keV and 1.5 MeV the ratio is in a region of ±20 % around 1.

Certainly also the inaccuracies in the geometry implementation, like shielding effects, or further background of the many detectors play a more important role when the cuts are applied. Besides the already mentioned charge sharing between the pixels also the uncertainties in the background composition and Geant4 inaccuracies (e.g. the range of high energetic electrons) contribute to the discrepancy between the ratio of measurement and simulation before and after the cuts were applied.

In [Sch11a] the number of background events between 2.7 MeV and 2.9 MeV could be reduced to two events and between 2750 keV and 3 MeV even to zero events by discarding events with more than two connected pixels and events in the outer pixels. To compare this number also the energy resolution has to be taken into account because especially in the background from ^{232}Th events in the surrounding lead many 2.6 MeV energy depositions from the ^{208}Tl decay appear. With the determined energy resolution of 2.8 % on the average nearly 17 events are measured above 2.7 MeV, see Figure 2.21.

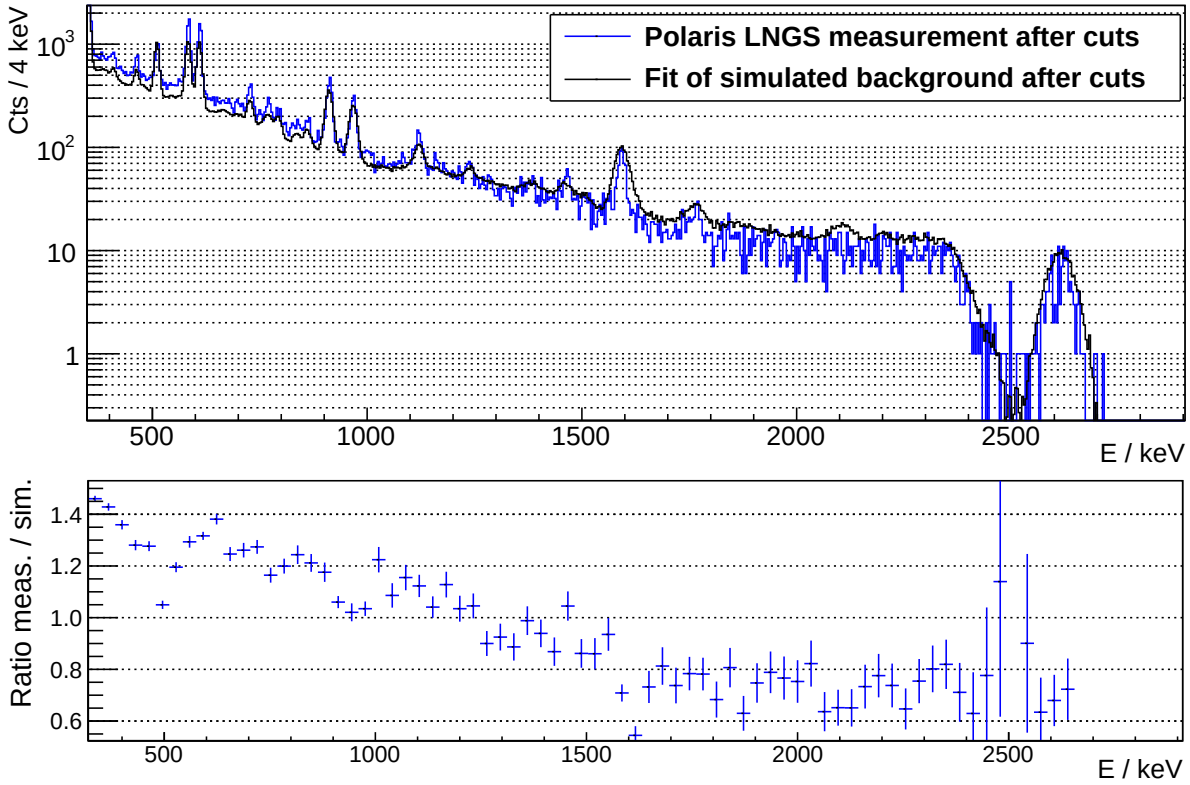

Figure 2.20.: LNGS Polaris measurement and simulated spectrum after cuts. The simulated contributions to the background were scaled with the factors determined from the full spectrum, see Figure 2.18. A slope in the ratio of measurement to simulations is visible. It can certainly be partly explained by charge sharing between the pixels that could not be taken into account in the simulation. The error bars in the ratio of measurement to simulation only indicate statistical errors from the partly sparse statistics.

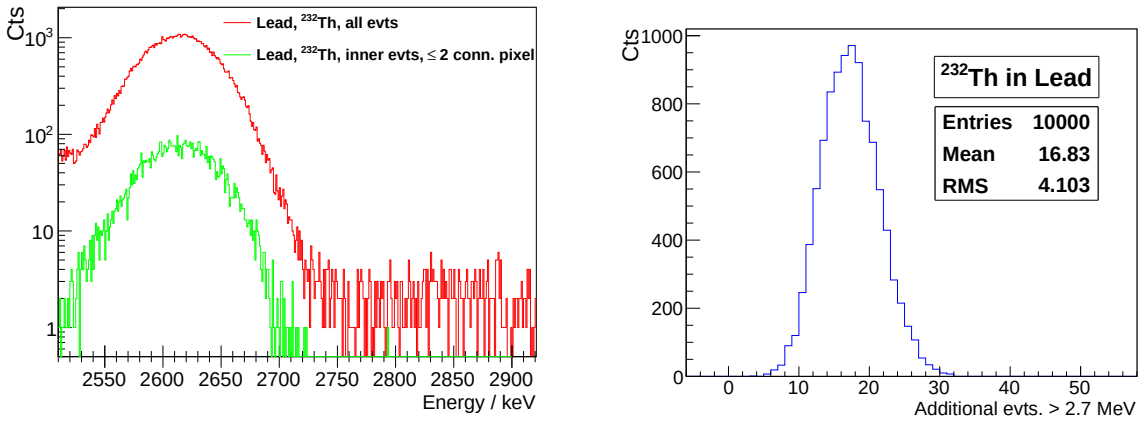

Figure 2.21.: With the determined energy resolution of 2.8 % at 2.6 MeV some events from the ^{208}Tl 2615 keV line can be measured above 2.7 MeV. In the case of the simulation of ^{232}Th in lead, this background up to 2750 keV is even higher than remaining background from coincident γ-summing because there are many 2.6 MeV energy depositions.

This number strongly varies with the presumed energy resolution. The number of events is reduced to zero above 2750 keV. For ^{232}Th in the PCB board still 0.8 events on the average are observed above 2.7 MeV. For the other background sources this effect is negligible.

By summing up all background sources and taking uncertainties to the number of observed events according to [Ber12] from [Fel98] for the case of no background, the estimated background for the data collected at LNGS is (0.8 ± 0.4) cts. The deviation between the simulation and the measurement is taken into account by assuming an uncertainty of 40 % for the time measure determined by the fit of the simulations to the experimental data. The simulated count rate is still in agreement with the observed two events.

For a higher accuracy, the simulations can be repeated with the exact Polaris geometry and with approaches to take also detector effects into account. For the purpose that was pursued in the scope of this work, i.e. verifying the first experimental results and to explore the vetoing power of large volume pixel detectors in general, the accuracy of about 30 % is sufficient.

Estimation of ^{116}Cd $0\nu\beta\beta$ sensitivity for a full Polaris System To predict the sensitivity of a full 18 detector Polaris system, the number of expected background events and their variation has to be estimated. Sensitivity is defined as the exclusion of background fluctuation at a certain CL, usually a 90 % upper limit. This number is used as an approximation for events that can be interpreted as signal events for the sensitivity estimate. As a measure of the background fluctuation often the square root of the expected Background $\sqrt{B}$ is taken, according to the $\sqrt{N}$ estimator in the case of Poissonian statistics. To obtain the desired CL, this number is scaled by a factor k determined from the area content of a Gaussian distribution (e.g. $k = 1.645$ for a 95 % upper limit and 90 % two sided CL, or $k = 1.28$ for a 90 % upper limit and 80 % two sided limit, see e.g. Appendix D).

This procedure is critical in the case of low statistics, as the Poissonian distribution is asymmetric for small N and approaches the Gaussians distribution only for large mean values μ (compare e.g. the case of an already large $\mu = 18.7$ and a large $\mu = 93.6$ shown in Figure 2.22). So applying the Gaussian factor k often does not lead to the desired CL. In the case of the determined background rate for a Polaris-like system the uncertainty is comparatively high. When scaling this background rate without taking into account the uncertainty the determined upper limit can be too low.

For these reasons another approach was taken. To determine the maximal fluctuation of the background on 90 % CL Poissonian distributed random numbers were generated. As mean value μ for each random number a Gaussian distributed variable was taken with the expected number of background events as mean and the error as σ. To obtain a PDF the resulting histogram was scaled with the number of generated events (10^5). The 90 % CL upper limit n_{up} on expected background is determined by finding the number

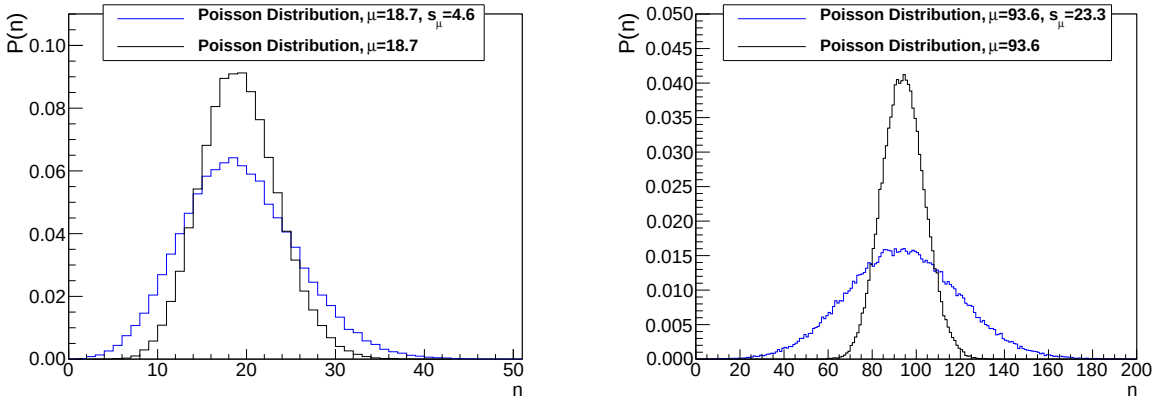

Figure 2.22.: Poisson distribution with uncertainty of mean μ (blue) and for common Poissonian distribution for exactly known μ (black). The uncertainty of μ was taken into account by inserting a Gaussian distributed μ in the Poisson distribution. Due to the uncertainty of μ, the resulting distribution is wider than a usual Poissonian distribution. This effect is especially strong for large values of μ with large uncertainty s_μ. So compared to a prediction for known μ a gain of accuracy from higher statistics ($\sqrt{N}$ law) can be neutralised by the uncertainty of μ.

n for which the cumulative distribution function (CDF) exceeds 90 %:

$$\sum_{n=0}^{n_{up}} P(n) \geq 0.9\,, \tag{2.2}$$

and the fluctuation n_{sens} as measure for the sensitivity then is taken to be the difference between μ and n_{up}.

Two examples for obtained PDFs can be seen in Figure 2.22. The distribution of the Poissonian distributions with Gaussian distributed μ is wider than the normal Poissonian distribution due to the additional spread of μ. Therefore also the upper limit is higher. For the cases shown in Figure 2.22, the upper limit without additional uncertainty on μ is $n_{sens} = 6.3$ and $n_{sens} = 14.4$ for $\mu = 18.7$ and $\mu = 93.6$ respectively (compare to $1.28 \cdot \sqrt{18.7} = 5.5$ and $1.28 \cdot \sqrt{93.6} = 12.4$, due to the high slope on the rising edge of the Poissonian distribution the upper limit is systematically underestimated by the $\sqrt{B}$ approach). When taking into account the uncertainty of the estimated mean value of events, the upper limits are calculated to be $n_{sens} = 8.27$ and $n_{sens} = 32.4$.

Essentially the gain in sensitivity from the $\sqrt{N}$ law for Poissonian distributed random numbers is neutralised by the high uncertainty of the μ itself. This effect becomes more and more severe with higher uncertainties and higher number of expected counts: The numbers for $\mu = 18.7$ are still similar, whereas the results for $\mu = 93.6$ differ by more than a factor of two. When reducing the uncertainties in the described case by a factor of two the upper limits are calculated to be $n_{sens} = 6.3$ and $n_{sens} = 19.4$ respectively.

Consequently, the uncertainty of expected counts has to be taken into account and has to be reduced as far as reasonably possible. The uncertainty of the determined

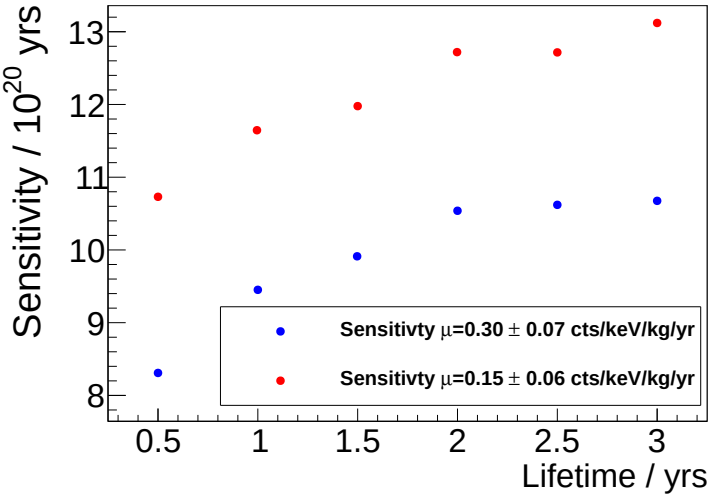

Figure 2.23: Sensitivity for Polaris-like large volume pixel detector. The sensitivity is determined on a 90 % CL exclusion of background fluctuation. For longer live times the uncertainty on the expected background level reduces the sensitivity (compare Figure 2.22). With a reduced background level the sensitivity is better, but not as much as the background reduction due to the large uncertainty.

background scaling factors was conservatively estimated from the ratio of simulation to measurement to be 40 %. To reduce the uncertainty on the main background source, i.e. events in the PCB board, an additional 10^8 events were simulated for ^{232}Th and also for ^{238}U. Simulating even more events was dismissed because a main source of uncertainty are the scaling factors that were determined from the fit to the experimental data. They cannot be reduced with higher statistics. Furthermore the uncertainty on the remaining background events is reduced according to the $\sqrt{N}$ law only. In total a background level of (0.30 ± 0.07) cts/keV/kg/yr was calculated for an energy region from 2.7 MeV to 2.9 MeV.

This background level can be reduced if the set-up is constantly flushed with radiopure nitrogen and the energy resolution is enhanced so that background caused by resolution effects, i.e. from the 2.6 MeV ^{204}Tl line, can be neglected (or the ROI is chosen less conservatively, e.g. ± 1 FWHM, equivalent to 2740 keV to 2890 keV). Then the background rate can be estimated to be (0.15 ± 0.06) cts/keV/kg/yr. The uncertainty is not reduced as much as the background level itself because the comparatively large uncertainties on the fitted scaling factors stay the same and background with a rather good known uncertainty is discarded.

By inserting the determined 90 % CL upper limits n_{sens} for the background fluctuation as measure for signal events in the formula for the half-life determination the sensitivities plotted in Figure 2.23 and listed in Table 2.7 were calculated. For a live time of about one year a sensitivity of about 10^{21} yrs can be achieved. The calculated sensitivity does not increase significantly with longer live times due to the rather large uncertainty on the interpolation of the determined to the predicted background. So the actual achievable sensitivity may be higher than the conservatively determined numbers given here and can certainly be enhanced considerably with enhanced evaluation methods for the data measured with a full scale Polaris set-up.

Livetime	$\mu = 0.30 \pm 0.7$ cts/keV/kg/yr		$\mu = 0.15 \pm 0.6$ cts/keV/kg/yr	
[yrs]	n_{sens}	Sensitivity [10^{20} yrs]	n_{sens}	Sensitivity [10^{20} yrs]
0.5	8.3	8.3	6.4	10.7
1.0	14.5	9.5	11.8	11.6
1.5	20.8	9.9	17.2	12.0
2.0	26.1	10.5	21.6	12.7
2.5	32.4	10.6	27.0	12.7
3.0	38.6	10.7	31.4	13.1

Table 2.7.: Estimated sensitivity for Polaris-like system (90 % CL). On the left side the expected sensitivity for the determined background level for the LNGS measurement is shown. If the resolution can be enhanced the background level can be reduced. The gain in predicted sensitivity is not as high as the background reduction because the uncertainty on the background level is not reduced in the same order as the background itself.

Comparison with current world leading limits for ^{116}Cd The current world leading limit on $0\nu\beta\beta$-decay for ^{116}Cd was established from the Solotvina experiment with ultra low background $CdWO_4$ scintillation detectors [Dan03]. There a limit of $T_{1/2}^{0\nu\beta\beta} > 1.7 \times 10^{23}$ yrs was measured. The achieved background level was stated as 0.04 cts/keV/kg/yr between 2.5 MeV and 3.2 MeV. With the given energy resolution of 8.9 % FWHM at 2.8 MeV this energy interval corresponds to about $\pm$ 1 FWHM around the expected decay energy of ^{116}Cd. The applied $CdWO_4$ detectors (4$\times$ 330 g) were enriched to 83 % in ^{116}Cd, which is equivalent to a gain of about a factor of 7.3 in source atoms per kg of detector mass compared to the number of source atoms per kg in CdZnTe. No volume cuts were applied and the $CdWO_4$ detectors are large and dense. Therefore the efficiency for full energy deposition was 83 % and thus higher than for smaller CdZnTe detectors. Together with the gain from enrichment this sums up to a factor of 34 compared to the assumed not enriched CdZnTe detectors with the applied cuts, and together with a factor of two from twice the mass under observation to a factor of 68. The live time of the experiment was about 1.5 yrs and a 90 % CL upper limit of $n_{sig,max} = 2.4$ signal events was determined.

To summarise, in a comparable live time the sensitivity of the Solotvina experiment cannot be reached mainly due to the fact that the detectors are not enriched in ^{116}Cd and the volume cuts that are very efficient for background reduction also strongly reduce the efficiency. On the other hand pixel detectors offer a much better energy resolution, which should enhance the sensitivity of an experiment. The sensitivity of a Solotvina like experiment to higher half-lives is strongly limited by its comparatively low energy resolution because the inevitable background from the $2\nu\beta\beta$-decay becomes more and more important for lower half-lives (see e.g. Section 1.2).

The impressive amount of background reduction that can be achieved with large

CdZnTe pixel detectors clearly shows the huge potential for this detector type if the main background sources can be reduced. A first step to background reduction may be replacing the commonly used FR4 PCB boards with cleaner materials, for example CuFlon [Jos11], and also other electronics components such as capacitors with devices already measured for the small pixel detectors.

2.4.3. Sensitivity of Large Volume Pixel Detectors for the $0\nu\beta\beta$-Decay to excited States

Besides the often discussed $0\nu\beta\beta$-decay to the ground state also a decay into an excited state of the daughter nucleus is possible. Double beta isotopes and their daughters are 0^+ nuclei. The mass driven $0\nu\beta\beta$-decay is only possible to 0^+ states. The transition to 2^+ states is also possible, but only if the underlying process is driven by a contribution from a right handed current. So the observation of a decay to an excited state can help to disentangle the underlying physics process. Besides it can also serve as cross check for the $0\nu\beta\beta$-decay case [Due11].

Especially for small detectors the probability of observing the energy deposition of the initial $0\nu\beta\beta$-decay in one detector while the de-excitation γ-particle escapes without energy deposition is high. If the de-excitation γ-particle deposits energy in another detector, preferably by photoelectric effect, the signature of this event is very unlikely to be mimicked by background events. In the case of $0\nu\beta^+\beta^+$ decays, the annihilation γ-particles from the positrons can also be used in a coincidence analysis to improve the signal to background ratio. Also high energetic γ-particles can cause 511 keV background after they interacted via pair creation, and furthermore the ^{208}Tl decay from the ^{232}Th chain contains a γ-particle with 510.8 keV that cannot be resolved from a 511 keV annihilation γ-particle with a CdZnTe detector. Consequently, the background suppression in this case can be lower than for other decays.

In Subsection 2.4.2 it was shown that the γ-background is very high for the Polaris system and several isotopes with β-γ coincidences and also several coincident γ-particles are present. Including also Compton scattered events from the $0\nu\beta\beta$-decay de-excitation γ-particle will increase the $0\nu\beta\beta$-decay detection efficiency, but will also significantly increase the number of events from arbitrary β-γ and γ-γ-background coincidences. As the background strongly increases with decreasing energy (see for example Figure 2.18), from this point of view it is desirable to have a balanced energy distribution between the energies of the electrons and the γ-particles to have the lowest possible background for both signals. A $0\nu\beta\beta$-decay with emission of several γ-particles is even more unlikely to be mimicked by background event, but the probability of an interaction of the electrons and the γ-particles inside the array is also very low.

For one layer CPG set-ups coincidence studies were already performed in [Mü07] and [Hei09]. The obtained results were in general slightly worse than for one detector analysis because for a two dimensional array of 1 cm^3 detectors the detection efficiency is

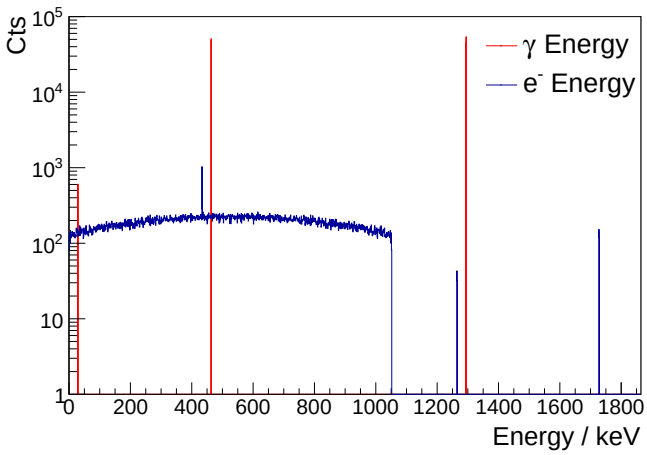

Figure 2.24: Energy spectrum of $0\nu\beta\beta$ decay of ^{116}Cd to the second excited state of ^{116}Sn (0^+) (data from decay0 event generator [Pon00]). The nucleus always decays via the 1294 keV intermediate state. Therefore always a 1294 keV γ-particle and a 463 keV γ-particle is emitted (the monoenergetic β-particles derive from internal conversion of the nucleus). The probability of a full energy deposition of both γ-particles and the electrons is very low. The detection efficiency for the decay to the first excited state (1294 keV) is much higher.

low. The low efficiencies could not be compensated by the achieved gain in background suppression. A Polaris-like set-up favours a coincidence analysis because the active volume of the detectors (without volume cuts) is six times larger than for a CPG detector and even with the full volume cuts still about three times larger. This strongly increases the interaction probability for high energetic γ-particles in one detector. In total, the dimensions of active CdZnTe mass (about 650 g) in the Polaris detector array are $6 \times 6 \times 3\,\mathrm{cm}^3$, compared to $4 \times 4 \times 4\,\mathrm{cm}^3$ for the full 64 CPG array (about 380 g). The three dimensional configuration of the detectors also increases the efficiency. The distance between the detectors is comparable for both set-ups. So at first glance, it seems likely that the efficiency for the Polaris system will be higher than for a 64 CPG detector set-up.

For a test of the possibilities of a coincidence analysis ^{116}Cd was chosen because it has the highest Q-value and is also the most promising candidate for the $0\nu\beta\beta$-decay to ground state. For a large scale experiment the detectors therefore will be enriched in ^{116}Cd. It decays to ^{116}Sn, which has several excited 0^+ and 2^+ states. The first excited state is the 1294 keV 2^+ state. Therefore the $0\nu\beta\beta$-decay cannot (or only with a very small branching ratio [Hir94]) happen via the mass driven mechanism, but for example in case of a right handed contribution to the electroweak interaction. The excited state decays under emission of a single 1294 keV γ-particle and the sum of the electron energies is 1519 keV. The second excited state is the 1757 keV 0^+ state, so this decay is possible in case of the mass driven mechanism. As shown in Figure 2.24, this excited state always decays to the 1294 keV state under emission of a 463 keV γ. Always two γ-particles are involved in this decay and its observation with a coincidence analysis is rather unlikely due to the low detection efficiency. There are also several higher energetic excited states, but because these decays are suppressed for low decay energies and thus lower phase space, for this analysis the decay to the first excited state was

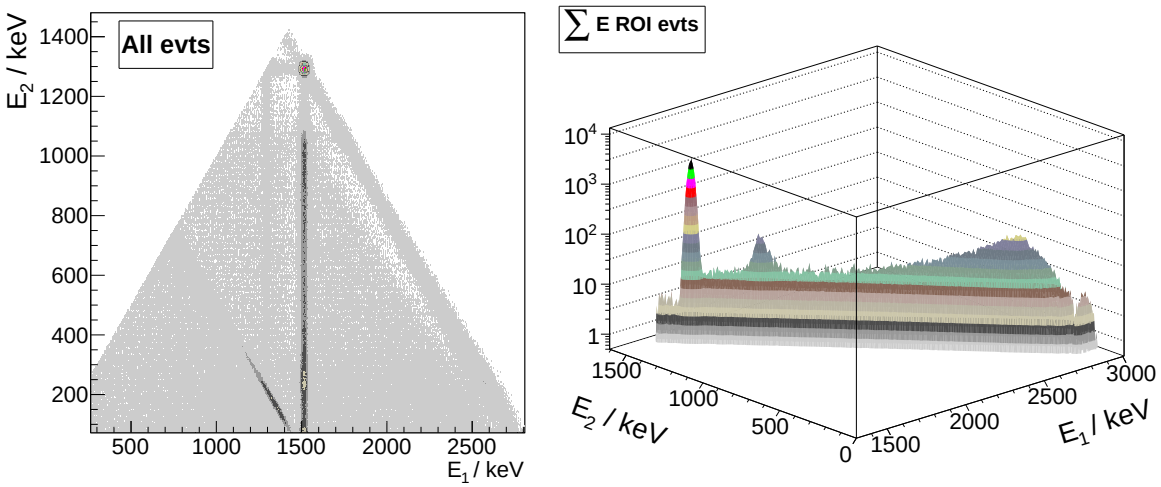

Figure 2.25.: Two detector energy deposition for $0\nu\beta\beta$-decay of ^{116}Cd to the first excited state of ^{116}Sn. *Left*: The energy deposition in two detectors, where the assignment of the energies (to be E_1 and E_2) was done by a $E_1 > E_2$ criterion. The three most striking features are the full energy deposition of the electrons (vertical line at $E_1 = 1515\,\text{keV}$), left to this line a line deriving from bremsstrahlung of the electrons that is detected in another detector (with no energy deposition of the 1294 keV γ-particle) and an accumulation of events from a full energy deposition of the electrons in one detector with a coincident full energy deposition of the γ-energy in the other detector ($E_2 = 1294\,\text{keV}$). The line on the right hand side of the plot denotes the full energy deposition of 2809 keV in two detectors. This can also happen by backscattering of the 1294 keV γ-particle into the initial detector after Compton scattering. *Right*: All two detector events with full energy deposition of 2809 keV (a detailed view of the mentioned line) is shown. By accepting only events with full 1294 keV γ-energy deposition in one detector and full 1515 keV e^- energy deposition in the other detector, the detection efficiency is reduced by more than 50 %, but in order to collect a major part of the continuous backscattering spectrum, search windows of more than 1 MeV for each detector are necessary. This will strongly increase the background level.

chosen.

With the pixel detectors several possibilities of background reduction are possible. In this analysis only events with energy deposition in exactly two detectors were taken into account for the reasons mentioned above. The simplest approach is to add up the energies in both detectors and accept only events with a sum energy of the Q-value of the decay. More restrictively, an energy distribution amongst the detectors that matches a full energy deposition of the electrons in one detector and a full energy deposition of the γ-particle in the other detector can be required. Additionally requiring connected pixel for the electron energy is useful to exclude Compton scattered γ-particles. To reduce background from β-γ coincidences also a confinement of the electron-like event or even both events to the inner voxels can be applied. But the lower energy region is dominated by γ-background, and the γ-particles can deposit energy all over the detectors

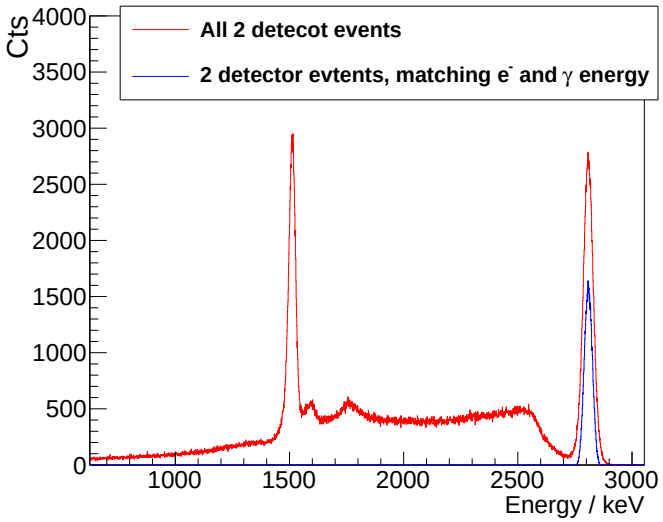

Figure 2.26: Energy spectrum of two detector events for the $0\nu\beta\beta$-decay of ^{116}Cd to the first excited state of ^{116}Sn. By requiring the detected energies to be only the expected γ-energy (1294 keV) in one detector and the expected e^- energy (1515 keV) for the other detector, the number of events with sum energy deposition matching 2809 keV is reduced by more than 50 %, also compare Figure 2.25. The 1294 keV line itself does not appear in the two detector spectrum as this would imply no energy deposition of the intrinsic electrons of the $0\nu\beta\beta$-decay.

due to their high penetration depth. Therefore this cut will not be as efficient as for the $0\nu\beta\beta$-decay case.

The effect of these cut possibilities on the $0\nu\beta\beta$-decay detection efficiency and the remaining background was determined from the simulations already used for Subsection 2.4.2. The events from the simulations were convoluted with the energy resolution obtained from the experimental background. A small energy window for the searches is important to exclude as many events from neighbouring background γ-lines. On the other hand, the search window has to be chosen wide enough to still obtain a decent detection efficiency. In this analysis a search window of $\pm 2\sigma$ of the energy resolution was taken. Assuming a Gaussian resolution, 95 % of a monoenergetic line in one detector events and 90 % of two detector events are contained in this energy window. A wider range only marginally increases the detection efficiency, while a smaller range strongly decreases the detection efficiency, e.g. to 47 % for $\pm 1\sigma$.

The results are listed in Table 2.8. With appropriate cuts the background level can be reduced to or even below the level of the single detector analysis (compare Table 2.4 in Subsection 2.4.2). On the other hand, the detection efficiency is reduced to about 1 % or even below, so by a factor of about 10 to 25 compared to the one detector analysis. When also taking into account the fact that the background level increases from the ROI of the $0\nu\beta\beta$-decay to ground state to the ROI of a single detector analysis (e.g. the most probable full energy deposition of the 1515 keV from the electrons without interaction of the γ-particle in the same detector) by much more than two orders of magnitude (compare Figure 2.20) the gain in signal to background ratio for a coincidence analysis is still excellent. In the case of the CPG detectors the background increases only by a factor of about five between 2.8 MeV and 1.5 MeV [Daw09b] and the detection efficiency even slightly increases with decreasing energy for a one detector analysis. Therefore the coincidence analysis results were not competitive to the single detector analysis as the

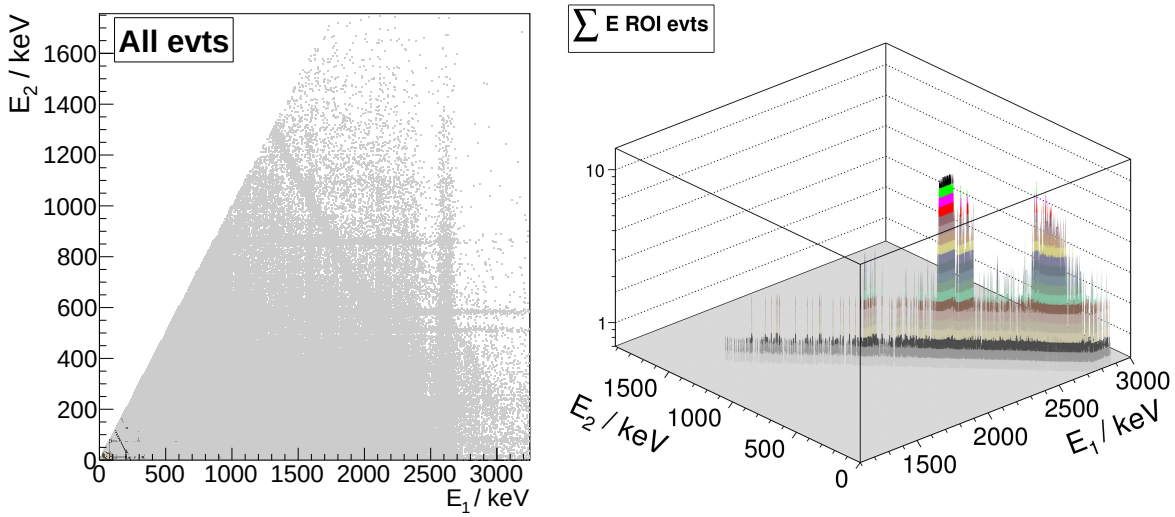

Figure 2.27.: Two detector energy deposition of events from ^{232}Th in the PCB board. Left: Due to the quantity of lines in the decay chain, the resulting two detector spectrum is smeared over a wide energy range. The horizontal and vertical lines derive from full energy deposition of a γ in one detector and an arbitrary energy deposition in the other detector. Also a diagonal line (ending at $E_1 = 2.6\,\mathrm{MeV}$) deriving from Compton-scattering of the 2.6 MeV ^{208}Tl line in one detector and Photoelectric effect of the scattered γ-particle in the second detector is clearly visible. Right: Events with sum energy matching the Q value of the $0\nu\beta\beta$-decay are dominated by combinations of arbitrary energy deposition together with full energy deposition of the 2.8 MeV (first peak) and the 510.8 keV and 583.2 keV (2nd and 3rd peak) lines. Only a few events are left with energies matching exactly the expected e^- and γ-energies from the $0\nu\beta\beta$-decay. Therefore, the additional background from all events with matching sum energy is much higher than the gain of detection efficiency (compare also Figure 2.25).

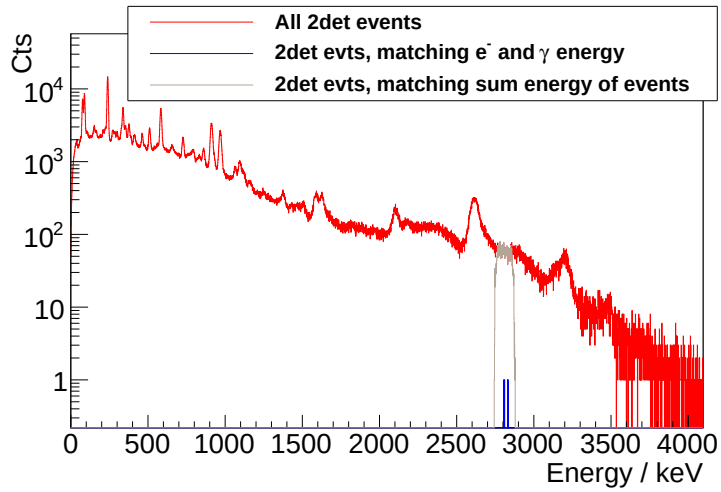

Figure 2.28: Background from ^{232}Th in PCB for events with two triggered detectors. Due to the high γ-background the number of events in the ROI with arbitrary energy depositions summing up to 2.8 MeV is still high, especially due to γ-particles from the ^{208}Tl γ-cascade. This background can be strongly reduced when accepting only events with energies exactly matching the expected e^- and γ-energies from the $0\nu\beta\beta$-decay, compare Figure 2.28.

Simul. Descript.	Total Sim. Evts.	Cut_1 rem. evts.	Cut_1 rem. evts. [%]	Cut_2 rem. evts.	Cut_2 rem. evts. [%]
$0\nu\beta\beta$ to 1294 keV	5×10^6	143957	2.9	68218	1.4
Passivation	10×10^6	803	8.0×10^{-3}	2	20×10^{-6}
^{232}Th in PCB Brd	130×10^6	6541	5.0×10^{-3}	5	3.8×10^{-6}
^{238}U in PCB Brd	130×10^6	241	0.2×10^{-3}	2	2×10^{-6}
^{222}Rn in Gas	10×10^6	98	1.0×10^{-3}	3	30×10^{-6}
^{232}Th in Lead	5000×10^6	1221	24×10^{-6}	1	20×10^{-9}
^{238}U in Lead	1000×10^6	8	0.8×10^{-6}	0	0

Simul. Descript.	2 det evts	Cut_3 rem. evts.	Cut_3 rem. evts. [%]	Cut_3 rem. evts.	Cut_3 rem. evts. [%]
$0\nu\beta\beta$ to 1294 keV	870×10^3	35041	0.70	15608	0.3
Passivation	966×10^3	0	0	0	0
^{232}Th in PCB Brd	2517×10^3	2	1.5×10^{-6}	1	0.8×10^{-6}
^{238}U in PCB Brd	1870×10^3	0	0	0	0
^{222}Rn in Gas	378×10^3	2	20×10^{-6}	0	0
^{232}Th in Lead	1354×10^3	0	0	0	0
^{238}U in Lead	154×10^3	0	0	0	0

Table 2.8.: Simulated two detector events for a Polaris-like system. Cut_1 denotes events with sum energy matching the $0\nu\beta\beta$-decay Q-value, Cut_2 are events with energy depositions matching full energy deposition of the electrons and γ-particle from the $0\nu\beta\beta$-decay, Cut_3 adds the constraint of an interaction of the electron-like energy deposition within the inner 9×9 pixels and Cut_3 additionally requires the same for the γ-like energy deposition.

gain in background reduction could not compensate the loss in efficiency. In contrast, as seen above, for a Polaris-like system a coincidence analysis can improve the obtainable results.

World leading limits for $0\nu\beta\beta$-decays to excited states in ^{116}Cd are given, like for the decay to ground state, by [Dan03]. For the decay to the first excited 2^+ state that is also analysed here a 90 % CL limit of 2.9×10^{22} yrs was given. Similar to the case of $0\nu\beta\beta$-decay to ground state discussed in Subsection 2.4.2, this limit cannot be improved in a few years live time with one Polaris system consisting of not enriched detectors. However, with a large scale set-up the detection efficiency will increase and therefore a coincidence analysis will yield an even better signal to background ratio and will therefore be an important instrument of data analysis, especially because the background from the $2\nu\beta\beta$-decay is irreducible and comparatively high compared to e.g. ^{130}Te due to the lower half-life of ^{116}Cd in this decay.

2.5. Survey of Background Contribution of Parylene-C Passivation

In principle background sources can be divided into external and internal (intrinsic) background. As semiconductor detectors have to be intrinsically clean to work as detectors, usually the external background is much higher than the intrinsic background. External background can be reduced by applying carefully chosen materials and additionally reducing the amount of material close to the detectors as far as possible. From the results of Section 2.4 it can be seen that external background from α-decays in materials close to the detectors is a major background source for COBRA's ROI, especially for the CPG detectors because they do not have as good veto capabilities as do pixel detectors. Also the volume to surface ratio is smaller for smaller volumes, such as the $1\,\mathrm{cm}^3$ CPG detectors. Consequently contaminations directly on the detector surface have to be reduced as much as possible.

To prevent the CdZnTe from degrading, e.g. due to increase of the surface leakage current from dirt or moisture, the detectors have to be protected with a coating. This coating usually is a few to a few tens of micrometers thick. It covers five sides of the detectors, so for a $1\,\mathrm{cm}^3$ CPG detector the passivation coating covers $5\,\mathrm{cm}^2$ and can therefore contribute significantly to the background level. The cathode side of the detectors is not covered with a passivation coating to enable an uncomplicated contacting.

The red standard passivation lacquer from the detector manufacturer was identified as a major source of background [Ree09]. With alternatively offered clear passivation lacquer, the background level could be reduced significantly [Koe08]. Since the passivation is treated as a corporate secret only little is known about the composition of this clear passivation and it is not directly available to COBRA. Therefore alternative passivation coatings are investigated. Two alternatives were proposed by the COBRA CdZnTe crystal growing group at Freiburger Materialforschungszentrum (FMF). A resin suitable for wafer application called Cyclotene was first investigated in [Sch09]. The second possibility is a vapour deposited polymer called Parylene C. To coat a surface with Parylene, at first a powder is evaporated in a vacuum chamber. This gas is then converted to a stable monomeric diradical by heating it. This gaseous monomer is transferred into a room temperature deposition chamber. There the Parylene polymerizes and adsorbs to surfaces. Parylene is preferred by the crystal growing group because its impenetrability to moisture is superior to Cyclotene, during its application no heating of the detectors for curing of the passivation is needed and it can be applied in very thin layers of a few micrometers. To determine the possible contribution to the background level from Parylene C, measurements were evaluated and the background level simulated together with T. Neddermann [Ned13].

A first measurement was done at the DLB at Dortmund. The impurity level of the Parylene C powder sample obtained from Plasma Parylene Systems, Rosenheim (Ger-

many), turned out to be too low to be measured with the DLB, so 500 g of Parylene C powder were measured by Matthias Laubenstein at LNGS. The results together with activities of the standard red passivation lacquer, the colourless passivation provided by EIDIS (both also measured by M. Laubenstein) and a measurement of Cyclotene done by the Verein für Kernverfahrenstechnik und Analytik Rossendorf e.V (VKTA) Rossendorf are listed in Table 2.9.

The limits of the colourless EIDIS passivation are comparatively weak because the manufacturer provided a sample of only 4.2 g. To obtain better results for the eV Colourless Paint sample, the sample was analysed with the inductively coupled plasma mass spectrometry (ICP-MS) method at the Laboratory of Chemistry at LNGS. Also a small fraction of Parylene C was analysed with ICP-MS at LNGS. The results of both measurements are listed in Table 2.10. Results were given by the Laboratory of Chemistry as parts per billion (ppb), denoting here 10^{-9} g of an element / g of sample. Assuming that decay chains are in equilibrium and the abundance in the sample matches the natural abundance a of the isotope of interest, the contaminations in ppb can be converted into the activity of a (long lived) isotope with half-life $T_{1/2}$ and atomic mass m_{atomic} via

$$1\,[\text{ppb}] = \frac{\ln(2)}{T_{1/2}} \cdot \frac{a \cdot N_A}{m_{atomic}} \cdot 10^{-3}\,[\text{mBq/kg}] \tag{2.3}$$

with the Avogadro constant N_A. Conversion factors for ^{232}Th, ^{238}U and ^{40}K are listed in Table 2.11.

When comparing the results determined with γ-spectroscopy (Table 2.9) and with ICP-MS (Table 2.10) for Parylene C, the results from both methods differ noticeably, even up to a factor of two. In general, the results obtained by ICP-MS are lower than the results obtained with γ-spectroscopy. A certain divergence is expected because the two approaches differ fundamentally. For example the activity of ^{40}K is measured directly with γ-spectroscopy, but because for ICP-MS ^{40}Ar is used to produce a plasma torch only the content of ^{39}K can be determined and the ^{40}K content has to be calculated assuming its natural abundance. For the U and Th chains the level of contamination is determined from different isotopes of the decay chains. While with ICP-MS the amount of the initial isotopes ^{232}Th and ^{238}U are measured, the activities from γ-spectroscopy are obtained from daughter nuclei of the chain (see Table 2.9). The different activities of ^{228}Ra and ^{228}Th of the ^{232}Th decay chain are a hint to an imbalance within the chain. Such an effect will certainly be stronger for the ^{238}U chain because it contains several isotopes with half-lives $> 10^3$ years (see e.g. Appendix C), but this cannot be verified because only one isotope from the ^{238}U chain could be detected.

For an estimation of the background contribution, a four micrometer thick coating on top of five sides of the full 64 detector prototype array was simulated. To avoid underestimation of the background level, the activity measurements obtained from γ-spectroscopy were taken as input for the simulation since they are higher than the values obtained from ICP-MS. The chains were not taken to be in equilibrium, but the

Isotope	eV Red Paint [mBq/kg]	Cyclotene [mBq/kg]	EIDIS clear paint [mBq/kg]	Parylene C [mBq/kg]
^{238}U:^{226}Ra	2100 ± 100	< 1000	< 140	18 ± 2
^{238}U:^{234}Th	1100 ± 300	< 5200	< 1500	< 110
^{238}U:^{234m}Pa	1600 ± 1000		< 4300	< 31
^{238}U:^{210}Pb		< 8600		
^{235}U	170 ± 30		< 15	< 6.8
^{232}Th:^{228}Ra	1100 ± 100	< 1200	< 180	8 ± 2
^{232}Th:^{228}Th	730 ± 70	< 370	< 190	3 ± 1
^{40}K	6900 ± 800	3500 ± 1400	< 1000	120 ± 20
^{137}Cs	< 15	1040 ± 180	< 56	< 1.7

Table 2.9.: Activities of two detector passivation lacquers provided by the detector manufacturer EIDIS, Cyclotene and Parylene C determined by γ-spectroscopy. The measurements were done by M. Laubenstein at LNGS except for the Cyclotene measurement that was done by the VKTA at Rossendorf. The origin of the high ^{137}Cs contamination for Parylene could not be clarified. Measurements are given with Gaussian standard distribution quantile $k = 1$ (68.3 % central CL) and upper limits with $k = 1.645$ (95 % upper CL).

Element	EIDIS clear paint [ppb]	EIDIS clear paint equiv. [mBq/kg]	Parylene C [ppb]	Parylene C equiv. [mBq/kg]
U	0.115 ± 0.010	1.4 ± 0.1	0.71 ± 0.10	8.8 ± 1.2
Th	0.146 ± 0.015	0.59 ± 0.06	0.91 ± 0.21	3.7 ± 0.9
K	1640 ± 400	51 ± 12	2750 ± 850	85 ± 26

Table 2.10.: Activities of clear detector passivations determined by ICP-MS (compare γ-spectrometric results listed in Table 2.9). The measurements were done by the chemistry lab at LNGS. ppb here refers to 10^{-9} g of element / g of sample. The activities are calculated as contributions of the ^{238}U and ^{232}Th chains and ^{40}K assuming 99.3 % natural abundance of ^{238}U, 100 % of ^{232}Th and 0.00117 % for ^{40}K, see Table 2.11 for details.

Conversion	natural Abundance	Atomic Weight [u]	$T_{1/2}$ [10^9 yrs]	Conversion [ppb] $\rightarrow$ [mBq/kg]	Conversion [mBq/kg] $\rightarrow$ [ppb]
K $\leftrightarrow$ ^{40}K	0.0117%	39.098	1.277	0.0310	32.3
Th $\leftrightarrow$ ^{232}Th	100%	232.038	14.05	4.06	0.246
U $\leftrightarrow$ ^{238}U	99.27%	238.029	4.468	12.3	0.081

Table 2.11.: Factors for [ppb] (10^{-9} g of element / g of sample) $\leftrightarrow$ [mBq/kg] conversion calculated according to Equation (2.3). For the conversion it is assumed that the decay chains are in equilibrium and the abundance of the isotopes equals the natural abundance.

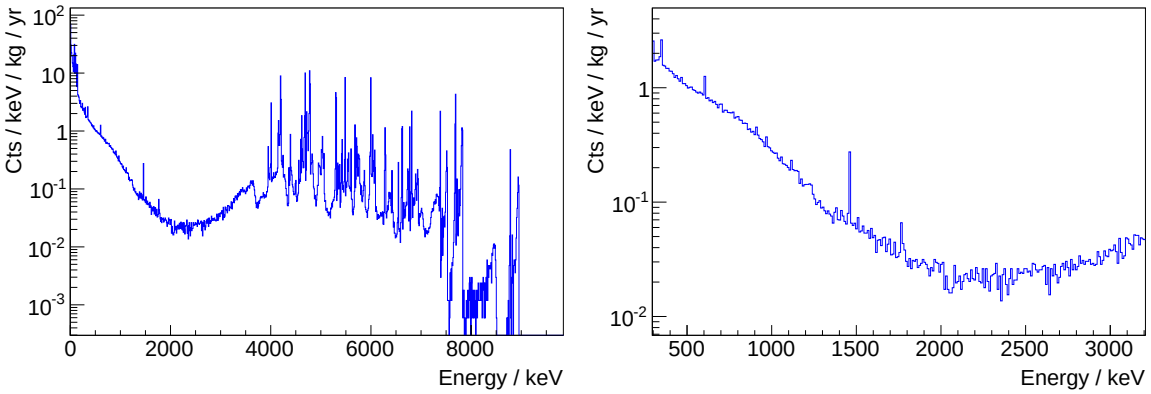

Figure 2.29.: Simulated Parylene C background spectrum for the full 64 CPG detector array, assuming the activities listed in Table 2.9. The finite energy resolution of the detectors was not taken into account. α-particles lose nearly no energy during their passage through the thin passivation coating, therefore sharp α-lines appear above 4 MeV. Clearly visible are the 1461 keV ^{40}K and the 609 keV ^{214}Bi line. The average background level in the ROI between 2.7 MeV and 2.9 MeV is 0.036 cts/keV/kg/yr.

activities of parts of the chains were adjusted according to the results listed in Table 2.9. For example, the sub-chain from ^{232}Th to ^{228}Ac was assigned an activity of 8 mBq/kg from ^{228}Ra, and from ^{228}Th until the last nuclides of the chain the activity of 3 mBq/kg from ^{228}Th was taken. When only upper limits could be determined, e.g. for ^{235}U, the upper limit was taken as activity. An exception to this procedure was made for the part of the ^{238}Th chain beginning with ^{234}U. The upper limit for this isotope is much higher than the measured value for ^{226}Ra and the upper limit for ^{234m}Pa. Therefore the upper limit of 31 mBq/kg of the mother isotope ^{234m}Pa was taken for the ^{234}U sub-chain.

The simulated spectrum is shown in Figure 2.29. As the coating layer is very thin, α-particles lose nearly no energy during their passage through the passivation. This leads to clearly distinguishable α peaks. Especially for low energies the background is comparatively high. Close to the ROI at 2.8 MeV it reaches a minimum. Between 2.7 MeV and 2.9 MeV the average background level is 0.036 cts/keV/kg/yr.

For the current set-up the achieved background level is in the order of 1 ct/keV/kg/yr. So a Parylene C coating will not be the dominating remaining background source for the 64 detector array. On the other hand, the background level is far too high for a large set-up. Here an overall background level of $10^{-4} - 10^{-3}$ cts/keV/kg/yr has to be reached. The background level obtained from the simulation can be lower than the actual one because partly only upper limits for some activities were used. Furthermore it may be possible that the material is cleaned during the evaporation and the radiopurity of the resulting coating can be lower than for the powder. However, these effects will not decrease the contamination level by several orders of magnitude. Even though Parylene C is a solution for the 64 detector array, it will consequently not be an option for the full-scale set-up.

2.6. Penetration Depth of High Energetic Beta Radiation

CPG detectors do not posses as good veto capabilities for α and β-particles as do like pixelated detectors. But the method of depth sensing (see Subsection 1.2.1) adds a certain veto capability also to CPG detectors. As can also be seen from the discussion in Section 2.4, the main remaining background in the ROI derives from α-particles and β-particles because their fraction and also their interaction probability is much higher in the ROI than for γ-particles.

The interaction depth information is especially valuable for the CPG detectors because the cathode metallization consists of platinum, which contains the α radiation source ^{190}Pt (see Section 3.1) Due to the high negative bias voltage of the cathode, also the positively charged decay products of airborne ^{222}Rn and other contaminants accumulate at the cathode. The currently applied silver conductive glue contains the β-radiation emitter $^{110\mathrm{m}}$Ag with β-energies of up to 2891 keV.

The range of α-particles in CdZnTe is very short and therefore the energy deposition is localised to a small area. Thus α-particles on the cathode or anode side can be vetoed efficiently and with a minimal loss of active volume. β-particles on the other hand have a much longer range in matter. Furthermore, they lose energy by ionisation all along their path through matter and do not move through the material in a straight line but in a kind of random walk due to many scattering processes along their track inside the material. The penetration depth of high energetic electrons was examined in the scope of this work.

Often the continuous slowing down approximation (CSDA) range is taken as an estimate for the average range of an electron in a material. The CSDA range is calculated by approximating an average energy loss of an electron along its path by its stopping power. The energy is reduced by the approximated average energy loss for each step until it is slowed down to rest [NIS]. The integral of all step lengths is the CSDA range. Therefore it equals not the average penetration depth of electrons in their initial direction of entrance in the material because the electrons change direction very often due to scattering. As can be seen from Table 2.12 the CSDA range rather equals the maximal penetration depth of the electrons in their initial direction of flight.

To have an estimate for the distribution of the penetration depth, Geant4 simulations with a CdZnTe $1 \times 1 \times 1\,\mathrm{cm}^3$ detector were done. To have depth information, the detector was set up of 0.1 mm slices of CdZnTe. Two types of simulations were done for several electron energies. At first monoenergetic electrons were shot perpendicular to the detector surface to obtain information on the maximal penetration depth. β-particles from natural decays on the detector surface have an isotropic angular distribution. Therefore the simulations were repeated with monoenergetic electrons on the detector surface with an isotropic distribution of initial direction.

For the determination of the interaction depth the production of bremsstrahlung has

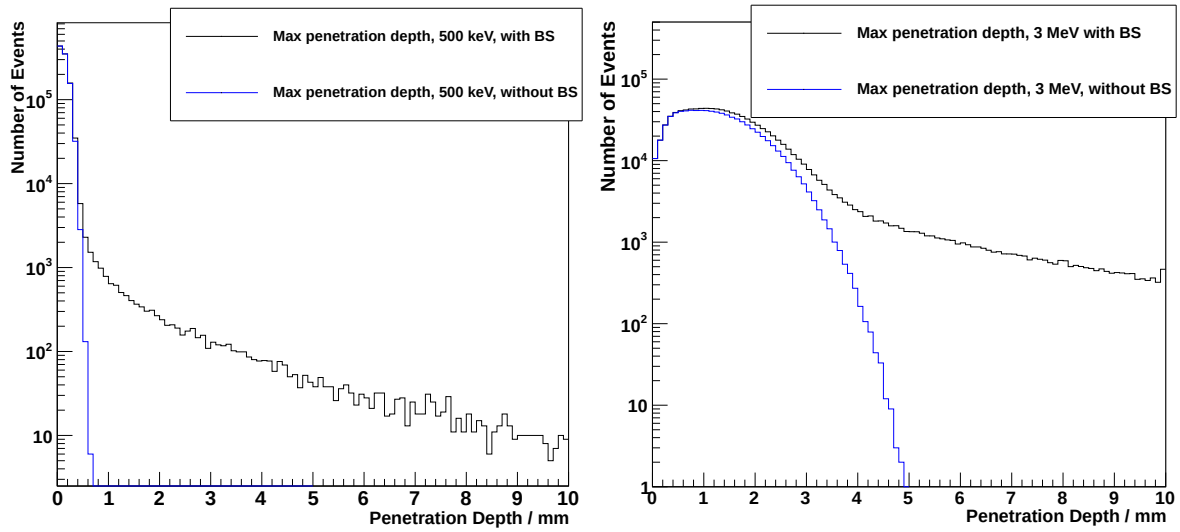

Figure 2.30.: Simulated penetration depth of monoenergetic 500 keV (left) and 3 MeV (right) electrons in CdZnTe. The electrons were shot perpendicular to the detector surface. The maximal penetration depth is continuously distributed due to scattering inside the detectors. The maximum penetration depth corresponds roughly to the CSDA range (see e.g. [NIS]). Because of bremsstrahlung energy is deposited in higher depth than the original penetration depth of the electrons. This effect is stronger for higher energies.

to be taken into account. For 500 keV and 3 MeV electrons shot perpendicular to the detector surface, the distribution of the simulated penetration depth is shown in Figure 2.30. Even though all electrons are stopped after less than one millimetre in the case of 500 keV electrons the irradiated bremsstrahlung can be detected all over the detector. With pulse shape analysis it is possible to distinguish such a multi site like event from a usual energy deposition of an electron. The fraction of events with bremsstrahlung increases strongly with higher electron energies. For the high energetic 3 MeV electrons also pair production from the produced bremsstrahlung is possible and was observed in the simulations in a small fraction of the events.

The obtained average and maximal penetration depths are listed in Table 2.12. As can be seen there high energetic electrons can deeply penetrate the detector. However the possible background reduction from the depth information is still very high. For the isotropic 3 MeV electrons more than 50 % of these external events can be discarded with a 1 mm depth cut to the cathode while reducing the detector volume by only 10 %, even when the measured interaction depth is assumed to be the maximal penetration depth of the electrons. In fact, the measured interaction depth will be lower than the maximal penetration depth, as explained as follows.

Electrons deposit energy all along their path through (dense) matter. Therefore, it is not totally clear what actual depth will be measured with the method explained in Subsection 1.2.1 for electrons that move vertically through the detector. In general, two

Source Type	Energy [keV]	Avrg Range with BS [mm]	Avrg Range without BS [mm]	Max Range without BS [mm]	E-Avrgd Range without BS [mm]	CSDA Range [mm]	Fraction of BS Evts [%]
beam	500	0.21	0.18	0.70	0.14	0.52	2.3%
beam	700	0.30	0.25	1.00	0.18	0.81	3.7%
beam	1000	0.46	0.38	1.50	0.26	1.25	5.7%
beam	1500	0.76	0.60	2.40	0.40	1.97	9.0%
beam	2000	1.07	0.84	3.40	0.55	2.66	12.2%
beam	3000	1.71	1.33	4.90	0.86	3.95	17.7%
isotropic	500	0.17	0.15	0.70	0.12	0.52	1.6%
isotropic	1000	0.33	0.27	1.50	0.20	1.25	3.9%
isotropic	3000	1.12	0.85	4.90	0.54	3.95	12.3%

Table 2.12.: Range of β-radiation in CdZnTe perpendicular to the detector surface. Due to scattering inside the material the average range is considerably lower than the CSDA range. The CSDA range was taken from [NIS]. The number of electrons producing bremsstrahlung (BS) increases significantly with higher electron energies. Listed here is the fraction of events where also the bremsstrahlung is measured in the detector. The E-Avrgd Range is the average path weighted with the energy deposition per volume (see text).

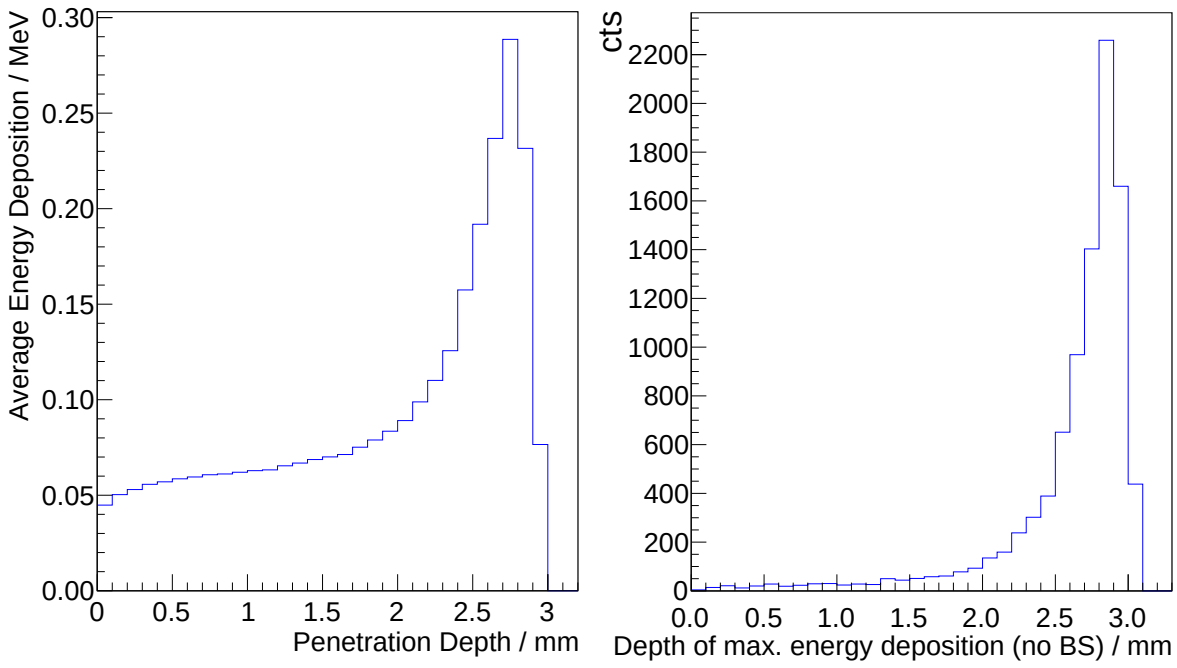

Figure 2.31.: Average energy deposition and depth of maximal energy deposition for 3 MeV electrons with a penetration depth of 3 mm. On the average the electrons deposit about 60 keV/mm along the first part of its track. The most energy is deposited at the end of the track, but for some events the highest energy deposition also occurs at lower depths.

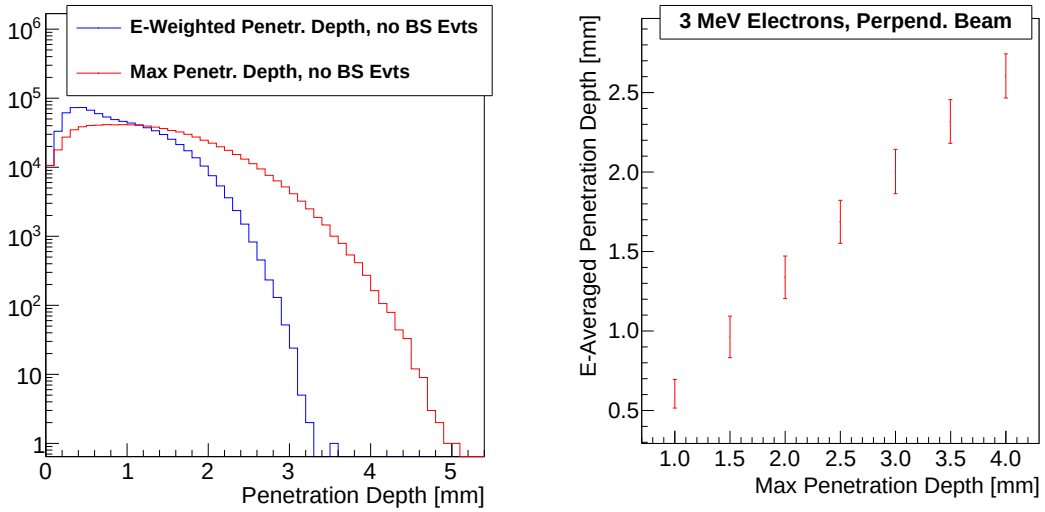

Figure 2.32.: Assumed measured penetration depth calculated as energy weighted average path. The energy weighted average path is significantly lower than the maximal penetration depth (compare also Figure 2.31).

possibilities are likely. Either, if a distinct maximal energy deposition exists, the point of this maximum may be measured as interaction depth. Electrons, unlike heavy particles like protons or α-particles, usually do not deposit most of their energy at the end of their path, a typical Bragg peak does not have to exist. To investigate this possibility, the maximal and average energy deposition was investigated. An example for 3 MeV electrons with a maximal penetration depth of 3 mm is shown in Figure 2.31. These plots are typical representatives for the distributions of these quantities. For higher penetration depths it was found that, on the average, the electrons lose most of their energy at the end of their path, but the spread is comparatively high. The maximum of the energy loss of the electrons is about 10 %-20 % below the maximal penetration depth.

The second, and more likely, possibility is to take the path of the electron and weight it with the amount of deposited charge. Then a possible measured interaction depth z_m is the path weighted with the deposited charge

$$z_m = \frac{\sum z_i \cdot E_i}{\sum E_i} \,. \tag{2.4}$$

This measured depth is lower than the point of maximal energy deposition and far lower than the maximal penetration depth of the electron, see Figure 2.31 and Figure 2.32 as well as Table 2.12. Thus the gain in background suppression to loss of active volume will be even better than assumed above.

The actual measurement of the calculated interaction depth compared to the true penetration depth of electrons is rather difficult due to the fact that β-particles have a continuous energy distribution. But a comparison of a simulation and a measured

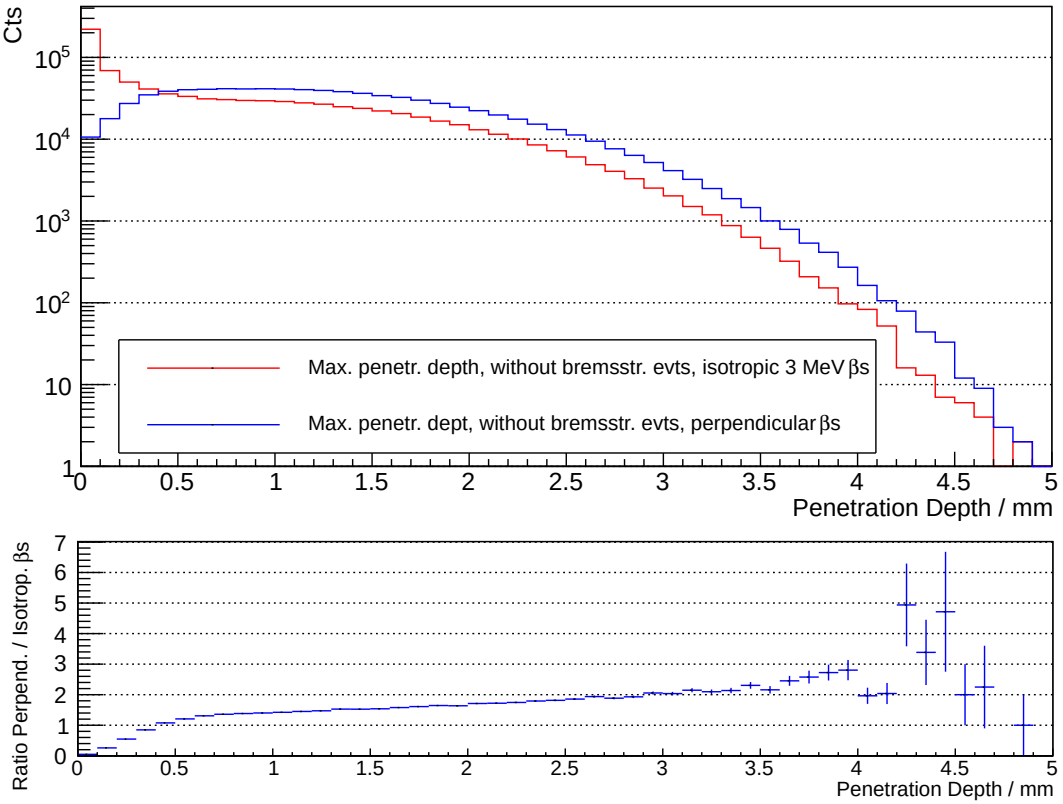

Figure 2.33.: Isotropic and directional 3 MeV β-radiation on CdZnTe detector surface. The number of β-particles with an isotropic distributed direction directly on the detector surface with a high penetration in the detector is comparatively high because the initial direction of the β-particles is changed nearly immediately by scattering within the material.

depth spectrum from a high energetic β-particle source, e.g. ^{90}Sr, can give approximate information. In [Teb11] first measurements with a ^{204}Tl source were done. But because the maximal β-particle energy of ^{204}Tl is only 764 keV and all the data was taken together with a ^{137}Cs source for calibration purposes, a direct comparison of these measurements with simulations is not possible. The measurements could not be repeated without the ^{137}Cs source as the detector that was especially prepared for these experiments failed shortly after the measurements. However, measurements for a better understanding of the interaction depth with a proton beam and β-particle sources are planned for the future.

While the simulation of beam-like electrons perpendicular to the detector surface is useful to investigate the general penetration depth, β-particles from radioactive decays on the cathode (or the anode) are usually isotropically distributed. Therefore the simulation was repeated for several energies with isotropically distributed electrons. As expected, the average penetration depth of these electrons is lower than for directed electrons. For low energies the ratio of directed to isotropically distributed electrons is

smaller than the factor of two that can be obtained by pure geometrical considerations, see Figure 2.33 as example for 3 MeV electrons. This is caused by the scattering of the electrons inside the detector.

The ratio steadily increases with higher penetration depth. Therefore the vetoing capacity of a depth cut to the cathode in the case of isotropically distributed electrons is higher for higher penetration depths, i.e. the suppression of high energetic β-particles from radioactive decays, as occurring in COBRA, can be done with lower depth cuts than for beam-like electrons.

3. Data Analysis

3.1. LNGS Data and Possible Background Contributions

By replacing the former red passivation lacquer with a clear coating and flushing the whole set-up with evaporated nitrogen the background level was reduced significantly [Koe08, Sch11a]. Together with the installation of the first 16 colourless detector layer in September 2011 a radon tight foil was set up to increase the efficiency of the nitrogen flushing [Teb11]. Furthermore permanent nitrogen refill was arranged to ensure permanent flushing and thus good data quality. In this chapter 12.7 kg days of data from the first 16 colourless detector layer taken between September 2011 and March 2012 is analysed. From the installed 16 detectors 15 were operational.

Compared to the former 16 detector set-up consisting of detectors passivated with red lacquer [Ree09, Mü07] and most of the data taken with the first detectors with clear passivation [Sch09, Koe08] the possibilities to reject and identify background are increased. The energy resolution is a factor of two to three better. Together with the comparatively large number of well operating detectors that is needed to gain sufficient statistics, with the achieved low background level the sensitivity to γ-lines is increased. With the depth information obtained from the recorded pulse shapes (see Chapter 1) another important tool became available. For the depth calculation the refined method Equation (1.11), which was developed and implemented into the COBRA pulse-shape data processing program MAnTiCORE [Sch11a] by M. Fritts, was used.

In Figure 3.1 a plot of deposited energy versus the calculated interaction depth is shown. Several features are visible in the spectrum and it becomes obvious how valuable the interaction depth information is. Most of the events above 2 MeV occurred at the cathode side ($z = 1$) of the detectors. Two clusters at about 3 MeV and 5 MeV are visible. In the full energy spectrum shown in Figure 3.2 it can be seen that these two clusters have the typical shape of α-decays with a broad peak width and a long low energy tail.

3.1.1. ^{210}Po α-Decays

A cut-out of the cluster around 5 MeV is shown in Figure 3.3. It derives from the $^{210}\mathrm{Po} \rightarrow {}^{206}\mathrm{Pb}$ α-decay with an energy of the α-particles of 5.30 MeV [Fir98]. Due to energy loss of the particles in the cathode metallisation and due to the fact that besides energy loss from ionisation α-particles also lose a small amount of energy by interaction with the

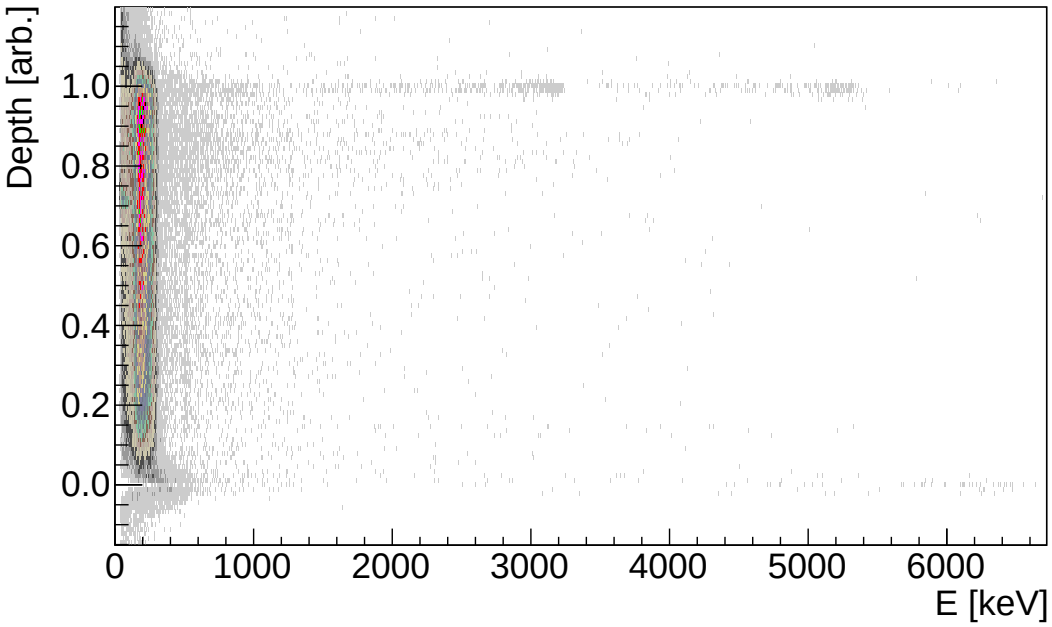

Figure 3.1.: Depth vs. energy plot of the first 16 detector layer data taken at LNGS. Higher depths denote the cathode side ($z = 1$), smaller depth the anode side of the detector ($z = 0$). The spectrum contains several features (see also text as well as Figure 3.2 and Figure 3.5). A line at about 500 keV is visible. These events are distributed relatively uniformly in depth z. At 3.2 MeV a cluster of events at the cathode side deriving presumably from ^{190}Pt events can be seen. At 5.3 MeV another cluster at the cathode side most likely deriving from ^{210}Po appears.

crystal lattice and thus producing phonons, the mean of the measured energy deposition is a bit below 5.3 MeV. Also a small shift to lower energies (certainly in the order of 1 %) of reconstructed energies of cathode events is noticed in [Fri12]. The small shift derives from a contribution of the holes that is no longer completely negligible for events at the cathode. The actual size of this shift is small and difficult to determine. Therefore, the effect is neglected in the energy reconstruction of MAnTiCORE. Additionally the presence of a deadlayer with a thickness of a few nm on the cathode side, which would also lead to a small energy loss, cannot be excluded.

^{210}Po is a daughter of ^{222}Rn from the ^{238}U decay chain (see also remarks on the ^{222}Rn shielding in Subsection 1.2.2 and Table C.1). Besides ^{210}Po the ^{222}Rn decay chain contains three other α-particle emitters with a high branching ratio. They emit α-particles with energies of 5.49 MeV (^{222}Rn), 6.00 MeV (^{218}Po) and 7.67 MeV (^{214}Po). In the LNGS background spectrum shown in Figure 3.2 no statistically significant clusters at these energies are visible, especially compared to the number of counts at 5.2 MeV. From the absence of these decays it can be concluded that the ^{210}Po contamination does not derive from ^{222}Rn still diffusing into the set-up despite the nitrogen flushing. It is rather due to pollution from ^{222}Rn of the detectors or carrier materials prior to the

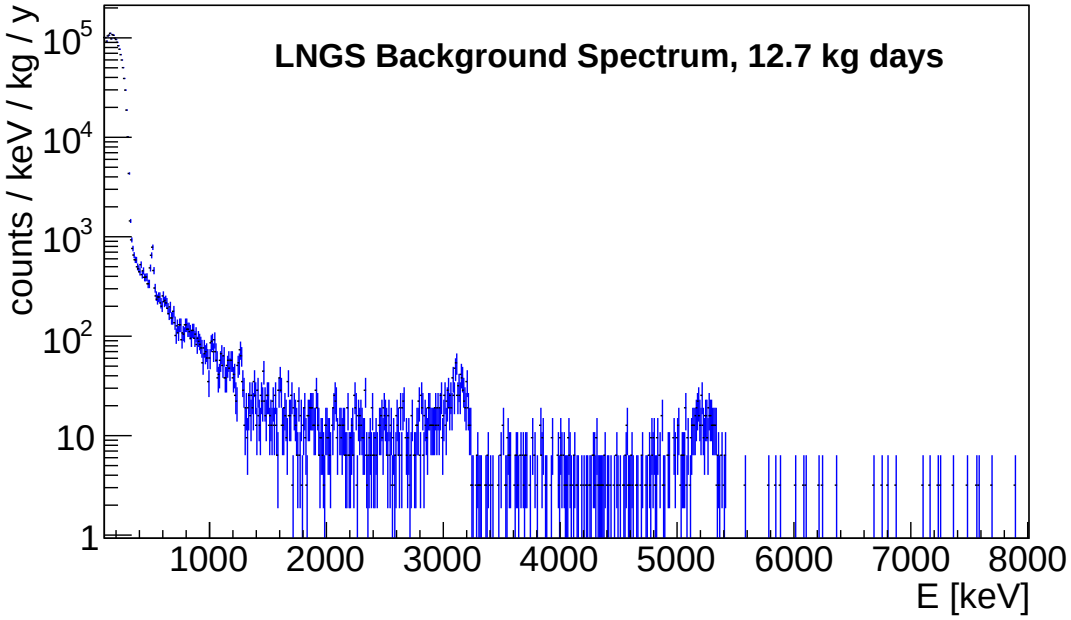

Figure 3.2.: Full LNGS background spectrum without depth cuts, compare Figure 3.1. The low energy spectrum is dominated by the intrinsic ^{113}Cd β-decay [Daw09a]. A γ-line at about 500 keV is clearly distinguishable from the background. At 3 MeV and 5 MeV two α-peaks with the typical low energy tail are visible. Above 5.5 MeV no clear signal of further peaks is present.

assembly of the detector layer. The ^{222}Rn chain contains the sub chain

$$^{210}\mathrm{Pb} \xrightarrow[\beta,\,0.06\,\mathrm{MeV}]{T_{1/2}=22.3\,\mathrm{y}} {}^{210}\mathrm{Bi} \xrightarrow[\beta,\,1.2\,\mathrm{MeV}]{T_{1/2}=5.0\,\mathrm{d}} {}^{210}\mathrm{Po} \xrightarrow[\alpha,\,5.3\,\mathrm{MeV}]{T_{1/2}=138\,\mathrm{d}} {}^{206}\mathrm{Pb}\,(\mathrm{stable})$$

with the long lived β-emitter ^{210}Pb. ^{222}Rn itself has a half-life of only 3.8 d. The most likely way of contamination is the decay of ^{222}Rn in the surrounding air. The emitted α-particle removes electrons from the atomic shell along its path. Therefore, the resulting ^{218}Po is positively charged [Heu95]. ^{218}Po or one of the decay products then deposits on surfaces. There they stick to the surface or can even diffuse several tenths of μm into the surface [Cle11]. The time it takes to decay down to ^{210}Pb is in the order of several tens of minutes to a few hours.

The ^{210}Pb contamination can be directly on the detector surface or on the surface of surrounding materials, in the case of the current detector holders in particular on the Delrin carriers. The detectors are set with the cathode side directly on top of a Delrin plate with openings for the contacting of the cathode. As the radon daughters are positively charged they are attracted especially by statically charged materials. Therefore plastics such as plexiglass but also Teflon strongly attract the Rn daughters. Delrin is not regarded to build up as much electrostatic charge as these materials. But nevertheless a certain amount of pollution will be unavoidable. Even though the Delrin holders are

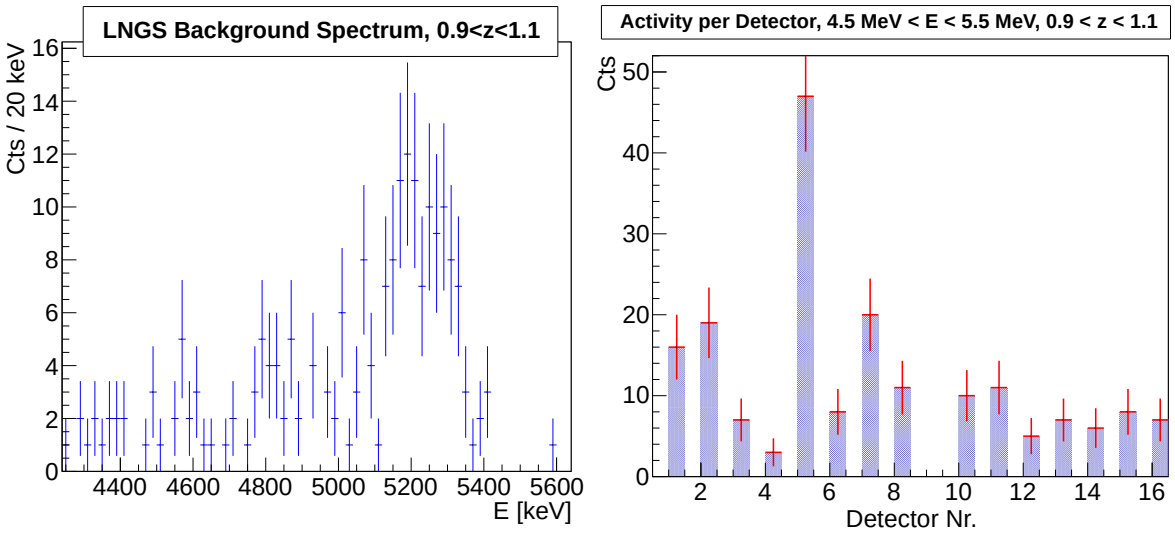

Figure 3.3.: Spectrum and count rates at the energy region of the ^{210}Po α-decay. The rate of detector 5 is significantly higher than the other counting rates. See also Figure 3.4 for comparison of the data taken in 2011 and 2012.

cleaned carefully with acetone and isopropanol before the assembly, during the time of assembly and the commissioning phase a certain amount of radon pollution accumulates. Depending on the material and radon concentration several hours are sufficient to produce measurable surface activity [Gui11]. Common radon concentrations are in the order of several ten Bq per m^3, e.g. $(35 \pm 2\,\mathrm{Bq/m^3})$ were measured in the old COBRA LNGS cabin, even $(142 \pm 2)\,\mathrm{Bq/m^3}$ in the new hut (both measurements were done by Matthias Laubenstein from the Special Techniques Services at LNGS) and $(12.9 \pm 0.2)\,\mathrm{Bq/m^3}$ in the DLB with ventilation of air from the outside and $(32.4 \pm 1.0)\,\mathrm{Bq/m^3}$ without ventilation [Ned13].

The surface contamination on the detectors themselves can be divided into contamination on top of the passivation lacquer and on the cathode. The area of the coated surfaces is five times as large as the blank cathode side. On the other hand already several ten μm of a passivation coating are sufficient to reduce and smear the energies of the α-particles significantly. Therefore α-particles from the ^{210}Po decays on the passivated surfaces will be detected at much lower energies and the energy spectrum will furthermore be smeared. The exact thickness of the current passivation coating and also important material properties such as the density and also variations of the thickness of the coating are not exactly known. As the attenuation of α-radiation is very sensitive to small changes in material composition and thickness, no reliable calculation or simulation of the expected shape and intensity of a measured spectrum is possible. Cleaning of the coated surfaces is difficult because most solvents also etch the passivation. Treating the surface with a (weak) solvent such as isopropanol therefore not only brings the risk of damaging the passivation coating but also the risk of introducing the surface con-

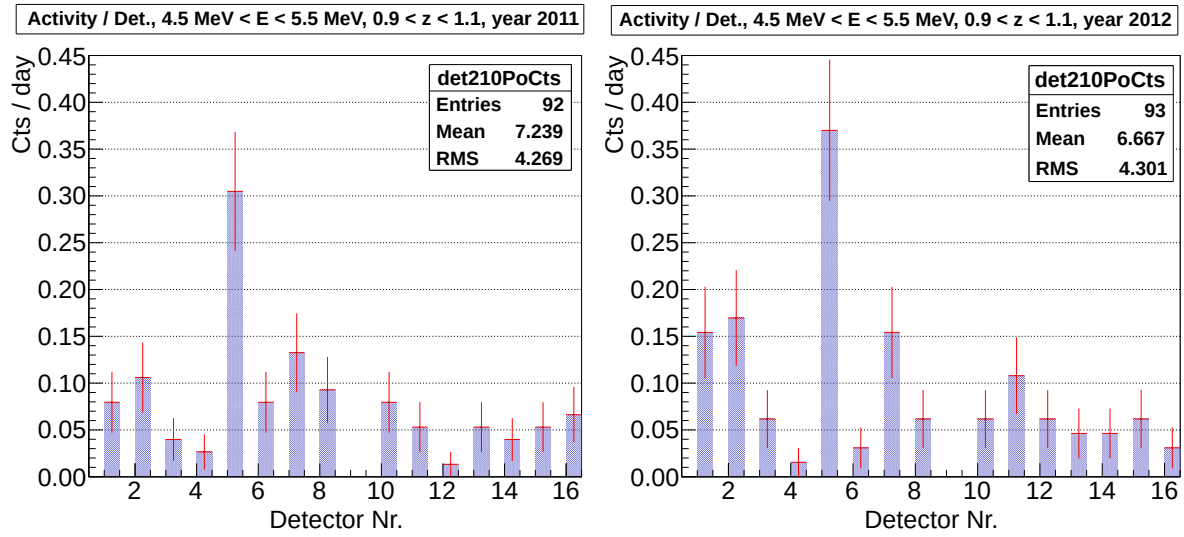

Figure 3.4.: Comparison of count rates in the ^{210}Po energy region for data taken in 2011 (left, 75.5 days measuring time) and 2012 (right, 64.9 days of measuring time).

taminations into the slightly solved upper layers of the passivation and thus irreversibly contaminating the coating itself.

The metallised cathode of the detectors is not coated. Furthermore a high negative voltage of about 1 kV is applied during measurements. For the characterisation of the detectors before the installation and also for testing of the layers during commissioning, the detectors are operated in normal air. Due to the negative high voltage of the cathode, the radon daughters are highly attracted, certainly even much stronger than to statically charged plastics. The detector characterisation measurements take several hours, the commissioning phase of the detector layers can even last a few days. Furthermore, lead sticks very well to metals and especially well to gold (this can e.g. be seen from gold coated solder pads for soldering with lead-containing solder). For these reasons the contamination on the cathode is expected to be higher than on the passivated surfaces. Cleaning the cathode is difficult because by mechanical force, i.e. wiping the surface, a damage of the only 100 nm thick gold coating is possible. In [Gui11] it is furthermore shown that the progenies of radon can diffuse even into copper. These contaminations cannot be removed by simply cleaning the surface, but a thin layer of the material has to be removed, e.g. by etching.

The energy versus depth plots in Figure 3.1 and Figure 3.5 show that nearly all of the events with matching ^{210}Po energy occur directly at the cathode. As explained above the α-particles from decays on the coated surfaces lose some of their energy. So ^{210}Pb contaminations will appear at lower energies, several of the events in Figure 3.5 with medium interaction depth derive from these decays. But even though the sum of the area of the passivated side surfaces is four times as high as the area of the cathode side, the number of ^{210}Po events directly at the cathode is much higher than the number of

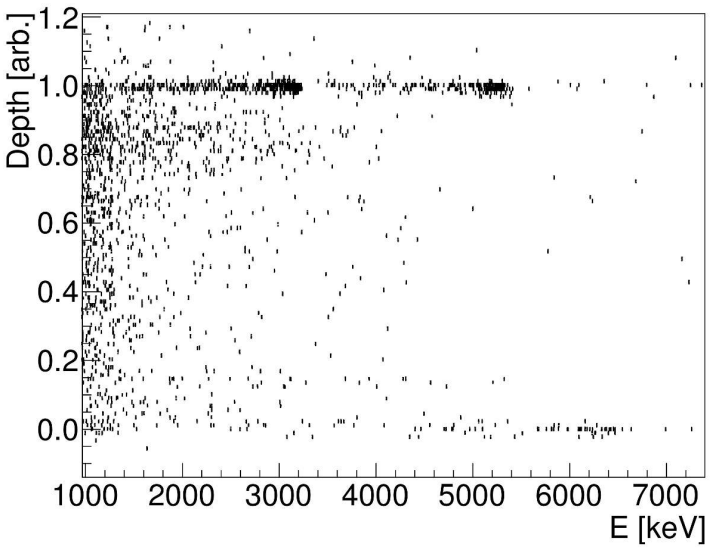

Figure 3.5: High energy cut-out of Figure 3.1. The main ^{210}Po and ^{190}Pt pollution is at the cathode side, but there are also lower energetic entries at medium depth. They probably derive from ^{210}Po decays on the coated surfaces where the α-particles lose noticeably energy while travelling through the coating. At about 6.4 MeV a cluster deriving from charge doubling ^{190}Pt events at the anode side ($z = 0$) is visible.

events with medium interaction depth between 2 MeV and 5 MeV. This indicates that for the reasons mentioned above the pollution on the cathode side is much higher than of the passivated sides.

As explained above the contamination at the cathode side can either be located directly on the cathode or a pollution of the Delrin carrier. As can be seen in Figure 3.3 and Figure 3.4 the count rates per detector for cathode events between 4.5 MeV and 5.5 MeV differ strongly. Especially the contamination on detector 5 is very high, about 25 % of all events occurred on this detector. That the comparatively large spread in the decay rates is certainly not only due to statistical fluctuations can be concluded from the fact that they appear in the three months of data taking in 2011 as well as the three months of data taking in 2012, see Figure 3.4. Taking this spread into account, a stronger contamination of the cathode is more likely than a contamination on the Delrin carrier. The Delrin carrier was cleaned carefully in an ultrasonic bath of first acetone and afterwards isopropanol. Remaining contamination on the Delrin surface therefore should be distributed uniformly all over the carrier. In contrast the treatment of the detectors may have differed significantly. For example a longer measurement time during characterisation may be an explanation for the higher contamination.

Even though the main ^{210}Po is located on the cathode and can be vetoed with the interaction depth information, cleaning of the cathode before assembly and storage of the detectors and the Delrin carrier during the assembly and commissioning as much as possible is worthwhile. Also cleaning the coated sides of the detectors, e.g. with clean distilled water to prevent solving the passivation lacquer, should be taken into account as presumably a large fraction of the background in the ROI derives from ^{210}Po decays with energy loss in the passivation.

The rate of cathode events between 4.5 MeV and 5.5 MeV during the 75.5 days of measurement in 2011 was (0.081 ± 0.008) cts/day/detector and during the 64.9 days of measurement at the beginning of 2012 it was (0.096 ± 0.010) cts/day/detector. The rate

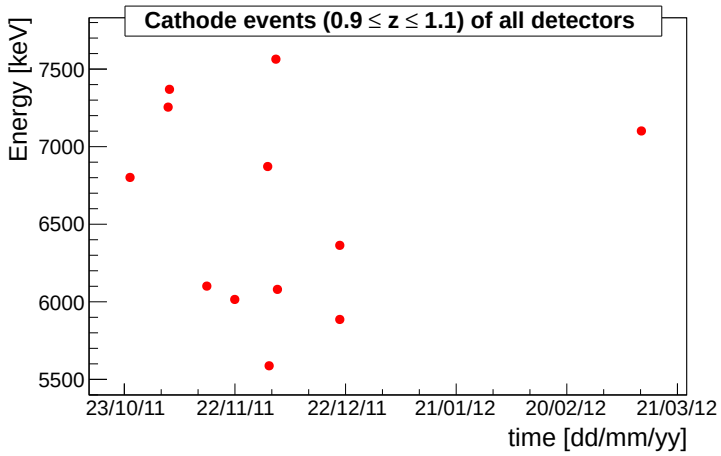

Figure 3.6: Time resolved plot of cathode events in the LNGS set-up with energy $\geq 5.5\,\mathrm{MeV}$. The events are evenly distributed over all detectors. It is not clear why the high energetic events nearly vanish after December 2011 as no changes to the set-up or the nitrogen flushing level were done. However, this indicates that the remaining diffusion of radon into the set-up is very small if present at all.

in 2012 is higher than in 2011. Due to the high half-life of ^{210}Pb of 22.3 y the rate is expected to be constant if the sub chain is in equilibrium. The half-life of ^{210}Pb of 22.3 y is long compared to the time between production and installation of the detectors, and especially between the characterisation measurements and the installation. The ^{210}Po half-life of 138 d is also comparatively long. Therefore it is possible that the decay chain was not in full equilibrium shortly after installation and the count rate slightly increased while approaching its equilibrium.

The decay rate can also increase if radon is still diffusing into the set-up despite the radon shielding. But with the low statistics the slightly higher rate in 2012 cannot be taken as a sound hint of an increasing background level. Furthermore, radon should also be visible by the aforementioned other α-decays of the radon chain, but in contrast in 2011 in the energy region from 5.5 MeV to 7.5 MeV 11 events were observed at the cathode side whereas only 1 event occurred in the same energy region in the 2012 data (see Figure 3.6). These events are equally distributed over all detectors. Striking is that nearly no events occurred after December 2011 even though neither the set-up nor the nitrogen flushing level was changed.

3.1.2. ^{190}Pt α-Decays

The second cluster of cathode events derives from ^{190}Pt in the electrode metallisation. The presence of this background source was already assumed in [Ree09] to be present in the first red detector layer. With the now available interaction depth information and the reduced background level the presence can now be confirmed. According to private communication with the detector manufacturer the electrode metallisation consists of a 100 nm thick gold coating on top of a 100 nm thick platinum coating. The typical variation of the coating thickness is approximatively 15 %.

Platinum contains the α-particle emitter ^{190}Pt with a small natural abundance of

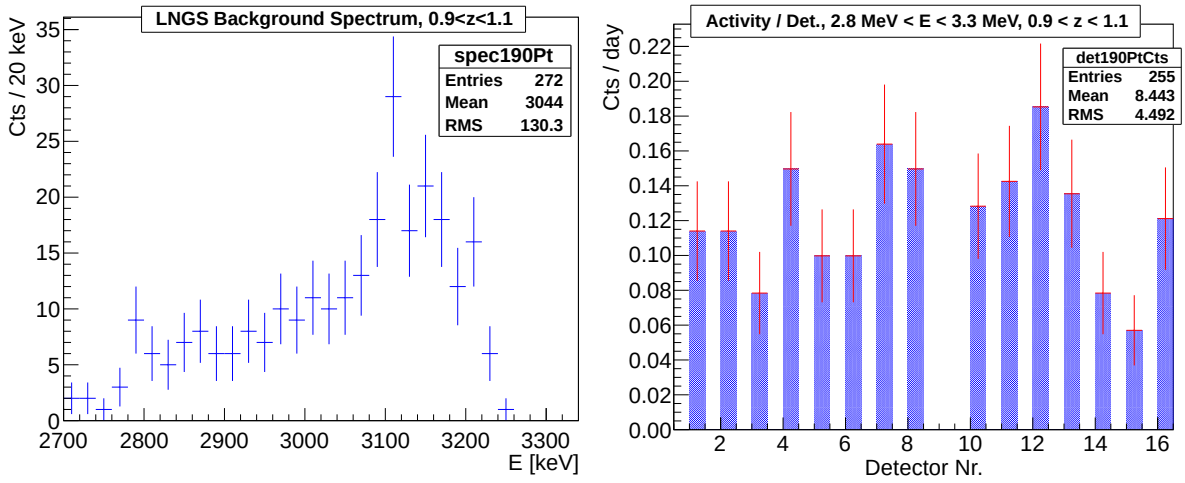

Figure 3.7.: Spectrum and count rates at the energy region of the ^{190}Pt decay. The events are distributed much more evenly amongst the detectors than for the ^{210}Po events, here also a variance of about 15 % in the cathode thickness has to be taken into account. The average count rate at the cathode between 2.8 MeV and 3.3 MeV is (0.12 ± 0.01) cts/day/detector.

(0.014 ± 0.001) %. [Bö05][1]. ^{190}Pt decays via two subsequent α-decays to ^{182}W [Fir98]

$$^{190}\mathrm{Pt} \xrightarrow[\alpha,\ (3164\pm15)\,\mathrm{keV}]{T_{1/2}=6.5\cdot10^{11}\,\mathrm{y}} {}^{186}\mathrm{Os} \xrightarrow[\alpha,\ (2757.7\pm2.4)\,\mathrm{keV}]{T_{1/2}=2.0\cdot10^{15}\,\mathrm{y}} {}^{182}\mathrm{W}\,.$$

Platinum is cleaned during the production process of metallic platinum. Furthermore, the half-life of ^{190}Pt is already very high, in fact more than an order of magnitude higher than the live time of the universe, and the half-life of ^{186}Os is even nearly four orders of magnitude higher. Therefore, it can be assumed that no or negligibly few decays from ^{186}Os are to be expected.

Mentionable are the high discrepancies of the natural abundance, the α-particle energy and the half-life in literature. [Tav06] lists measurements with resulting half-lives in the range of $(3.2-6.9)\times10^{11}$ years. Also the natural abundance differs, e.g. the online decay data bases [KAE12, Chu99] give an abundance of 0.01 %. α-particle energies range from (3164 ± 15) keV [Fir98] over (3175 ± 14) keV [KAE12] up to (3180 ± 6) keV [Chu99].

The measured LNGS cathode spectrum around 3 MeV is shown in Figure 3.7 together with the distribution of these events amongst the detectors. The drop in the spectrum above the α-decay energy of about 3.2 MeV is clearly visible. On the lower energy side a long tail that is typical for α-particles is noticeable (compare also Figure 3.2). Compared to the ^{210}Po events the distribution of events amongst the detectors is quite uniform. Between 2.8 MeV and 3.3 MeV the average count rate of cathode events is (0.12 ± 0.01) cts/day/detector.

The number of observed events can be compared to the number of expected events. Here, the determination of the detection efficiency is difficult. From geometric consid-

[1] see also `http://www.nist.gov/pml/data/comp.cfm`

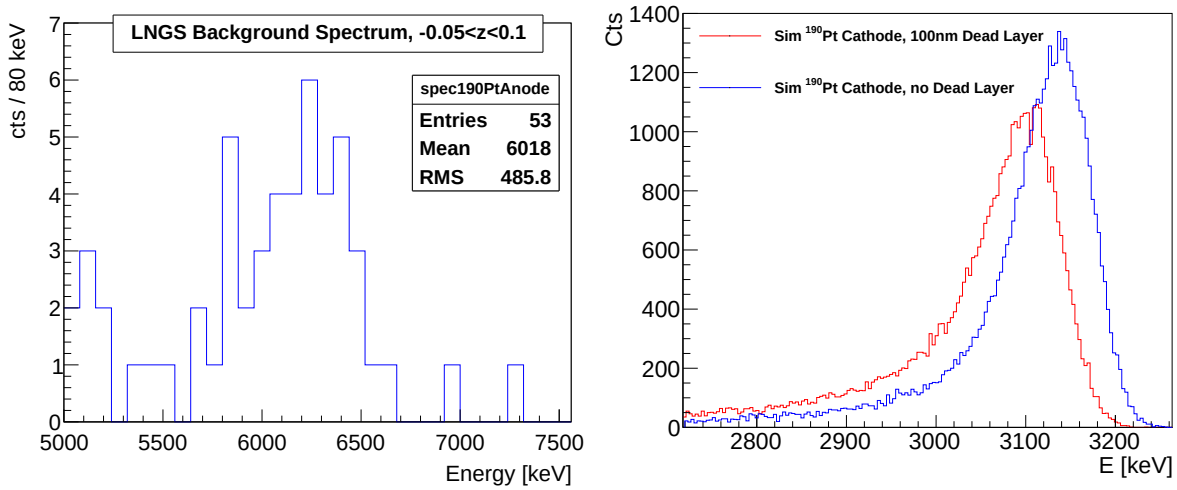

Figure 3.8.: ^{190}Pt at the anodes (left) and simulations of ^{190}Pt (3175 keV α-particles) at the cathode (right). Due to the charge doubling effect for anode events [Teb11] (see also Subsection 1.2.1) the calculated charge for events at the anodes is twice as high as for normal events. Therefore the 3.2 MeV α-decays on the anode side appear at about 6 MeV. The reproduction of the ^{190}Pt peak at the cathode side is difficult as detector effects and small uncertainties in the geometry have a large influence. The simulations were convoluted with an energy resolution of 2 % FWHM at 3 MeV. For the simulation without a dead layer the detection efficiency was determined to be 46 % and for the simulation with an additional 100 nm dead layer to be 43 % in a region of 2.8 MeV - 3.3 MeV. When taking into account only the broad part of the 100 nm dead layer peak (2.95 MeV - 3.3 MeV) the detection efficiency is calculated to be 38 %. As the measured peak seems to be even a bit wider than the simulated peak with 100 nm dead layer, a detection efficiency of (40 ± 5) % for a counting interval of 2.8 MeV - 3.3 MeV can be assumed.

erations one can assume the number of observed events to be in the order of 50 % of the occurred decays. Like for the ^{210}Po events a simulation is difficult. For the reason mentioned for ^{210}Po, the measured peak is broader than expected from a simple simulation, see Figure 3.8. From the simulation of 3.175 keV α-particles in a 100 nm thick platinum metallisation 46 % of all simulated events are found in an energy region from 2.8 MeV to 3.3 MeV when taking also into account an energy resolution of 2 % FWHM at 3 MeV. When trying to take into account the detector effects by adding a small dead layer of 100 nm below the cathode, the maximum of the observed energy distribution is decreased and the distribution is slightly widened. For this simulation a detection efficiency of 43 % was determined and the maximum of the distribution is below 3.1 MeV. The peak in the measured spectrum is even wider than in this simulation, but the maximum is above 3.1 MeV. Below 2.8 MeV the measured spectrum drops to about 10 % of its height in the region of about 3.1 MeV. The simulated spectrum with 100 nm dead layer drops to 10 % of its maximal height at about 2.95 MeV and the detection efficiency in this simulation is 38 % for an energy interval from 2.95 MeV to 3.3 MeV. Taking all this into account, the detection efficiency for the measurement can be estimated to be

about $(40 \pm 5)\,\%$ for a counting interval from 2.8 MeV to 3.3 MeV.

Taking the half-life $T_{1/2} = 6.5 \times 10^{11}\,\mathrm{y}$ from [Fir98], the natural abundance (mole fraction) $a = (0.014 \pm 0.001)\,\%$ from [Bö05] and calculating the average atomic mass from numbers given therein to be $\langle m_{Pt} \rangle = (195.1 \pm 0.2)\,\mathrm{amu}$ and approximating the platinum layer to have a thickness of $(100 \pm 15)\,\mathrm{nm}$ for the $1\,\mathrm{cm}^3$ detectors the expected measured count rate is (assuming a measurement time $\Delta t = t_2 - t_1 \ll T_{1/2}$)

$$A(t) = -\epsilon \frac{\Delta N}{\Delta t} = -\epsilon \frac{N(t_2) - N(t_1)}{\Delta t} \overset{\text{Taylor Ser.}}{\approx} N_0 \cdot \epsilon \cdot \frac{\ln(2)}{T_{1/2}} = 0.11\,\frac{\mathrm{cts}}{\mathrm{det} \cdot \mathrm{day}}\,, \tag{3.1}$$

where N_0 is the number of ^{190}Pt atoms per detector cathode and ϵ is the assumed detection efficiency of 40 %. The measured rate is (0.12 ± 0.11) cts/detector/day. Giving a reliable estimate for the uncertainty of the expected number of events is not possible because the measured half-lives given in literature differ strongly and in [Fir98] no uncertainty for the half-life is given at all. Instead a half-life for the ^{190}Pt decays on the basis of the number of observed events can be calculated. From Figure 3.5 and Figure 3.1 it can be concluded that nearly no ^{210}Po events contribute to the cathode events below 3.5 MeV. Therefore it can be assumed that all 255 cathode events between 2.8 MeV and 3.3 MeV derive from ^{190}Pt. With the numbers given above and taking the uncertainty of the detection efficiency as systematic error, the half-life of ^{190}Pt can be deduced to be

$$T_{1/2} = N_0 \cdot \epsilon \cdot \frac{\ln(2)}{N_{oberved}} \cdot t_{meas.} = (5.8 \pm 1.0\,(\mathrm{stat.}) \pm 0.7\,(\mathrm{syst.})) \times 10^{11}\,\mathrm{y} \tag{3.2}$$

for the measurement time of 140.4 days of the first colourless detector layer. This half-life is in good agreement with the one given in [Fir98] and rather disfavours the lower half-lives given in [Tav06].

Also the metallisation of the anodes consists of platinum and gold. The amount of platinum and gold is much smaller because the anode grids cover only about 30 % of the anode side. Due to the effect of charge doubling for anode side events observed in [Teb11] (see also Subsection 1.2.1), the measured energy for many anode side events is twice as high as for cathode side events. Therefore the ^{190}Pt decays on the anode side appear at about 6.2 MeV. The cluster of these events can be clearly seen in Figure 3.5 and is also shown in Figure 3.8.

The decay of ^{190}Pt to the first excited state of ^{186}Os under emission of a 137.2 keV γ-particle was measured for the first time [Bel11]. There, a half-life of $T_{1/2} = 2.6^{+0.4}_{-0.3}(\mathrm{stat.}) \pm 0.6\,(\mathrm{syst.}) \times 10^{14}\,\mathrm{y}$ was determined. This half-life is even more than two orders of magnitude higher than for the decay to the ground state. The expected decay rate is 0.02 decays/detector/month, or 16 decays/64 detectors/y for the whole 64 detector array. This small number of events will not be detectable in the background from the ^{190}Pt decays to ground state because due to the small difference in the energy

of the emitted α-particles, the decays to excited states will vanish in the low energy tail of the decays to ground state.

A coincidence analysis can be applied to disentangle these two decays, but the detection efficiency for two detector events will be smaller than the detection efficiency for the decay to the ground state. Between the cathode side of a detector and the anodes of the detector below is a Delrin layer and a gap of about 1 cm. The probability for an interaction via photoelectric effect is comparatively high for a 137.2 keV γ-particle. On the one hand this will increase the detection efficiency, but on the other hand it also means that a coincidence analysis will certainly only be useful for γ-particles that are emitted towards the detector below the cathode. This reduces the detection efficiency by a factor < 0.5. Furthermore, only 75 % of all detectors do have a detector below their cathode side. Therefore $\epsilon < 0.2$ can be assumed and even with more than one year of data taking with the full 64 detector array it will be difficult to detect the ^{190}Pt decay to the first excited state.

3.1.3. Search for γ-Lines

The only γ-line in the background spectrum that can be detected with higher statistical significance is at about 510 keV. It can be concluded that this line derives from γ-particles because the calculated interaction depths are distributed all over the detector, see Figure 3.1. This line was first observed in [Sch09] in data taken with four cyclotene passivated detectors and four detectors with the colourless passivation from EIDIS. The line was observed after the installation of the Cyclotene passivated detectors and could not be detected in the data of the four detectors with clear EIDIS coating that had already been running for several months. The resolution of the Cyclotene passivated detectors was by more than a factor of two better than for the other four detectors. Also the amount of nitrogen flushed data with low background before the installation of the Cyclotene passivated detectors was low. Therefore it is possible that the peak was already present but was not noticeable.

Between the measurements with the Cyclotene passivated detectors and the measurement with the 16 colourless detector layer the set-up was moved from the former COBRA cabin to the new space in the former location of the Heidelberg-Moscow experiment [KK01b]. Within the scope of the move the inner 5 cm lead layer was replaced with lead with an ^{210}Pb activity < 3 Bq/kg. The inner copper parts were thoroughly cleaned by the LNGS Chemistry laboratory (see Appendix E). During the installation of the 16 detector layer all detectors, the detector holders and even the calibration tubes that go directly into the set-up were replaced. Assuming that the 500 keV line in the older data and in the new data of the 16 detector has the same origin, many sources of background, e.g. surface contaminations of the inner copper parts or the Cyclotene passivation, can be excluded.

To investigate the events in the region of the 500 keV peak, the reduction of β- and α-decays on the electrodes with a cut on the interaction depth is useful. In the following

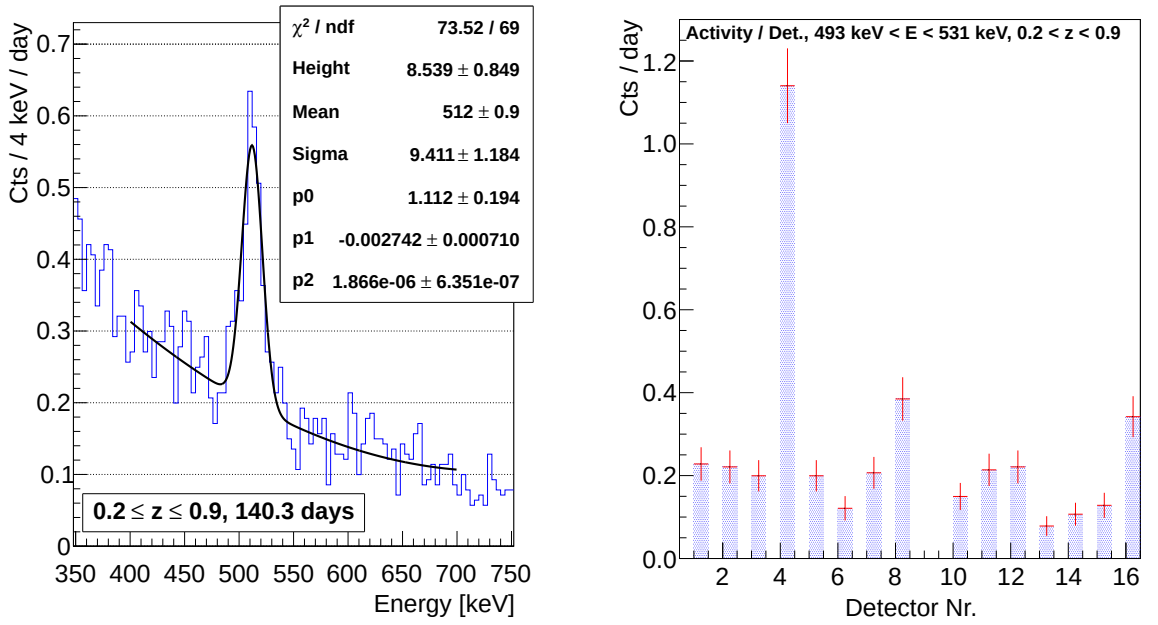

Figure 3.9.: Fit of the 511 keV line in the sum spectrum and distribution of 511 keV $\pm 2\sigma$ events amongst the detectors. The line is clearly visible and fits well to a 511 keV positron annihilation γ. The count rate slowly decreases with time, see Figure 3.11. Most of the events were detected in the upper three detectors, especially in detector 4, compare also Figure 3.10. To exclude electronic disturbances as cause of this line about 20 % of the 511 keV $\pm 2\sigma$ event pulses from detector 4 were inspected by eye, but no irregularities were found.

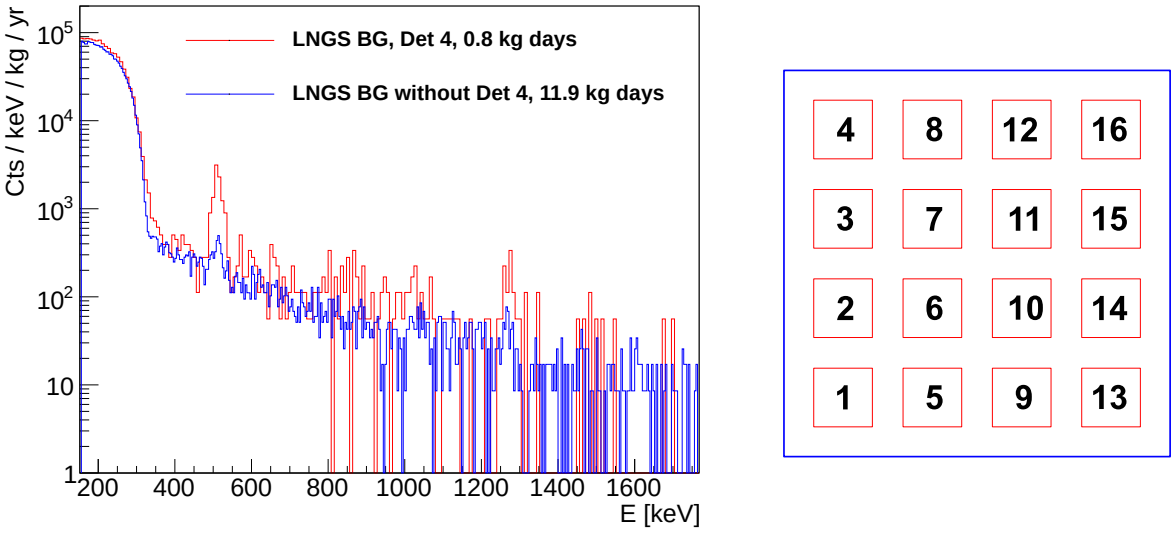

Figure 3.10.: Comparison of the spectrum of detector 4 with the sum spectrum of all other detectors and configuration of the detectors within a detector layer. The 511 keV peak is much higher in the data of detector 4 than for the rest of the detectors. As can be seen from Figure 3.9 three of the upper four detectors (4, 8 and 16) have an increased count rate at 511 keV.

Data	Mean [keV]	Resolution FWHM [%]	Cts / day from Fit	Cts / day from counting
2011	511.6 ± 1.2	4.5 ± 0.6	2.5 ± 0.3	2.7 ± 0.3
2012	512.7 ± 1.5	4.1 ± 0.9	1.8 ± 0.3	1.5 ± 0.3
2011 and 2012	512.0 ± 0.9	4.3 ± 0.5	2.1 ± 0.2	2.0 ± 0.2

Table 3.1.: Fitted data of the 511 keV peak. The average energy resolution matches the energy resolution of 4 % determined from calibration data of detector 4. The decrease of the counting rate is unlikely to derive from statistical fluctuations. As the Gaussian fit fits not exactly to the data (compare Figure 3.11), the counting method ($\pm 2\sigma$ for peak region, $2\,\sigma$ above and $2\,\sigma$ below for background region) is more reliable. The counting rate is given as counts per day for the whole detector layer.

in general only events with an interaction depth $0.2 \leq z \leq 0.9$ were taken into account. In Figure 3.9 the peak and the rate of decays in the region of the peak for each detector are shown. To fit the peak, a Gaussian distributed signal was used. To describe the background close to the peak, a quadratic polynomial was applied. The fitted mean $\mu = (512 \pm 1)\,\text{keV}$ of the peak matches well to the 511 keV positron annihilation energy. The deviation of about 1 keV (0.2 %) is very small compared to the detector resolution of about 4 % FWHM at 500 keV. Also most direct γ-lines from nuclear decays could be excluded in [Sch09] as origin of the line by taking into account the intensities of other lines from the same decays that should also be present in the energy spectrum. This rather favours a β^+ decay as the source of the contamination.

The distribution of the count rates per detector, also plotted in Figure 3.9, shows an excess of 511 keV events in detector four. A comparison of the spectrum of this detector with a sum spectrum of the other 14 detectors shows that the line is also visible in the data of the other detectors, but the rate is much higher for detector four, see Figure 3.10. Also the detectors eight and sixteen show a significantly increased count rate. These four detectors form together with detector twelve the upper column of the detector layer. This could be a hint to a contamination of the holder material or the surrounding copper in this region of the layer, but detector twelve does not show an excess of events. To exclude an origin of this peak from electronic disturbances about 20 % of the pulse shapes of detector four in the region of the 511 keV peak were inspected manually, but no suspicious pulse shapes were found. In [Sch09] a uniform distribution of the events in all detectors with an average rate of about 1.3 cts per detector and day was determined. This count rate is similar to the activity in detector four.

A comparison of the data from 2011 and 2012 showed that the count rate of the 511 keV events decreases with time, see Figure 3.11. To have a better estimate for the count rates, the method of counting was applied to the data to decrease the influence of the assumed shape of the fit function. Therefore, the counts in the signal interval of $\pm 2\sigma$ around the fitted peak were summed and background determined from a 2σ region above and a $2\,\sigma$ region below the signal region was subtracted. The results of the fits

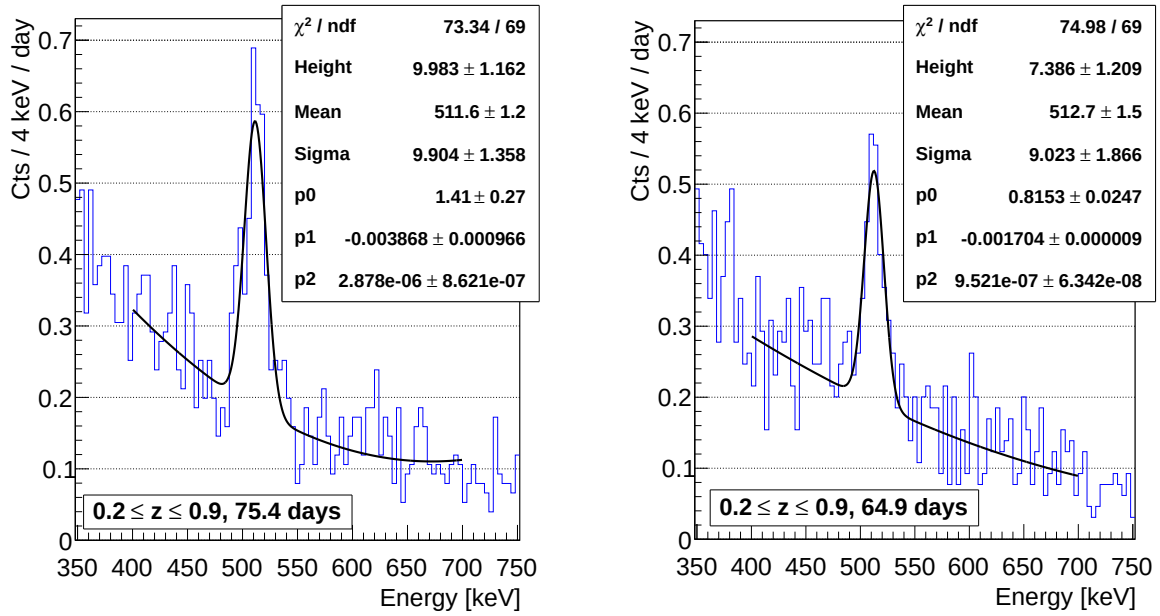

Figure 3.11.: Spectrum and fit of 510 keV line with quadratic BG approximation for 2011 (left) and 2012 (right) data. The general background rate around the 511 keV peak is similar in the 2011 and 2012 data whereas the height of the peak decreases. The determined resolution of ∼4 % FWHM at 510 keV matches the resolution of detector 4 obtained from calibration data. This also disfavours electronic disturbances as a cause of this peak.

and the counting are listed in Table 3.1.

As the decrease of the activity is clearly visible during the measurement time, the assumption $\Delta t \ll T_{1/2}$ and thus Equation (3.2) is not valid. However, from the number of counts an estimate for the half-life of a decay can be obtained by solving

$$\frac{N(t_1 \leq t \leq t_2)}{N(t_3 \leq t \leq t_4)} = \frac{\int_{t_1}^{t_2} -N_0 \frac{\ln(2)}{T_{1/2}} \exp\left(-\frac{\ln(2)}{T_{1/2}} \cdot t\right)}{\int_{t_3}^{t_4} -N_0 \frac{\ln(2)}{T_{1/2}} \exp\left(-\frac{\ln(2)}{T_{1/2}} \cdot t\right)} = \frac{\mathrm{e}^{\left(-\frac{\ln(2)}{T_{1/2}} \cdot t_1\right)} - \mathrm{e}^{\left(-\frac{\ln(2)}{T_{1/2}} \cdot t_2\right)}}{\mathrm{e}^{\left(-\frac{\ln(2)}{T_{1/2}} \cdot t_3\right)} - \mathrm{e}^{\left(-\frac{\ln(2)}{T_{1/2}} \cdot t_4\right)}} \tag{3.3}$$

numerically. Simplifying, it can be assumed that the measurement time equals approximately the whole passed time (i.e. $t_1 = 0$ days, $t_2 = 75.5$ days, $t_2 = t_3$, $t_4 = 140.4$ days) as the calculation will only give a rough estimate of the half-life anyway. This is partly due to the exponential dependency in Equation (3.3) which leads to large changes in $T_{1/2}$ for comparatively small changes in the count rates. To have an estimate for the uncertainty of the obtained half-life, Gaussian distributed random numbers N_1 and N_2 with mean and sigma according to the measured count rates listed in Table 3.1 were generated. For these random numbers Equation (3.3) was solved numerically. The resulting distributions of the half-lives are plotted in Figure 3.12. From this distribution a

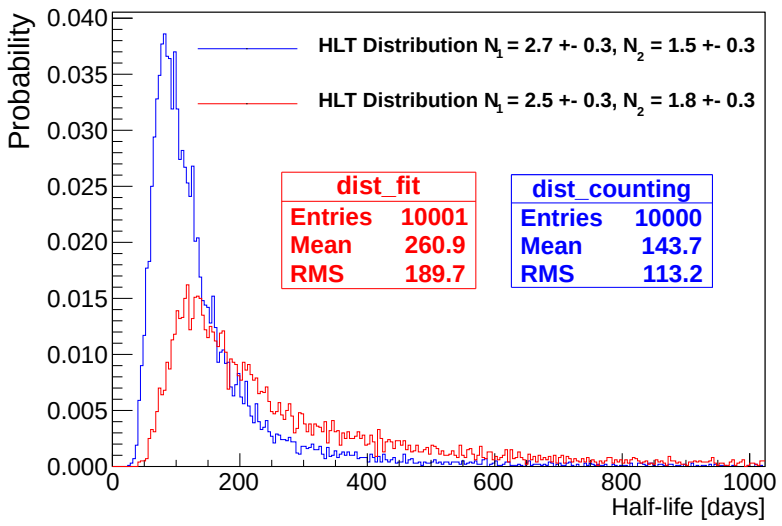

Figure 3.12: Distribution of half-lives for the 511 keV peak determined from MC random variables. Equation (3.3) was solved numerically assuming Gaussian distributed values of the count rates listed in Table 3.1. Due to the exponentials in eq. (3.3), small changes in N_1 and N_2 lead to large changes in the calculated half-life. Therefore the distribution is very broad, especially for $N_1 \approx N_2$.

68.27 % (1σ) CL can be determined. For the rates determined by counting in the peak region, a half-life of $T_{1/2} = 112^{+106}_{-42}$ days was calculated. A similar calculation for the rates determined by the fit is more difficult. The confidence intervals of the two count rates nearly overlap. This results in a broad distribution for the resulting half-lives with a very long tail towards high half-lives and leads to a very high upper uncertainty of the calculated half-life of $T_{1/2} = 275^{+5345}_{-159}$ days. As the method of counting to determine the peak contents is supposed to be more precise for the reasons mentioned above, the half-life of the decay can be regarded to be > 70 days and smaller than several hundred days.

The half-life of the decay that causes the 511 keV line is probably smaller than two years but still a high count rate is present after nearly three years between the first observation and the installation of the new detectors. Therefore, the origin of the line from activation of the detectors by cosmic rays during the storage prior to the installation is likely. A significantly earlier production date or a different storage of some detectors may be an explanation for the excess in activity for some detectors. In [Por00] CdTe was irradiated with 1.7 GeV protons to have an estimate for activation from cosmic rays. Observed isotopes with either a half-life of more than ten days or with a long-lived daughter nuclide are listed in Table 3.2.

No nuclides with a long half-life and also a high branching ratio for β^+ decay are found there. The only β^+ emitter with a long half-life of 106.7 d is ^{88}Y. But the branching ratio is only 0.2 % and thus the γ-lines from the competing EC decay should be clearly visible in the spectrum. Interestingly ^{85}Sr with a γ-line at 514 keV is a daughter of the isotope ^{85m}Y, which is produced by proton irradiation. In [Sch09] this isotope was quoted as one of the few possible background sources, but no reasonable explanation for the origin of the contamination could be found. However, the cross sections for the production of most of the isotopes listed in Table 3.2 are similar, at least for the irradiation with 1.7 GeV protons. Therefore, it is unlikely that only one of the isotopes is produced

Isotope	Mode of decay	Half-life	γ-lines [keV]	Long-lived daughters	Exp. Cross Section [mb]
^{129m}Te	IT (63%), β^- (37%)	33.6 d	695.9 (3%)	^{129}I (15.7×10^6 y)	7.5 ± 0.9
^{129}I	β^-	15.7×10^6 y	39.6 (7.6%)	-	-
^{121m}Te	IT (88.6%), EC (11.4%)	154 d	212.2 (81.4%), 1102.1 (2.5%)	-	5.4 ± 0.6
^{121}Te	EC	16.78 d	507.6 (17.7%), 573.1 (80.3%)	-	3.4 ± 0.5
^{126}Sb	β^-	12.46 d	414.8 (83.3%), 666.3 (99.6%)	-	1.4 ± 0.2
^{124}Sb	β^-	60.2 d	602.7 (97.8%), 1690.9 (47.3%)	-	6.2 ± 0.4
^{114m}In	EC	49.51 d	190.27 (14.7%), 725.2 (4%)	-	1.3 ± 0.3
^{105}Ag	EC	41.29 d	280.4 (30.2%), 344.5 (41.4%)	-	10.5 ± 0.5
^{101}Pd	β^+ (5%), EC (95%)	8.47 h	296.3 (19.2%), 590.4 (12.1%)	^{101}Rh (3.3 y)	8.0 ± 2.0
^{101}Rh	EC	3.3 y	198.0 (73%), 325.2 (11.8%)	-	-
^{99}Rh	β^+ (4%), EC (87%)	16.1 d	353.1 (30%), 528.2 (33%)	-	3.5 ± 0.5
^{88}Nb	β^+ (96.7%), EC (7.2%)	14.5 m	1057.1 (100%), 1082.6 (100%)	^{88}Zr (83.4 d), ^{88}Y (106.7 d)	1.0 ± 0.3
^{88}Zr	EC	83.4 d	392.9 (97.2%)	^{88}Y (106.7 d)	10.9 ± 0.7
^{88}Y	β^+ (0.2%), EC (99.8%)	106.7 d	898.0 (93.7%), 1836.0 (99.2%)	-	3.3 ± 0.5
^{85m}Y	β^+ (58.1%), EC (42.2%)	4.86 h	231.7 (22.8%)	^{85}Sr (64.8 d)	4.3 ± 0.6
^{85}Sr	EC	64.8 d	514.0 (96%)	-	-
^{75}Br	β^+ (73.1%), EC (27.1%)	1.61 h	141.2 (7%), 286.5 (88%)	^{75}Se (119.8 d)	2.0 ± 0.2
^{75}Se	EC	119.8 d	264.7 (59%), 400.7 (11%)	-	-

Table 3.2.: Long lived isotopes produced in CdTe by proton irradiation (1.7 GeV), taken from [Por00], the rel. intensities noted in brackets next to the γ-energies are taken from [KAE12]. Listed are isotopes with either a half-life > 10 d or a long lived daughter nuclide. If the long-lived daughter nuclide was not produced in the proton irradiation the data was looked up from [KAE12].

Isotope	Mode of decay	Half-life [d]	γ-lines [keV]	Unstable Daughter Nuclides
^{89}Sr	β^-	50.5	909.0 (0.01%)	-
^{91}Y	β^-	58.5	1204.8 (0.3%)	-
^{124}Sb	β^-	60.2	602.7 (98.3%), 1691.0 (47.8%)	-
^{91m}Nb	EC	60.9	1204.8 (2.9%)	-
^{95m}Tc	EC, IT	61.0	582.1 (30.0%), 835.1 (26.6%)	-
^{95}Zr	β^-	64.0	724.2 (44.2%), 756.7 (54.0%)	^{95}Nb
^{95}Nb	β^-	35.0	765.8 (99.8%)	-
^{85}Sr	EC	64.8	514.0 (96%)	-
^{58}Co	β^+ (14.9%), EC (85.1%)	70.9	810.8 (99%)	-
^{56}Co	β^+ (19.0%), EC (81%)	77.3	846.8 (100%), 1238.3 (67.6%)	-
^{73}As	EC	80.3	53.4 (10.3%)	-
^{88}Zr	EC	83.4	392.9 (100%)	^{88}Y
^{46}Sc	β^-	83.8	889.3 (100%), 1120.5 (100%)	-
^{83}Rb	EC	86.2	520.4 (44.7%), 529.6 (29.3%)	-
^{113}Sn	EC	115.1	391.7 (65.0%)	-
^{75}Se	EC	119.8	264.7 (58.9%), 279.5 (25.0%)	-
^{139}Ce	EC	137.6	165.9 (80%)	-
^{121m}Te	EC (88.6%), IT (11.4%)	154.0	212.2 (81%)	^{121}Te
^{121}Te	EC	16.8	507.6 (17.7%), 573.1 (80.3%)	-
^{102}Rh	β^- (20%), EC (80%)	207.0	475.1 (38.4), 556.4 (96.0)	-
^{65}Zn	EC	244.3	1115.5 (50.6%)	-
^{110m}Ag	β^- (98.6%), IT (1.4%)	249.8	657.8 (94.0%), 937.5 (34.1%)	-
^{57}Co	EC	271.8	122.1 (85.6%), 136.5 (10.7%)	-
^{54}Mn	EC	312.1	834.8 (100%)	-
^{109}Cd	EC	462.6	88.0 (3.6%)	-
^{134}Cs	β^-	754.2	604.7 (97.6%), 795.9(85.5%)	-
^{22}Na	β^+ (89.9%), EC (10.1%)	950.3	1274.5 (99.9%)	-

Table 3.3.: Isotopes with half-lives $50\,\mathrm{d} < T_{1/2} < 3\,\mathrm{y}$ and mass number $10 < A < 140$. Data taken from [KAE12, Chu99, Fir98].

significantly more often than all the others, and besides the 511 keV line also other lines should be clearly visible in the spectrum.

In Table 3.3 isotopes and their unstable daughter nuclides with a half-life between 50 d and 3 y and an atomic mass number $10 < A < 140$ are listed. This mass range covers most of the common nuclides. Isotopes from the natural decay chains (see e.g. Appendix C), which have a higher atomic mass number, can be inspected separately, but here again more lines should be visible for a contamination from the natural decay chains. Besides ^{85}Sr no nuclide with a high intensity γ-emission close to 500 keV was found. ^{121}Te has a line at 507.6 keV, but it also has a γ-line at 573.1 keV that has an intensity that is a factor of four higher.

The only long-lived β^+ emitter with a high β^+ intensity compared to its γ-lines is ^{22}Na. It has a half-life of 2.6 years (950.3 days). This is considerably higher than the estimated half-life, but as explained above, the upper uncertainty of the estimated value is weak and therefore a higher half-life than the one given above cannot be generally excluded. ^{22}Na has only one γ-line at 1274.5 keV. At this energy also a possible feature in the LNGS background spectrum of detector four is visible, see Figure 3.14. With the extended likelihood method described in Section 3.3 a fit at this energy was performed. The result is shown in Figure 3.15. The peak maximum seems to be slightly below 1274.5 keV. Therefore, the fit was repeated with a 0.5 % lower energy at 1268.1 keV (the implemented extended likelihood method is supposed to fit the signal strength at a known energy and is not intended to also estimate the mean of a Gaussian signal). The signal mainly appears in detector four, and an energy shift of 0.5 % is considerably smaller than its energy resolution of 2.6 % FWHM at 1275 keV. However, both fits are consistent with a signal strength $n_{sig} > 0$ at a CL > 99 %.

A ^{22}Na wire source is applied for calibration purposes at LNGS. Therefore a direct comparison is possible. In Figure 3.13 a calibration spectrum and the background spectrum of detector four are shown. Due to the very low number of events in the background spectrum above 600 keV the assumption of a ^{22}Na origin cannot be proved, but the agreement of the calibration and the background spectrum seems to be very good. Even the Compton edge of the 1275 keV line fits well.

^{22}Na is produced by spallation of atmospheric argon [Per65], but it can also be produced by activation with neutrons or protons, e.g. in Al [Ste74], or spallation in a nuclear reactor or nuclear weapons tests. It is not obvious where a contamination of the detectors or the surrounding materials with ^{22}Na could have happened. A contamination from the calibration source can be nearly excluded as mainly one detector is affected and the position of this detector is far away from the calibration tubes that are used to guide the wire source. However, as one main limiting factor of the identification of the line is the limited amount of data, more installed detectors and longer measurement time will be needed to probe the origin of the line with higher reliability.

Besides the 511 keV and the 1275 keV peak also a hint to the presence of the ^{40}K line is visible in the spectrum, see Figure 3.14. Also for this line a fit with the extended likeli-

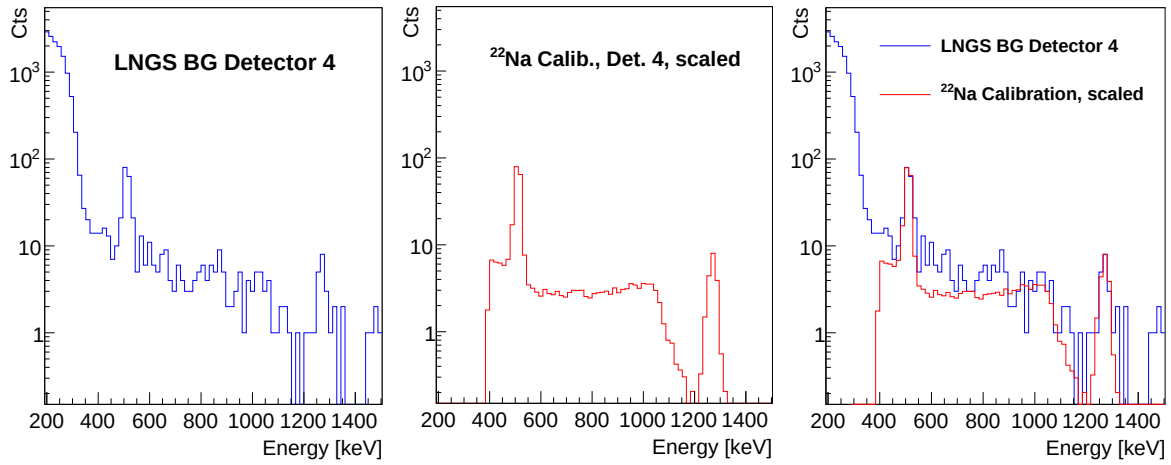

Figure 3.13.: LNGS background spectrum and ^{22}Na calibration for detector 4. Besides the 511 keV line also a feature at about 1275 keV is visible. Both lines fit to ^{22}Na. A ^{22}Na source is used for calibration purposes at LNGS. A comparison of a calibration run and the background spectrum shows good agreement, even though it is not clear where the contamination could derive from. The calibration spectrum was scaled so that the height of the 511 keV lines match.

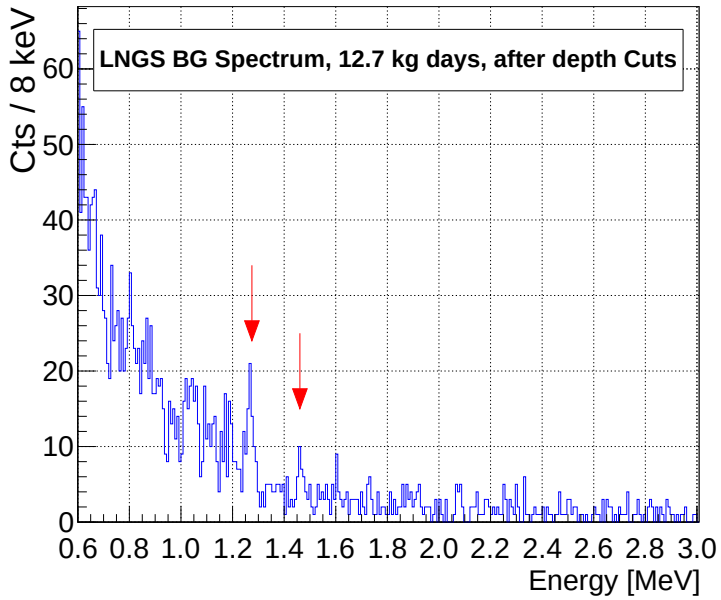

Figure 3.14: Possible γ-lines in the LNGS spectrum. To reduce background from α- and β-decays on the cathode and the anodes, a depth cut $0.1 \leq z \leq 0.95$ was applied. Besides the possible peak at 1.28 MeV (left red arrow) also a peak at 1.46 MeV (right red arrow), the γ-line of ^{40}K, are present, compare also Figure 3.15 and Figure 3.16. The small excess close to the energy of the ^{208}Tl 2.6 MeV double escape line (1.59 MeV) is too narrow to derive from a γ-line and derives most probably from statistical fluctuations.

hood method was done. The result is shown in Figure 3.16. It is consistent with a signal strength $n_{sig} > 0$ with a CL $> 99\,\%$. If a passivation coating thickness of about $20\,\mu$m is assumed and the results for the Parylene C simulation determined in Section 2.5 are scaled to the ^{40}K of the EIDIS passivation lacquer, it can be concluded that the amount of ^{40}K from the passivation coating should not be visible with the current background level. Possible sources of ^{40}K contamination can be intrinsic impurities of the RG178 HV coaxial cables, the Kapton signal cables or the applied glues. Also remnants of surface contaminations of the Delrin detector holders, the cables or the detectors themselves despite careful cleaning prior to the assembly are possible.

However, none of the discussed nuclides that can cause the γ-peaks in the spectrum can produce background in the ROI of COBRA. The main background comes from the α-sources discussed above and can be significantly reduced with a cut to the interaction depth. By requiring an interaction depth of $0.1 \leq z \leq 0.95$, the background level in the ROI between 2.7 MeV and 2.9 MeV ($\approx \pm 2\times$FWHM of the average detector resolution) can be reduced from (11.4 ± 1.3) cts/keV/kg/y (79 cts) to (4.5 ± 0.8) cts/keV/kg/y (31 cts). Thus, by reducing the active detector volume by about 15 %, the background level can be reduced by about 60 %. With more restrictive cuts and advanced pulseshape analysis, as proposed by Matthew Fritts, the background level and also the sensitivity can even be improved further.

3.2. Requirements of an Analysis Method

3.2.1. General Considerations

To obtain an estimate $\widehat{\theta}(\mathbf{x})$ of a physical parameter θ and an estimate for an interval $\theta_1 \leq \theta \leq \theta_2$ for this parameter from measured values $\mathbf{x}$, mainly two approaches are used. They are commonly known as the frequentist (or often also called classical) and the Bayesian approach [Jam81, Ber12]. Even though the obtained results are often similar, the underlying concepts differ fundamentally.

In the frequentist approach the point of view is taken that analysed data derive from (infinitely often) repeatable experiments. The underlying physical parameters of interest are unknown, but constant. On the other hand, the observed data samples differ from realisation to realisation of the experiment and thus are treated as random samples. The data, and therefore also the reported value $\widehat{\theta}(\mathbf{x})$, is dependent on the unknown, but fixed parameter θ. Probability distributions can only be defined for the random variables, i.e. for the measured values as $f(\mathbf{x}|\theta)$ and for the estimated results as $f(\widehat{\theta}(\mathbf{x})|\theta)$. In this context the concept of a *confidence interval* is used to give an estimate for the precision of the method. For a certain CL of β, the confidence interval is defined in such a way that the calculated confidence interval $[\theta_1, \theta_2]$ for the outcome of an experiment contains the true value θ for a fraction β of all experiments (i.e. the outcome of an experiment

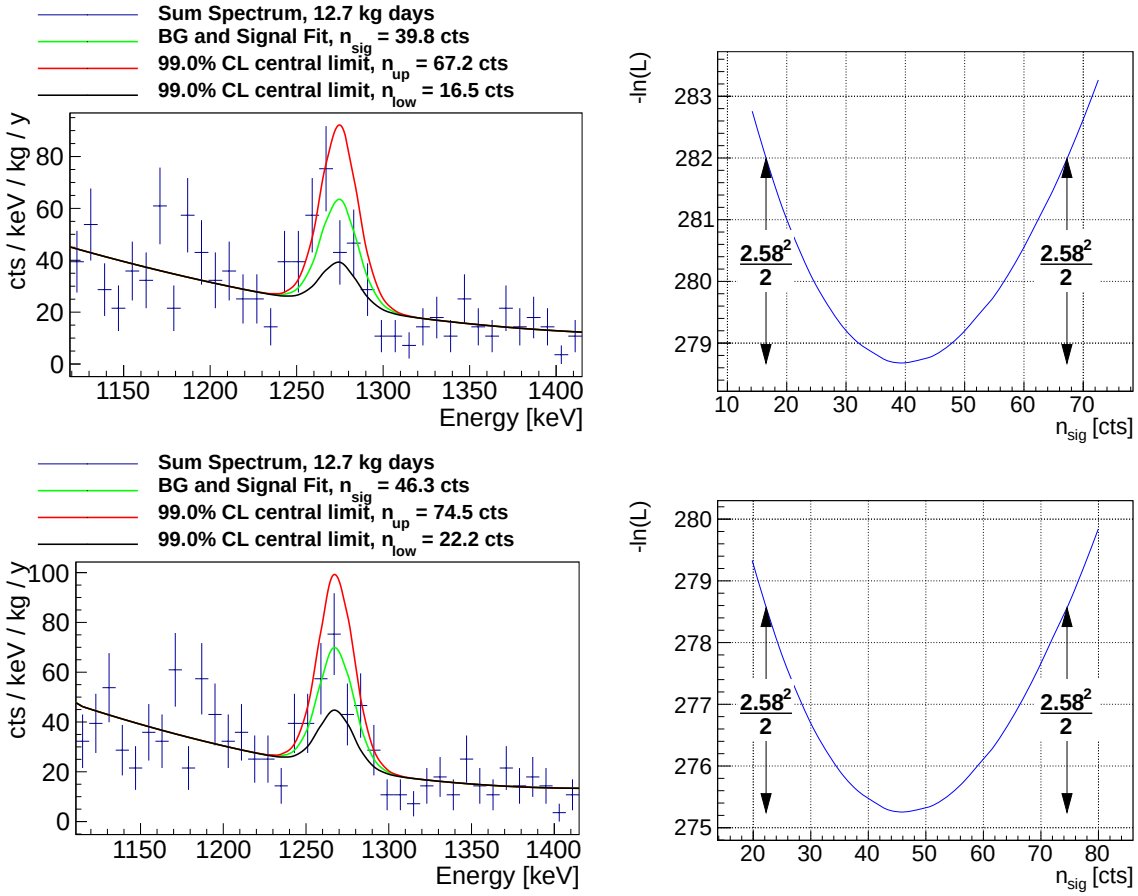

Figure 3.15.: Fit to the 1275 keV line with the extended likelihood method described in Section 3.3. As the line seems to be slightly shifted to smaller energies the fit was repeated with a shift of 0.5 % to the right (at 1268 keV), see bottom plot. Both fit results are consistent with $n_{sig} > 0$ with a CL $> 99\,\%$ ($k_\alpha = 2.58$).

can be repeated with a certain *frequency*):

$$\beta = P\left(\theta_1 \leq \widehat{\theta} \leq \theta_2 | \theta\right) = \int_{\theta_1}^{\theta_2} f(\widehat{\theta}'|\theta)\,\mathrm{d}\,\widehat{\theta}' \tag{3.4}$$

If the fraction of experiments that contain the true θ in the estimated interval really equals β, the method is said to have a good *coverage*. If θ is contained less frequently than β the method suffers from so called undercoverage, if it is contained more frequently it has an overcoverage. Often overcoverage is regarded to be 'conservative' and is accepted rather willingly than undercoverage, but in general it should be aimed for an estimator with neither (or only slight) over- and undercoverage.

In [Fel98] a method to construct such confidence intervals, the so called unified approach to the classical statistical analysis of small signals, was introduced. There an

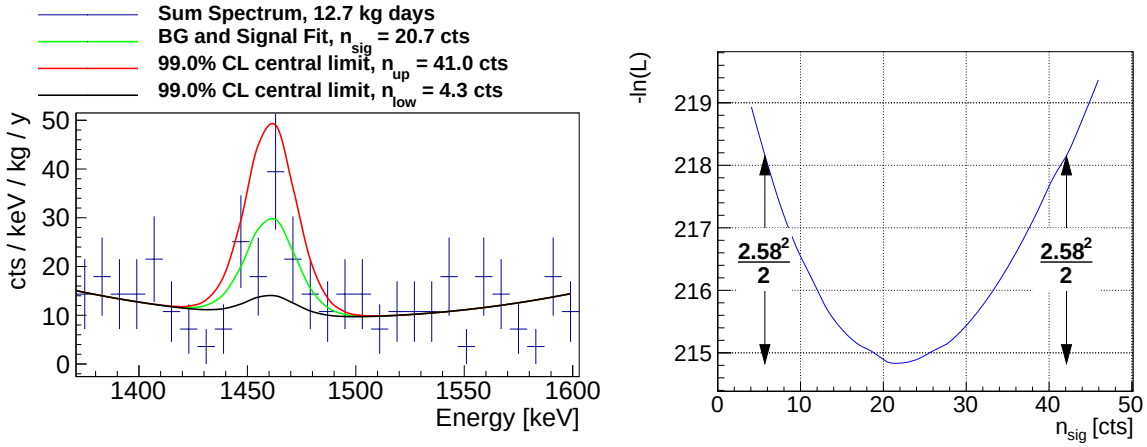

Figure 3.16.: Fit to ^{40}K line at 1460.8 keV with the extended likelihood method described in Section 3.3. The fit result is consistent with $n_{sig} > 0$ with a CL $> 99\,\%$ ($k_\alpha = 2.58$).

example for a Poisson distributed signal and known background is shown. This method even automatically switches from an upper limit (i.e. no signal was observed) to a central CL limit. This method therefore is suitable for classical counting experiments with known background. However, additional information like the shape of the signal and the background distribution in a measured energy spectrum is not taken into account. This is very valuable information that can increase the sensitivity significantly. Hence, this method is not optimal for experiments that have access to such additional information.

In the Bayesian approach the point of view concerning measured data and physical parameters is inverted. Here, the physics parameter θ itself is treated as a random variable and the decision is made on the basis of the *degree of belief* $p(\theta|\mathbf{x})$ in the true value θ for the measured result $\mathbf{x}$. It is derived from Bayes' Theorem and is given as the PDF (often also called *posterior PDF*)

$$p(\theta|\mathbf{x}) = \frac{\mathcal{L}(\mathbf{x}|\theta)\, p(\theta)}{P(\mathbf{x})}\,. \tag{3.5}$$

Here $\mathcal{L}(\mathbf{x}|\theta)$ is the joint PDF for the observed data given a certain value of θ, the so called likelihood function (see also below). $p(\theta)$ is the so called prior PDF and $P(\mathbf{x}) = \int \mathcal{L}(\mathbf{x}|\theta')\, p(\theta')\, \mathrm{d}\,\theta'$ is just a constant to normalise $p(\theta|\mathbf{x})$ to unity. The prior $p(\theta)$ represents all (subjective) belief on θ before the measurement is carried out. There are no general rules how to obtain $p(\theta)$. It is usually chosen on the basis of experience (e.g. previous experiments), to avoid an unphysical parameter region (e.g. negative mass values) or even 'researcher intuition'. The outcome of an analysis can differ strongly depending on the choice of the prior. The prior therefore is one of the main points of criticism from non-Bayesians.

The value $\widehat{\theta}$ for which $p(\theta|\mathbf{x})$ takes on its maximum value is taken as (point) estimate for θ. For this point a so called Bayesian or *credible interval* $[\theta_1, \theta_2]$ is constructed so

that it contains the true parameter θ with a probability of β:

$$\beta = \int_{\theta_1}^{\theta_2} p(\theta|\mathbf{x})\,\mathrm{d}\,\theta\,. \tag{3.6}$$

Due to the choice of the prior, these intervals can differ significantly from the frequentist confidence intervals determined from Equation (3.4), and their numerical calculation can be computationally extensive. Since the computational power increased significantly, also the interest in Bayesian analysis has increased during the last years and today several Bayesian analysis tools exist, e.g. the Bayesian Analysis Tool (BAT) [Bea11, Cal09].

Whether the frequentist or the Bayesian method is the better statistical choice was often discussed passionately. A comparison and some remarks can be found in [Cou95].

The frequently, or maybe even most commonly, used method of Maximum Likelihood (ML) is often regarded to have certain properties of both approaches.[2] It is described in most statistic textbooks in detail, e.g [Cow98, Cas02, Jam08], so here the general idea will be explained only briefly. For measured statistically independent values $\mathbf{x} = (x_1, \ldots, x_N)$ with PDF $f(x_i, \theta)$ the joint PDF

$$\mathcal{L}(\mathbf{x}|\theta) = \prod_{i=1}^{N} f(x_i, \theta) \tag{3.7}$$

is called likelihood function. The estimator $\widehat{\theta}$ is the value of θ that maximises $\mathcal{L}(\mathbf{x}|\theta)$. For numerical reasons usually the negative log likelihood function

$$-\ln \mathcal{L}(\mathbf{x}|\theta) = -\sum_{i=1}^{N} \ln(f(x_i, \theta)) \tag{3.8}$$

is evaluated because a sum can be calculated easier than a product and most computer programs are designed to find a minimum of a function, and not a maximum. The maximum of $\mathcal{L}(\mathbf{x}|\theta)$ and the minimum of $-\ln \mathcal{L}(\mathbf{x}|\theta)$ are equivalent because the logarithm is a monotonically increasing function. The global extremum of the function can either be found by differentiating and solving

$$\frac{\partial\, \mathcal{L}(\mathbf{x}|\theta)}{\partial\, \theta} = 0 \qquad \text{or} \qquad -\frac{\partial\, \ln \mathcal{L}(\mathbf{x}|\theta)}{\partial\, \theta} = 0 \tag{3.9}$$

or by finding the extremum numerically, e.g. with the minimisation program MINUIT [Jam75]. To obtain information on the uncertainties of a likelihood fit also two methods exist [Jam81, Ber12]. The first is to obtain the covariance matrix V by inverting the second derivative matrix of the log-likelihood function at its maximum $\widehat{\theta}$

$$\left(\widehat{V}^{-1}\right)_{ij} = -\frac{\partial^2 \ln \mathcal{L}}{\partial\, \theta_i\, \partial\, \theta_j}\bigg|_{\widehat{\theta}} \qquad . \tag{3.10}$$

[2] The statistician G. Casella once referred to 'Likelihoodists' as 'Bayesians - but they don't know it', `www.stat.ufl.edu/~casella/Talks/BayesRefresher.pdf`

For a parabolically shaped likelihood function this method is suitable. The second method is sometimes referred to as the method of MINOS, because the MINUIT routine that is called for the error estimation has this name. In this method the limits of a certain confidence interval are obtained directly from the contour of the log likelihood function. The equivalent limits to k_α Gaussian standard deviations (k_α is often also referred to as the Gaussian quantile or the coverage factor, see also Appendix D) can be obtained by determining the points θ' where the log likelihood function increased by

$$-\ln \mathcal{L}(\theta') = -\ln \mathcal{L}_{\min} + \frac{{k_\alpha}^2}{2} \tag{3.11}$$

from its minimum value. This method was originally proposed by CERN staff in the 1960s, but nowadays it is also applied by statisticians, e.g. in the profile likelihood method [Rol01, Rol05]. In the case of central confidence intervals the obtained limits will in general be asymmetric. Even though the intervals often have a good coverage in the classical sense, a good coverage is not guaranteed and should be checked for the problem at hand.

To judge an estimator $\hat{\theta}$ mainly four properties should be revised. Desirable in an estimator is that it is consistent, unbiased, efficient and robust. Consistency means that the estimate $\widehat{\theta}$ should converge to the true value of θ as the amount of available data increases:

$$\lim_{n\to\infty} \widehat{\theta} = \theta\,. \tag{3.12}$$

It can be shown that this is true for ML estimators in general [Blo98, Jam08]. The bias of the estimator is defined as the difference between the expectation value of the estimator and the true value θ of the parameter [Cas02]

$$b_{\hat{\theta}} = E(\hat{\theta}) - \theta\,. \tag{3.13}$$

The bias can be regarded as a measure of accuracy of an estimator and $b_{\hat{\theta}} = 0$ is desired. The consistency of the ML estimator implies that it is at least asymptotically unbiased. For low statistics it has to be checked carefully whether the estimator is unbiased. This can be seen from the certainly most famous examples of ML estimators with a small bias, namely the ML estimator of the variance σ^2 of a Gaussian distributed random variable

$$\widehat{\sigma^2} = \frac{1}{n}\sum_{i=1}^{n}(x_i - \widehat{\mu})^2 \quad , \quad E\left[\widehat{\sigma^2}\right] = \frac{n-1}{n}\sigma^2 \neq \sigma^2 \tag{3.14}$$

and the ML estimator for the decay time τ and the decay constant $\lambda = 1/\tau$ of an exponential distribution:

$$f(t,\tau) = \tfrac{1}{\tau}\,\mathrm{e}^{-t/\tau}\,, \quad \widehat{\tau} = \tfrac{1}{n}\sum_{i=1}^{n} t_i\,, \quad E\left[\widehat{\tau}(t_1,\ldots,t_n)\right] = \tau \tag{3.15}$$

$$\text{but} \quad f(t,\lambda) = \lambda\,\mathrm{e}^{-t\,\cdot\,\lambda}\,, \quad \widehat{\lambda} = \tfrac{1}{\widehat{\tau}}\,, \quad E\left[\widehat{\lambda}\right] = \lambda\tfrac{n}{n-1} \neq \lambda \tag{3.16}$$

see e.g. [Cow98] for details. Therefore an estimator has to be tested for a bias either analytically or with MC simulations. Even though ideally an estimator should be unbiased, sometimes a small bias can be acceptable if other advantages like numerical stability or a small variance of the estimator are regarded to be very beneficial. Nevertheless the magnitude of the bias has to be determined to estimate the trustworthiness of the method.

An estimator is called efficient if its variance is as small as possible. With the Cramér-Rao lower bound it can be shown that under very general conditions the ML estimator is at least asymptotically efficient [Blo98, Jam08].

Sometimes the PDF of a parameter or of the measured data in general is not exactly known. If deviations in the data and the assumed PDF have only little influence on the resulting estimate, an estimator is called robust.

Usually not all of these requirements can be completely satisfied. For example ML estimators have a good variance, but if the assumed PDF is not correct, the obtained result can differ strongly from the true value, i.e. especially efficiency and robustness are often contradictory.

Besides the choice of the statistical analysis philosophy another often discussed issue is the treatment of parameters near unphysical boundaries. For example the neutrino mass or the count rate of a decay are known to be positive (or zero). In the Bayessian approach this information can be added in the prior $p(\theta)$, and it is also possible to artificially introduce such a boundary in the likelihood function of the ML estimator. Minimization programs such as MINUIT also contain options to restrict the range of the fitted variables. The drawback of these methods is that it is usually not possible to construct an unbiased estimator with such a restricted parameter range if the true value θ is close to a boundary. If the true value, e.g. the count rate, is zero, an unbiased estimator has to result in negative estimates half of the time. If due to the aforementioned restrictions only positive results are calculated, the true value $\theta = 0$ can never be obtained by combining the results of several experiments. Therefore here the point of view described in [Jam91] is taken. There it is proposed to apply an unbiased method and to publish the obtained result of the experiment (and not only calculated limits), even if it is in the unphysical region.

For the search for $0\nu\beta\beta$-decay in COBRA data special requirements arise. The set-up consists of many detectors. These detectors differ in properties like energy resolution and live time. The energy resolution can also vary over time. The estimator therefore has to be able to combine the data of many single measurements.

3.2.2. Former Binned Likelihood Approach

For the data collected before the background reduction by about an order of magnitude, which was achieved by constant nitrogen flushing and replacement of a red detector passivation lacquer, a binned ML approach was applied for the determination of $0\nu\beta\beta$-decay limits [Blo07, Daw09b]. Its properties, advantages and disadvantages will be

explained shortly in the following. For each detector and each measurement period a histogram for the observed counts is generated. For the fit the bin content of each histogram bin is regarded as a random variable following the Poisson distribution

$$f(n_i|\mu) = \frac{\mu^{n_i}}{n_i!}\,\mathrm{e}^{-\mu}\,. \tag{3.17}$$

n_i is the number of observed events in bin i and $\mu = \mu_{sig} + \mu_{bg}$ is the expected value of the sum of background and signal events (signal and background strength). As each measured bin content of a detector histogram and each measurement period can be regarded as independent, the resulting likelihood function is the product of the PDFs (3.17) for a single bin (compare Equation (3.7)). μ itself has an energy (bin) dependence following the expected signal and background distribution, that is, a Gaussian shaped signal at the Q-value of the decay and an exponentially decreasing background. Alternatively also a signal distribution in the form of a histogram, e.g. a simulated $0\nu\beta^+\beta^+$ spectrum, can be applied. The log likelihood function (omitting μ independent summands) is

$$\ln\mathcal{L} = \sum_{\text{Period}}\sum_{\text{Det}}\sum_{\text{Bin}} \left(n_{\text{Bin}}\,\ln(\mu_{\text{Bin}}) - \mu_{\text{Bin}}\right)\,. \tag{3.18}$$

The signal rate is the same for all detectors, but the background rate can vary for each detector. For the background estimation a function

$$f_{BG}(E) = p_7 \cdot \left(p_0 + p_1 \cdot \mathrm{e}^{-p_2\,E} + p_3 \cdot \mathrm{e}^{-p_4\,E} + \frac{p_5}{p_6\,\sqrt{2\,\pi}} \cdot \mathrm{e}^{-\frac{(E-E_{peak})^2}{2\,{p_6}^2}} \right) \tag{3.19}$$

containing two exponentials, one to describe the spectrum at higher energies and one for the lower energies, and a constant term together with known γ-peaks is fitted to the sum spectrum of all detectors. In a first step, parameters describing the composition of these background events (in total five to seven parameters) are fitted to the experimental data in a wide energy range of 400 keV to 3200 keV. Afterwards these parameters are fixed for the $0\nu\beta\beta$-decay fit, but a further parameter, p_7, which is used to scale the overall background level for each detector individually, is varied in the final fit for the $0\nu\beta\beta$-decay signal.

The method fulfils many of the desired requirements. Different energy resolutions and also energy resolutions that vary over time can be taken into account. The binning of the data is useful for a comparatively high background level. If the number of data points is high, the calculation of an unbinned likelihood function is computationally extensive and can become numerically unstable. Histogramming of the data reduces the amount of summands that have to be calculated in the likelihood function.

On the other hand the histogramming also means a loss of available information. For a small amount of data the outcome of the fit becomes also strongly dependent on the chosen bin width. For the already achieved background level of 5 cts/keV/kg/y, histogramming of the data can even be counterproductive regarding the reduction of

summands in the likelihood function. With this background rate an average of only 17 cts/detector/y in a region of 2.5 MeV to 3.1 MeV are expected. For a measurement period of three months this will be only about four events per detector. So even for such a wide energy interval most of the histogram bins will be empty and there will be more histogram bins than data points. For a background level of 1 ct/keV/kg/y, which is achievable with new sophisticated pulse-shape analysis methods for the planned 64 detector array, the amount of data will even be lower and most histograms will be completely empty.

The idea to allow for an individual background level for each detector is in general good. But here again the limited amount of information has to be taken into account. A fit with many parameters becomes highly unreliable for a small amount of data. Even if the parameters for the background shape are fixed during the final fit and only the relative height of the background is varied, a total number of 65 parameters has to be fitted for the whole 64 detector array. This is already in the order of the total number of data points for the background level of 1 cts/keV/kg/y.

A further aspect is the robustness of the estimator. In general the background can be described well with the two exponential functions. But there is no verified model for the current background composition. Deviations from the assumed exponential behaviour of the background distribution can distort the result of a fit and lead to large discrepancies in the actual ROI. This holds especially for the treatment of the background in the former binned likelihood approach. In order to gather enough data, the background is fitted in a wide energy range. This range is much wider than the range that is used for the actual fit for the $0\nu\beta\beta$-signal. As the amount of data is higher at lower energies due to the higher background, the influence of this data will be higher than for the higher energetic data that is closer to the actual ROI. Currently unknown or uncertain background, for example the only recently explored ^{190}Pt decay that is very close to the ROI at 2.8 MeV, could be suppressed in the background fit from data at much lower energies.

3.3. Extended Maximum Likelihood

For the reasons illustrated in Subsection 3.2.2 a new fit approach for the $0\nu\beta\beta$-decay search in COBRA data has to be found. The method has to combine the data of all detectors in a meaningful way, i.e. it has to take the different energy resolutions of the detectors into account. Modelling an own background level for each detector is in principle regarded to be desirable, but is not feasible with the low data for a single detector.

The two most promising candidates for a fit method are the Bayesian approach and the method of maximum likelihood. From the authors point of view, the method of maximum likelihood is preferred. Bayesian analysis is a very powerful tool. But the subjective choice of a prior, even though it often is regarded as virtue, also brings the risk

of a strong bias. Furthermore, the concept of coverage of a classical confidence interval is regarded to be a good measure for the reliability of an estimator. Therefore, the method of extended maximum likelihood was evaluated as candidate for the replacement of the binned likelihood method.

3.3.1. General Idea of the Extended Maximum Likelihood Method

Advantageous of the binned likelihood approach is that it makes use of the information obtained from the shape of the measured spectrum, as well as the Poissonian nature of nuclear decays by modelling each bin as a Poissonian random variable. In the common form of Equation (3.7) of the likelihood function usually only the shape of the measured spectrum is used. If both the information from the Poisson nature of the decay as well as the shape of the spectrum can be exploited, a smaller variance and thus a more efficient estimator is expected.

Furthermore the proper implementation as Poissonian random variables is very important for a good coverage. The main variable of interest is in fact not the realisation n_{sig} of signal events in the actual data sample, but the expected value μ_{sig} of the distribution of signal events. The Poissonian variation of n_{sig} as realisation of μ_{true} therefore has to be taken into account to achieve a good coverage for the confidence interval of $\mu_{\mathrm{sig}}^{\mathrm{fit}}$. Of course for the point estimate, i.e. the estimate of signal events, the number of fitted signal events and the expected value of the distribution are identical: $n_{\mathrm{sig}}^{\mathrm{fit}} = \mu_{\mathrm{sig}}^{\mathrm{fit}}$. Therefore in the following both notations will be used synonymously, but it should be kept in mind that the actual estimate and its confidence interval are calculated for μ_{sig}.

The difference between the confidence intervals for $n_{\mathrm{sig}}^{\mathrm{fit}}$ and $\mu_{\mathrm{sig}}^{\mathrm{fit}}$ can be seen from an example. Let us assume a realisation of $n_{\mathrm{sig}} = 6$ events in a data sample (measurement) for the true expected value $\mu_{\mathrm{sig}} = 10$ events. Good estimators will yield $n_{\mathrm{sig}}^{\mathrm{fit}} = \mu_{\mathrm{sig}}^{\mathrm{fit}} = 6$ counts as point estimate. Concerning the confidence interval two questions can be asked. First: How many signal events are truly contained in this measured data set? Second: If six events were measured in this particular data set, what can we assume for the true expected value μ_{sig}? The answers to both questions will clearly be different. In our case we have to ask the second question.

In the extended likelihood approach [Cow98] the Poisson distribution (3.17) of the number n of measured events is taken into account by multiplying the likelihood function of the background PDF with the Poisson probability to observe n events

$$\mathcal{L}(\mathbf{x}|\mu, \boldsymbol{\theta}) = \frac{\mu^n}{n!}\,\mathrm{e}^{-\mu} \prod_{i=1}^{n} f(x_i|\boldsymbol{\theta})\,. \tag{3.20}$$

$\boldsymbol{\theta} = (\theta_1, \ldots, \theta_k)$ are the parameters of the model for the measured spectrum, i.e. for example the mean and variance of a Gaussian signal and parameters to describe the background.

In our case the total number of observed events n consists of n_s signal and n_b background events, and the expected value for n therefore is $\mu = \mu_s + \mu_b$. If the energy

dependent PDF of the signal events is $f_s(x|\boldsymbol{\theta})$ and $f_b(x|\boldsymbol{\theta})$ for the background then the PDF for the sum of signal and background is

$$f(\mathbf{x}|\mu,\boldsymbol{\theta}) = \frac{\mu_s}{\mu_s+\mu_b}\, f_s(\mathbf{x}|\boldsymbol{\theta}) + \frac{\mu_b}{\mu_s+\mu_b}\, f_b(\mathbf{x}|\boldsymbol{\theta}), \quad \text{with} \quad \int f(\mathbf{x}|\boldsymbol{\theta})\,\mathrm{d}\,x = 1\,. \tag{3.21}$$

Combining Equation (3.20) and Equation (3.21) gives the final negative log-likelihood function (omitting parameters independent from μ and $\boldsymbol{\theta}$)

$$-\ln\mathcal{L}(\mathbf{x}|\mu,\boldsymbol{\theta}) = (\mu_s+\mu_b) - \sum_{i=1}^{n} \ln\left(\mu_s\, f_s(x_i|\boldsymbol{\theta}) + \mu_b\, f_b(x_i|\boldsymbol{\theta})\right)\,. \tag{3.22}$$

Here, the full information of each event is preserved and the data of all detectors is naturally combined to equal one homogeneous detector set-up.

3.3.2. Implementation and Consistency Tests

For semiconductor detectors the distribution of (monoenergetic) signal events has a Gaussian shape. It is implemented with a normal distribution

$$f_s(x_i|E_0,\sigma^2) = \mathcal{N}(E_0,\sigma^2) = \frac{1}{\sigma\sqrt{2\,\pi}}\mathrm{e}^{-\frac{(x_i-E_0)^2}{2\,\sigma^2}}\,. \tag{3.23}$$

The mean of the Gaussian distribution and its variance are not taken as free parameters in the fit. E_0 is given as the Q-value of the $0\nu\beta\beta$-decay and σ is determined from calibration data. The PDFs of the likelihood function have to be normalised to unity in the fit range. In the actual implementation the signal distribution is therefore normalised to unity for the energy interval of the fit to match $\int_{x_1}^{x_2} f_s(x|E_0,\sigma^2)\,\mathrm{d}\,x = 1$.

The modelling of the background distribution is more difficult. Often a sum of an exponentially decreasing background and a constant term is assumed. In this case, the expected value for the background strength has to be split to $\mu_b = \mu_{b_1} + \mu_{b_2}$. The normalisation of the exponential background PDF

$$f_{b_1}(x|\tau) = c_1\mathrm{e}^{-\frac{x}{\tau}}\,, \quad c_1 = \frac{1}{\tau\left(\mathrm{e}^{-\frac{x_1}{\tau}} - \mathrm{e}^{-\frac{x_2}{\tau}}\right)} \tag{3.24}$$

is dependent on the background fit parameter τ itself. In the implementation of the likelihood fit this normalisation has to be recalculated for every variation in τ. A fit of this background model to LNGS data taken with the first four colourless detectors and the Cyclotene passivated detectors [Sch09] is shown in Figure 3.17. Due to the features in the background discussed in Section 3.1, a fit range of 1.5 MeV to 3.0 MeV was taken. The result of the fit is strongly dependent on the fit range. Especially the parameters of the exponential part have large uncertainties.

These are hints that the background cannot be precisely described with this model. The exponential dependence can also lead to numerical instabilities. Furthermore, a

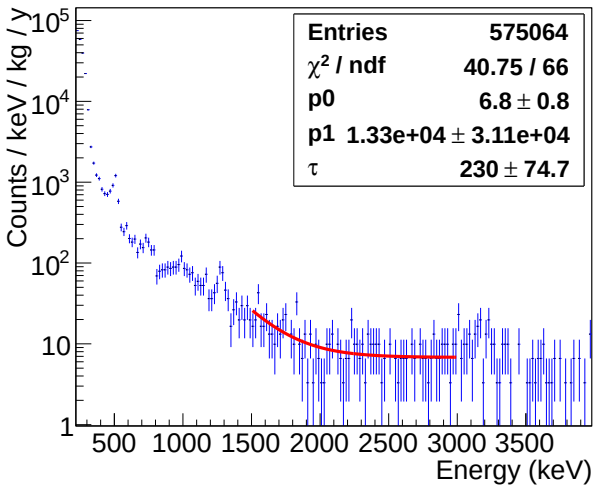

Figure 3.17: Fit of $f(E) = p_0 + p_1 \cdot e^{-\frac{E}{\tau}}$ to LNGS data taken with the first four colourless and Cyclotene passivated detectors to determine input parameters for MC data samples. The features mentioned in Section 3.1 (^{190}Pt, the 511 keV and the 1275 keV γ-line) are also clearly visible in this spectrum. The ^{190}Pt decay at the cathode leads to an increasing background level above 3 MeV. The fit to the background was performed in an energy range of 1.5 MeV to 3 MeV. The fit results for the exponential function strongly depend on the fit ranges.

wide fit range and therefore also data far away from the actual ROI has to be used to have a good estimate for its parameters. As already stated in Subsection 3.2.2 this can lead to an inappropriate background description in the ROI.

On the other hand, the slope of the background spectrum is small for wide energy ranges. That means that for a smaller fit range also a polynomial can be appropriate to describe the background. The usage of a polynomial can also be seen as an approximation of the background by expanding the true background function to a Taylor series. The remainder term of a Taylor series is smaller for smaller derivatives of the function at the point of expansion. This makes this approach especially suitable for a smooth background. Therefore also a likelihood function with a linear or a quadratic function describing the background was implemented. The choice of the order of the polynomial has to be taken on the basis of the background shape in the ROI. The quadratic approximation should in principle give a better background approximation but can also lead to a larger variance of the estimator and even numerical instabilities due to the higher order of the parameter space. The shape of the background in the main ROI at 2.8 MeV is comparatively flat (see Figure 3.19 and Figure 3.17) and can certainly be described with a linear approximation in a fit range that is not too wide.

For the minimisation of the negative log likelihood function the MINUIT [Jam75, Jam04] package, which is included in the ROOT framework as the C++ Minuit2 libraries, is used. The minimisation in a multidimensional parameter space is always difficult, and it is prone to numerical instabilities. The MINUIT package is known to have good minimisation algorithms that can help to avoid these instabilities and is therefore widely used.

For the error estimation according to Equation (3.11) the MINUIT method MINOS is applied. In this method the parameter uncertainty, in the implemented case a 90 % CL upper limit for the number n_{sig} of signal events with $k_\alpha = 1.282$, are obtained by scanning the shape of $-\ln \mathcal{L}$. The procedure is to vary the parameter n_{sig}, then fix it and minimise $-\ln \mathcal{L}$ with respect to all other parameters. This is repeated until the Relation

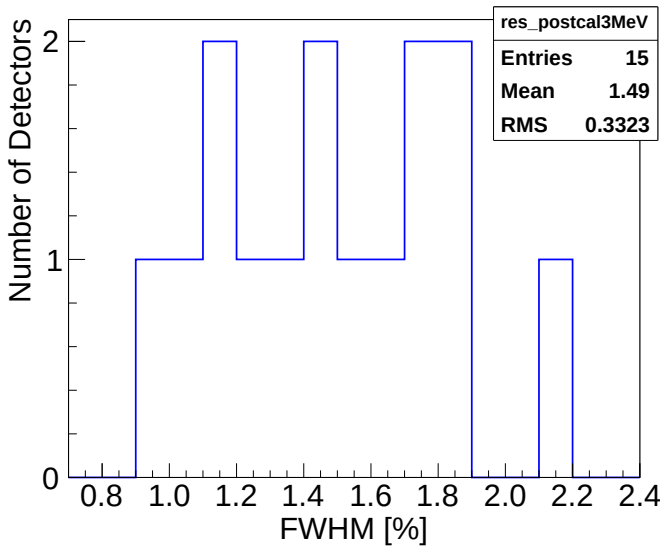

Figure 3.18: Distribution of detector resolutions of the first 16 colourless detector layer at 2.8 MeV. The resolution was interpolated from ^{22}Na and ^{228}Th calibration data. 15 of the 16 installed detectors were operational. The resolution information of these detectors were taken as input for the generated MC data samples for the ML estimator validation. The resolution of the new detectors is good, but it differs by up to a factor of two between the individual detectors. This has to be taken into account in the analysis method of the data.

(3.11) is fulfilled and the resulting n_{sig} is taken as boundary for the uncertainty interval. With this procedure parameter correlations and non-linearities are treated properly by MINOS.

Random data samples were generated to evaluate the estimator. Parameters for the background shape were taken from the fit to the LNGS background. The τ parameter for the exponential decrease was fixed to the fitted value, but the signal and background strength was treated as a Poisson variable. 10,000 data samples each for a background level of $bg = [1, 2, 5, 10]$ cts/keV/kg/y in the region of 1.5 MeV up to 3.0 MeV and $\mu_s = [0, 1, 5, 10]$ signal events at an energy of 2.8 MeV were generated. Values for the resolution of the detectors and their spread were taken from LNGS calibration data of the first 16 colourless detector layer, see Figure 3.18. The main focus lies on the behaviour of the method for small statistics. Therefore data samples equivalent to one year of data taking with the 64 detector array were generated. The data samples with $bg = 1$ cts/keV/kg/y for the 1.5 MeV to 3.0 MeV region are comparable to half a year of data taken with the current 16 detector layer with a background level of about 5 cts/keV/kg/y in a region of 2.7 MeV to 2.9 MeV.

The ML fit was performed for all data samples. It was noticed that the fit with the exponentially decreasing background is numerically more unstable than the polynomial background fits. It needs a higher amount of data and good start parameters to converge. For the tests of this algorithm a fit range of 1.5 MeV to 3.0 MeV and a range of 2.0 MeV to 3.0 MeV was chosen.

For the algorithm with the interpolating polynomial background a trade-off has to be made in the choice of the fit range. A wider fit interval has more data points and therefore less statistical uncertainty. To have enough data for the background and the signal determination a fit range equivalent to at least $\pm 6\sigma$ of the detector resolution should be taken. For an energy resolution of 2 % FWHM at 2.8 MeV this is equivalent

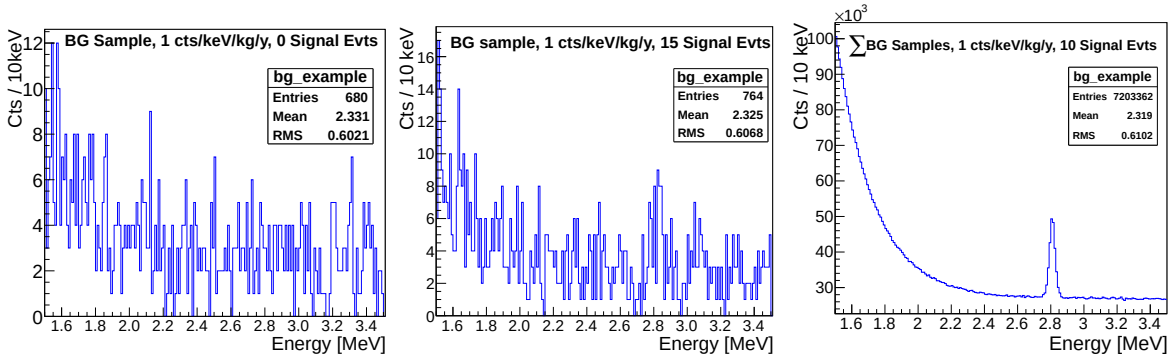

Figure 3.19.: Examples of generated MC data for one year of data taking with one detector layer and a background level of 1 cts/keV/kg/y. Here the problem of low statistics becomes obvious. Although a signal strength of 10 cts/y is clearly visible in the large data sample on the right (here all of the 10,000 created data samples were combined) even a comparatively strong signal of 15 events nearly vanishes in the background fluctuation (middle). The spectra with no signal (left) and the strong signal are hardly distinguishable with the naked eye. It should also be noted that the spectra are composed from the data of 16 detectors with different energy resolution (compare Figure 3.18). Therefore, a straight fit to the plotted histograms is not possible, but the data of each detector has to be treated separately. This can be achieved with the unbinned extended ML approach.

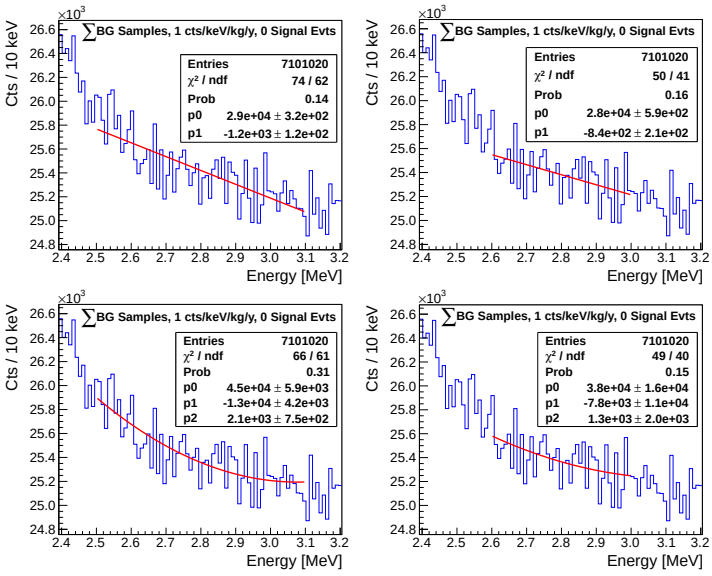

Figure 3.20: Fits of polynomial background to MC data sample in the ROI around 2.8 MeV. A linear (top row) and quadratic (bottom row) function was fitted to a sum spectrum of all 10,000 MC data samples for 1 cts/keV/kg/y. For a fit region of $2.5 - 3.1$ MeV (left plots) the quadratic approximation fits much better than the linear one. The best χ^2/ndf ratio is achieved with the quadratic background approximation in a fit range of $2.5 - 3.1$ MeV.

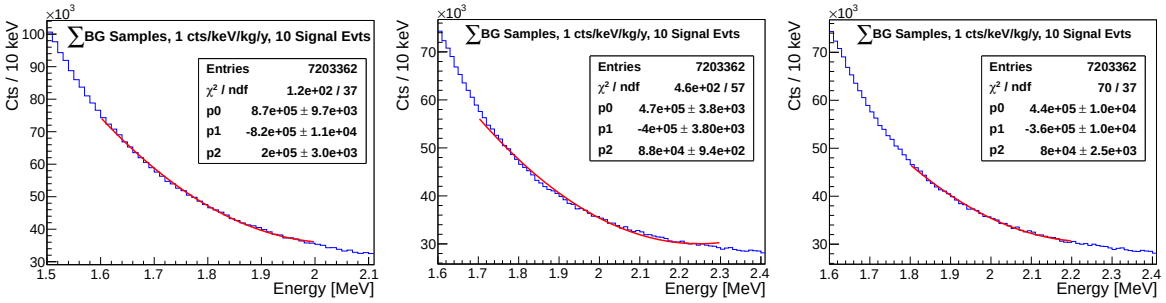

Figure 3.21.: Fit of quadratic background approximation to lower energetic background region. The slope of the spectrum is higher for these energies than at 2.8 MeV. The quadratic approximation is no longer sufficient to describe the background well in a wider fit range (middle). For a smaller fit range the approximation is better (right). As expected from the remainder of a Taylor series the divergence becomes stronger with higher slope (compare χ^2/ndf of left and right plot).

to about 150 keV. On the other hand the quadratic approximation is less precise for wide energy ranges, especially for a higher slope in the background shape. The choice of appropriate fit intervals was taken on the basis of tests with the 1 cts/keV/kg/y data sample with zero signal events, see Figure 3.20 and Figure 3.21. As minimal fit range an interval of ±200 keV and an additional interval of ±300 keV were chosen for the fit in the ROI. For these fit ranges the approximation to the MC background is still acceptable. For lower energies the fit range should be chosen smaller or the exponential background approximation should be taken. With a fit range of ±200 keV the fit with quadratic background approximation yields still good results for fits at 2.0 MeV and 1.8 MeV, see Figure G.7, Appendix G. In general a smaller fit range can be chosen for lower energies because the absolute energy resolution is also smaller and the number of events is higher.

Detailed results of the tests are listed in Appendix F and plotted in Appendix G. An example of the most important parameters for the fit with quadratic background approximation for the data sets with $\mu_{\text{true}} = 5$ cts and a background level of 1 cts/keV/kg/y is shown in Figure 3.23. The fits with the linear background approximation tend to a small negative bias. The bias is larger for the wider fit range of 2.5 MeV to 3.1 MeV. This can be explained with the exponential shape of the generated background. In the wider fit range the background in the centre of the fit interval is systematically below the fitted linear background, see Figure 3.22 for an extreme case in the lower energetic region. The method fills the missing background events up with signal events, what leads to the underestimation of the signal strength. This effect is smaller for a narrower fit range and a smaller slope of the exponentially decreasing background.

For the quadratic background approximation the estimator seems to have a small negative bias for low background rates, but for higher background rates the estimated signal strength seems to be slightly too high. However, the true signal strength is still contained in an interval of $\pm 2\sigma$ of the variance σ^2 of all 10,000 fit results for each set of

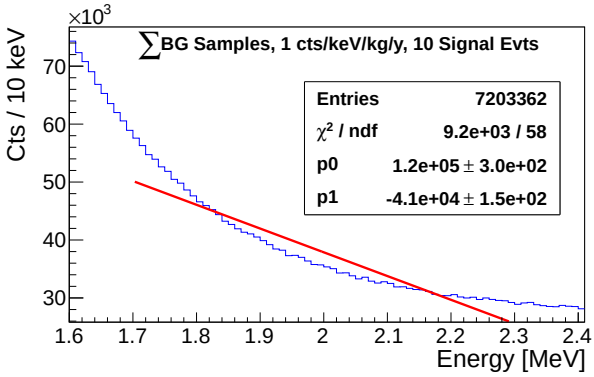

Figure 3.22: Fit of a linear BG to the lower energetic region of the generated data samples. The inappropriate fit interval was chosen to demonstrate the underestimation of the BG in the centre of the fit interval. In the ROI at about 2.8 MeV the disagreement is much lower, see Figure 3.20. The lack of events in the centre of the fit interval can lead to a systematic underestimation of the signal strength. The effect is much smaller for the quadratic BG approximation.

data samples.

The fits with the exponential background model tend to a small positive bias. The presence of this small bias, even though exactly the same spectral shape was fitted to the data that was used to produce the MC data samples, shows how important the consistency tests are. As can be seen from the example given in Section 3.2 even the fit of the decay constant to pure exponentially decreasing data is biased (note that in the implemented case not λ but τ was taken as parameter). Therefore a small bias in a much more complex model with additional constant background and Gaussian signal is not surprising.

However, the bias of all estimators is small compared to the variance of the determined signal. The worst bias to statistical spread ratio, which was determined to be $b/\sigma = 3.7\,\%$, is found for the linear background approximation with the wider fit range.

The variance of the fit methods with the linear and the exponential background function are nearly identical. The statistical spread of the fits with the quadratic background is about 10 % higher. For this background model the increase in the fit range yields a higher improvement in variance than for the other two. The reasons for the slightly higher variance are probably the additional parameter compared to the linear fit and the much smaller amount of data compared to the exponential background fits due to the smaller fit interval.

All three methods have a constantly good coverage. In general a small, still acceptable undercoverage of about 1 % is observed. For the commonly applied 90 % CL upper limits the worst determined true coverage was found to be $(87.9 \pm 0.9)\,\%$, it occurred in the fit with the quadratic background approximation in the smaller fit range. The $0\nu\beta\beta$-decay signal strength for the COBRA 64 detector array prototype is far below the achievable background level. Therefore, no observation but only upper limits are expected and the coverage is the most important property of the fit method to be sure that trustworthy limits are obtained. Note that the good coverage of the expected value $\mu^{\mathrm{sig}}_{\mathrm{true}}$ of the Poissonian distributed signal could only be achieved because the Poissonian distribution of the signal and the background strength is taken into account by the extended likelihood method.

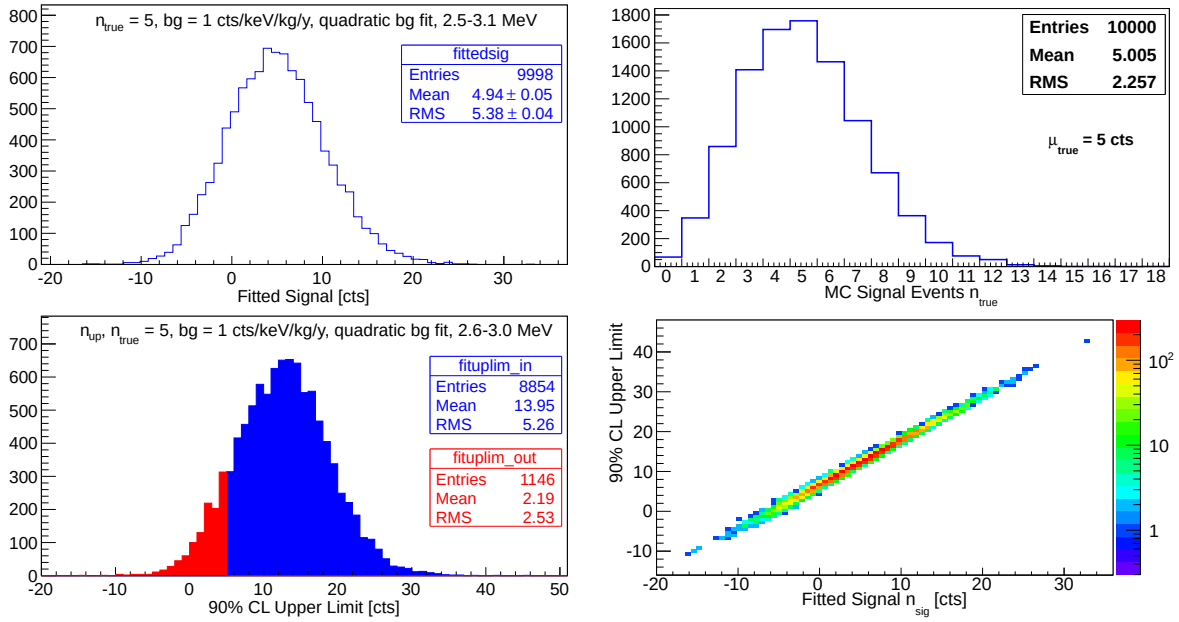

Figure 3.23.: Fit results for $\mu_{\text{sig}} = 5\,\text{cts}$ and a background level of $1\,\text{cts/keV/kg/yr}$. The upper left plot shows the distribution of the fitted number of signal events. The mean of the fitted signal events is consistent with the true value $\mu_{\text{true}} = 5\,\text{cts}$ of the MC data samples. In the upper right plot the Poisson distribution of the signal events in the MC data samples is plotted. The lower left plot shows the distribution of the determined 90 % CL upper limits. $(89.5 \pm 0.9)\%$ of the limits are higher than $\mu_{\text{true}} = 5\,\text{cts}$, this value is consistent with the desired CL of 90 %. The statistical spread of the upper limits is $(6.04 \pm 0.04)\,\text{cts}$. It is slightly higher than the statistical spread of the fitted signal events of $(5.38 \pm 0.04)\,\text{cts}$. On the lower right side the correlation between the number of fitted events and the determined upper limit is shown. From this plot, similar to the higher variance of the two distributions, it can be seen that even though a general linear correlation exists, the upper limit cannot be determined by simply adding a constant factor to the fitted signal.

From the point of reliability of convergence the linear background approximation has the best performance. All fits have converged with this algorithm. The exponential fit method also converged for all fits in the 1.5 MeV to 3.0 MeV fit region, but the fit failed in up to 3.5 % of all cases for the smaller fit region of 2.0 MeV to 3.0 MeV. The failure of this method for the smaller fit range has three causes. First, the statistics are lower. Second, the exponential dependence of the likelihood Equation (3.24) is in general more sensitive to fluctuations than the polynomial approach. Certainly the main reason is the smaller slope of the background in the higher energetic region. Above 2 MeV the generated spectra are dominated by the constant background contribution. This reduces the sensitivity to the decay constant τ. The method is also computational more extensive than for the polynomial approximation. For the consistency tests several hundred CPU hours of computational time were needed, about a factor of ten more than

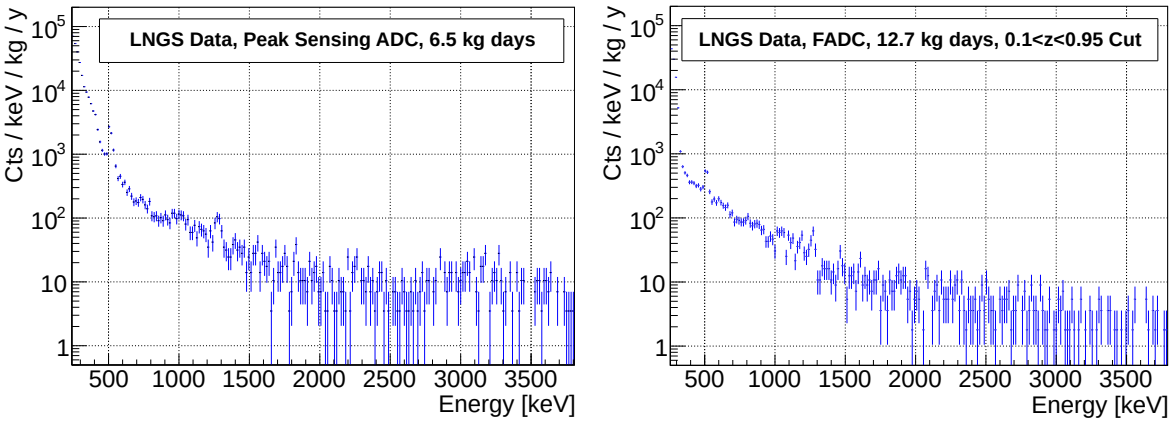

Figure 3.24.: Sum spectra of data taken with the old peak sensing ADC (left) and the new 16 detector layer with FADC readout (right). With the peak sensing ADC no interaction depth reconstruction was possible. Therefore, the BG at the cathode (see Section 3.1) cannot be discarded in this data and the BG level increases in the energy region of the ^{190}Pt decay. Both spectra show the same features at 0.51 MeV and 1.3 MeV (see also Section 3.1).

for the polynomial case. The quadratic background approximation has a good stability for both fit ranges. For most of the data sets all fits converged, the by far worst rate of failure was 0.3 %.

In summary it can be said that all fit algorithms have a good performance. The linear approximation should only be applied for a flat background and with a narrower fit range. The exponential fit is especially appropriate for lower energetic regions with more data and a higher slope, but it should only be applied if there is strong evidence for an exponentially decreasing shape of the background level. The quadratic background approximation has a slightly higher variance than the other two methods. But on the other hand it has the smallest bias and a good robustness. It is reliable for a background distribution with little and also with higher slope. Due to the smallest bias and the high robustness in the scope of this work it will be applied to LNGS data as the preferred method.

3.3.3. Results

$0\nu\beta\beta$ Limits for ^{116}Cd and ^{130}Te

Due to their heigh Q-values ^{116}Cd and ^{130}Te are the most promising $0\nu\beta\beta$-decay candidates in COBRA. Therefore these two decays are examined with the new extended likelihood approach. The fit method was applied to two data sets. The first data set was taken with the formerly used peak sensing ADC and up to eight detectors with colourless passivation (EIDIS clear passivation and Cyclotenen, see [Koe08, Sch09]). Most of these detectors had a far worse energy resolution than the recently installed 16 detector layer. Also neither the pulse shape nor interaction depth information is available. Therefore,

discarding background events at the cathode and also the unreliable small area directly below the anodes is not possible. This leads to an increasing background level in the energy region of the ^{190}Pt decay. To have a low background level only data with nitrogen flushing of the set-up is included in this data set. In total 6.5 kg days of data with nitrogen flushing were acquired.

The second data set is the data taken with the new 16 detector layer (12.7 kg days, see Section 3.1). For this data set the depth cut $0.1 < z < 0.95$ was applied for background reduction and discarding the unreliable area below the anodes. Sum spectra of both data sets are shown in Figure 3.24.

Due to the large differences in the data taking methods and the background shape it was decided to analyse the data sets separately. Fits at the Q-values of ^{116}Cd (2813.5 keV) and ^{130}Te (2527.0 keV) were done for each data set with a fit interval of $\pm$300 keV.

Both intervals contain, in principle, the 2614.5 keV γ-line of the ^{208}Tl decay from the ^{232}Th chain. No obvious signal is visible in the spectrum at this energy. Also at the energies of the other γ-lines from the ^{232}Th chain no significant peaks are visible. Adding another Gaussian signal at 2614.5 keV to take the ^{208}Tl line into account would increase the number of fit parameters and therefore decrease the sensitivity to the actual $0\nu\beta\beta$-decay signal. To check for the presence of a line at 2614.5 keV the extended likelihood fit was performed in a fit interval of $\pm$300 keV around this energy. The results are shown in Figure 3.25. A signal strength of

$$n_{208Tl} = 1.9^{+5.9}_{-4.7}\,\text{cts, Peak Sens. ADC data}\,, \quad n_{208Tl} = 0.5^{+3.6}_{-2.9}\,\text{cts, FADC data} \tag{3.25}$$

(uncertainties on central 68 % CL) was determined. As can also be seen from Figure 3.25 the fits to both data sets are consistent with $n_{208Tl} = 0$ and adding a further line at 2614.5 keV to the background model was discarded.

From the limit on observed $0\nu\beta\beta$-decay signal events n_{up} during the live time t a half-life limit can be obtained from

$$T_{1/2} \geq \varepsilon \cdot \frac{\ln(2) \cdot N_0}{n_{up}} \cdot t\,, \quad (T_{1/2} \gg t) \tag{3.26}$$

with the number of source atoms N_0 and the detection efficiency ε. N_0 is taken from Table 1.2.

The efficiency has to be calculated for each data set and each Q-value separately because the detectors have slightly different weights ($\sim$ 6.5 g/detector for the old and $\sim$ 5.9 g/detector for the new detectors) and different cuts are applied (see above). To determine the efficiency of a full energy deposition of a $0\nu\beta\beta$-decay in the detector two approaches were tested. $0\nu\beta\beta$-decays were simulated in a segmented 1.02 cm^3 (5.9 g, edge length 1.005 cm) CdZnTe detector and in a segmented 1.12 cm^3 (6.5 g, edge length 1.040 cm) CdZnTe detector. The detectors were divided into 100 slices along the z direction. It was noticed that the small variation in the edge length has an even smaller influence on the detection efficiency ($\sim$ 0.5 % absolute or $\sim$ 1 % relative).

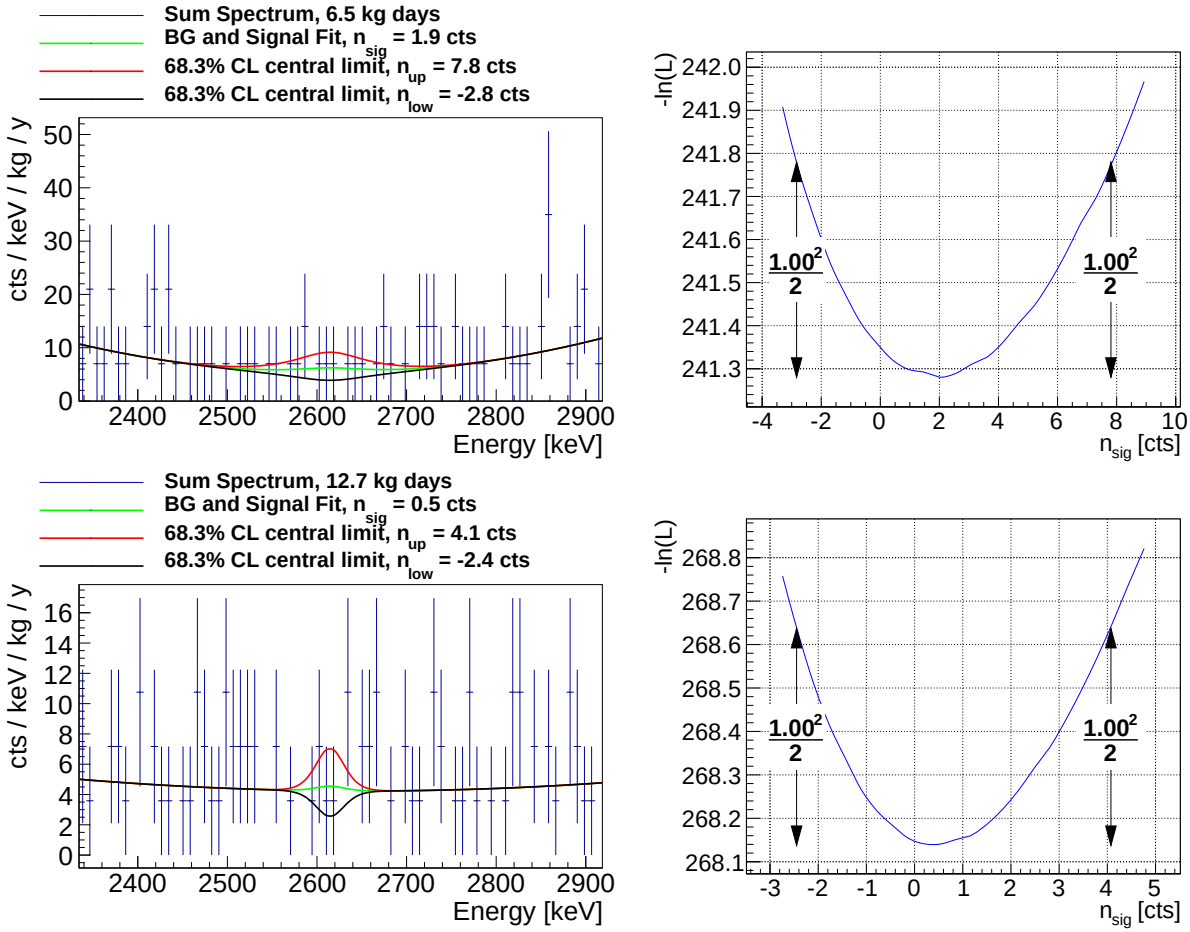

Figure 3.25.: Fit results for the ^{208}Tl line (2614.5 keV). Both data sets are consistent with no detected decays. Shown are the fitted spectra and the negative log likelihood function $-\ln(\mathcal{L})$ calculated as explained in Subsection 3.3.2. The arrows indicate the 68 % CL central limits ($k_\alpha = 1$) on the fitted signal events.

The first approach for the determination of the detection efficiency was the energy (or deposited charge) weighted path length calculation explained in Section 2.6. The z-distribution of a ^{116}Cd VENOM simulation for all simulated events and events with full energy deposition are shown in Figure 3.26. Close to the edges of the detector the probability of an escape of one or even both electrons from the detector is high. Therefore the probability of a full energy deposition for events close to the edges is low. This means that the reduction of efficiency for shallow depth cuts is lower than the actual loss of active volume. For the ^{116}Cd simulation and a cut on interaction depth of $0.05 < z < 0.9$ the determined efficiency is $\varepsilon = 46\,\%$. Without z-cuts the efficiency was calculated to be $\varepsilon = 49\,\%$.

The second approach is to sum only the energy deposition in z-slices within the cut region and to ignore energy deposition in all other slices. The detector parts outside the

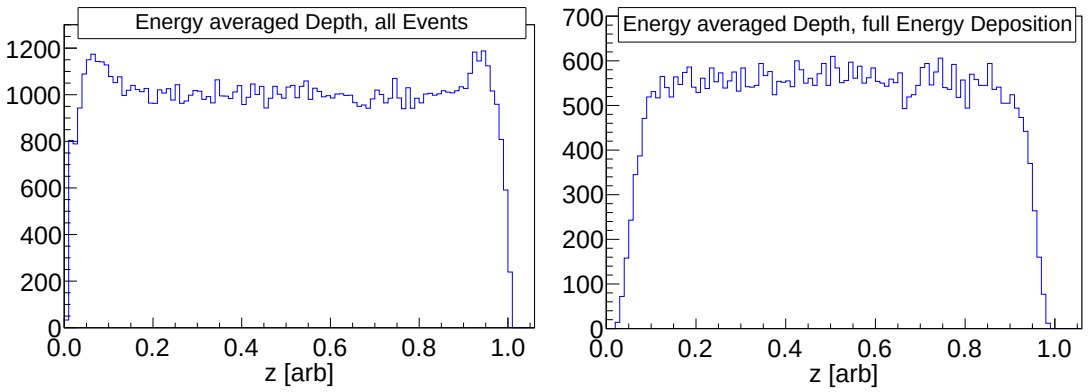

Figure 3.26.: Distribution of energy (charge) weighted interaction depth (see Section 2.6) of a VENOM ^{116}Cd $0\nu\beta\beta$-decay simulation. Close to the edges the probability for electrons to escape the detector is high. For these events a short path length is calculated. Therefore a cluster at $z \sim 0$ and $z \sim 1$ arises in the left plot of the interaction depth of all simulated events. For the same reason the probability of a full energy deposition close to the edges is low. This can be seen in the drop of the number of full energy events at $z \sim 0$ and $z \sim 1$ in the right plot of events with deposition of the full $0\nu\beta\beta$-decay energy in the detector.

z-range cuts are treated as insensitive material. For the ^{116}Cd simulation this approach yields an efficiency of $\varepsilon = 41\,\%$ for a full energy deposition. This efficiency is smaller than the efficiency determined with the energy weighted path-length method. The reduction of efficiency for this method is equivalent to the loss of active volume.

In general the method of the energy weighted path-length is regarded to be more realistic than the second method. On the other hand both methods do not take detector effects, such as electron trapping, into account. These effects will lead to a slightly lower true detection efficiency in a real measurement than determined from the simulation. Presumably this influence will be comparatively small, but nevertheless the slightly more conservative efficiencies determined with the second method will be used to prevent an overestimation of ε.

For the data taken with the peak sensing ADC a depth cut of $0.05 < z < 1$ in the simulated data was applied to take the uncertainty in the energy reconstruction directly below the anodes into account.

The fit to the data taken with the peak sensing ADC resulted in

$$^{116}\text{Cd:}\quad \varepsilon = 47\,\%,\quad n_{sig} = -6.0\,\text{cts},\quad n_{up} = 6.9\,\text{cts}\,,\quad T_{1/2}^{0\nu\beta\beta} > 1.5 \times 10^{20}\,\text{y}\,(90\,\%\,\text{CL})$$
$$^{130}\text{Te:}\quad \varepsilon = 52\,\%,\quad n_{sig} = -1.8\,\text{cts},\quad n_{up} = 5.6\,\text{cts}\,,\quad T_{1/2}^{0\nu\beta\beta} > 1.0 \times 10^{21}\,\text{y}\,(90\,\%\,\text{CL})$$

see Figure 3.27 for the determined spectra and the shape of the negative log-likelihood function $-\ln(\mathcal{L})$. With the data taken with the FADC the following results were ob-

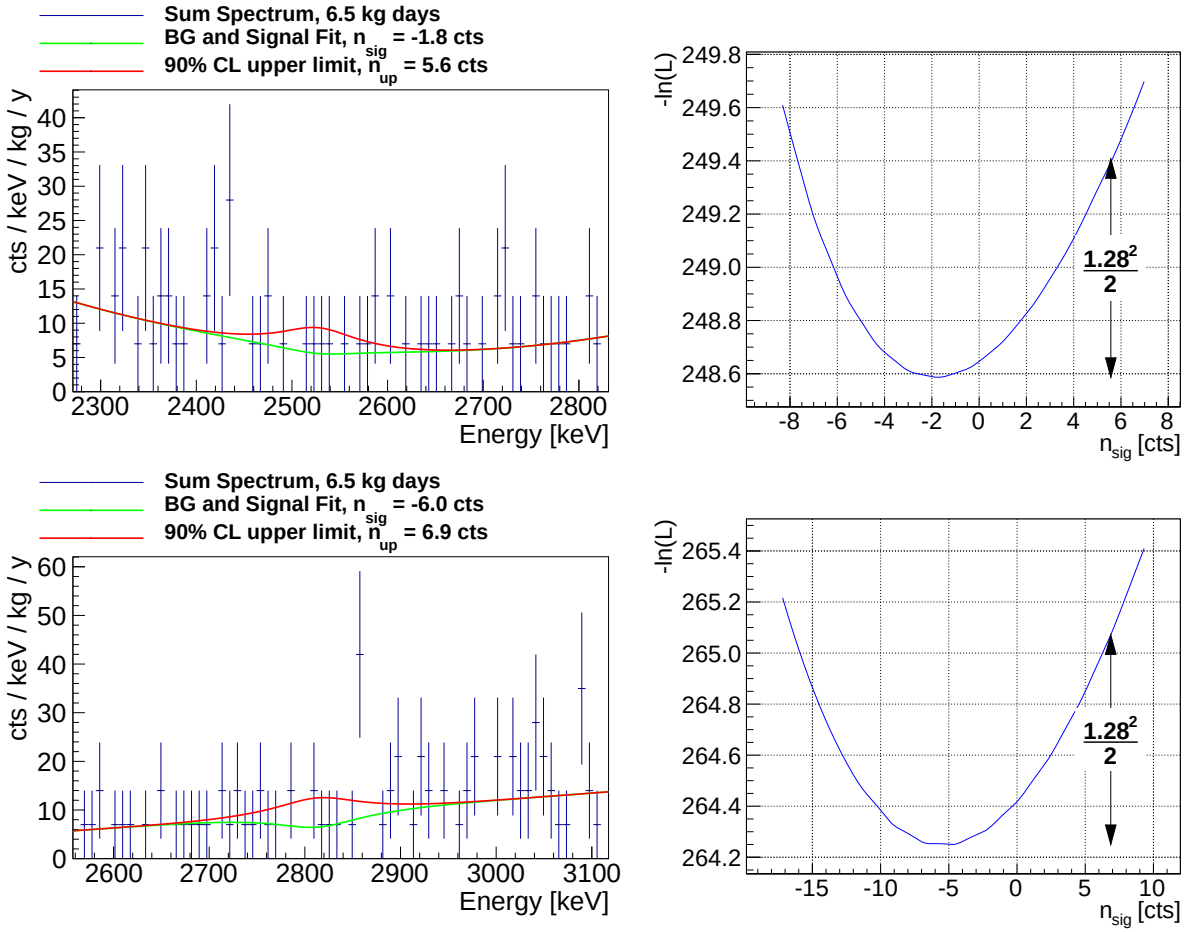

Figure 3.27.: Fit results for the colourless detector data taken with the old peak sensing ADC. Shown are the fitted spectra and the negative log likelihood function $-\ln(\mathcal{L})$ calculated as explained in Subsection 3.3.2. The arrows indicate the 90 % CL upper limits ($k_\alpha = 1.282$) on the fitted signal events. The upper plots show the results for ^{130}Te and the lower plots the results for ^{116}Cd.

tained

$$^{116}\text{Cd:}\quad \varepsilon = 41\,\%,\quad n_{sig} = 2.2\,\text{cts},\quad n_{up} = 7.1\,\text{cts}\,,\quad T_{1/2}^{0\nu\beta\beta} > 2.4\times10^{20}\,\text{y}\,(90\,\%\,\text{CL})$$
$$^{130}\text{Te:}\quad \varepsilon = 46\,\%,\quad n_{sig} = 3.3\,\text{cts},\quad n_{up} = 8.6\,\text{cts}\,,\quad T_{1/2}^{0\nu\beta\beta} > 1.1\times10^{21}\,\text{y}\,(90\,\%\,\text{CL})$$

see Figure 3.28. Even though there is a small statistical excess for ^{130}Te, the obtained number of signal events for the FADC data are still consistent with $n_{sig} = 0$

$$n_{\text{sig}}^{^{116}\text{Cd}} = 2.2^{+3.7}_{-3.0}\,,\quad n_{\text{sig}}^{^{130}\text{Te}} = 3.3^{+4.0}_{-3.3}\quad \text{(both on 68 \% central CL)}. \tag{3.27}$$

The better energy resolution of the data taken with the new detectors results in smaller confidence intervals, compare $-\ln(\mathcal{L})$ shown in the figures. On the other hand

statistical fluctuations in the signal region can have a higher influence because the ROI, and therefore also the amount of statistics, is smaller than for a worse energy resolution. Due to such statistical fluctuations the results for ^{130}Te from the data taken with the new 16 detector layer are only slightly better than the data taken with the old peak sensing ADC data despite the better resolution and more live time.

The world best limits for the examined decays are $T_{1/2}^{0\nu\beta\beta} > 1.7 \times 10^{23}$ y [Dan03] for ^{116}Cd and $T_{1/2}^{0\nu\beta\beta} > 2.8 \times 10^{24}$ y [And11] for ^{130}Te. The results of [Dan03] were already discussed at the end of Section 2.4.2. The results of [And11] were obtained with 19.75 kg y data taken with an array of tellurium oxide bolometers. The bolometers were partly enriched in ^{130}Te. The average energy resolution at 2530 keV was ~ 0.3 % FWHM and the achieved background level in the ROI ~ 0.2 cts/keV/kg/y [Arn08].

Previously published COBRA results for a former test set-up [Daw09b] were $T_{1/2}^{0\nu\beta\beta} > 9.4 \times 10^{19}$ y for ^{116}Cd and $T_{1/2}^{0\nu\beta\beta} > 5.0 \times 10^{20}$ y for ^{130}Te. These results were obtained for 18 kg days of data taken with a test layer with a background level of ~ 100 cts/keV/kg/y in the region of 2.7 MeV to 2.9 MeV. The average resolution of the detectors was about a factor three worse than for the new 16 detector layer. For the detection efficiency values of $\varepsilon = 61$ % for ^{116}Cd and $\varepsilon = 65$ % for ^{130}Te were assumed (see also remarks in Section 2.2). The now obtained half-life limits are better by more than a factor of two. For the first time ever COBRA reached the region of $T_{1/2}^{0\nu\beta\beta} > 10^{20}$ y for ^{116}Cd and $T_{1/2}^{0\nu\beta\beta} > 10^{21}$ y for ^{130}Te.

Sensitivity Studies for the 64 and 64,000 Detector Array

With the generated MC data samples also an estimation of the ^{116}Cd $0\nu\beta\beta$-decay sensitivity for the 64 detector prototype set-up and the 64,000 detector large scale set-up is possible. Sensitivity for $0\nu\beta\beta$-decay is not defined as discovery potential, but as the potential to exclude the true value of the half-life up to certain value [GC11]. For this exclusion usually a 90 % CL upper limit is chosen.

The generated MC data samples with a background level of 1 cts/keV/kg/y for the 64 detector array are equivalent to data taken with the 64,000 detector large scale experiment with 10^{-3} cts/keV/kg/y, which is the worst background level aimed for with COBRA. For the sensitivity test data samples for the 64 array with a background rate of 5 cts/keV/kg/y between 2.4 MeV and 3.2 MeV, which is the current background rate between 2.7 MeV and 2.9 MeV, and 1 cts/keV/kg/y, what can certainly be achieved with more restrictive cuts, were generated. The detector resolution was again taken from the calibration data of the first 16 colourless detector layer. In previous sensitivity studies the average detector mass of 6.5 g/detector of the first detector layer with red passivation was used. With this weight the total source mass of a 64 detector array is 0.416 kg. The average weight of the currently installed detectors is 5.9 g/detector, what equals 0.378 kg for the whole 64 detector array. As several of the old detectors will be reworked and then will be applied in the 64 detector array an average mass of 6.0 g/detector was assumed

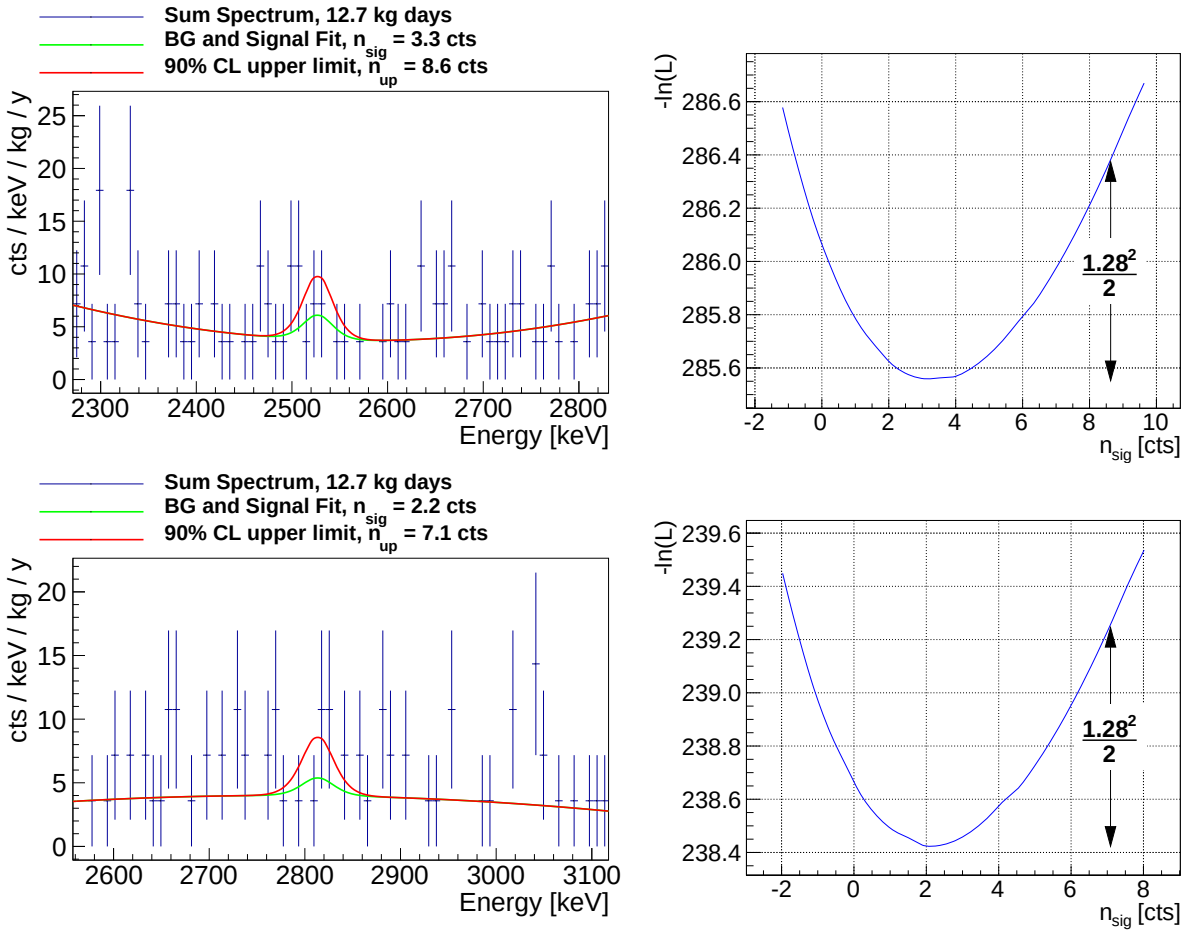

Figure 3.28.: Fit results for the colourless detector data taken with the new FADC. Shown are the fitted spectra and the negative log likelihood function $-\ln(\mathcal{L})$ calculated as explained in Subsection 3.3.2. The arrows indicate the 90 % CL upper limits ($k_\alpha = 1.282$) on the fitted signal events. The upper plots show the results for ^{130}Te and the lower plots the results for ^{116}Cd. For the plotted signal shape the individual detector resolutions and live times were taken into account. In comparison to Figure 3.27 the improved energy resolution of the detectors are clearly noticeable.

for the sensitivity study. This equals a total mass of 0.384 kg. The obtained limit on the number of signal events is, for a given background index in [cts/keV/kg/y], independent from the actual source mass. Therefore, the obtained results can easily be scaled to different detector weights.

Detailed results of the fits are listed and plotted in Appendix H. From the obtained limit n_{up} on the number of signal events (on 90 % CL) half-lives were calculated with Equation (3.26), assuming the efficiency $\varepsilon = 41\,\%$ determined in the previous paragraph. The estimations for the 64 detector array are shown in Figure 3.29. The uncertainties of the half-lives derive from the statistical spread of the 90 % CL upper limits on the number of determined signal events. As can be seen from the plot a sensitivity of $T_{1/2} > 10^{21}$ y can be achieved within a realistic measurement time of two years, even with the already achieved background level of 5 cts/keV/kg/y.

As mentioned above, also an approximation for the 64,000 detector array with a background index of 10^{-3} cts/keV/kg/y is possible. For the large scale array enrichment in ^{116}Cd to 90 % was assumed. The sensitivities for a live time of 1 y, 2 y, 3 y, 5 y and 10 y are plotted in Figure 3.30. The aimed sensitivity of $T_{1/2} > 10^{26}$ y can be achieved with 10 y of live time.

With better detectors, maybe by cooling the detectors and more sophisticated signal processing algorithms further improvement in energy resolution will certainly be possible. To investigate the influence, MC data samples with an average resolution of 1.0 % FWHM at 2.8 MeV were created and analysed. Such an improvement in energy resolution still seems to be feasible and realistic for CdZnTe as it was already achieved with several detectors, see Figure 3.18. The results of the sensitivity estimates with the better resolution are shown in Figure 3.30. By improving the resolution by a factor of 1.5 the sensitivity is increased by a factor of 1.2 to 1.3. For 10 y of live time a sensitivity of $(1.3 \pm 0.6) \times 10^{26}$ y is estimated.

Further improvement of the energy resolution beyond 1 % FWHM to achieve an even higher sensitivity will be very difficult. Instead, the most efficient approach will certainly be to use bigger detectors. At the moment, the main source of background seems to derive from α-particles from surface contamination, see results of Section 3.1 and Section 2.4. By increasing the current detector size of $(1 \times 1 \times 1)\,\mathrm{cm}^3$ to the size of $(2.0 \times 2.0 \times 1.5)\,\mathrm{cm}^3$ of the large scale pixel detectors the volume to surface ratio is increased by a factor of 1.8 from 0.17 to 0.30. A reduction of the background level in the same order is realistic. Furthermore, also the detection efficiency ε will be increased with larger detectors. The increase in efficiency is especially beneficial as ε enters linearly in the half-life calculation (3.26). Additionally a higher source mass is possible with larger detectors. Taking all effects into account an improvement in sensitivity by at least a factor of two seems to be possible with large volume CdZnTe detectors.

Another often applied approximation of the sensitivity of an experiment can be obtained from the background fluctuation. For a background index θ_B [cts/keV/kg/y] the number of expected background counts and its Poissonian uncertainty in an energy

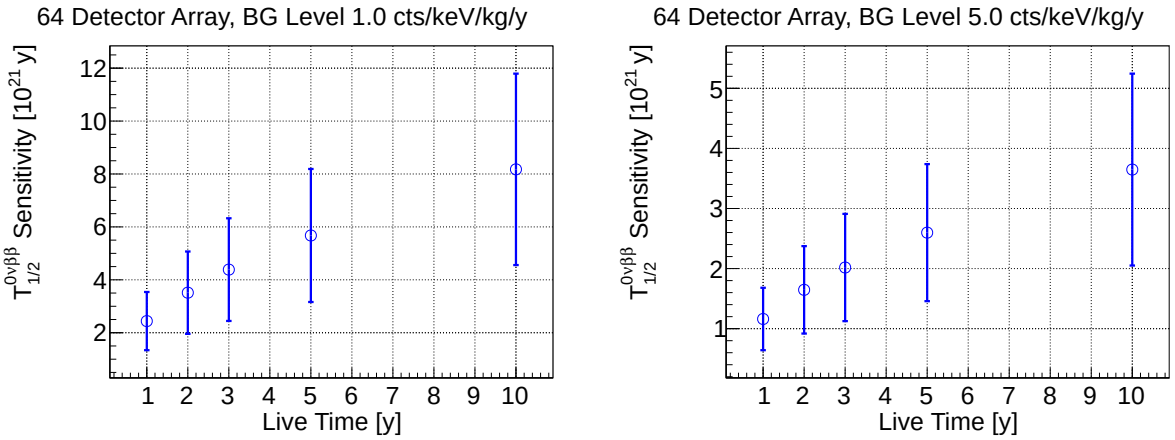

Figure 3.29.: Sensitivity of the 64 detector array for a BG level of 1 and 5 cts/keV/kg/y. The reduction of the BG by a factor of 5 increases the sensitivity by approximately $\sqrt{5} = 2.2$. With about two years of live time a sensitivity to $T_{1/2} > 10^{21}$ y (on 90 % CL) for the $0\nu\beta\beta$-decay of ^{116}Cd is achievable, even with the higher BG level. The error bars were calculated from the statistical fluctuations of the fit results.

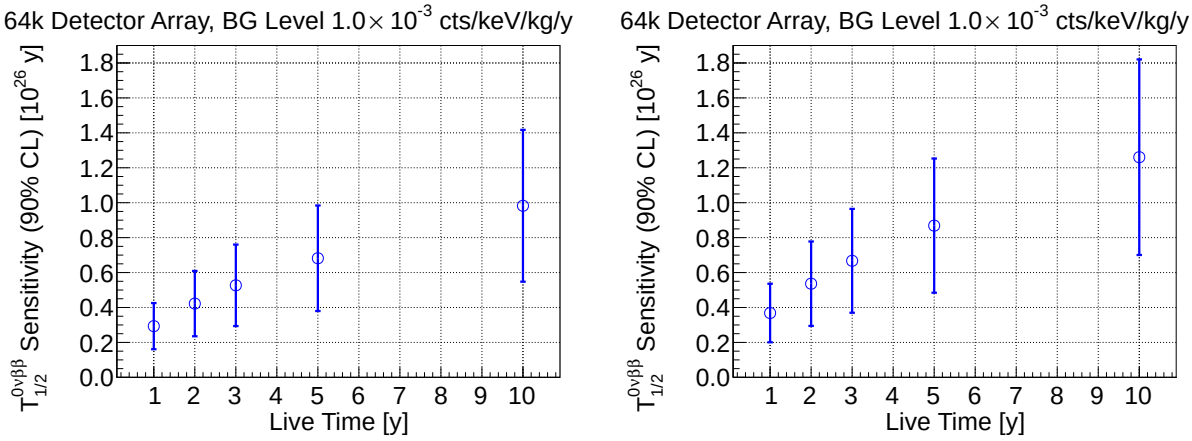

Figure 3.30.: Sensitivity of the 64,000 detector array (6.0 g/detector, enriched in ^{116}Cd to 90 %) for a BG level of 10^{-3} cts/keV/kg/y and an average energy resolution of 1.5 % FWHM (left) and 1.0 % FWHM (right) at 2.8 MeV. The numbers were obtained by scaling the results of the sensitivity estimations of the 64 detector array, see text and Figure 3.29.

region ΔE for an experiment with source mass M are

$$n_b = \theta_B \cdot \Delta E \cdot M \cdot t\,, \quad \sigma_{n_b} = k_\alpha \cdot \sqrt{\theta_B \cdot \Delta E \cdot M \cdot t} \tag{3.28}$$

during the measurement time t. k_α is the coverage factor for the desired confidence level, e.g. $k_\alpha = 1.282$ for an upper 90 % CL, see Appendix D.

Taking the background fluctuation σ_{n_b} as approximation for the upper limit on determined signal events n_{up} and calculating the number N_0 of source isotopes from the isotopic abundance a, the stoichiometric factor s ($s = 0.9$ for $Cd_{0.9}Zn_{0.1}Te$), Avogadro's number N_A and the weighted molar mass $\langle M_{CdZnTe}\rangle = 234.5\,\frac{\mathrm{g}}{\mathrm{mol}}$ as

$$N_0 = \frac{N_A \cdot M \cdot s \cdot a}{\langle M_{CdZnTe}\rangle} \tag{3.29}$$

yields for Equation (3.26)

$$T_{1/2} > \frac{\ln(2)}{k_\alpha} \cdot \varepsilon \cdot \frac{N_A \cdot a \cdot s}{\langle M_{CdZnTe}\rangle} \cdot \sqrt{\frac{M \cdot t}{\theta_B \cdot \Delta E}}\,. \tag{3.30}$$

This approximation has mainly three drawbacks. First, the approximation of the variance of a Poisson variable according to Equation (3.28) is only valid for a large number of events. The Poisson distribution is asymmetric for low statistics, see also remarks in Section 2.4.2. Second, it gives no information on the uncertainty of the sensitivity estimation. The uncertainties due to statistical fluctuations obtained with the extended likelihood fit to MC data are in the order of nearly 50 % and therefore are also of interest for a serious sensitivity estimation. Third, there is no general agreement on the actual width of ΔE. Often the resolution (FWHM) of the detector is taken. This systematically overestimates the achievable sensitivity because it is chosen too small. Only 76 % of a Gaussian peak are contained in a range of one FWHM ($\approx \pm 1.18\,\sigma$), see e.g. Appendix D. Therefore no real experiment would chose such a small energy window for the signal estimation. Furthermore also an area for the background estimation has to be taken into account. [ISO00] proposes an interval of 2.5×FWHM for the signal region and at least the same width for the interval of the background estimation. This yields $\Delta E = 5\times$FWHM, what leads to a reduction of the estimated sensitivity by a factor of $\sqrt{5} = 2.2$ compared to the often used $\Delta E = 1\times$FWHM.

Furthermore, the information on the signal and background shape is not taken into account. The insensitivity to this information will lead to a lower sensitivity estimation compared to the estimation with the extended likelihood method applied to MC data samples. Here the insufficiency of the approximation (3.30) becomes obvious. A wider, more realistic ΔE, which will result in better sensitivity estimates for the extended likelihood method because more data is available, will lead to worse sensitivities with Equation (3.30).

However, in Figure 3.31 Equation (3.30) is plotted for $\Delta E = 2\times$FWHM. For this ΔE the sensitivity estimation agrees well with the results from the MC data evaluation for

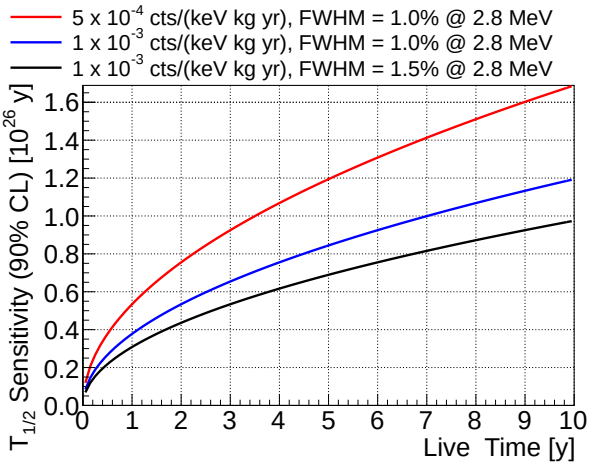

Figure 3.31: Sensitivity estimations obtained with Equation (3.30) ($\varepsilon = 41\,\%$, $\Delta E = 2\times$FWHM and $k_\alpha = 1.28$) for several resolutions and background levels. For the BG window of $\Delta E = 2\times$FWHM the estimates of the 10^{-3} cts/keV/kg/y background level agree well will the sensitivity estimates obtained from analysis of MC data with the extended likelihood method shown in Figure 3.30. If a higher ΔE is taken the obtained limits are weaker than from the fits to the MC data.

both energy resolutions. For the evaluation of the 64 detector MC data with different background levels also an increase of sensitivity comparable to the $\sqrt{1/\theta_B}$ dependence of Equation (3.30) was noted, see Figure 3.29. But in general it can be said that the sensitivity estimates determined with the extended likelihood method from MC data are more reliable for the reasons given above.

It should also be noted that the exclusion sensitivity on the basis of a 90 % CL upper limit is not equivalent to a sensitivity for a discovery. If a true $0\nu\beta\beta$-decay half-life for ^{116}Cd of $T_{1/2}^{0\nu\beta\beta} = 1.0 \times 10^{26}$ y is assumed an average of 2.3 observed $0\nu\beta\beta$-decays per year is expected in the whole 64,000 detector array (90 % enrichment in ^{116}Cd, 6.0 g/detector, $\varepsilon = 41\,\%$). Data samples for the 10^{-3} cts/keV/kg/y background level and the resolution of 1.5 % FWHM at 2.8 MeV for a live time of 10 y were generated. The data sets contain a Poissonian distributed signal with $\mu_{\text{true}}^{\text{sig}} = 23.0$ cts. The results are shown in Figure 3.32. The extended ML method shows again a good performance . The mean of the distribution of fitted signal events (23.1 ± 0.2) is higher than the statistical spread of the fitted signal (17.9 cts). The coverage of the determined confidence intervals is also good. Nevertheless, about 38 % of all experiments will calculate a lower limit for μ_{sig} that is still consistent with $\mu_{\text{sig}} = 0$ (on 68 % CL for a central confidence interval). To have a good discovery potential for half-lives in the order of 10^{26} y several of the experimental parameters, i.e. source mass, background level and energy resolution, have to be improved even further.

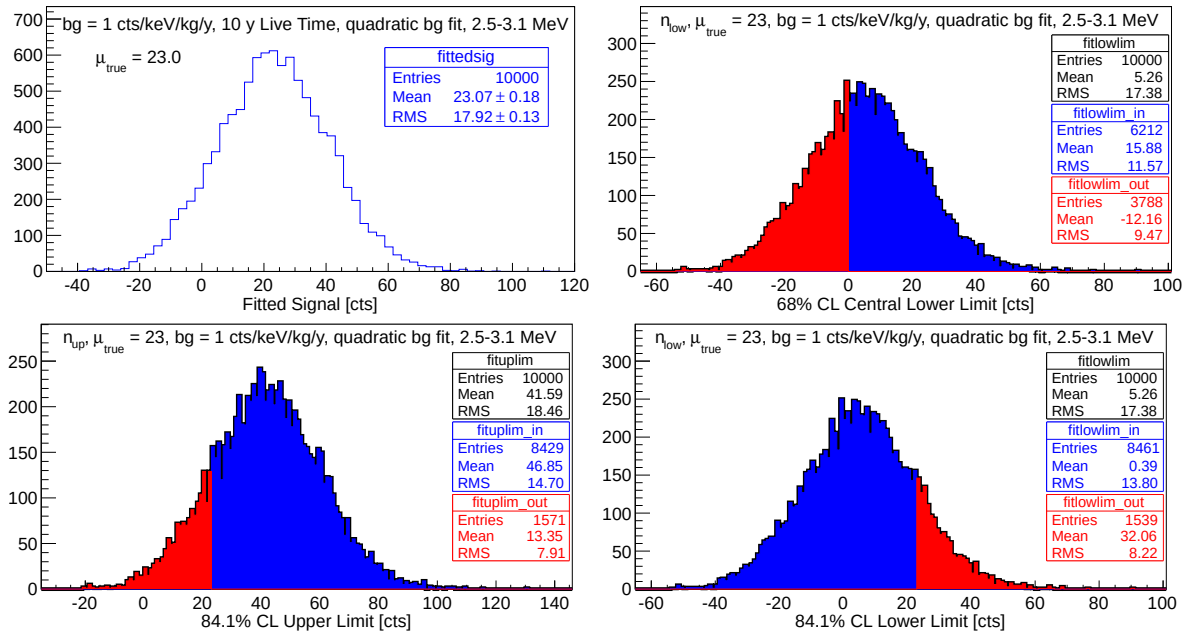

Figure 3.32.: Fit results of MC data equivalent to 10 y of data taking with the 64,000 detector array with a BG level of 10^{-3} cts/keV/kg/y and a $0\nu\beta\beta$ half-life of ^{116}Cd of $T_{1/2}^{^{116}\mathrm{Cd}} = 10^{26}$ y. Note that the MC data for the 64 detector array with a BG level of 1 cts/keV/kg/y was used. These data sets can be used for the sensitivity approximation of the 64,000 detector array as the number of detectors and the BG level are both scaled by a factor of 1000.
On the upper left plot the distribution of the fitted signals is shown. The average of the distribution ($\bar{\mu}_{\mathrm{fit}}^{\mathrm{sig}} = 23.1$ cts) is in very good agreement with the true expected value of the MC data ($\mu_{\mathrm{true}}^{\mathrm{sig}} = 23.0$ cts) and more than $1\,\sigma$ (17.9 cts) above zero. Nevertheless, the lower limits of nearly 38 % of all results will be consistent with $\mu_{\mathrm{sig}} = 0$ (on 68 % central CL), see top right plot. The fit method shows a good coverage also for 68 % ($1\,\sigma$) central confidence limits, see bottom plots (note: 68 % CL central limit means that for 68 % of all determined confidence intervals the true value will be contained, but also that $\frac{32\,\%}{2} = 16\,\%$ of all resulting lower limits μ_{low} are higher than $\mu_{\mathrm{true}}^{\mathrm{sig}}$, which is equivalent to an 84 % CL lower limit, and also 16 % of all resulting upper limits μ_{up} are smaller than $\mu_{\mathrm{true}}^{\mathrm{sig}}$, which is equivalent to an 84 % CL upper limit).

4. Summary and Outlook

The COBRA experiment is currently in the R&D phase for a large scale $0\nu\beta\beta$-decay experiment. The final experiment will have a source mass of several hundred kg of CdZnTe semiconductor detectors to achieve a sensitivity in the order of 10^{26} y.

In this work a significant contribution was made to the enhancement of the sensitivity of the current R&D set-up and studies were carried out to obtain estimates for the large-scale experiment.

In close cooperation with Oliver Schulz and Jan Tebrügge the complete DAQ readout chain was replaced in order to enable pulse shape readout. With the new readout electronics an enhancement of the energy resolution and lower vulnerability to electromagnetic interferences was achieved. The preamplifier and linear amplifier electronics to operate the whole 64 CPG detector R&D array was produced together with the mechanical and electronics workshops of the TU Dortmund department of physics.

The pulse shape readout offers new possibilities of background reduction, such as the rejection of unphysical electromagnetic disturbances or the calculation of the interaction depth of an energy deposition. By applying an analysis of the interaction depth to data taken with the experimental set-up at LNGS, two major sources of background were identified and the background level in COBRA's region of interest around 3 MeV was reduced by about 60 %. It was shown that the α-decay of ^{190}Pt, which is contained in the 100 nm thick detector electrode metallisation with a natural abundance of 0.014 %, was the main source of background. It can be totally eliminated by rejecting events with an interaction depth close to the detector electrodes. The half-lives of ^{190}Pt quoted in literature differ significantly. With data from the COBRA set-up a half-life for the α-decay of ^{190}Pt of $T_{1/2} = (5.8 \pm 1.0\,(\text{stat.}) \pm 0.7\,(\text{syst.})) \times 10^{11}$ y was determined. This value favours rather the higher literature values.

^{210}Po α-decays from the ^{210}Pb sub chain of the ^{238}U natural decay chain were identified as a second source of background. These contaminations derive from decay products of airborne ^{222}Rn. Energy depositions from these α-decays were detected at the cathode of the detectors. It is assumed that the major part of the remaining background derives from ^{210}Po decays on top of the detector passivation. The α-particles lose energy during their passage through the passivation and can therefore deposit energy in COBRA's region of interest.

In the current COBRA R&D set-up CdZnTe CPG detectors are applied, but CdZnTe can also be operated as pixelated detectors. These detector types have a large potential for background suppression. In Monte Carlo simulations the possibilities for a large

volume pixel detector were investigated. Experimental results from [Sch11a] could be reproduced. It was shown that the background level can be reduced by several orders of magnitude by applying fiducial volume cuts. These cuts are very efficient for α- and β-particles, but the background from high energetic γ-particles can not be completely discarded and will be the main source of remaining background. However, even with a not low background optimised detector system a background level of less than one count/keV/kg/y can be achieved. This shows that large volume pixel detectors are a good candidate for a large scale COBRA set-up and should be further investigated.

The COBRA simulation program VENOM was extended. Methods to significantly reduce the required computation time and data storage, a new position generator and an interface to load geometries defined in the GDML markup language were implemented. By comparing experimental and simulated data it was shown that the results obtained from simulations do not match perfectly because detector effects, such as charge transport and trapping, are not implemented in VENOM, but are in general reliable in the order of several per cent.

An unbinned extended maximum likelihood fitter was developed to search for a $0\nu\beta\beta$-decay signal in data with low statistics. The fit method was thoroughly tested with Monte Carlo data and showed a good performance, i.e. a small bias, good coverage and robustness. With 12.7 kg days of data taken at LNGS, half-life limits for the $0\nu\beta\beta$-decay of $T_{1/2}^{0\nu\beta\beta} > 2.4 \times 10^{20}$ y of ^{116}Cd and $T_{1/2}^{0\nu\beta\beta} > 1.1 \times 10^{21}$ y for ^{130}Te on 90 % CL were obtained. These are the highest limits achieved by COBRA so far.

From Monte Carlo studies an approximation for the expected sensitivity with the full 64 detector R&D array for the $0\nu\beta\beta$-decay of ^{116}Cd were deduced. For a live time of about one year an expected sensitivity of $T_{1/2} > 10^{21}$ y was determined. For a large scale set-up with a source mass of about 400 kg of CdZnTe and a background level of 10^{-3} cts/keV/kg/y a sensitivity of up to 10^{26} y for 10 years live time was estimated.

The results of this work show that COBRA is a promising candidate for a large scale $0\nu\beta\beta$-decay experiment. In the future, two major challenges have to be mastered. Ways for a further reduction of the background have to be found in order to achieve the aimed background level of 10^{-3} cts/keV/kg/y. Additional investigation into pulse shape analysis of CPG pulses, new cleaning procedures for the detector surfaces and the use of pixelated detectors are promising approaches. Furthermore, concepts to scale the CPG and pixel detector R&D set-ups to a large scale set-up have to be found and investigated. Isotopic enrichment in ^{116}Cd is also a key issue to achieve a sensitivity in the order of 10^{26} y with a large scale set-up.

Acknowledgements / Danksagung

During my time with COBRA and E IV I had the privilege and the pleasure to meet many brilliant, interesting and kind people (many of them even being all of the three :-). For all the encouragement and the support I received I am really grateful and want to say thank you. As there are several people whose mother tongue is not German, I would like to start by thanking them.

Even though I got to know Dr. Matthew Fritts only during the last year of my thesis, with his important contributions to COBRA's progress he leaves quite an impression. I am indebted to him for proofreading parts of my thesis and giving me helpful feedback.

A special pleasure was to get to know our exchange students Fuluny Jang and David Sutherland. I enjoyed meeting these brilliant and devoted students and treasure the great time that we had together. Special thanks go to Fuluny Jang for proof reading parts of my thesis.

Thanks also to all my COBRA colleagues who supported me and brought joy and fun to the collaboration meetings and long, hard LNGS shifts.

Mein besonderer Dank dafür, dass er mir die Möglichkeit zur Promotion eröffnet hat, gebührt Herrn Prof. Dr. Claus Gößling. Sehr hoch schätze ich auch, dass er in seinem Lehrstuhl ein freundschaftliches und produktives Klima geschaffen hat, das den Lehrstuhl E IV auch in anstrengenden Zeiten stets zu einem sehr angenehmen Arbeitsplatz machte. Insbesondere weiß ich, genau wie meine Kollegen, das Vertrauen und die Anerkennung gegenüber unserer Arbeit zu schätzen, die er uns stets entgegen brachte und uns somit motivierte, stets unser Bestes zu geben.

Prof. Dr. Kai Zuber, der COBRA initiierte und einen sehr großen Teil seiner Zeit und Kraft in das Projekt investierte, möchte ich insbesondere dafür danken, dass er sich trotz seines stets überfüllten Terminkalenders die Zeit genommen hat, um die Zweitkorrektur meiner Arbeit zu übernehmen.

Dr. Bärbel Siegmann danke ich zum einen dafür, dass Sie sich dazu bereit erklärt hat, Beisitzer bei meiner Prüfung zu sein. Zum anderen möchte ich ihr für die Möglichkeit danken, bereits als Doktorand im Fortgeschrittenen Praktikum mitwirken zu dürfen.

Dr. Oliver Schulz, der mich bereits während meiner Diplomarbeit begleitete, möchte ich für die vielen Dinge danken, die ich von ihm lernen durfte. Zurückblickend hätte ich nicht damit gerechnet, so viele Kenntnisse in Elektronik, IT, Projektplanung etc. während der Promotion erwerben zu können. Dass dies zum großen Teil nur möglich

war, da ich von Olis unglaublichem Wissens- und Erfahrungsschatz profitieren durfte, weiß ich sehr zu schätzen. Da ich Oli als Kollegen und auch als Menschen hoch achte, bedeutet mir sein Vertrauen und seine Anerkennung, die er mir entgegen brachte, sowie die Freundschaft, die sich im Laufe der Promotion entwickelt hat, sehr viel.

Ein besonderer Glücksfall war es für mich, mit meinen engen Freunden Till Neddermann und Tobias Wittig für so lange Zeit am gleichen Lehrstuhl arbeiten zu können. Dass sie seit nunmehr neun Jahren die schlechten Scherze und dummen Sprüche von Tills Bürokollegen ertragen (und auch das Risiko der "Ansteckungsgefahr" des Dummschwätzens nicht scheuen) nötigt mir größten Respekt ab. Für den Rückhalt, den mir beide sowohl im privaten Leben als auch am Lehrstuhl gegeben haben und ihre Freundschaft möchte ich ihnen aus tiefstem Herzen danken. Dass ich mit Till zum Teil an den gleichen Projekten arbeiten durfte freute mich insbesondere, da ich ihn auch sehr als zuverlässigen und kompetenten Kollegen schätze.

Für den unglaublich tollen Zusammenhalt und die sehr gute Zusammenarbeit möchte ich all meinen Dortmunder Kollegen danken, da ich weiß, dass beides in dem Maße, wie ich es erfahren durfte, alles andere als selbstverständlich ist. Silke Rajek möchte ich insbesondere dafür danken, dass sie sich mit großer Ausdauer auch vielen unliebsamen und zeitraubenden Aufgaben widmet und uns dadurch in dieser Beziehung oft den Rücken frei gehalten hat. Jan Tebrügge gebührt großer Dank, da wir ohne seinen großen Beitrag insbesondere zum Bau der Elektronik noch lange nicht da stünden, wo wir mittlerweile sind. Die Eigenschaften eines hervorragenden Ausdauersportlers hat er u.a. wieder einmal dadurch gezeigt, dass er meine gesamte (evtl. etwas längliche) Arbeit sehr sorgfältig Korrektur gelesen und einiges zur besseren Verständlichkeit beigetragen hat. Dafür, genauso wie für die Freundschaft, die du mir entgegen gebracht hast, auch noch mal vielen Dank, und hier schon mal ein kleiner Anfang für die Rückzahlung der vielen Kommata, die ich dir noch schulde ,,,,,,,,,,,,,,,,,,,,,,,, ;-)

Allen Korrekturlesern möchte ich hier auch noch mal dafür danken, dass sie sich die Zeit dafür genommen haben. Vor allem PD Dr. Reiner Klingenberg, der durch seine unheimlich kompetente und nette Art auch viel zur guten Stimmung am Lehrstuhl beiträgt, rechne ich die vielen Stunden hoch an, die er sich trotz permanenter Arbeitsüberlastung genommen hat, um große Teile meiner Arbeit zu lesen und angeregt darüber zu diskutieren.

Nicht nur das Klima bei EIV sondern auch in der COBRA Kollaboration allgemein empfand ich stets als sehr produktiv und kollegial. All meinen COBRA Kollegen danke ich hierfür und hoffe, dass dies in der Kollaboration noch lange so bleibt. Insbesondere den Dresdner "Cobranden der ersten Stunde" Daniel Gehre sowie Maria und Benjamin Janutta danke ich für die vertrauensvolle Zusammenarbeit. Dr. Matthias Junker bin ich durch die äußerst wichtige Unterstützung, die er uns stets am LNGS zukommen lies, zu Dank verpflichtet.

Im Laufe meiner Promotion durfte ich mich an der Betreuung einiger Diplom-, Bachelor- und Masterarbeiten beteiligen. Kathrin Rumberg (geb. Schreiner), Jan

Tebrügge, Michael Homann, Thomas Quante und Julia Rietenbach danke ich für ihr Engagement im Rahmen ihrer Arbeiten und für die Beiträge, die sie für COBRA geleistet haben.

Wie bereits erwähnt weiß ich das tolle Klima bei uns am Lehrstuhl sehr zu schätzen. Daher möchte ich auch all meinen Lehrstuhlkollegen für die vergangenen Jahre danken, vor allen Dingen denjenigen, die zur Organisation der vielen Lehrstuhlausflüge, Weihnachtsfeiern, Weihnachtsmarktbesuche, Kino-, Film- und Fußballabende... beigetragen haben. Auf privater Seite ist mir, neben meinen COBRA Kollegen, insbesondere Silke Altenheiner durch ihre offene Art (und dadurch, dass auch sie selbst in ihrer Freizeit heldenhaft Tills und Silkes komischen Büronachbarn ertragen hat) ans Herz gewachsen.

Unseren Technikern Theo Villet und Markus Alex sowie unserer Sekretärin Andrea Teichmann danke ich für ihre stete Hilfsbereitschaft und Unterstützung. Insbesondere Markus rechne ich die sehr flexible Handhabung seiner Feierabende hoch an.

Ohne die hervorragenden Werkstätten des Fachbereiches Physik wäre die Durchführung meiner Arbeit nicht möglich gewesen. Daher gebührt auch den elektronischen und mechanischen Werkstätten ein sehr großer Dank und ein großes Lob für ihre hervorragende Arbeit. Jens Sparfeld, der uns stets engagiert unterstützt und im Rahmen des Baus der neuen Elektronik einige tausend Bauteile verlötet hat, möchte ich hierbei meinen besonderen Dank aussprechen.

Der große Rückhalt, den ich auf privater Seite genießen durfte, war sehr wichtig für mich. Hierfür danke ich natürlich in erster Linie meiner Familie. Die Gewissheit, stets bedingungslos auf euch zählen zu können, bedeutet mir unheimlich viel und hat mir immer das wichtige Gefühl von Sicherheit gegeben. Dafür, dass ihr stets für mich da ward, euch Sorgen um mich gemacht und mich umsorgt und unterstützt habt kann ich gar nicht genug danken.

Meinen Eltern möchte ich für alles, was sie mir mit auf den Weg gegeben haben, danken. Das Durchhaltevermögen und die Zielstrebigkeit, die ich ihnen verdanke, waren für das Studium unerlässlich. Die Begeisterung für den Sport, die sie (nach anfänglichem standhaften Widerstand) bei mir weckten, hat auch während schwieriger und stressiger Zeiten dafür gesorgt, dass ich die Balance nicht ganz verloren habe (und die vielen gemeinsamen Aktivitäten, wie das Spazieren gehen sowie das Rollerskate- und Rad fahren, haben dafür gesorgt, dass ich trotz des öfteren "Frustessens" immer noch auf dem Rad und nicht selbst als Kugel durch die Gegend rolle).

Meiner "großen" Schwester möchte ich für die vielen langen, interessanten und unterhaltsamen Gespräche während meiner "Heimaturlaube" und unserer Telefonate danken und dafür, dass sie immer an mich denkt. Es war und ist schön, eine "große" Schwester zu haben, zu der man aufschauen und auf die man stolz seien kann.

Da in den letzten Jahren nicht übermäßig viel Freizeit blieb, bin ich auch sehr dankbar für die Zeit, die ich mit meinen Freunden verbringen konnte. Hierbei denke ich insbesondere an die wundervollen Urlaube mit Katrin Schünemann, Judith Wilhelm und

Till Neddermann. Diese Zeit war sehr wichtig für mich, um Abstand von der Arbeit zu gewinnen und mich zu erholen. Vielleicht lässt sich das am Besten mit den Worten von James Thurber beschreiben: “Who flies afar from the sphere of our sorrow is here today and here tomorrow” (The Moth and the Star, 1940). Der viele Spaß den wir zusammen hatten, die vielen wundervollen Orte die wir zusammen gesehen und die Zeit, die wir miteinander verbracht haben, bedeuten mir sehr viel und haben nicht unwesentlich dazu beigetragen, dass ich genug Kraft sammeln konnte, um mit meiner Arbeit weiter zu machen und sie abzuschließen.

Für die vielen gemeinsamen Abende, an denen wir zusammen Musik gemacht und viel miteinander gelacht haben, möchte ich mich bei Tobias Wittig bedanken. Seine Freundschaft und die Begeisterung für die Musik, die er bei mir geweckt hat, sind beide äußerst wertvoll für mich geworden.

A. Applied Cumulative Distribution Function (CDF) Transformations

As uniformly $(0, 1]$ distributed random variables are available from many random generators, it is desirable to create a random variable Y with arbitrary CDF $F_Y(y) = P(Y \leq y)$ and PDF $f_Y(y)$

$$F_Y(y) = \int_{-\infty}^{y} f_Y(t)\,\mathrm{d}t \tag{A.1}$$

from a uniformly distributed random variable X in $(0, 1]$ with PDF $f_X(x) = 1$ and CDF $U_X(x)$

$$U_X(x) = \int_{0}^{x} 1\,\mathrm{d}t = x\,. \tag{A.2}$$

As usual for the random variables themselves (a random variable is defined as a function that maps a sample space S into the real numbers) capital letters (X, Y etc.) are used and lower case letters (x, y etc.) denote values for the corresponding possible realisations of the random variable (i.e. the real numbers that are mapped into).

A simple approach like inserting X into the desired PDF does not lead to a random variable with the desired distribution. This can be seen from the following rules that apply for the transformation of random variables [Cas02]:

For a random variable X with CDF $F_X(x)$ and the transformation $Y = g(X)$ the CDF $F_Y(y)$ is given by

$$F_Y(y) = F_X(g^{-1}(y)) \tag{A.3}$$

if $g(x)$ is an increasing function and by

$$F_Y(y) = 1 - F_X(g^{-1}(y)) \tag{A.4}$$

for a decreasing function $g(x)$.

Then, if $g(x)$ is a monotone function and $g^{-1}(y)$ has a continuous derivative, the PDF of Y is

$$f_Y(y) = f_X(g^{-1}(y)) \left| \frac{\mathrm{d}}{\mathrm{d}y} g^{-1}(y) \right| . \tag{A.5}$$

So for example inserting uniformly distributed random variables X in $g(x) = \exp(-x)$ results not in random variables with exponentially decreasing PDF (as needed e.g. for

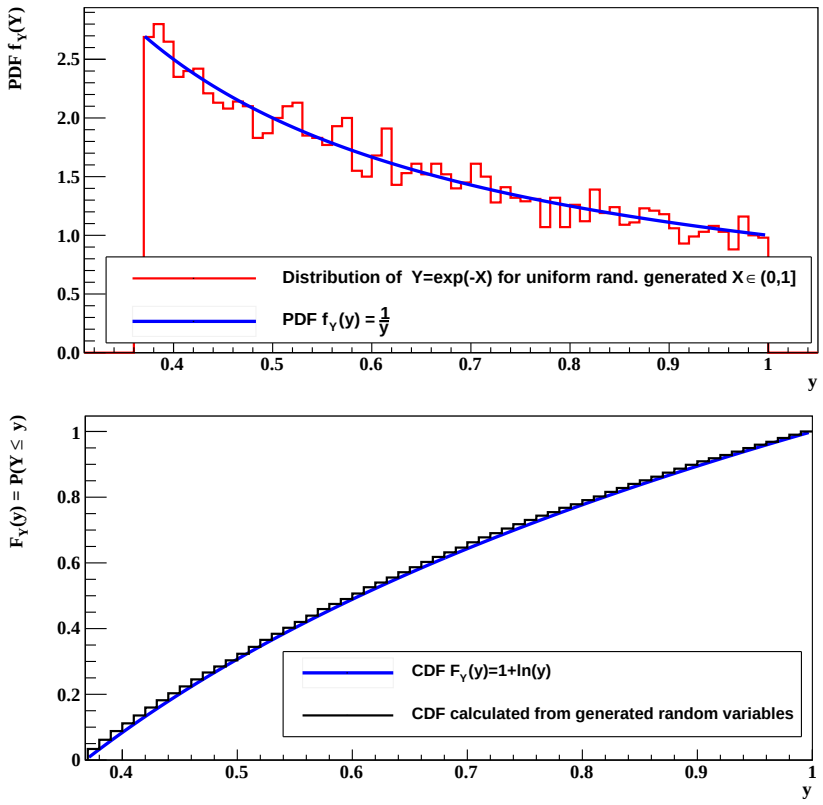

Figure A.1.: PDF (top) and CDF (bottom) of a random variable Y resulting from inserting a uniform $U(0,1]$ random variable X in an exponential function $g(X) = \exp(-X)$.

the modelling of the background in Subsection 3.3.2), but in random variables Y with PDF $f_Y(y) = \frac{1}{y}$ and CDF $F_Y(y) = 1 + \ln(y)$ (see Figure A.1).

So an appropriate transformation to a new random variable $Y = g(X)$ with the required CDF is needed. To find a proper transformation $g(x)$ of $U_X(x)$ Equation (A.3) can be applied:

$$F_Y(y) = F_Y(g(x)) \overset{(A.3)}{=} U_X(g^{-1}(y)) \overset{(A.2)}{=} g^{-1}(y) = x\,. \tag{A.6}$$

So by solving

$$F_Y(g(x)) = x \tag{A.7}$$

the appropriate transformation can be found and the random variable

$$Y = F_Y^{-1}(x) \tag{A.8}$$

follows the required distribution. For example for an exponentially decreasing background in $y\,\epsilon\,[y_0, y_1]$ with decay constant λ the required PDF is

$$f_Y(y) = \frac{\lambda}{\exp(-\lambda\, y_0) - \exp(-\lambda\, y_1)} \mathrm{e}^{-\lambda\, y}\,. \tag{A.9}$$

Then the following equation has to be solved to obtain the random variable Y with the PDF (A.9) from uniformly $(0, 1]$ distributed X:

$$F_Y(y) = \int_{y_0}^{y} f_Y(t)\,\mathrm{d}t = \frac{\lambda}{\exp(-\lambda\, y_0) - \exp(-\lambda\, y_1)} \left(\mathrm{e}^{-\lambda\, y_0} - \mathrm{e}^{-\lambda\, y}\right) = x \tag{A.10}$$

$$\Rightarrow Y = -\tfrac{1}{\lambda}\, \ln\left(X\, \mathrm{e}^{-\lambda\, y_1} + \mathrm{e}^{-\lambda\, y_0}(1 - X)\right)\,. \tag{A.11}$$

For the position generator described in Subsection 2.1.2 PDFs had to be transformed from Cartesian to cylindrical and to spherical coordinates. In the cylindrical case the the tube segment is described by a length h_1, an inner- and an outer radius r_1 and r_2 and a start and end angle ϕ_1 and ϕ_2. So random variables for one radius $r\,\epsilon\,[r_1, r_2]$, one angle $\phi\,\epsilon\,[\phi_1, \phi_2]$ and one height $h\,\epsilon\,[-h_1/2, h_1/2]$ have to be generated from three uniformly distributed random variables Z_1, Z_2, Z_3. The required CDF is given by

$$F_{R,\Phi,H}(r, \phi, h) = \frac{1}{V} \int \mathrm{d}V = \frac{1}{(\phi_2 - \phi_1)(h_1)(\frac{{r_2}^2}{2} - \frac{{r_1}^2}{2})} \int_{r_1}^{r} \int_{\phi_1}^{\phi} \int_{-\frac{h_1}{2}}^{h} r'\,\mathrm{d}r'\,\mathrm{d}\phi'\,\mathrm{d}h'\,. \tag{A.12}$$

To obtain the transformation for one variable, the others have to be integrated out and the analogous of Equation (A.8) has to be solved. To obtain for example the radius random variable R from Z_1, the following has to be solved

$$F_R(r) = \frac{1}{(\phi_2 - \phi_1)(h_1)\left(\frac{{r_2}^2}{2} - \frac{{r_1}^2}{2}\right)} \int_{r_1}^{r} \int_{\phi_1}^{\phi_2} \int_{-\frac{h_1}{2}}^{\frac{h_1}{2}} r'\,\mathrm{d}r'\,\mathrm{d}\phi\,\mathrm{d}h \;= z_1$$

$$\Leftrightarrow \frac{r^2 - {r_1}^2}{{r_2}^2 - {r_1}^2} = z_1 \qquad \Rightarrow \qquad R = \sqrt{Z_1({r_2}^2 - {r_1}^2) + {r_1}^2}\,. \tag{A.13}$$

Analogously the other random variables can be derived

$$\Phi = Z_2(\phi_2 - \phi_1) + \phi_1 \tag{A.14}$$

$$H = \left(Z_3 - \frac{1}{2}\right) h_1 \tag{A.15}$$

To describe a spherical segment (G4Sphere) in spherical coordinates the variables inner and an outer radius r_1 and r_2 and angles ϕ_1, ϕ_2, θ_1 and θ_2 are required. Thus, the three random variables R, Φ, Θ have to be generated. For spherical coordinates the CDF is given by

$$F_{R,\Phi,\Theta}(r, \phi, \theta) = \frac{1}{V} \int \mathrm{d}V = \frac{1}{(\phi_2 - \phi_1)(\cos\theta_1 - \cos\theta_2)(\frac{{r_2}^3}{3} - \frac{{r_1}^3}{3})} \int_{r_1}^{r} \int_{\phi_1}^{\phi} \int_{\theta_1}^{\theta} r'\,\sin\theta'\,\mathrm{d}r'\,\mathrm{d}\phi'\,\mathrm{d}\theta'\,. \tag{A.16}$$

The resulting formulas are (analogously obtained to the cylindrical case):

$$R = \sqrt[3]{Z_1({r_2}^3 - {r_1}^3) + {r_1}^3} \tag{A.17}$$

$$\Phi = Z_2(\phi_2 - \phi_1) + \phi_1 \tag{A.18}$$

$$\Theta = \arccos\left[Z_3\left(\cos\theta_2 - \cos\theta_1\right) + \cos\theta_1\right]\,. \tag{A.19}$$

B. Large Pixel Background Reduction Plots

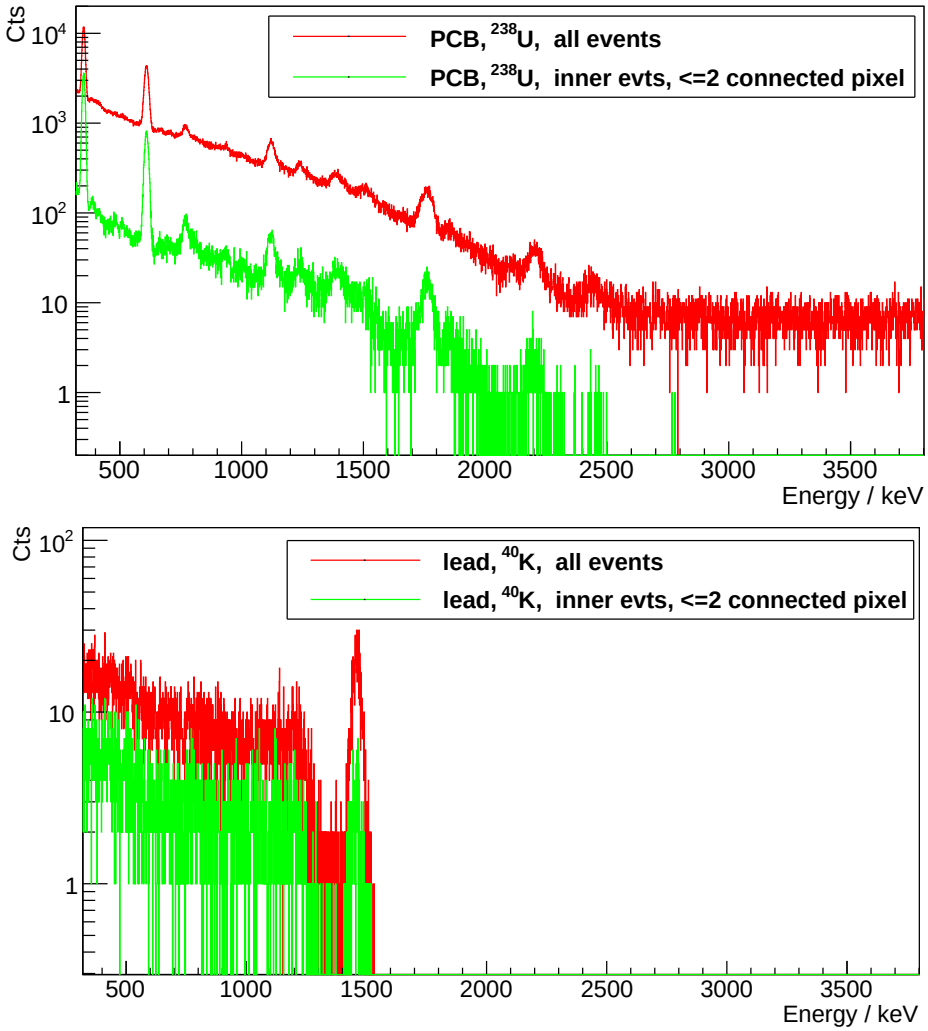

Figure B.1.: Background reduction for ^{238}U in PCB board and ^{40}K in lead. For the ^{238}U in the PCB the contribution of γ-particles is much higher than for the background sources shown in Figure B.2. Therefore the level of background suppression is much lower. The background from ^{40}K in the surrounding lead consists only of γ-particles. So the background reduction is worst here.

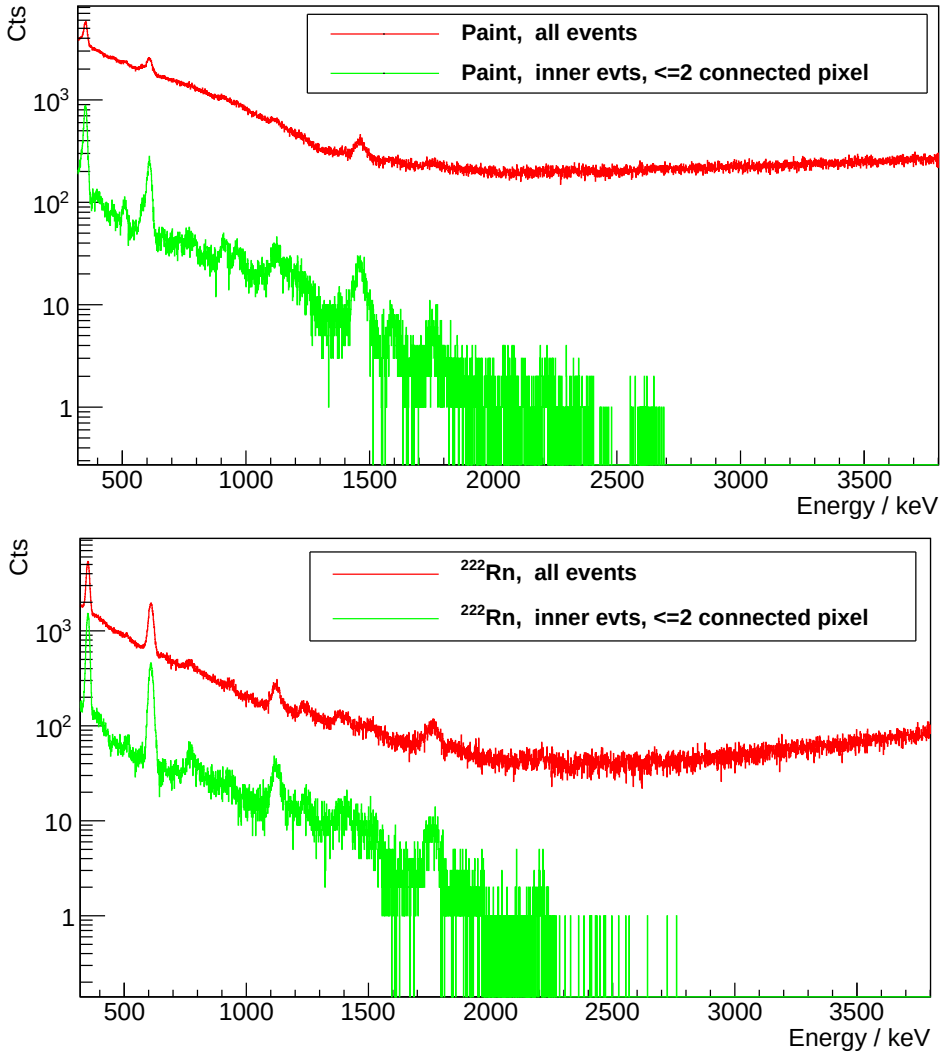

Figure B.2.: Background reduction for passivation paint and ^{222}Rn. The background can be reduced significantly with the cuts as mainly β-particles contribute and they always deposit energy in the outer pixels of the detector. The large contribution of β-particles is due to the small distance of the materials to the detectors, the low attenuation within the materials and because there is no or only little shielding material between the background source and the detector. The large fraction of β-particles can also be seen from the small γ peaks compared e.g. to events in the PCB board or the lead.

C. Tables of ^{238}U and ^{232}Th Decay Chains

Isotope	Decay Mode	Daughter Nuclide	Intensity [%]	Q-Value [MeV]	Half-life
^{238}U	α	^{234}Th	100	4.27	4.468×10^9 yrs
^{234}Th	β	^{234m}Pa	100	0.27	24.10 d
^{234m}Pa	β	^{234}U	99.84	2.27	1.17 min
^{234}U	α	^{230}Th	100	4.86	2.455×10^5 yrs
^{230}Th	α	^{226}Ra	100	4.77	7.538×10^4 yrs
^{226}Ra	α	^{222}Rn	100	4.87	1600 yrs
^{222}Rn	α	^{218}Po	100	5.59	3.8235 d
^{218}Po	α	^{214}Pb	99.98	6.12	3.10 min
^{214}Pb	β	^{214}Bi	100	1.02	26.8 min
^{214}Bi	β	^{214}Po	99.98	3.27	19.9 min
^{214}Po	α	^{210}Pb	100	7.83	164.3 us
^{210}Pb	β	^{210}Bi	100	0.06	22.3 yrs
^{210}Bi	β	^{210}Po	100	1.16	5.013 d
^{210}Po	α	^{206}Pb	100	5.41	138.38 d
^{206}Pb	Stable	-	100		

Table C.1.: Isotopes of the ^{238}U decay chain with Q-values and half-lives. Branchings with branching ratios $< 1\,\%$ were omitted. Data taken from [Fir98].

Isotope	Decay Mode	Daughter Nuclide	Intensity [%]	Q-Value [MeV]	Half-life
^{232}Th	α	^{228}Ra	100	4.083	1.405×10^{10} yrs
^{228}Ra	β	^{228}Ac	100	0.046	5.75 yrs
^{228}Ac	β	^{228}Th	100	2.127	1.17 min
^{228}Th	α	^{224}Ra	100	5.52	6.15 h
^{224}Ra	α	^{220}Rn	100	5.789	3.66 d
^{220}Rn	α	^{216}Po	100	6.405	55.6 s
^{216}Po	α	^{212}Pb	100	6.906	0.145 s
^{212}Pb	β	^{212}Bi	100	0.574	10.64 h
^{212}Bi	β	^{212}Po	64.1	2.254	60.55 min
^{212}Bi	α	^{208}Tl	35.9	6.207	60.55 min
^{212}Po	α	^{208}Pb	100	8.954	0.299 μs
^{208}Tl	β	^{208}Pb	100	5.001	3.053 min
^{208}Pb	Stable	-			

Table C.2.: Isotopes of the ^{232}Th decay chain with Q-values and half-lives. Branchings with branching ratios $< 1\,\%$ were omitted. Data taken from [Fir98].

D. Statistic Remarks

D.1. The Normal (Gaussian) Distribution

The Normal Distribution (also called Gaussian Distribution) is defined as

$$N(x) = \frac{1}{\sigma\sqrt{2\,\pi}}\,\exp -\frac{1}{2}\left(\frac{x-\mu}{\sigma}\right)^2 \tag{D.1}$$

with mean (or expectation) μ and standard deviation σ (and variance σ^2). With $\mu = 0$ and $\sigma = 1$ it is called the standard normal distribution (see Figure D.3). It is often used to describe the PDF of measured variables. For a measurement of a variable with expectation value μ and variance σ^2 the probability to obtain a measured value of x with

$$\begin{aligned} |x-\mu| &\leq 1\,\sigma \text{ is } 68.27\%\,. \\ |x-\mu| &\leq 2\,\sigma \text{ is } 95.45\%\,. \\ |x-\mu| &\leq 3\,\sigma \text{ is } 99.73\%\,. \end{aligned}$$

The other way round, a measured value x will be in a range of

$$|x-\mu| \leq 1.6449\,\sigma$$

with a probability of 90 % (90 % CL). This is a central confidence interval. For a one sided upper confidence interval with 90 % CL holds

$$-\infty < x-\mu \leq 1.28155\,\sigma\,,$$

see also Figure D.2 and Tables D.1 and D.2. The number of standard deviations that corresponds to a certain CL is often also referred to as the Quantile or coverage factor k_α.

To obtain the relation between σ and FWHM one has to solve

$$\begin{aligned} N(x_{1/2}) &\stackrel{!}{=} \frac{N(\mu)}{2} \\ \Leftrightarrow \frac{1}{2}\,\frac{1}{\sigma\sqrt{2\,\pi}} &\stackrel{!}{=} \frac{1}{\sigma\sqrt{2\,\pi}}\,\exp -\frac{1}{2}\left(\frac{x_{1/2}-\mu}{\sigma}\right)^2 \\ \Rightarrow x^{\pm}_{1/2} &= \mu \pm \sqrt{2\,\ln(2)}\,\sigma\,. \end{aligned}$$

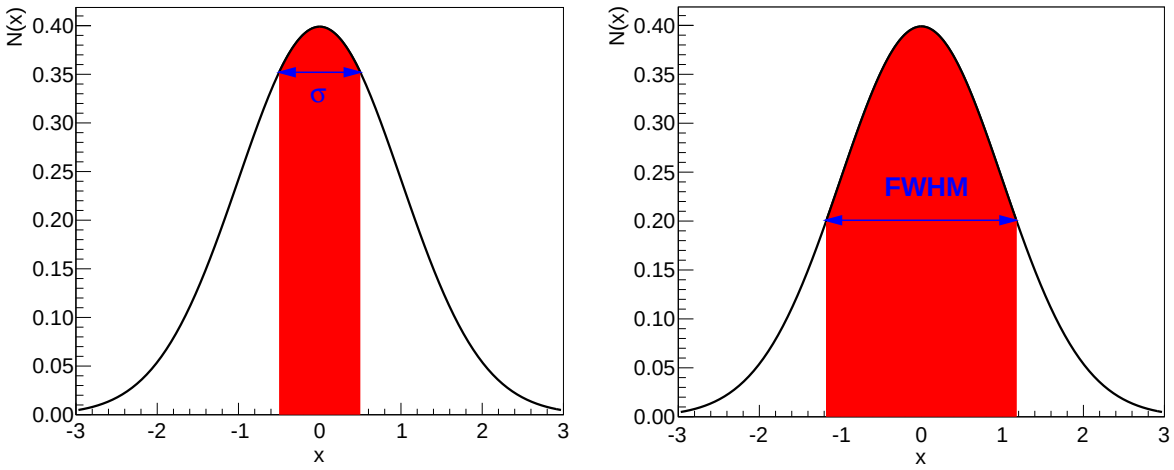

Figure D.1.: σ and FWHM of the standard normal distribution.

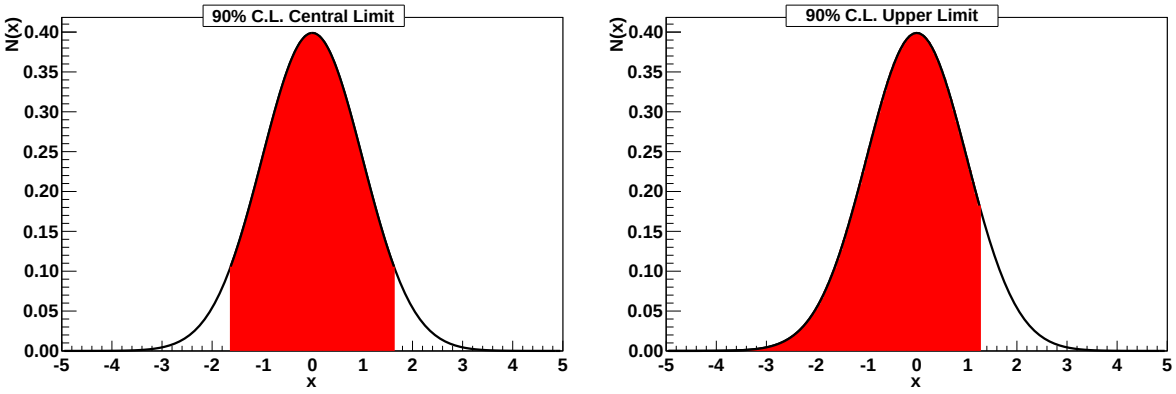

Figure D.2.: 90 % central and upper limit equivalent areas (red) for a Gaussian Distribution.

This yields

$$FWHM = x^{+}_{1/2} - x^{-}_{1/2} = 2\sqrt{2\,\ln(2)}\,\sigma = \sqrt{8\,\ln(2)}\,\sigma \approx 2.35\,\sigma\,, \tag{D.2}$$

see Figure D.1 for illustration.

D.2. Integrated Normal Distribution and Error Function

The CDF (the probability to obtain a measurement x in an interval $(-\infty, x]$) of the normal distribution is given by

$$\Phi(x) = \frac{1}{\sqrt{2\,\pi}} \int_{-\infty}^{x} \exp -\frac{(t-\mu)^2}{2\,\sigma^2}\,\mathrm{d}\,t\,. \tag{D.3}$$

This integral can not be solved analytically. It is connected to the often used Gauss error function

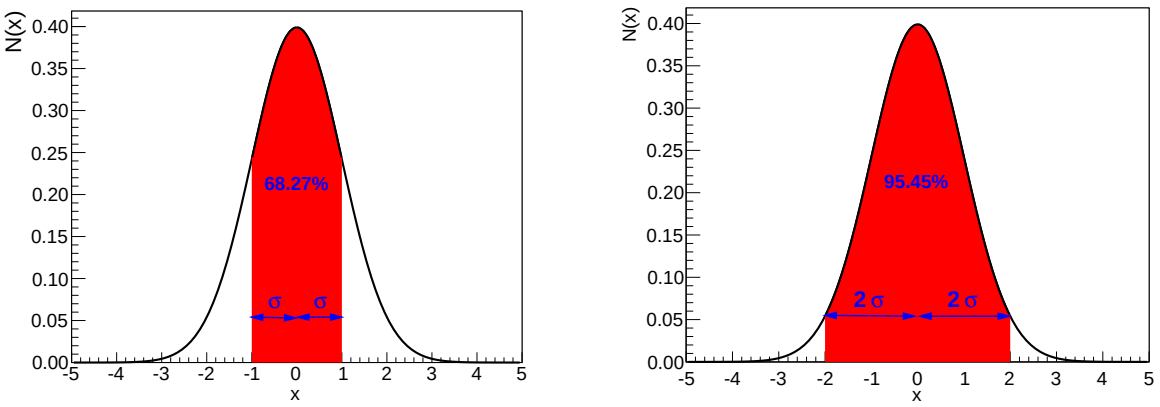

Figure D.3.: Standard Gauss distribution ($\mu = 0$, $\sigma = 1$). The red areas are equivalent to the probability to obtain $|x - \mu| \leq 1\sigma = 68.27\%$ (left) and $|x - \mu| \leq 2\sigma = 95.45\%$ (right).

$$\mathrm{erf}(x) = \frac{2}{\sqrt{\pi}} \int_0^x \mathrm{e}^{-t^2} \mathrm{d}t \tag{D.4}$$

($\mathrm{erf}(0) = 0$ and $\mathrm{erf}(\infty) = 1$) via

$$\Phi(x) = \frac{1}{2} \left(1 + \mathrm{erf} \left(\frac{x - \mu)}{\sqrt{2}\,\sigma} \right) \right) .$$

Tabulated values for $\Phi(x)$ are listed in Table D.2. $\mathrm{erf}(x)$ and also the inverse error function $\mathrm{erf}^{-1}(x)$ are also implemented in ROOT's TMath class.

x	0.00	0.01	0.02	0.03	0.04	0.05	0.06	0.07	0.08	0.09
0.0	0.5000	0.5040	0.5080	0.5120	0.5160	0.5199	0.5239	0.5279	0.5319	0.5359
0.1	0.5398	0.5438	0.5478	0.5517	0.5557	0.5596	0.5636	0.5675	0.5714	0.5753
0.2	0.5793	0.5832	0.5871	0.5910	0.5948	0.5987	0.6026	0.6064	0.6103	0.6141
0.3	0.6179	0.6217	0.6255	0.6293	0.6331	0.6368	0.6406	0.6443	0.6480	0.6517
0.4	0.6554	0.6591	0.6628	0.6664	0.6700	0.6736	0.6772	0.6808	0.6844	0.6879
0.5	0.6915	0.6950	0.6985	0.7019	0.7054	0.7088	0.7123	0.7157	0.7190	0.7224
0.6	0.7257	0.7291	0.7324	0.7357	0.7389	0.7422	0.7454	0.7486	0.7517	0.7549
0.7	0.7580	0.7611	0.7642	0.7673	0.7704	0.7734	0.7764	0.7794	0.7823	0.7852
0.8	0.7881	0.7910	0.7939	0.7967	0.7995	0.8023	0.8051	0.8078	0.8106	0.8133
0.9	0.8159	0.8186	0.8212	0.8238	0.8264	0.8289	0.8315	0.8340	0.8365	0.8389
1.0	0.8413	0.8438	0.8461	0.8485	0.8508	0.8531	0.8554	0.8577	0.8599	0.8621
1.1	0.8643	0.8665	0.8686	0.8708	0.8729	0.8749	0.8770	0.8790	0.8810	0.8830
1.2	0.8849	0.8869	0.8888	0.8907	0.8925	0.8944	0.8962	0.8980	0.8997	0.9015
1.3	0.9032	0.9049	0.9066	0.9082	0.9099	0.9115	0.9131	0.9147	0.9162	0.9177
1.4	0.9192	0.9207	0.9222	0.9236	0.9251	0.9265	0.9279	0.9292	0.9306	0.9319
1.5	0.9332	0.9345	0.9357	0.9370	0.9382	0.9394	0.9406	0.9418	0.9429	0.9441
1.6	0.9452	0.9463	0.9474	0.9484	0.9495	0.9505	0.9515	0.9525	0.9535	0.9545
1.7	0.9554	0.9564	0.9573	0.9582	0.9591	0.9599	0.9608	0.9616	0.9625	0.9633
1.8	0.9641	0.9649	0.9656	0.9664	0.9671	0.9678	0.9686	0.9693	0.9699	0.9706
1.9	0.9713	0.9719	0.9726	0.9732	0.9738	0.9744	0.9750	0.9756	0.9761	0.9767
2.0	0.9772	0.9778	0.9783	0.9788	0.9793	0.9798	0.9803	0.9808	0.9812	0.9817
2.1	0.9821	0.9826	0.9830	0.9834	0.9838	0.9842	0.9846	0.9850	0.9854	0.9857
2.2	0.9861	0.9864	0.9868	0.9871	0.9875	0.9878	0.9881	0.9884	0.9887	0.9890
2.3	0.9893	0.9896	0.9898	0.9901	0.9904	0.9906	0.9909	0.9911	0.9913	0.9916
2.4	0.9918	0.9920	0.9922	0.9925	0.9927	0.9929	0.9931	0.9932	0.9934	0.9936
2.5	0.9938	0.9940	0.9941	0.9943	0.9945	0.9946	0.9948	0.9949	0.9951	0.9952
2.6	0.9953	0.9955	0.9956	0.9957	0.9959	0.9960	0.9961	0.9962	0.9963	0.9964
2.7	0.9965	0.9966	0.9967	0.9968	0.9969	0.9970	0.9971	0.9972	0.9973	0.9974
2.8	0.9974	0.9975	0.9976	0.9977	0.9977	0.9978	0.9979	0.9979	0.9980	0.9981
2.9	0.9981	0.9982	0.9982	0.9983	0.9984	0.9984	0.9985	0.9985	0.9986	0.9986
3.0	0.9987	0.9987	0.9987	0.9988	0.9988	0.9989	0.9989	0.9989	0.9990	0.9990
3.1	0.9990	0.9991	0.9991	0.9991	0.9992	0.9992	0.9992	0.9992	0.9993	0.9993
3.2	0.9993	0.9993	0.9994	0.9994	0.9994	0.9994	0.9994	0.9995	0.9995	0.9995
3.3	0.9995	0.9995	0.9995	0.9996	0.9996	0.9996	0.9996	0.9996	0.9996	0.9997
3.4	0.9997	0.9997	0.9997	0.9997	0.9997	0.9997	0.9997	0.9997	0.9997	0.9998

Table D.1.: Values of the integrated standard Gauss Distribution $F(x) = \frac{1}{\sqrt{2\,\pi}} \int_{-\infty}^{x} \mathrm{e}^{-z^2/2}\,\mathrm{d}z$ (applied e.g. to obtain upper CL limits).

x	0.00	0.01	0.02	0.03	0.04	0.05	0.06	0.07	0.08	0.09
0.0	0.0000	0.0080	0.0160	0.0239	0.0319	0.0399	0.0478	0.0558	0.0638	0.0717
0.1	0.1125	0.1236	0.1348	0.1459	0.1569	0.1680	0.1790	0.1900	0.2009	0.2118
0.2	0.1585	0.1663	0.1741	0.1819	0.1897	0.1974	0.2051	0.2128	0.2205	0.2282
0.3	0.2358	0.2434	0.2510	0.2586	0.2661	0.2737	0.2812	0.2886	0.2961	0.3035
0.4	0.3108	0.3182	0.3255	0.3328	0.3401	0.3473	0.3545	0.3616	0.3688	0.3759
0.5	0.3829	0.3899	0.3969	0.4039	0.4108	0.4177	0.4245	0.4313	0.4381	0.4448
0.6	0.4515	0.4581	0.4647	0.4713	0.4778	0.4843	0.4907	0.4971	0.5035	0.5098
0.7	0.5161	0.5223	0.5285	0.5346	0.5407	0.5467	0.5527	0.5587	0.5646	0.5705
0.8	0.5763	0.5821	0.5878	0.5935	0.5991	0.6047	0.6102	0.6157	0.6211	0.6265
0.9	0.6319	0.6372	0.6424	0.6476	0.6528	0.6579	0.6629	0.6680	0.6729	0.6778
1.0	0.6827	0.6875	0.6923	0.6970	0.7017	0.7063	0.7109	0.7154	0.7199	0.7243
1.1	0.7287	0.7330	0.7373	0.7415	0.7457	0.7499	0.7540	0.7580	0.7620	0.7660
1.2	0.7699	0.7737	0.7775	0.7813	0.7850	0.7887	0.7923	0.7959	0.7995	0.8029
1.3	0.8064	0.8098	0.8132	0.8165	0.8198	0.8230	0.8262	0.8293	0.8324	0.8355
1.4	0.8385	0.8415	0.8444	0.8473	0.8501	0.8529	0.8557	0.8584	0.8611	0.8638
1.5	0.8664	0.8690	0.8715	0.8740	0.8764	0.8789	0.8812	0.8836	0.8859	0.8882
1.6	0.8904	0.8926	0.8948	0.8969	0.8990	0.9011	0.9031	0.9051	0.9070	0.9090
1.7	0.9109	0.9127	0.9146	0.9164	0.9181	0.9199	0.9216	0.9233	0.9249	0.9265
1.8	0.9281	0.9297	0.9312	0.9328	0.9342	0.9357	0.9371	0.9385	0.9399	0.9412
1.9	0.9426	0.9439	0.9451	0.9464	0.9476	0.9488	0.9500	0.9512	0.9523	0.9534
2.0	0.9545	0.9556	0.9566	0.9576	0.9586	0.9596	0.9606	0.9615	0.9625	0.9634
2.1	0.9643	0.9651	0.9660	0.9668	0.9676	0.9684	0.9692	0.9700	0.9707	0.9715
2.2	0.9722	0.9729	0.9736	0.9743	0.9749	0.9756	0.9762	0.9768	0.9774	0.9780
2.3	0.9786	0.9791	0.9797	0.9802	0.9807	0.9812	0.9817	0.9822	0.9827	0.9832
2.4	0.9836	0.9840	0.9845	0.9849	0.9853	0.9857	0.9861	0.9865	0.9869	0.9872
2.5	0.9876	0.9879	0.9883	0.9886	0.9889	0.9892	0.9895	0.9898	0.9901	0.9904
2.6	0.9907	0.9909	0.9912	0.9915	0.9917	0.9920	0.9922	0.9924	0.9926	0.9929
2.7	0.9931	0.9933	0.9935	0.9937	0.9939	0.9940	0.9942	0.9944	0.9946	0.9947
2.8	0.9949	0.9950	0.9952	0.9953	0.9955	0.9956	0.9958	0.9959	0.9960	0.9961
2.9	0.9963	0.9964	0.9965	0.9966	0.9967	0.9968	0.9969	0.9970	0.9971	0.9972
3.0	0.9973	0.9974	0.9975	0.9976	0.9976	0.9977	0.9978	0.9979	0.9979	0.9980
3.1	0.9981	0.9981	0.9982	0.9983	0.9983	0.9984	0.9984	0.9985	0.9985	0.9986
3.2	0.9986	0.9987	0.9987	0.9988	0.9988	0.9988	0.9989	0.9989	0.9990	0.9990
3.3	0.9990	0.9991	0.9991	0.9991	0.9992	0.9992	0.9992	0.9992	0.9993	0.9993
3.4	0.9993	0.9994	0.9994	0.9994	0.9994	0.9994	0.9995	0.9995	0.9995	0.9995

Table D.2.: Values of the integrated standard Gauss Distribution $G(x) = \frac{1}{\sqrt{2\,\pi}} \int_{-x}^{x} \mathrm{e}^{-z^2/2}\,\mathrm{d}z$ (symmetric intervall around 0, applied to obtain central CL levels).

E. Copper Cleaning Procedure

Before the recommissioning of the set-up in the new LNGS location, the inner copper parts were cleaned thoroughly by the LNGS Chemistry and Chemical Plants Division in their laboratory. It was taken care that the copper parts were brought to the laboratory directly before the cleaning and were brought to the tunnel again directly after the cleaning procedure to prevent as much activation of the Copper from cosmic rays as possible. The cleaning procedure was written down by the staff in Italian. This is a translation of the described procedure.

Required Materials

- Polyethylene bags or plastic beaker
- Ultrasonic bath
- Acid soap for ultrasonic bath (ELMA Clean 60, prod. No. 289440605 from Carlo Erba), solution of 3 %
- Cidric acid (5 %)
- Demineralised water

Cleaning Procedure

- The copper parts are put in Polyethylene bags with a solution of about 3 % of ELMA 60 (if they are very dirty a 5 % solution is used)
- The bags are put in an ultrasonic bath for about 40 minutes
- Afterwards the copper parts are rinsed carefully with demineralised water
- The cleaned copper parts are put in clean Polyethylene bags with a solution of cidric acid (5 %)
- The bags are put in an ultrasonic bath for about 1 h
- Afterwards the copper parts are rinsed carefully with demineralised water again
- Afterwards they are wiped with a cloth that does not leave residues to remove most of the remaining water

- The copper parts are completely dried in an oven
- Afterwards they are put immediately in vacuum sealed plastic bags to keep them clean

F. Tables of Extended Likelihood Tests

Fit Range [MeV]	μ_{true}	BG Level [cts/keV/kg/y]	Fitted n_{sig}	σ n_{sig}	Bias b/σ [%]	Coverage [%]	Failed Fits [%]
1.5 − 3.0	0	1	0.05 ± 0.04	4.3	1.1	89.6	0.00
1.5 − 3.0	0	2	0.00 ± 0.06	6.0	-0.1	89.8	0.00
1.5 − 3.0	0	5	0.11 ± 0.10	9.6	1.1	90.0	0.00
1.5 − 3.0	0	10	0.26 ± 0.14	13.7	1.9	89.8	0.00
1.5 − 3.0	1	1	1.07 ± 0.05	4.5	1.5	89.3	0.00
1.5 − 3.0	1	2	1.03 ± 0.06	6.2	0.5	89.3	0.00
1.5 − 3.0	1	5	1.08 ± 0.10	9.7	0.9	89.7	0.00
1.5 − 3.0	1	10	1.27 ± 0.14	13.5	2.0	90.2	0.00
1.5 − 3.0	5	1	5.04 ± 0.05	5.0	0.9	89.3	0.00
1.5 − 3.0	5	2	5.05 ± 0.07	6.5	0.8	89.4	0.00
1.5 − 3.0	5	5	5.18 ± 0.10	9.9	1.8	89.9	0.00
1.5 − 3.0	5	10	5.36 ± 0.14	13.7	2.7	90.5	0.00
1.5 − 3.0	10	1	9.98 ± 0.06	5.5	-0.3	88.8	0.00
1.5 − 3.0	10	2	10.02 ± 0.07	7.0	0.4	89.4	0.00
1.5 − 3.0	10	5	9.98 ± 0.10	10.3	-0.2	89.3	0.00
1.5 − 3.0	10	10	10.23 ± 0.14	14.0	1.6	90.2	0.00
2.0 − 3.0	0	1	0.08 ± 0.04	4.3	1.8	89.9	3.52
2.0 − 3.0	0	2	0.08 ± 0.06	6.1	1.3	90.0	2.43
2.0 − 3.0	0	5	0.21 ± 0.10	9.7	2.2	90.2	0.34
2.0 − 3.0	0	10	0.24 ± 0.14	14.0	1.7	89.7	0.32
2.0 − 3.0	1	1	1.09 ± 0.05	4.6	2.0	89.5	2.77
2.0 − 3.0	1	2	1.12 ± 0.06	6.3	2.0	89.6	1.63
2.0 − 3.0	1	5	1.17 ± 0.10	9.9	1.7	89.9	0.35
2.0 − 3.0	1	10	1.28 ± 0.14	13.9	2.0	90.3	0.37
2.0 − 3.0	5	1	5.02 ± 0.05	5.0	0.4	89.3	3.13
2.0 − 3.0	5	2	5.11 ± 0.07	6.6	1.7	90.0	1.79
2.0 − 3.0	5	5	5.26 ± 0.10	10.1	2.6	90.0	0.33
2.0 − 3.0	5	10	5.34 ± 0.14	14.1	2.4	90.5	0.32
2.0 − 3.0	10	1	9.90 ± 0.06	5.6	-1.7	88.8	3.28
2.0 − 3.0	10	2	10.05 ± 0.07	7.0	0.7	89.5	1.97
2.0 − 3.0	10	5	10.05 ± 0.10	10.4	0.5	89.2	0.36
2.0 − 3.0	10	10	10.20 ± 0.14	14.4	1.4	89.8	0.44

Table F.1.: Fit results MC data tests for extended likelihood, expon. background assumption.

Fit Range [MeV]	μ_{true}	BG Level [cts/keV/kg/y]	Fitted n_{sig}	σ n_{sig}	Bias b/σ [%]	Coverage [%]	Failed Fits [%]
2.5 − 3.1	0	1	-0.10 ± 0.04	4.3	-2.4	89.0	0.00
2.5 − 3.1	0	2	-0.21 ± 0.06	6.1	-3.4	88.9	0.00
2.5 − 3.1	0	5	-0.25 ± 0.10	9.6	-2.6	89.8	0.00
2.5 − 3.1	0	10	-0.37 ± 0.14	13.7	-2.7	89.1	0.00
2.5 − 3.1	1	1	0.92 ± 0.05	4.6	-1.7	88.8	0.00
2.5 − 3.1	1	2	0.86 ± 0.06	6.2	-2.3	89.0	0.00
2.5 − 3.1	1	5	0.73 ± 0.10	9.8	-2.7	89.2	0.00
2.5 − 3.1	1	10	0.65 ± 0.14	13.6	-2.5	89.6	0.00
2.5 − 3.1	5	1	4.88 ± 0.05	5.0	-2.5	88.6	0.00
2.5 − 3.1	5	2	4.84 ± 0.07	6.5	-2.4	89.2	0.00
2.5 − 3.1	5	5	4.83 ± 0.10	10.0	-1.7	89.0	0.00
2.5 − 3.1	5	10	4.76 ± 0.14	13.8	-1.7	89.6	0.00
2.5 − 3.1	10	1	9.82 ± 0.06	5.6	-3.2	88.1	0.00
2.5 − 3.1	10	2	9.84 ± 0.07	7.0	-2.3	88.9	0.00
2.5 − 3.1	10	5	9.62 ± 0.10	10.3	-3.7	88.6	0.00
2.5 − 3.1	10	10	9.58 ± 0.14	14.1	-3.0	88.8	0.00
2.6 − 3.0	0	1	-0.08 ± 0.04	4.5	-1.7	89.2	0.00
2.6 − 3.0	0	2	-0.16 ± 0.06	6.3	-2.6	89.1	0.00
2.6 − 3.0	0	5	-0.11 ± 0.10	9.9	-1.1	89.4	0.00
2.6 − 3.0	0	10	-0.09 ± 0.14	14.1	-0.6	89.3	0.00
2.6 − 3.0	1	1	0.94 ± 0.05	4.7	-1.2	89.0	0.00
2.6 − 3.0	1	2	0.92 ± 0.06	6.4	-1.2	89.1	0.00
2.6 − 3.0	1	5	0.87 ± 0.10	10.1	-1.3	89.3	0.00
2.6 − 3.0	1	10	0.94 ± 0.14	14.0	-0.4	89.6	0.00
2.6 − 3.0	5	1	4.92 ± 0.05	5.2	-1.6	88.7	0.00
2.6 − 3.0	5	2	4.90 ± 0.07	6.7	-1.5	89.3	0.00
2.6 − 3.0	5	5	4.97 ± 0.10	10.3	-0.3	89.5	0.00
2.6 − 3.0	5	10	5.00 ± 0.14	14.2	0.0	90.1	0.00
2.6 − 3.0	10	1	9.84 ± 0.06	5.7	-2.9	88.1	0.00
2.6 − 3.0	10	2	9.89 ± 0.07	7.2	-1.6	89.1	0.00
2.6 − 3.0	10	5	9.72 ± 0.11	10.6	-2.6	88.6	0.00
2.6 − 3.0	10	10	9.86 ± 0.14	14.5	-1.0	89.4	0.00

Table F.2.: Fit results MC data tests for extended likelihood, linear background assumption.

Fit Range [MeV]	μ_{true}	BG Level [cts/keV/kg/y]	Fitted n_{sig}	σ n_{sig}	Bias b/σ [%]	Coverage [%]	Failed Fits [%]
2.5 − 3.1	0	1	-0.07 ± 0.05	4.7	-1.5	89.0	0.01
2.5 − 3.1	0	2	-0.14 ± 0.07	6.6	-2.2	89.1	0.01
2.5 − 3.1	0	5	-0.02 ± 0.10	10.3	-0.2	89.5	0.00
2.5 − 3.1	0	10	0.17 ± 0.15	14.7	1.1	89.7	0.17
2.5 − 3.1	1	1	0.97 ± 0.05	4.9	-0.6	88.8	0.03
2.5 − 3.1	1	2	0.96 ± 0.07	6.7	-0.7	89.0	0.00
2.5 − 3.1	1	5	0.98 ± 0.11	10.6	-0.2	89.6	0.00
2.5 − 3.1	1	10	1.15 ± 0.15	14.7	1.0	89.7	0.14
2.5 − 3.1	5	1	4.94 ± 0.05	5.4	-1.1	89.0	0.02
2.5 − 3.1	5	2	4.94 ± 0.07	7.0	-0.8	89.4	0.00
2.5 − 3.1	5	5	5.09 ± 0.11	10.7	0.8	89.7	0.00
2.5 − 3.1	5	10	5.19 ± 0.15	14.8	1.3	90.6	0.17
2.5 − 3.1	10	1	9.87 ± 0.06	5.9	-2.2	88.6	0.00
2.5 − 3.1	10	2	9.94 ± 0.07	7.5	-0.8	89.2	0.00
2.5 − 3.1	10	5	9.82 ± 0.11	11.0	-1.6	89.0	0.00
2.5 − 3.1	10	10	10.04 ± 0.15	15.1	0.3	89.7	0.30
2.6 − 3.0	0	1	-0.10 ± 0.05	5.1	-2.1	88.9	0.01
2.6 − 3.0	0	2	-0.17 ± 0.07	7.0	-2.5	89.2	0.00
2.6 − 3.0	0	5	-0.04 ± 0.11	11.0	-0.4	89.3	0.00
2.6 − 3.0	0	10	0.27 ± 0.16	15.8	1.7	89.8	0.00
2.6 − 3.0	1	1	0.95 ± 0.05	5.3	-0.9	88.7	0.03
2.6 − 3.0	1	2	0.94 ± 0.07	7.3	-0.8	88.5	0.00
2.6 − 3.0	1	5	0.96 ± 0.11	11.3	-0.3	88.6	0.00
2.6 − 3.0	1	10	1.20 ± 0.16	15.8	1.3	89.8	0.00
2.6 − 3.0	5	1	4.92 ± 0.06	5.8	-1.5	88.5	0.00
2.6 − 3.0	5	2	4.90 ± 0.08	7.6	-1.3	87.9	0.02
2.6 − 3.0	5	5	5.11 ± 0.11	11.5	0.9	89.5	0.00
2.6 − 3.0	5	10	5.10 ± 0.16	15.9	0.6	90.4	0.00
2.6 − 3.0	10	1	9.91 ± 0.06	6.3	-1.4	89.3	0.02
2.6 − 3.0	10	2	9.95 ± 0.08	8.0	-0.6	88.1	0.00
2.6 − 3.0	10	5	9.79 ± 0.12	11.9	-1.8	88.5	0.00
2.6 − 3.0	10	10	10.10 ± 0.16	16.3	0.6	89.7	0.00

Table F.3.: Fit results MC data tests for extended likelihood, quadratic background assumption.

G. Plots of Extended Likelihood Tests

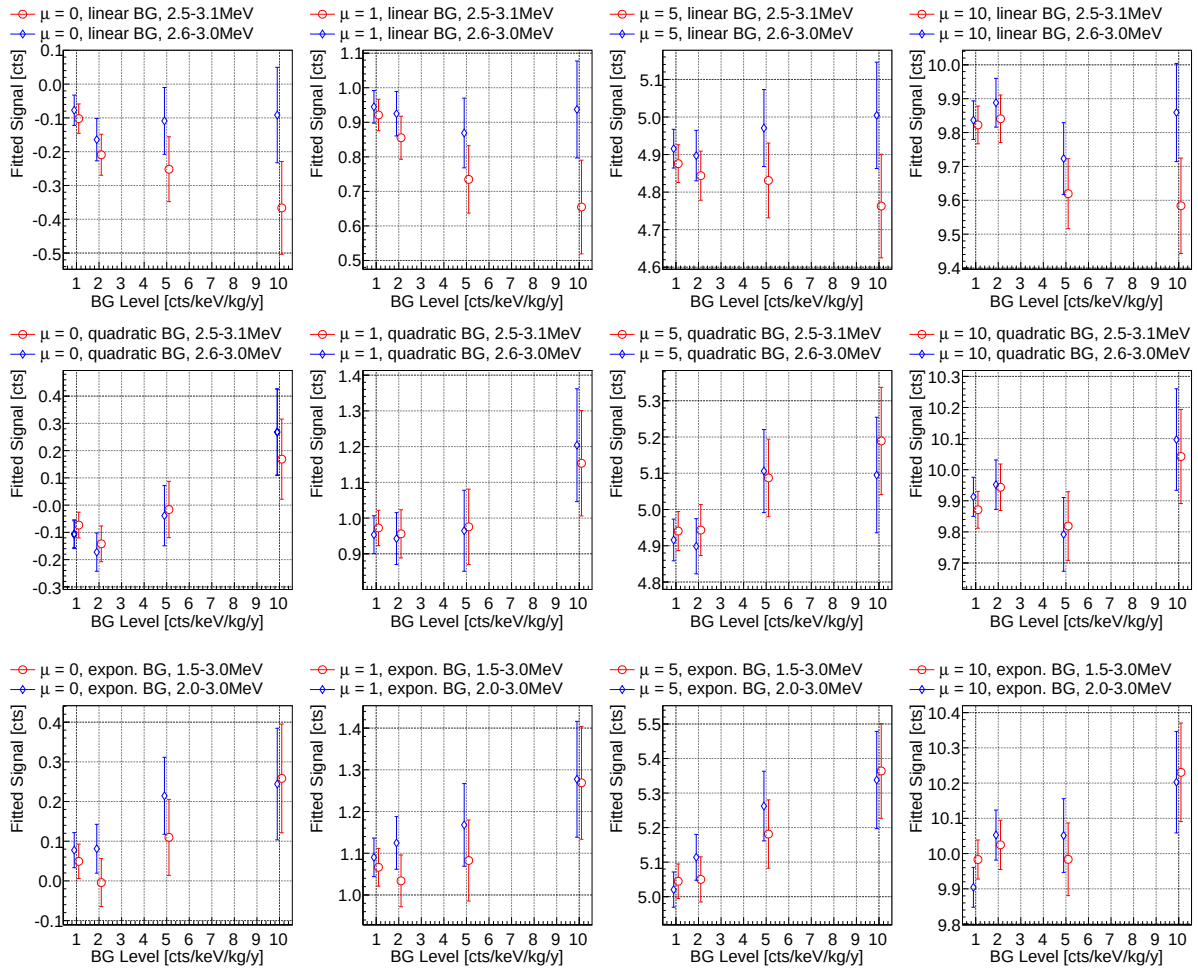

Figure G.1.: Average determined signal strength for different background fit functions and MC data background levels. The markers in the plots were slightly shifted from their true values (1, 2, 5 and 10 cts/keV/kg/y) for a better visibility. The performance of the fit with linear background in the 2.6-3.0 MeV region has the worst performance. An increasing negative bias towards higher background levels is noticeable. The quadratic BG approximation also tends to a small negative bias for low background levels, whereas the exponential fit has a positive bias that seems to be increasing with higher energies. However, the bias of all fit methods is only a few per cent of the statistical spread of the method, compare Figure G.4, and the determined upper limits have a good coverage, see Figure G.2.

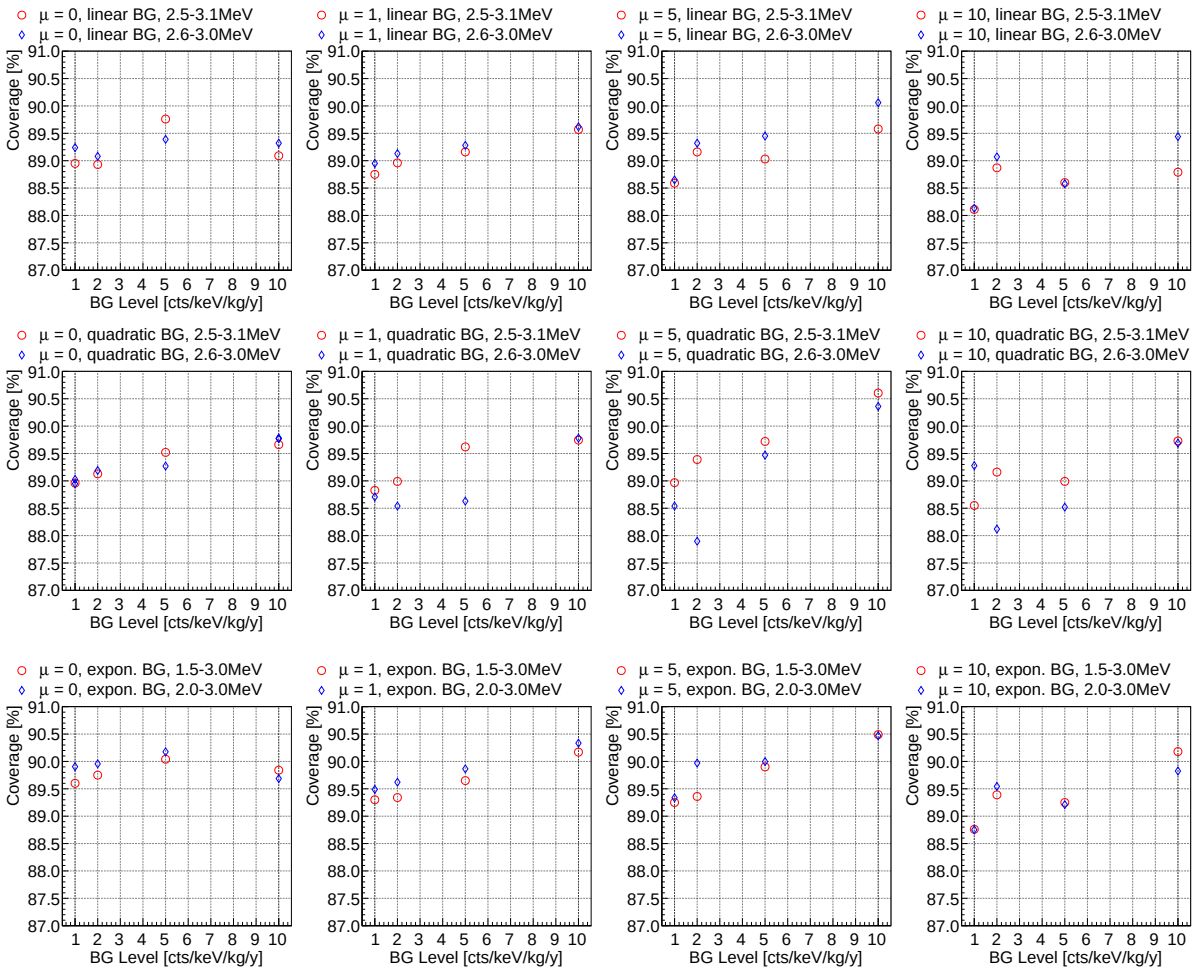

Figure G.2.: Determined coverage for different background fit functions and MC data background levels. The desired upper CL is 90 %. The coverage of all methods is good for a wide range of the background and the signal strength. The polynomial background approximation tends to a small undercoverage, but even the lowest determined coverage of 87.9 % (compare also tables in Appendix F) is still close to the desired 90 %.

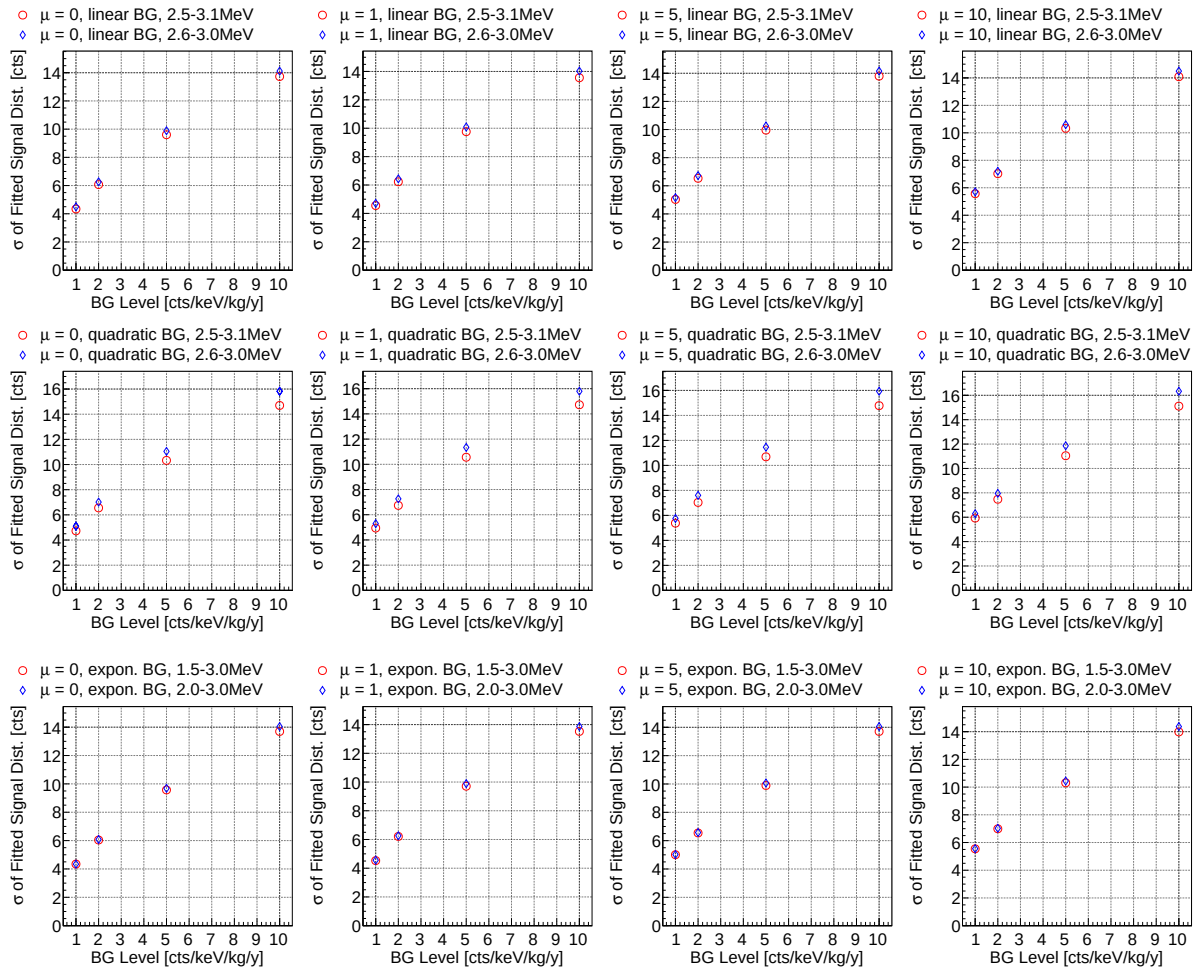

Figure G.3.: Statistical spread σ ($= \sqrt{V(n_{sig})}$ of method variance $V(n_{sig})$) of the fitted signal strength for different background fit functions and MC data background levels. The spread of the fits with the linear background approximation is nearly identical to the exponential BG fit (compare also tables in Appendix F). The statistical spread of the quadratic background approximation is in general about 10% larger than for the other two methods.

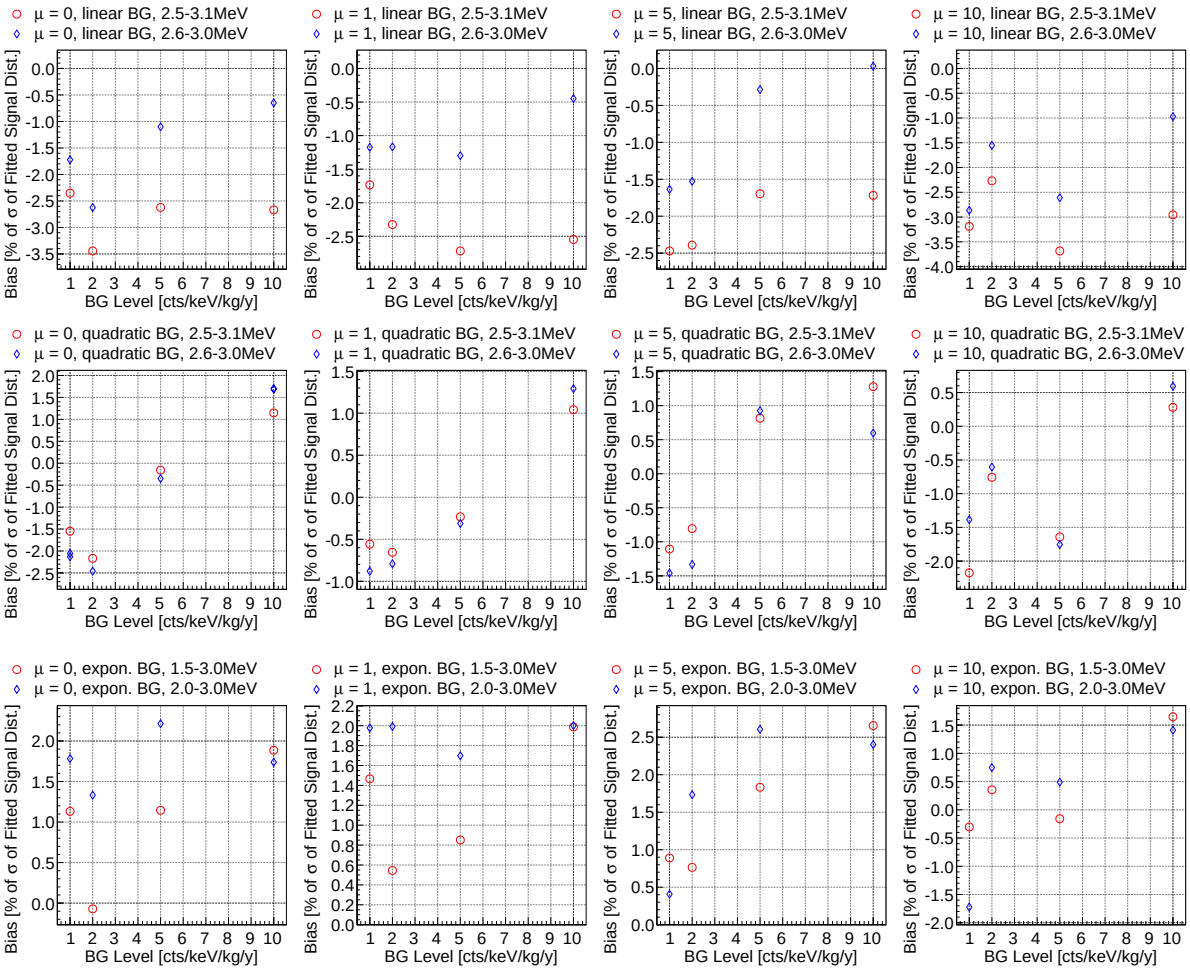

Figure G.4.: Fit bias normalised to statistical spread σ of fit results (b/σ) for different background fit functions and MC data background levels. The linear BG approximations tends to a small negative bias, it has the largest bias of all three methods. The quadratic BG has a small negative bias for a low BG level, but it increases slightly with increasing BG level. The exponential fit method tends to a small positive bias. However, all biases are small ($< 4\,\%$) compared to the variance of the fit methods.

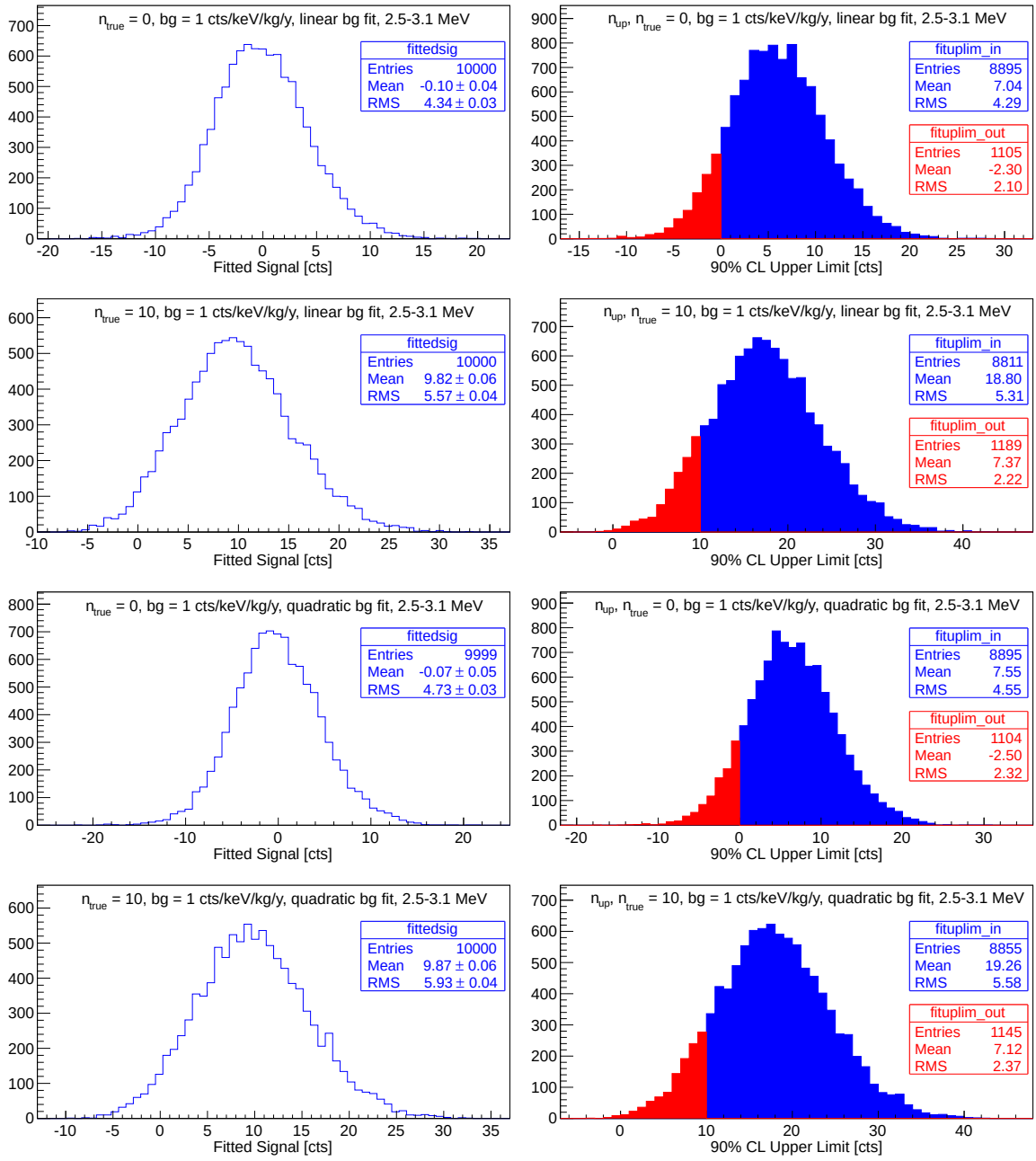

Figure G.5.: Example distributions of fit results for polynomial background approximation for the 1 cts/keV/kg/y MC data sample. Shown are the distributions of the point estimate and the distribution of 90 % CL upper limits.

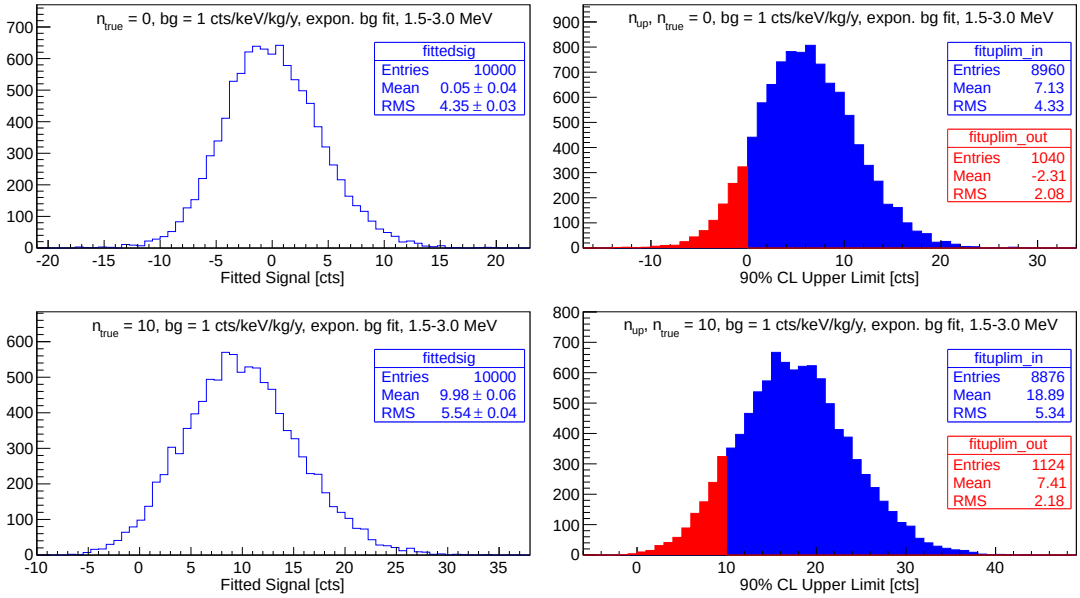

Figure G.6.: Example distributions of fit results for the exponential background approximation for the 1 cts/keV/kg/y MC data sample. Shown are the distributions of the point estimate and the distribution of 90 % CL upper limits.

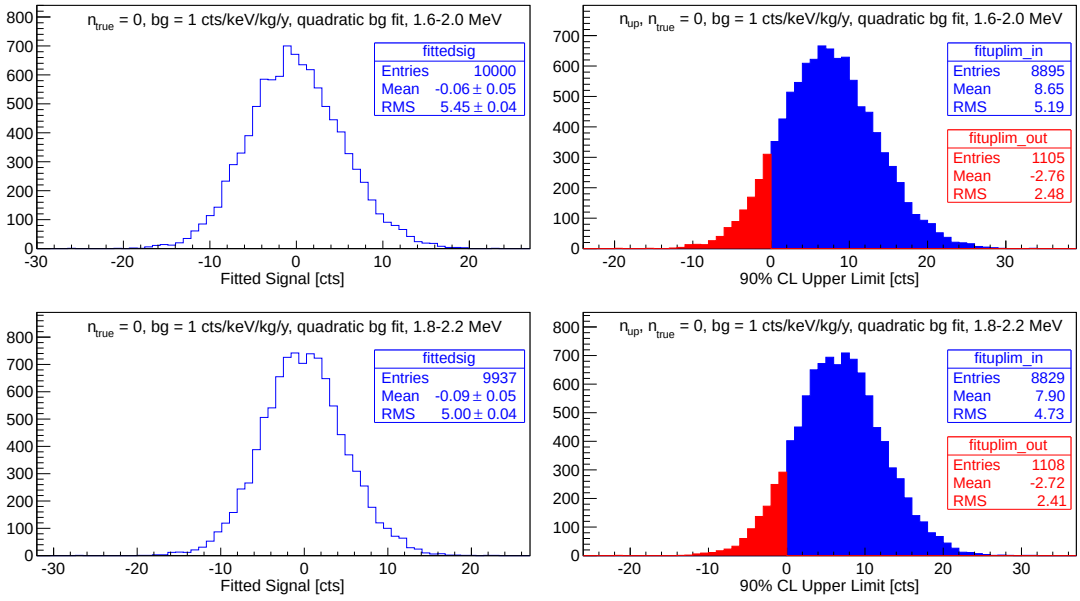

Figure G.7.: Distributions of fit results for the quadratic background approximation for the 1 cts/keV/kg/y MC data sample (0 signal events) at lower energies. The fit was performed for a signal search in the centre of the fit interval. The quadratic approximation is still valid for lower energies despite the higher slope of the background. The obtained number of signals shows a small negative bias, but it is smaller than 2 % of the statistical spread of the distribution. The coverage of about 89 % nearly matches the desired CL of 90 %. In the fitrange from 1.8-2.2 MeV 63 fits (0.63 %) did not converge.

H. CPG Array Sensitivity Results

BG $\left[\frac{\text{cts}}{\text{keV kg y}}\right]$	Live Time [y]	n_{sig}^{fit}	$\sigma(n_{sig}^{fit})$	n_{up}^{fit}	$\sigma(n_{up}^{fit})$	$T_{1/2}^{lim}$ [y]
5	1	-0.27 ± 0.12	12.2	16.0	12.9	$(1.2 \pm 0.5) \times 10^{21}$
5	2	-0.22 ± 0.17	17.2	22.6	17.9	$(1.6 \pm 0.7) \times 10^{21}$
5	3	-0.16 ± 0.21	21.2	27.6	21.9	$(2.0 \pm 0.9) \times 10^{21}$
5	5	0.04 ± 0.27	27.3	35.7	28.0	$(2.6 \pm 1.1) \times 10^{21}$
5	10	0.66 ± 0.39	38.9	50.9	39.6	$(3.6 \pm 1.6) \times 10^{21}$
1	1	0.00 ± 0.06	5.6	7.6	6.2	$(2.4 \pm 1.1) \times 10^{21}$
1	2	0.06 ± 0.08	7.7	10.6	8.4	$(3.5 \pm 1.6) \times 10^{21}$
1	3	-0.04 ± 0.09	9.4	12.7	10.1	$(4.4 \pm 1.9) \times 10^{21}$
1	5	0.08 ± 0.12	12.3	16.4	13.0	$(5.7 \pm 2.5) \times 10^{21}$
1	10	-0.07 ± 0.17	17.3	22.7	18.0	$(8.2 \pm 3.6) \times 10^{21}$

Table H.1.: Sensitivity results from fits with the extended likelihood method to MC data for the 64 detector array. The data sets contained no signal ($n_{sig}^{true} = 0$). The extended likelihood method shows again a good performance. From the 90 % CL upper limit on present signal events n_{sig}^{up} and its statistical spread $\sigma(n_{sig}^{up})$ half-life limits according to Equation (3.26) were calculated. For the efficiency the number $\varepsilon = 41\,\%$ deduced in Section 3.3.3 was used.

BG $\left[\frac{\text{cts}}{\text{keV kg y}}\right]$	FWHM @ 2.8 MeV [%]	Live Time [y]	n_{sig}^{fit}	$\sigma(n_{sig}^{fit})$	n_{up}^{fit}	$\sigma(n_{up}^{fit})$	$T_{1/2}^{lim}$ [y]
1	1.5	1	0.00 ± 0.06	5.6	7.6	6.2	$(2.9 \pm 1.3) \times 10^{25}$
1	1.5	2	0.06 ± 0.08	7.7	10.6	8.4	$(4.2 \pm 1.9) \times 10^{25}$
1	1.5	3	-0.04 ± 0.09	9.4	12.7	10.1	$(5.3 \pm 2.3) \times 10^{25}$
1	1.5	5	0.08 ± 0.12	12.3	16.4	13.0	$(6.8 \pm 3.0) \times 10^{25}$
1	1.5	10	-0.07 ± 0.17	17.3	22.7	18.0	$(9.8 \pm 4.3) \times 10^{25}$
1	1.0	1	0.02 ± 0.04	4.4	6.1	5.1	$(3.7 \pm 1.7) \times 10^{25}$
1	1.0	2	0.04 ± 0.06	6.1	8.3	6.8	$(5.4 \pm 2.4) \times 10^{25}$
1	1.0	3	0.01 ± 0.07	7.3	10.0	8.1	$(6.7 \pm 3.0) \times 10^{25}$
1	1.0	5	0.08 ± 0.09	9.5	12.8	10.2	$(8.7 \pm 3.8) \times 10^{25}$
1	1.0	10	-0.10 ± 0.13	13.4	17.7	14.1	$(1.3 \pm 0.6) \times 10^{26}$

Table H.2.: Sensitivity results from fits with the extended likelihood method to MC data for the 64,000 detector array (enriched to 90 % in ^{116}Cd). The other parameters are the same as given in Table H.1. The improvement of the energy resolution from 1.5 % FWHM to 1.0 % FWHM at 2.8 MeV leads to a sensitivity improvement of a factor 1.2 to 1.3.

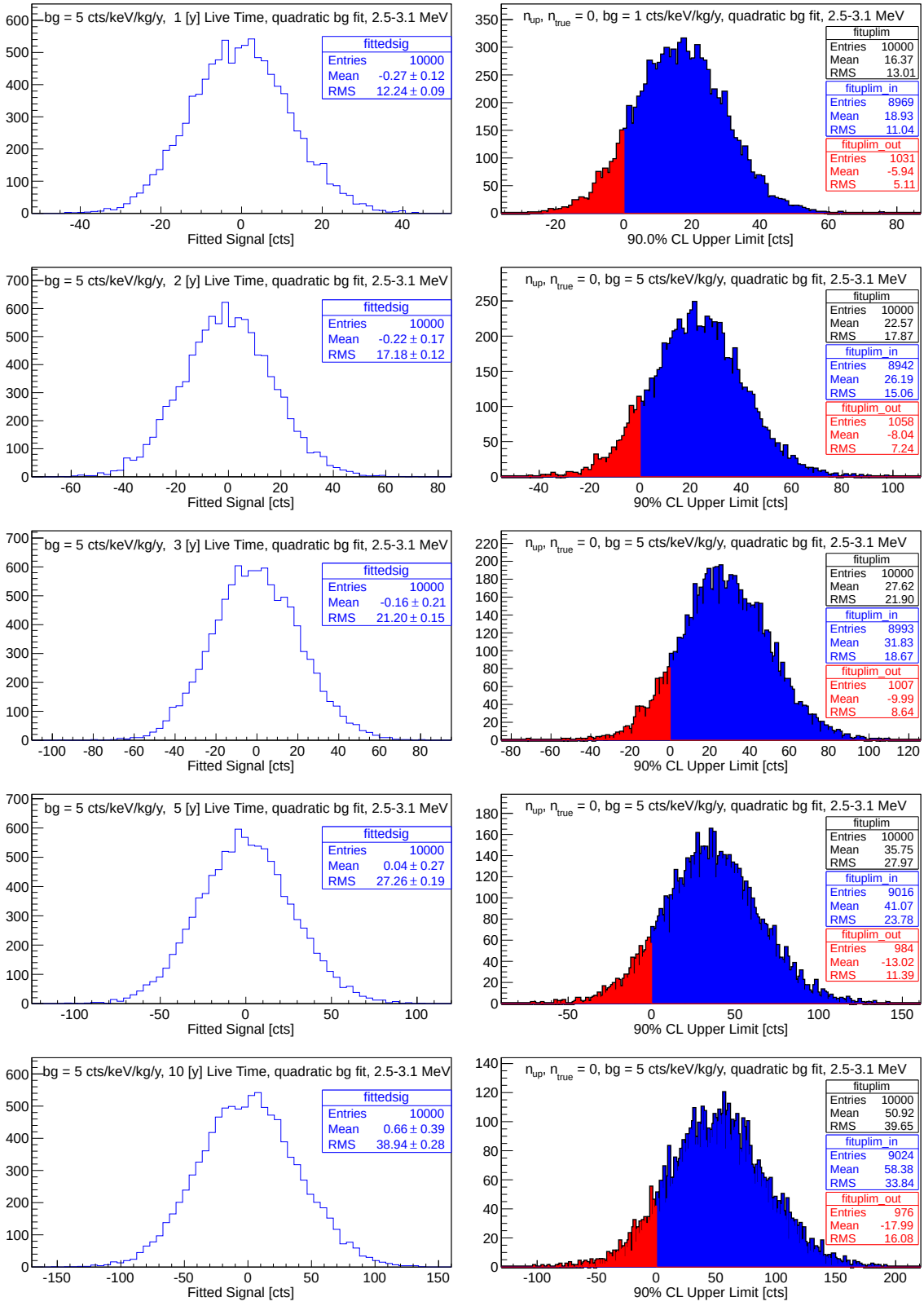

Figure H.1.: Distributions of fit results for the 64 detector array MC data with 5 /cts/keV/kg/y BG level.

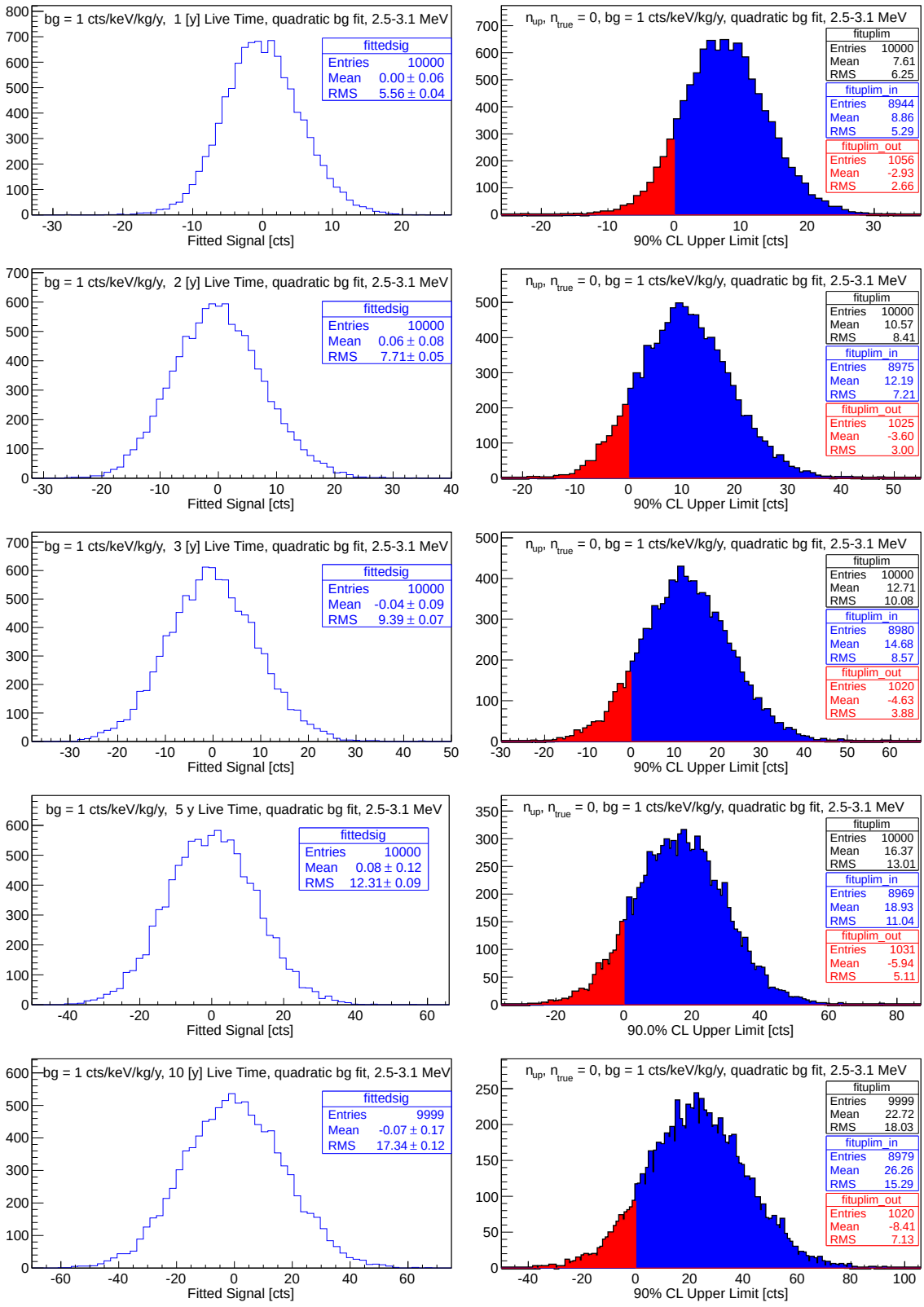

Figure H.2.: Distributions of fit results for the 64 detector array MC data with 1 /cts/keV/kg/y BG level. These data samples are equivalent to the 64,000 detector array with a background level of 10^{-3} /cts/keV/kg/y.

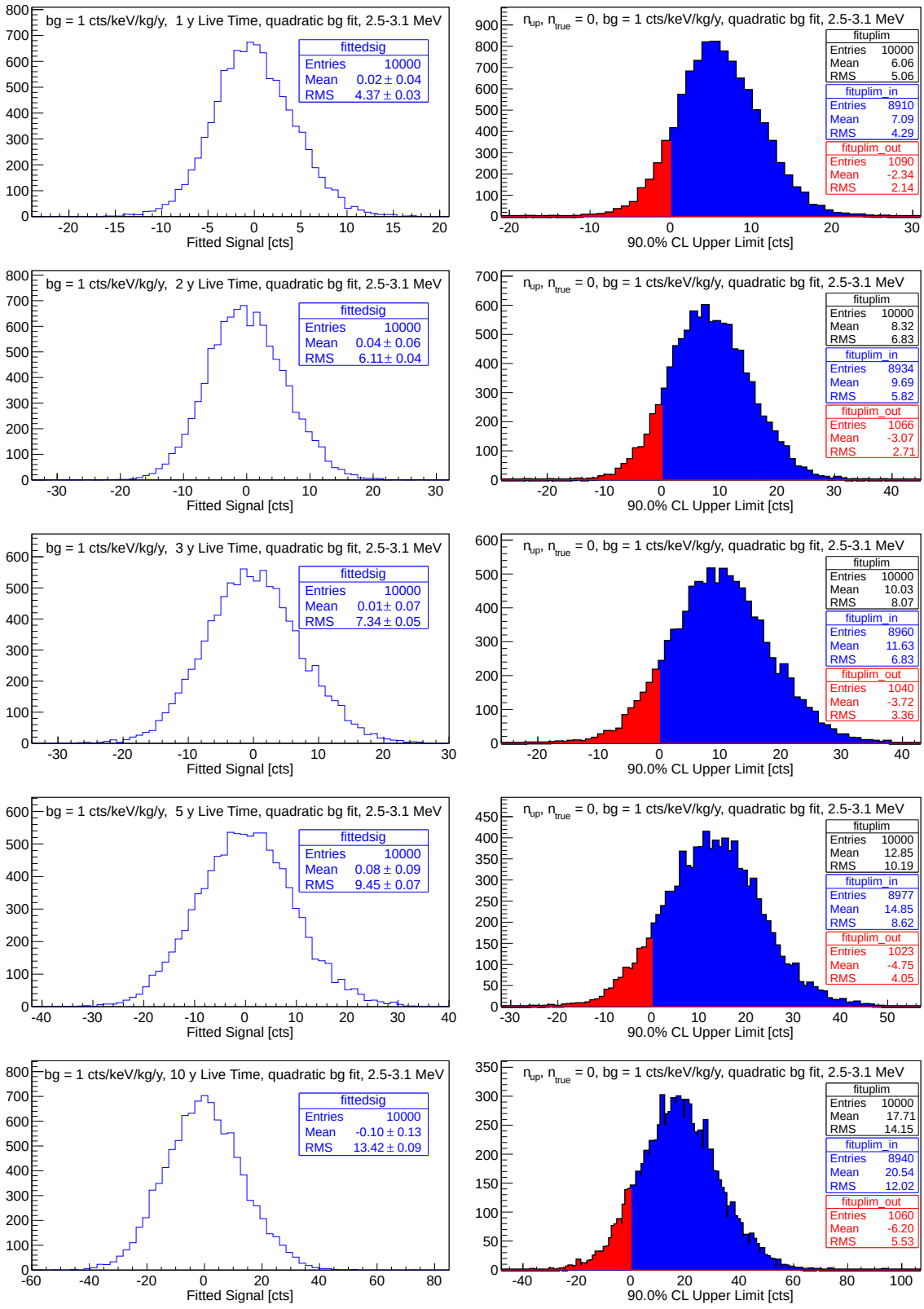

Figure H.3.: Distributions of fit results for the 64 detector array MC data with 1 /cts/keV/kg/y BG level and improved energy resolution to 1 % FWHM at 2.8 MeV. These data samples are equivalent to the 64,000 detector array with a background level of 10^{-3} /cts/keV/kg/y.

Publications

Articles

M. Schwenke, ... T. Koettig et al.
Exploration of Pixelated detectors for double beta decay searches within the COBRA experiment
Nuclear Instruments and Methods in Physics Research A, (2011)

T. Koettig on behalf of the COBRA collaboration
Search for Neutrinoless Double Beta Decay with the COBRA Experiment
PoS ICHEP 2010 (2010)

J.V. Dawson, ... T. Koettig et al.
Experimental study of double-β decay modes using a CdZnTe detector array
Physical Review C 80, 025502 (2009)

J.V. Dawson, ... T. Koettig et al.
An investigation into the ^{113}Cd beta decay spectrum using a CdZnTe array
Nuclear Physics A 818, 264-278 (2009)

Conference Talks

T. Koettig on behalf of the COBRA collaboration
Search for Neutrinoless Double Beta Decay with CdZnTe Semiconductor Detectors
International Workshop on Neutrinoless Double Beta Decay and Neutrino Oscillation
November 2011, Osaka (Japan)

T. Koettig
Search for Neutrinoless Double Beta Decay with the COBRA Experiment
International Student Workshop on Neutrinoless Double Beta Decay
November 2010, Assergi, LNGS (Italy)

T. Koettig
Aktuelle Ergebnisse des COBRA Experimentes
Gemeinsame DPG Frühjahrstagung der Fachverbände Extraterrestrische Physik (EP), ... Hadronen und Kerne (HK), ... Teilchenphysik (T), ... und Philosopie der Physik (AGPhil)
March 2010, Bonn (Germany)

T. Koettig on behalf of the COBRA Collaboration
Status des COBRA Experimentes
Joint Spring Meeting of the DPG division Hadronic and Nuclear Physics and the Nuclear Physics Board of the European Physical Society (EPS)
March 2009, Bochum (Germany)

Conference Posters

T. Koettig for the COBRA collaboration
Search for Neutrinoless Double Beta Decay with the COBRA Experiment
35th International Conference on High Energy Physics (ICHEP)
July 2010, Paris (France)

T. Koettig on behalf of the COBRA collaboration
COBRA – An Ultra-Low-Background Application of CdZnTe
16th International Workshop on Room Temperature Semiconductor X-Ray and Gamma-Ray Detectors (IEEE RTSD)
October 2008, Dresden (Germany)

Bibliography

[Abe11] K. Abe et al. Indication of Electron Neutrino Appearance from an Accelerator-Produced Off-Axis Muon Neutrino Beam. *Physical Review Letters*, 107(4):041801 (2011). doi:10.1103/PhysRevLett.107.041801.

[Ago03] S. Agostinelli et al. Geant4 - a simulation toolkit. *Nucl. Instrum. Methods Phys. Res., Sect. A*, 506(3):250 – 303 (2003). doi:10.1016/S0168-9002(03)01368-8.
URL http://www.sciencedirect.com/science/article/pii/S0168900203013688

[Ahm01] Q. R. Ahmad et al. Measurement of the rate of $\nu_e + d \rightarrow p + p + e^-$ interactions produced by ^{8}b solar neutrinos at the sudbury neutrino observatory. *Phys. Rev. Lett.*, 87:071301 (2001). doi:10.1103/PhysRevLett.87.071301.
URL http://link.aps.org/doi/10.1103/PhysRevLett.87.071301

[Ahn06] M. H. Ahn et al. Measurement of neutrino oscillation by the K2K experiment. *Phys. Rev. D*, 74:072003 (2006). doi:10.1103/PhysRevD.74.072003. ArXiv preprint 0606032.
URL http://link.aps.org/doi/10.1103/PhysRevD.74.072003

[Ahn12] J. K. Ahn et al. Observation of Reactor Electron Antineutrinos Disappearance in the RENO Experiment. *Phys. Rev. Lett.*, 108:191802 (2012). doi:10.1103/PhysRevLett.108.191802. ArXiv preprint 1204.0626.
URL http://link.aps.org/doi/10.1103/PhysRevLett.108.191802

[Ale09] M. Alex. A microcontroller based solution for remote laboratory data acquisition and control. Diploma Thesis, TU Dortmund (2009).

[All06] J. Allison et al. Geant4 developments and applications. *Nuclear Science, IEEE Transactions on*, 53(1):270 –278 (2006). doi:10.1109/TNS.2006.869826.

[An12] F. P. An et al. Observation of Electron-Antineutrino Disappearance at Daya Bay. *Phys. Rev. Lett.*, 108:171803 (2012). doi:10.1103/PhysRevLett.108.171803. ArXiv preprint 1203.1669.
URL http://link.aps.org/doi/10.1103/PhysRevLett.108.171803

[And11] E. Andreotti et al. ^{130}Te neutrinoless double-beta decay with CUORICINO. *Astroparticle Physics*, 34:822–831 (2011). doi:10.1016/j.astropartphys.2011.02.002.

[Apo10] J. Apostolakis et al. Validation and verification of Geant4 standard electromagnetic physics. *Journal of Physics: Conference Series*, 219(3):032044 (2010). URL http://stacks.iop.org/1742-6596/219/i=3/a=032044

[Arn08] C. Arnaboldi et al. Results from a search for the $0\nu\beta\beta$-decay of ^{130}Te. *Phys. Rev. C*, 78:035502 (2008). doi:10.1103/PhysRevC.78.035502. ArXiv preprint 0802.3439.
URL http://link.aps.org/doi/10.1103/PhysRevC.78.035502

[Arn11] R. Arnold et al. Measurement of the $\beta\beta$ Decay Half-Life of ^{130}Te with the NEMO-3 Detector. *Phys. Rev. Lett.*, 107:062504 (2011). doi:10.1103/PhysRevLett.107.062504.
URL http://link.aps.org/doi/10.1103/PhysRevLett.107.062504

[Aug12] M. Auger et al. Search for Neutrinoless Double-Beta Decay in ^{136}Xe with EXO-200. *Phys. Rev. Lett.*, 109:032505 (2012). doi:10.1103/PhysRevLett.109.032505.
URL http://link.aps.org/doi/10.1103/PhysRevLett.109.032505

[Bah68] J. N. Bahcall, N. A. Bahcall and G. Shaviv. Present Status of the Theoretical Predictions for the ^{37}Cl Solar-Neutrino Experiment. *Phys. Rev. Lett.*, 20:1209–1212 (1968). doi:10.1103/PhysRevLett.20.1209.
URL http://link.aps.org/doi/10.1103/PhysRevLett.20.1209

[Bar10] A. S. Barabash. Precise half-life values for two-neutrino double-β decay. *Phys. Rev. C*, 81:035501 (2010). doi:10.1103/PhysRevC.81.035501. ArXiv preprint 1003.1005.
URL http://link.aps.org/doi/10.1103/PhysRevC.81.035501

[Bea11] F. Beaujean, A. Caldwell, D. Kollár and K. Kröninger. BAT – The Bayesian Analysis Toolkit. *Journal of Physics: Conference Series*, 331(7):072040 (2011). URL http://stacks.iop.org/1742-6596/331/i=7/a=072040

[Bel04] A. Bellerive. Review of solar neutrino experiments. *Int.J.Mod.Phys.*, A19:1167–1179 (2004). doi:10.1142/S0217751X04019093. ArXiv preprint 0312045.

[Bel11] P. Belli et al. First observation of α decay of ^{190}Pt to the first excited level ($E_{\mathrm{exc}} = 137.2$ keV) of ^{186}Os. *Phys. Rev. C*, 83:034603 (2011). doi:10.1103/PhysRevC.83.034603.
URL http://link.aps.org/doi/10.1103/PhysRevC.83.034603

[Bel12a] P. Belli et al. Search for double-β decay processes in ^{106}Cd with the help of a $^{106}CdWO_4$ crystal scintillator. *Phys. Rev. C*, 85:044610 (2012). doi: 10.1103/PhysRevC.85.044610.
URL `http://link.aps.org/doi/10.1103/PhysRevC.85.044610`

[Bel12b] G. Bellini et al. Cosmic-muon flux and annual modulation in Borexino at 3800 m water-equivalent depth. *Journal of Cosmology and Astroparticle Physics*, 2012(05):015 (2012). ArXiv preprint 1202.6403.
URL `http://stacks.iop.org/1475-7516/2012/i=05/a=015`

[Ber12] J. Beringer et al. Review of Particle Physics. *Phys. Rev. D*, 86:010001 (2012). doi:10.1103/PhysRevD.86.010001.
URL `http://link.aps.org/doi/10.1103/PhysRevD.86.010001`

[Bet36] H. A. Bethe and R. F. Bacher. Nuclear Physics A. Stationary States of Nuclei. *Rev. Mod. Phys.*, 8:82–229 (1936). doi:10.1103/RevModPhys.8.82.
URL `http://link.aps.org/doi/10.1103/RevModPhys.8.82`

[Blo98] V. Blobel and E. Lohrmann. *Statistische und numerische Methoden der Datenanalyse*. Teubner-Studienbücher: Physik. Teubner, Stuttgart (1998).

[Blo07] T. Bloxham et al. First results on double β-decay modes of Cd, Te, and Zn Isotopes. *Phys. Rev. C*, 76:025501 (2007). doi:10.1103/PhysRevC.76.025501.
URL `http://link.aps.org/doi/10.1103/PhysRevC.76.025501`

[Bon11] Bongrand, Mathieu for the NEMO-3 Collaboration. Results of the NEMO-3 Double Beta Decay Experiment. *ArXiv e-prints*, 1105.2435 (2011).
URL `http://arxiv.org/abs/1105.2435`

[Bos11] M. Boswell et al. MaGe-a Geant4-Based Monte Carlo Application Framework for Low-Background Germanium Experiments. *IEEE Transactions on Nuclear Science*, 58:1212–1220 (2011). doi:10.1109/TNS.2011.2144619.

[Bru97] R. Brun and F. Rademakers. Root — an object oriented data analysis framework. *Nucl. Instrum. Methods Phys. Res., Sect. A*, 389(1–2):81 – 86 (1997). doi:10.1016/S0168-9002(97)00048-X.
URL `http://www.sciencedirect.com/science/article/pii/S016890029700048X`

[Bö05] J. K. Böhlke et al. Isotopic Compositions of the Elements, 2001. *Journal of Physical and Chemical Reference Data*, 34(1):57–67 (2005). doi:10.1063/1.1836764.
URL `http://link.aip.org/link/?JPR/34/57/1`

[Cab63] N. Cabibbo. Unitary symmetry and leptonic decays. *Phys. Rev. Lett.*, 10:531–533 (1963). doi:10.1103/PhysRevLett.10.531.
URL `http://link.aps.org/doi/10.1103/PhysRevLett.10.531`

[Cal09] A. Caldwell, D. Kollár and K. Kröninger. Bat – the bayesian analysis toolkit. *Computer Physics Communications*, 180(11):2197 – 2209 (2009). doi:10.1016/j.cpc.2009.06.026.
URL `http://www.sciencedirect.com/science/article/pii/S0010465509002045`

[Cas02] G. Casella and R. Berger. *Statistical inference*. Duxbury advanced series in statistics and decision sciences. Thomson Learning (2002).

[Chu99] S. Chu, L. Ekström and R. Firestone. The lund/lbnl nuclear data search (1999). Accessed 07/2012.
URL `http://nucleardata.nuclear.lu.se/nucleardata/toi/`

[Chy06] R. Chytracek, J. McCormick, W. Pokorski and G. Santin. Geometry description markup language for physics simulation and analysis applications. *IEEE Trans.Nucl.Sci.*, 53:2892 (2006). doi:10.1109/TNS.2006.881062.

[Cir10] G. Cirrone et al. Validation of the Geant4 electromagnetic photon cross-sections for elements and compounds. *Nucl. Instrum. Methods Phys. Res., Sect. A*, 618(1–3):315 – 322 (2010). doi:10.1016/j.nima.2010.02.112.
URL `http://www.sciencedirect.com/science/article/pii/S0168900210003682`

[Cle11] M. Clemenza, C. Maiano, L. Pattavina and E. Previtali. Radon-induced surface contaminations in low background experiments. *Eur.Phys.J.*, C71:1805 (2011). doi:10.1140/epjc/s10052-011-1805-0.

[Cou95] R. D. Cousins. Why isn't every physicist a Bayesian? *Am.J.Phys.*, 63:398 (1995). doi:10.1119/1.17901.

[Cow56a] C. Cowan, F. Harrison, L. Langer and F. Reines. A Test of neutrino anti-neutrino identity. *Nuovo Cim.*, 3:649–651 (1956). doi:10.1007/BF02744440.
URL `http://www.springerlink.com/content/1115401x0u153496/?MUD=MP`

[Cow56b] C. Cowan et al. Detection of the free neutrino: A Confirmation. *Science*, 124:103–104 (1956). doi:10.1126/science.124.3212.103.
URL `http://www.sciencemag.org/content/124/3212/103`

[Cow98] G. Cowan. *Statistical Data Analysis*. Oxford University Press (1998).

[Dan03] F. A. Danevich et al. Search for 2 β decay of cadmium and tungsten isotopes: Final results of the Solotvina experiment. *Phys.Rev.*, C68:035501 (2003). doi: 10.1103/PhysRevC.68.035501.

[Dav55] R. Davis. Attempt to Detect the Antineutrinos from a Nuclear Reactor by the $Cl^{37}(\overline{\nu},\ e^{-})A^{37}$ Reaction. *Phys. Rev.*, 97:766–769 (1955). doi:10.1103/PhysRev.97.766.
URL `http://link.aps.org/doi/10.1103/PhysRev.97.766`

[Dav68] R. Davis, D. S. Harmer and K. C. Hoffman. Search for neutrinos from the sun. *Phys. Rev. Lett.*, 20:1205–1209 (1968). doi:10.1103/PhysRevLett.20.1205.
URL `http://link.aps.org/doi/10.1103/PhysRevLett.20.1205`

[Dav11] G. S. Davies. NOνA: Present and Future. *ArXiv e-prints*, 1110.0112 (2011).
URL `http://arxiv.org/abs/1110.0112`

[Daw09a] J. Dawson et al. An Investigation into the 113-Cd Beta Decay Spectrum using a CdZnTe Array. *Nucl. Phys. A*, 818:264–278 (2009).

[Daw09b] J. V. Dawson et al. Experimental study of double-β decay modes using a CdZnTe detector array. *Phys. Rev. C*, 80:025502 (2009). doi:10.1103/PhysRevC.80.025502.
URL `http://link.aps.org/doi/10.1103/PhysRevC.80.025502`

[Det08] J. Detwiler, R. Henning, R. Johnson and M. Marino. A generic surface sampler for monte carlo simulations. *IEEE T. Nucl. Sci.*, 55(4):2329 –2333 (2008). doi: 10.1109/TNS.2008.2001063.

[Doi93] M. Doi and T. Kotani. Neutrinoless Modes of Double Beta Decay. *Progress of Theoretical Physics*, 89(1):139–159 (1993). doi:10.1143/PTP.89.139.
URL `http://ptp.ipap.jp/link?PTP/89/139/`

[Due11] M. Duerr, M. Lindner and K. Zuber. Consistency Test of Neutrinoless Double Beta Decay with one Isotope. *Phys.Rev.*, D84:093004 (2011). doi:10.1103/PhysRevD.84.093004.

[Ell87] S. R. Elliott, A. A. Hahn and M. K. Moe. Direct evidence for two-neutrino double-beta decay in ^{82}Se. *Phys. Rev. Lett.*, 59:2020–2023 (1987). doi:10.1103/PhysRevLett.59.2020.
URL `http://link.aps.org/doi/10.1103/PhysRevLett.59.2020`

[End11] Endicott Interconnect Detection & Imaging Systems. Semiconductor Detector Material Properties (2011).
URL `http://www.evmicroelectronics.com/pdf/material_prop.pdf`

[Fel98] G. J. Feldman and R. D. Cousins. A Unified approach to the classical statistical analysis of small signals. *Phys.Rev.*, D57:3873–3889 (1998). doi: 10.1103/PhysRevD.57.3873.

[Fir98] R. B. Firestone. *Table of Isotopes*. John Wiley & Sons, Inc., 8 edition (1998).

[Fri12] M. Fritts. Analytical model for event reconstruction in coplanar grid detectors. *Preprint submitted to Elsevier* (2012).

[Fuk98] Y. Fukuda et al. Evidence for oscillation of atmospheric neutrinos. *Phys. Rev. Lett.*, 81:1562–1567 (1998). doi:10.1103/PhysRevLett.81.1562.
URL `http://link.aps.org/doi/10.1103/PhysRevLett.81.1562`

[Fur39] W. Furry. On Transition Probabilities in Double Beta-Disintegration. *Phys.Rev.*, 56:1184–1193 (1939). doi:10.1103/PhysRev.56.1184.
URL `http://link.aps.org/doi/10.1103/PhysRev.56.1184`

[Gan12] A. Gando et al. Measurement of the double-β decay half-life of ^{136}Xe with the KamLAND-Zen experiment. *Phys. Rev. C*, 85:045504 (2012). doi:10.1103/PhysRevC.85.045504.
URL `http://link.aps.org/doi/10.1103/PhysRevC.85.045504`

[GC11] J. Gómez-Cadenas et al. Sense and sensitivity of double beta decay experiments. *J. Cosmol. Astropart. Phys.*, 2011(06):007 (2011). doi:10.1088/1475-7516/2011/06/007. ArXiv preprint 1010.5112.
URL `http://stacks.iop.org/1475-7516/2011/i=06/a=007`

[Gea10] Geant4 Collaboration. *Geant4 User's Guide for Application Developers*. Geant4 Collaboration, 4.9.4 edition (2010).
URL `http://geant4.web.cern.ch/geant4/support/index.shtml`

[Gil08] G. Gilmore. *Practical Gamma-ray Spectroscopy*. John Wiley & Sons, Inc., 2nd edition (2008).

[Giu10] A. Giuliani. Searches for neutrinoless double beta decay. *Acta Phys.Polon.*, B41:1447–1468 (2010).
URL `http://th-www.if.uj.edu.pl/acta/vol41/abs/v41p1447.htm`

[GM35] M. Goeppert-Mayer. Double beta-disintegration. *Phys.Rev.*, 48:512–516 (1935). doi:10.1103/PhysRev.48.512.

[Gon11] M. Goncharov et al. Probing the nuclides ^{102}Pd, ^{106}Cd, and ^{144}Sm for resonant neutrinoless double-electron capture. *Phys. Rev. C*, 84:028501 (2011). doi: 10.1103/PhysRevC.84.028501.
URL `http://link.aps.org/doi/10.1103/PhysRevC.84.028501`

[Gui11] V. E. Guiseppe et al. A Radon Progeny Deposition Model. In R. Ford, editor, *American Institute of Physics Conference Series*, volume 1338 of *American Institute of Physics Conference Series*, pages 95–100 (2011). doi:10.1063/1.3590915.

[Hal84] F. Halzen and A. D. Martin. *Quarks and Leptons, An Introductory Course in Modern Particle Physics*. John Wiley & Sons, Inc. (1984).

[Hau09] S. Hauf et al. Progress and Validation of Geant4 Based Radioactive Decay Simulation Using the Examples of Simbol-X and IXO. *ArXiv e-prints*, 0912.0233 (2009).
URL `http://arxiv.org/abs/0912.0233`

[Hau10] S. Hauf et al. Radioactive decay simulation with Geant4: experimental benchmarks and developments for X-ray astronomy applications. *ArXiv e-prints*, 1012.0139 (2010).
URL `http://arxiv.org/abs/1012.0139`

[He96] Z. He et al. 1-D position sensitive single carrier semiconductor detectors. *Nucl. Instrum. Methods Phys. Res., Sect. A*, 380(1–2):228 – 231 (1996). doi:10.1016/S0168-9002(96)00352-X.
URL `http://www.sciencedirect.com/science/article/pii/S016890029600352X`

[He01] Z. He. Review of the Shockley–Ramo theorem and its application in semiconductor gamma-ray detectors. *Nucl. Instrum. Methods Phys. Res., Sect. A*, 463(1–2):250 – 267 (2001). doi:10.1016/S0168-9002(01)00223-6.
URL `http://www.sciencedirect.com/science/article/pii/S0168900201002236`

[He05] Z. He and B. W. Sturm. Characteristics of depth-sensing coplanar grid CdZnTe detectors. *Nucl. Instrum. Methods Phys. Res., Sect. A*, 554(1–3):291 – 299 (2005). doi:10.1016/j.nima.2005.06.064.
URL `http://www.sciencedirect.com/science/article/pii/S0168900205013288`

[Hei09] M. Heine. Eine Suche nach Doppelbeta-Zerfällen von Cadmium-, Zink- und Tellur-Isotopen mit Positronen-Emission. Diploma Thesis, TU Dresden (2009).

[Heu95] G. Heusser. Low-radioactivity background techniques. *Ann.Rev.Nucl.Part.Sci.*, 45:543–590 (1995). doi:10.1146/annurev.ns.45.120195.002551.

[Hir88] K. Hirata et al. Experimental study of the atmospheric neutrino flux. *Physics Letters B*, 205(2–3):416 – 420 (1988). doi:10.1016/0370-2693(88)91690-5.

URL http://www.sciencedirect.com/science/article/pii/0370269388916905

[Hir94] M. Hirsch, K. Muto, T. Oda and H. V. Klapdor-Kleingrothaus. Nuclear structure calculation of $0\beta^+\,\beta^+$, β^+/EC and EC/EC decay matrix elements. *Zeitschrift für Physik A Hadrons and Nuclei*, 347:151–160 (1994). 10.1007/BF01292371.
URL http://dx.doi.org/10.1007/BF01292371

[Hos06] J. Hosaka et al. Three flavor neutrino oscillation analysis of atmospheric neutrinos in Super-Kamiokande. *Phys. Rev. D*, 74:032002 (2006). doi: 10.1103/PhysRevD.74.032002. ArXiv preprint 0604011.
URL http://link.aps.org/doi/10.1103/PhysRevD.74.032002

[Ing50] M. G. Inghram and J. H. Reynolds. Double Beta-Decay of Te^{130}. *Phys. Rev.*, 78:822–823 (1950). doi:10.1103/PhysRev.78.822.2.
URL http://link.aps.org/doi/10.1103/PhysRev.78.822.2

[ISO00] Determination of detection limit and decision threshold for ionizing radiation measurements - Part 3: Fundamentals and application to counting measurements by high resolution gamma spectrometry, without the influence of sample treatment (2000).

[Iva11] V. Ivanchenko et al. Recent Improvements in Geant4 Electromagnetic Physics Models and Interfaces. *Progress in Nuclear Science and Technology*, 2:898–903 (2011).
URL http://www.aesj.or.jp/publication/pnst002/data/898-903.pdf

[Jam75] F. James and M. Roos. Minuit: A System for Function Minimization and Analysis of the Parameter Errors and Correlations. *Comput. Phys. Commun.*, 10:343–367 (1975). doi:10.1016/0010-4655(75)90039-9.

[Jam81] F. James. DETERMINING THE STATISTICAL SIGNIFICANCE OF EXPERIMENTAL RESULTS. CERN Report Number CERN-DD-81-02, C80-09-14-3 (1981).
URL http://cdsweb.cern.ch/record/1050342/files/dd-81-02.pdf

[Jam90] F. James. A Review of Pseudorandom Number Generators. *Comput.Phys.Commun.*, 60:329–344 (1990). doi:10.1016/0010-4655(90)90032-V.

[Jam91] F. James and M. Roos. Statistical notes on the problem of experimental observations near an unphysical region. *Phys.Rev.*, D44:299–301 (1991). doi: 10.1103/PhysRevD.44.299.

[Jam04] F. James and M. Winkler. *MINUIT User's Guide*. CERN, Geneva (2004).
URL http://seal.cern.ch/documents/minuit/mnusersguide.pdf

[Jam08] F. James. *Statistical methods in experimental physics*. World Scientific, 2. ed., repr. edition (2008).

[Jos11] J. M. Jose et al. Timepix background studies for double beta decay experiments. *Journal of Instrumentation*, 6(11):C11030 (2011).
URL `http://stacks.iop.org/1748-0221/6/i=11/a=C11030`

[KAE12] KAERI (Korea Atomic Energy Research Institute). Table of nuclides (Accessed 07/2012).
URL `http://atom.kaeri.re.kr/`

[Kay10] W. Kaye, Y. Boucher, F. Zhang and Z. He. Calibration and operation of the polaris 18-detector cdznte array. In *Nuclear Science Symposium Conference Record (NSS/MIC), 2010 IEEE*, pages 3821 –3824 (2010). doi: 10.1109/NSSMIC.2010.5874527.

[Kie05] H. Kiel. Determination of the Half Lives of Rare Decays of Cd, Te and Zn Isotopes for the COBRA Experiment. Ph.D. thesis, TU Dortmund (2005).

[Kim11] J. C. Kim et al. Charge sharing in common-grid pixelated CdZnTe detectors. *Nucl. Instrum. Methods Phys. Res., Sect. A*, 654(1):233 – 243 (2011). doi: 10.1016/j.nima.2011.06.038.
URL `http://www.sciencedirect.com/science/article/pii/S0168900211011545`

[KK01a] H. Klapdor-Kleingrothaus, A. Dietz, H. Harney and I. Krivosheina. Evidence for neutrinoless double beta decay. *Mod.Phys.Lett.*, A16:2409–2420 (2001). doi:10.1142/S0217732301005825.

[KK01b] H. Klapdor-Kleingrothaus et al. Latest results from the HEIDELBERG-MOSCOW double beta decay experiment. *The European Physical Journal A - Hadrons and Nuclei*, 12:147–154 (2001). doi:10.1007/s100500170022.
URL `http://dx.doi.org/10.1007/s100500170022`

[KK06] H. Klapdor-Kleingrothaus and I. V. Krivosheina. The evidence for the observation of 0nu beta beta decay: The identification of 0nu beta beta events from the full spectra. *Mod. Phys. Lett.*, A21:1547–1566 (2006). doi: 10.1142/S0217732306020937.

[Kob73] M. Kobayashi and T. Maskawa. *cp*-violation in the renormalizable theory of weak interaction. *Progress of Theoretical Physics*, 49(2):652–657 (1973). doi: 10.1143/PTP.49.652.
URL `http://ptp.ipap.jp/link?PTP/49/652/`

[Koe08] T. Koettig. Optimisation of Contacting and Energy Resolution of CdZnTe Detectors with Respect to Low Background Application. Diploma Thesis, TU Dortmund (2008).

[Kol10] V. S. Kolhinen et al. Double-β decay q value of ^{150}Nd. *Phys. Rev. C*, 82:022501 (2010). doi:10.1103/PhysRevC.82.022501.
URL `http://link.aps.org/doi/10.1103/PhysRevC.82.022501`

[Kom11] E. Komatsu et al. Seven-year Wilkinson Microwave Anisotropy Probe (WMAP) Observations: Cosmological Interpretation. *The Astrophysical Journal Supplement Series*, 192(2):18 (2011).
URL `http://stacks.iop.org/0067-0049/192/i=2/a=18`

[Kra05] C. Kraus et al. Final results from phase II of the Mainz neutrino mass searchin tritium β decay. *The European Physical Journal C - Particles and Fields*, 40:447–468 (2005). 10.1140/epjc/s2005-02139-7.
URL `http://dx.doi.org/10.1140/epjc/s2005-02139-7`

[L'E88] P. L'Ecuyer. Efficient and Portable Combined Random Number Generators. *Communications of the ACM*, 31:742–749 (1988).
URL `http://dl.acm.org/citation.cfm?id=62969`

[Leo94] W. R. Leo. *Techniques for Nuclear and Particle Physics Experiments*. Springer, 2nd rev. edition (1994).

[Luk94] P. N. Luke. Single-polarity charge sensing in ionization detectors using coplanar electrodes. *Appl. Phys. Lett.*, 65:2884 (1994).

[Maj37] E. Majorana. Teoria simmetrica dell'elettrone e del positrone. *Il Nuovo Cimento (1924-1942)*, 14:171–184 (1937). 10.1007/BF02961314.
URL `http://dx.doi.org/10.1007/BF02961314`

[Mak62] Z. Maki, M. Nakagawa and S. Sakata. Remarks on the Unified Model of Elementary Particles. *Progress of Theoretical Physics*, 28(5):870–880 (1962). doi:10.1143/PTP.28.870.
URL `http://ptp.ipap.jp/link?PTP/28/870/`

[Mam11] F. Mamedov, P. Čermák, K. Smolek and I. Štekl. Measurement of radon diffusion through shielding foils for the SuperNEMO experiment. *Journal of Instrumentation*, 6(01):C01068 (2011).
URL `http://stacks.iop.org/1748-0221/6/i=01/a=C01068`

[Mat98] M. Matsumoto and T. Nishimura. Mersenne Twistor: A 623-diminsionally equidistributed uniform pseudorandom number generator. *ACM Transactions on Modeling and Computer Simulation*, 8:3–30 (1998).

[McC10] P. M. McCowan and R. C. Barber. q value for the double-β decay of ^{136}Xe. *Phys. Rev. C*, 82:024603 (2010). doi:10.1103/PhysRevC.82.024603.
URL `http://link.aps.org/doi/10.1103/PhysRevC.82.024603`

[Mei11] G. Meierhofer and the GERDA collaboration. Gerda - a new neutrinoless double beta experiment using 76 ge. *Journal of Physics: Conference Series*, 312(7):072011 (2011).
URL `http://stacks.iop.org/1742-6596/312/i=7/a=072011`

[Mü07] D. Münstermann. Construction of a Low Background Facility for the COBRA Experiment and its Performance. Ph.D. thesis, TU Dortmund (2007).

[Ned13] T. Neddermann. Thesis currently in preparation. Ph.D. thesis, TU Dortmund (2013).

[NIS] NIST. Estar. Homepage. Accessed on 2012/07/01.
URL `http://physics.nist.gov/PhysRefData/Star/Text/ESTAR.html`

[Nuc10] A. Nucciotti. Neutrino mass calorimetric searches in the MARE experiment. *ArXiv preprints*, 1012.2290 (2010).
URL `http://arxiv.org/abs/1012.2290`

[Oeh04] S. Oehl. A Shielding System Against Neutrons for the COBRA-Experiment and Characterisation of CdZnTe Detectors with the Transient Current Technique. Diploma Thesis, TU Dortmund (2004).

[Ott08] E. W. Otten and C. Weinheimer. Neutrino mass limit from tritium β decay. *Reports on Progress in Physics*, 71(8):086201 (2008). doi:10.1088/0034-4885/71/8/086201. ArXiv preprint 0909.2104.

[Pav08] M. Pavan et al. Control of bulk and surface radioactivity in bolometric searches for double-beta decay. *Eur.Phys.J.*, A36:159–166 (2008). doi:10.1140/epja/i2007-10577-0.

[Per65] R. W. Perkins and J. M. Nielsen. Cosmic-ray produced radionuclides in the environment. *Health Physics*, 11:1297–1304 (1965).

[Pon60] B. Pontecorvo. ELECTRON AND MUON NEUTRINOS. *Sov.Phys.JETP*, 10:1236–1240 (1960).

[Pon00] O. Ponkratenko, V. Tretyak and Y. Zdesenko. The Event generator DECAY4 for simulation of double beta processes and decay of radioactive nuclei. *Phys.Atom.Nucl.*, 63:1282–1287 (2000). doi:10.1134/1.855784,10.1134/1.855784.

[Por00] E. Porras et al. Production rate of proton-induced isotopes in different materials. *Nucl. Instrum. Methods Phys. Res., Sect. B*, 160(1):73–125 (2000). Cited By (since 1996): 5.

[Pov08] B. Povh, K. Rith, C. Scholz and F. Zetsche. *Particles and Nuclei: An Introduction to the Physical Concepts*. Springer, 6th edition (2008).

[Rac37] G. Racah. Sulla simmetria tra particelle e antiparticelle. *Il Nuovo Cimento (1924-1942)*, 14:322–328 (1937). 10.1007/BF02961321.
URL http://dx.doi.org/10.1007/BF02961321

[Rah11] S. Rahaman et al. Double-beta decay Q values of 116Cd and 130Te. *Physics Letters B*, 703(4):412 – 416 (2011). doi:10.1016/j.physletb.2011.07.078.
URL http://www.sciencedirect.com/science/article/pii/S0370269311008975

[Raj] S. Rajek. Thesis currently in preparation. Ph.D. thesis, TU Dortmund.

[Ree09] C. J. Reeve. Data analysis and background studies for the cobra neutrinoless double-beta decay experiment. Ph.D. thesis, University of Sussex (2009).

[Rei56] F. Reines and C. L. Cowan. The Neutrino. *Nature*, 178:446–449 (1956). doi:10.1038/178446a0.
URL http://www.nature.com/nature/journal/v178/n4531/abs/178446a0.html

[Rod12] W. Rodejohann. Neutrinoless double beta decay and neutrino physics. *ArXiv e-prints*, 1206.2560 (2012).
URL http://arxiv.org/abs/1206.2560

[Rol01] W. A. Rolke and A. M. López. Confidence intervals and upper bounds for small signals in the presence of background noise. *Nucl. Instrum. Methods Phys. Res., Sect. A*, 458(3):745 – 758 (2001). doi:10.1016/S0168-9002(00)00935-9.
URL http://www.sciencedirect.com/science/article/pii/S0168900200009359

[Rol05] W. A. Rolke, A. M. López and J. Conrad. Limits and confidence intervals in the presence of nuisance parameters. *Nucl. Instrum. Methods Phys. Res., Sect. A*, 551(2–3):493 – 503 (2005). doi:10.1016/j.nima.2005.05.068.
URL http://www.sciencedirect.com/science/article/pii/S016890020501291X

[Sch09] K. Schreiner. Evaluation of Mounting and Passivation Techniques for Low-Background CdZnTe Detectors. Diploma Thesis, TU Dortmund (2009).

[Sch10] S. Schira. Charakterisierung des Detektorsystems der Dortmund-Low-Background-Facility. Bachelor thesis, TU Dortmund (2010).

[Sch11a] O. Schulz. Exploration of new Data Acquisition and Background Reduction Techniques for the COBRA Experiment. Ph.D. thesis, TU Dortmund (2011).

[Sch11b] M. Schwenke et al. Exploration of pixelated detectors for double beta decay searches within the COBRA experiment. *Nucl.Instrum.Meth.*, A650:73–78 (2011).

[Sch12a] A. Schuberta et al. The MAJORANA DEMONSTRATOR: A Search for Neutrinoless Double-beta Decay of Germanium-76. *AIP Conf.Proc.*, 1441:480–482 (2012). doi:10.1063/1.3700592. ArXiv preprint 1109.1567.
URL `http://link.aip.org/link/?APC/1441/480/1`

[Sch12b] B. Schwingenheuer. Searches for neutrinoless double beta decay. *Journal of Physics: Conference Series*, 375(4):042007 (2012). ArXiv preprint 1201.4916.
URL `http://stacks.iop.org/1742-6596/375/i=4/a=042007`

[Sci09] N. D. Scielzo et al. Double-β-decay Q values of ^{130}Te, ^{128}Te, and ^{120}Te. *Phys. Rev. C*, 80:025501 (2009). doi:10.1103/PhysRevC.80.025501.
URL `http://link.aps.org/doi/10.1103/PhysRevC.80.025501`

[Smo12] C. Smorra et al. Direct mass measurements of cadmium and palladium isotopes and their double-β transition q values. *Phys. Rev. C*, 85:027601 (2012). doi:10.1103/PhysRevC.85.027601.
URL `http://link.aps.org/doi/10.1103/PhysRevC.85.027601`

[Ste74] E. P. Steinberg and L. Winsberg. Recoil properties of ^{22}Na and ^{24}Na produced in the interaction of ^{27}Al with 3- to 300-GeV protons. *Phys. Rev. C*, 10:1925–1927 (1974). doi:10.1103/PhysRevC.10.1925.
URL `http://link.aps.org/doi/10.1103/PhysRevC.10.1925`

[Suh98] J. Suhonen and O. Civitarese. Weak-interaction and nuclear-structure aspects of nuclear double beta decay. *Physics Reports*, 300(3–4):123 – 214 (1998). doi:10.1016/S0370-1573(97)00087-2.
URL `http://www.sciencedirect.com/science/article/pii/S0370157397000872`

[Tav06] O. Tavares, M. Terranova and E. Medeiros. New evaluation of alpha decay half-life of 190Pt isotope for the Pt–Os dating system. *Nucl. Instrum. Methods Phys. Res., Sect. B*, 243(1):256 – 260 (2006). doi:10.1016/j.nimb.2005.08.122.
URL `http://www.sciencedirect.com/science/article/pii/S0168583X05016472`

[Teb11] J. Tebrügge. New read-out electronics and pulse shape analysis for the COBRA experiment. Diploma Thesis, TU Dortmund (2011).

[Tip87] P. A. Tippler. *College Physics*. Worth Pub (1987).

[Tre95] V. Tretyak and Y. G. Zdesenko. Tables of double beta decay data. *Atom.Data Nucl.Data Tabl.*, 61:43–90 (1995).

[Wei35] C. Weizsacker. Zur Theorie der Kernmassen. *Z.Phys.*, 96:431–458 (1935).

[Wol10] J. Wolf. The katrin neutrino mass experiment. *Nucl. Instrum. Methods Phys. Res., Sect. A*, 623(1):442 – 444 (2010). doi:10.1016/j.nima.2010.03.030. Particle Physics.
URL `http://www.sciencedirect.com/science/article/pii/S0168900210005942`

[Zha07] F. Zhang, Z. He and C. Seifert. A Prototype Three-Dimensional Position Sensitive CdZnTe Detector Array. *IEEE Transactions on Nuclear Science*, 54(4):843–848 (2007). doi:10.1109/TNS.2007.902354.

[Zha12] F. Zhang et al. Characterization of the H3D ASIC Readout System and 6.0 cm^3 3-D Position Sensitive CdZnTe Detectors. *Nuclear Science, IEEE Transactions on*, 59(1):236 –242 (2012). doi:10.1109/TNS.2011.2175948.

[Zub01] K. Zuber. COBRA: Double beta decay searches using CdTe detectors. *Phys.Lett.*, B519:1–7 (2001). doi:10.1016/S0370-2693(01)01056-5.

[Zub12] K. Zuber. *Neutrino physics*. Series in high energy physics, cosmology, and gravitation. CRC Press, 2nd edition (2012).

List of Figures

List of Tables

Acronyms

$0\nu\beta\beta$-**decay** neutrinoless double beta decay. 11–17, 23, 24, 26, 43, 53, 55–57, 59–61, 72–78, 113–115, 117, 122, 124, 125, 127, 129, 132, 134, 137, 138

$2\nu\beta\beta$-**decay** two-neutrino double beta decay. 11–14, 17, 18, 72, 78

ADC analog to digital converter. 28, 124, 127–129

ALICE A Large Ion Collider Experiment, homepage `http://aliceinfo.cern.ch`. 35

AMANDA Antarctic Muon And Neutrino Detection Array, pilot project for IceCube experiment, see `http://icecube.wisc.edu/`. 28

ASIC application-specific integrated circuit. 52

ATLAS A Toroidal LHC Apparatus, homepage `http://atlas.ch/`. 35

BAT Bayesian Analysis Tool. 111

BG background. 102, 122, 124, 132, 134, 135, 163, 165, 166, 171–173

CA collecting anode. 18–22, 28, 30, 31

CDF cumulative distribution function. 70, 143–145, 152

CdZnTe Cadmium Zinc Telluride, a room temperature semiconductor material. 14, 16–21, 23, 49, 51–53, 55, 60, 72–74, 79, 83–85, 87, 125, 131, 137, 138

CERN Conseil Européen pour la Recherche Nucléaire, Particle physics laboratory at Genf, Switzerland, homepage `http://cern.ch`. 39, 112

CKM Cabibbo–Kobayashi–Maskawa. 8

CL Confidence Level. 9, 15, 69, 71, 72, 78, 81, 103, 106, 108–110, 118, 122, 123, 125, 126, 128–135, 138, 151, 154, 155, 164, 167–169

CLHEP Class Library for High Energy Physics, C++ libraries, homepage `http://proj-clhep.web.cern.ch`. 36

COBRA CdZnTe $0\nu\beta\beta$ Research Apparatus. 15–18, 21–29, 33, 35, 39, 43, 49, 52, 57, 63–65, 79, 88, 89, 92, 99, 108, 113, 115, 122, 124, 129, 137–141, 175, 176

CP Charge- and Parity Symmetry. 8

CPG coplanar grid. 18–22, 27, 32, 33, 41, 42, 49, 50, 52, 64, 73, 74, 76, 79, 82, 83, 137, 138

CPU Central Processing Unit. 42, 123

CSDA continuous slowing down approximation. 83–85

CSG Constructed Solid Geometry. 38

CUORE Cryogenic Underground Observatory for Rare Events, homepage `http://crio.mib.infn.it/wigmi/pages/cuore.php`. 57

DAQ data acquisition. 28, 32, 137

DESY Deutsches Elektronen-Synchrotron, Hamburg, homepage `http://www.desy.de`. 33

DLB Dortmund Low Background Facility. 24, 39, 40, 42, 43, 45–49, 51, 52, 79, 92

EC Electron Capture. 11, 17, 103–105

EIDIS EI Detection & Imaging Systems, formerly eV Microelectronics, formerly eV Products, `http://www.evmicroelectronics.com/`. 29, 57, 80, 81, 99, 108, 124

EM Electromagnetic. 24, 28, 29, 35, 36

EMI electromagnetic interference. 24–26, 28–32

ESA European Space Agency, homepage `http://www.esa.int`. 35

EXO Enriched Xenon Observatory, homepage `http://www-project.slac.stanford.edu/exo/`. 15, 16

FADC fast analog to digital converter. 28, 31, 32, 124, 127, 128, 130

FMF Freiburger Materialforschungszentrum. 79

FWHM full width at half maximum. 17, 28, 46, 52, 53, 71, 72, 97, 101, 102, 106, 108, 119, 129, 131–134, 151, 152, 170, 173

GB grid bias. 18–21, 24, 31, 32

GDML Geometry Description Markup Language, homepage `http://gdml.web.cern.ch/GDML/`. 38–41, 43, 45, 49, 54, 138

Geant4 GEometry ANd Tracking, C++ based software framework for the simulation of particles through matter [All06, Ago03], see also `http://http://geant4.cern.ch`. 35–40, 42, 43, 45, 46, 49, 50, 52, 53, 58, 61, 64, 67, 83

GERDA GERmanium Detector Array for the search of $0\nu\beta\beta$-decay in ^{76}Ge at LNGS, homepage: `http://www.mpi-hd.mpg.de/gerda/`. 16

HdM Heidelberg-Moscow $0\nu\beta\beta$-decay experiment. 15, 23, 26

HV high voltage. 18, 20, 21, 24, 27, 30–32, 108

IC integrated circuit. 30

ICP-MS inductively coupled plasma mass spectrometry. 80, 81

ID identifier. 40, 41

IT Isomeric Transition, γ transition from an isomeric state of a nucleus [Gil08]. 104, 105

KATRIN KArlsruhe TRItium Neutrino experiment, homepage `http://www.katrin.kit.edu/`. 9

LNGS Laboratori Nazionali del Gran Sasso, underground physics laboratory close to l'Aquila, Italy, homepage `http://www.lngs.infn.it/`. 22, 23, 25, 31, 52, 53, 56, 63, 65, 66, 69, 72, 80, 81, 90–92, 95, 96, 99, 106, 107, 117–119, 124, 137–140, 157

MAJORANA $0\nu\beta\beta$-decay experiment for ^{76}Ge, homepage `http://www.npl.washington.edu/majorana/`. 16

MAnTiCORE Multiple-Analysis Toolkit for the COBRA Experiment. 89, 90

MARE Microcalorimeter Arrays for a Rhenium Experiment, homepage `http://mare.dfm.uninsubria.it`. 10

MC Monte Carlo. 35, 43, 103, 113, 118–123, 129, 131, 133–135, 167–173

MINOS MINUIT algorithm to calculate parameter errors. 112, 118, 119

MINUIT Numerical minimization program developed at CERN, also implemented in ROOT as MINUIT2, see also `http://lcgapp.cern.ch/project/cls/work-packages/mathlibs/minuit/index.html` for documentation. 111–113, 118

ML Maximum Likelihood. 111–113, 119, 120, 134

mwe meters of water equivalent. 22

NCA non-collecting anode. 18–22, 28, 30, 31

NIM Nuclear Instrumentation Module. 31

NIST National Institute of Standards and Technology, homepage `http://www.nist.gov/index.html`. 43, 60

PCB Printed Circuit Board. 29, 31, 53–55, 57, 60, 62, 63, 65, 69, 71, 73, 77, 147, 148

PDF probability density function. 38, 69, 70, 110, 111, 113, 114, 116, 117, 143–145, 151

PDG Particle Data Group, homepage `http://pdg.lbl.gov/`. 8

PE Polyethylene. 23–25

PMNS Pontecorvo-Maki-Nakagava-Sakata. 8–10

POM Polyoxymethylene, a thermoplastic. 27

ppb parts per billion. 80

R&D Research and Development. 16, 17, 22, 25, 26, 33, 137, 138

ROI Region Of Interest. 23, 24, 26, 27, 35, 56–60, 63–65, 71, 76, 77, 79, 82, 83, 94, 108, 115, 118, 120–122, 129

ROOT Object orientated analysis framework developed at CERN [Bru97], see also `http://root.cern.ch/`. 36, 39, 118, 153

SE single ended. 29–32

SM Standard Model of Particle Physics. 7, 10, 11

VENOM Vicious Evil Network Of Mayhem, Geant4 based simulation program for COBRA. 35–43, 126, 127, 138

VKTA Verein für Kernverfahrenstechnik und Analytik Rossendorf e.V. 80, 81

VME Versa Module Eurocard (Bus), IEEE 1014-1987. 32

voxel volumetric pixel. 37, 41, 53–55, 57, 59, 60, 63, 75

WMAP Wilkinson Microwave Anisotropy Probe, homepage `http://map.gsfc.nasa.gov/`. 9

XML Extensible Markup Language, data format for encoding documents both human- and machine readable. 39